4036

Dynamic Interaction in Cable-Connected Equipment

Kee-Jeung Hong

Armen Der Kiureghian

Jerome L. Sackman

Structural Engineering, Mechanics & Materials

Department of Civil & Environmental Engineering

University of California, Berkeley

Berkeley, California 94720

A report on research sponsored by Pacific Gas & Electric Company (PG&E)

and the California Energy Commission

Spring 2003

ABSTRACT

Conductor cables used in electrical substations are typically made of helically wrapped aluminum wires. A theoretical model is developed to describe the nonlinear moment-curvature relationship of such cables by accounting for the friction and slippage between wires in neighboring layers.

A first-order differential condition for slippage of the wire is derived by noting that a wire can slip if the unbalanced tension force in a differential element of the wire, which is caused by bending, equals the maximum friction force on the wire that can be generated. The wire remains in a stick state if the unbalanced tension force is less than the maximum friction force that can be generated. In each cross section of the cable, two regions are identified: a region of stick and a region of slip. In the stick region, the continuity of axial strain in each wire along with the Bernoulli-Euler-Navier kinematic beam assumption is used to determine the axial force in the wire. In the slip region, the condition for the slippage of the wire is used to determine the axial force in the wire. The resultant moment of the cable is nonlinearly related to the curvature of the cable; this nonlinear relationship also depends on the axial strain (or axial force) in the cable. Accordingly, the secant bending stiffness of the cable varies between two extreme limits. These correspond to the extreme cases of fully slipping and fully stuck wires.

A finite element model for the cable is developed by using the geometrically exact rod model and fitting the nonlinear moment-curvature-tension relationship of the cable with a bilinear elasto-plastic constitutive model. Kinematic hardening is assumed to represent the nonlinear bending behavior of the cable. Comparisons are made between predictions by the finite element model and tests conducted by other investigators under static and dynamic conditions.

The finite element model developed is used to investigate the effect of dynamic interaction between two idealized equipment items connected by a conductor cable and subjected to ground motion. It is shown that the dynamic cable force can be significantly larger than the cable force under static equilibrium conditions. Furthermore, it is shown that the equipment response in the connected system can be strongly amplified relative to the response of the stand-alone equipment, particularly for the equipment item having the higher frequency. A simple predictive formula to estimate the amplification of equipment response due to the interaction effect is de-

veloped, and a practical design rule for selecting the cable slackness to limit the interaction effect in the cable-connected system is derived.

Table of Contents

List of Figures

List of Tables

Acknowledgement

This study was supported by Contract No. # with Pacific Gas & Electric Company through the Pacific Earthquake Engineering (PEER) Center.

1 INTRODUCTION

1.1 Motivation

The motivation for this study arises from a real and important problem related to the reliability of electrical substation equipment subjected to earthquake events. Observed damage to electrical substation equipment in several past earthquakes suggests that dynamic interaction between interconnected equipment items could be an important contributing factor (Benuska 1990, Hall 1995, Schiff 1995). Electrical substation equipment, such as transformers, circuit breakers, switches, surge arresters, etc., are often qualified for seismic action by shake table tests before they are installed (IEEE 1997). However, once installed, they are connected to other equipment through either flexible or rigid conductors. During an earthquake, the interconnection may give rise to dynamic interaction between the equipment items and thereby amplify the demand on an equipment item relative to its stand-alone demand. An equipment item, which is qualified in a stand-alone configuration, may not be able to withstand the amplified demand. This would lead to damage of the equipment and possible disruption in the functioning of the substation.

In our previous studies (Der Kiureghian *et al.* 1999, 2000, 2001; Hong *et al.* 2001), we demonstrated the interaction effect for equipment items connected with linear or nonlinear rigid conductors, as well as for equipment items connected by flexible conductors. The flexible conductor, commonly called a conductor cable, is typically made of helically wrapped aluminum wires, as shown in Figure 1.1. In Der Kiureghian *et al.* (2000) and Hong *et al.* (2001), a simple elastic finite element model were used to describe the behavior of the conductor cable in bending. However, in reality, the behavior of such conductor cables is far more complex due to the possibility of slippage between the wires. This study aims at developing a more refined model of the conductor cable, which properly accounts for the slippage of wires and for large displacement and rotation, and its use in assessing the interaction effect between cable-connected equipment items. The final goal is to develop simple predictive formulas, which can be used in practice to assess the interaction effect and to provide guidelines for the design of conductor cables that have sufficient slackness to reduce the adverse interaction effect to a manageable level. The specific objectives of the study are described in greater detail in Section 1.3 below.

1.2 Review of Relevant Past Work

Cables made of helically wrapped wires are used as elements in many structures, such as cable-stayed and bridges, tall-guyed towers, power transmission lines, and as flexible conductors in electrical substations. Figure 1.1 shows one such cable used as a flexible conductor. The cable consists of several layers of wire, each layer having a lay angle relative to the axis of the cable, wrapped around a core. Usually the layers have opposing lay angles to prevent unwrapping of the wires under tension force.

In mechanics, the word "cable" is usually used to describe an ideal structural member with axial but no flexural stiffness. In this study, we will use this term to describe the flexible conductor, which has a large axial stiffness and small flexural and torsional stiffnesses. Under dynamic loads, such a structural member, if it has sufficient slackness, may experience large displacements and rotations. Furthermore, under bending stress, wires in the cable may slip relative to one another. In this section we review previous work related to the mechanical modeling and dynamic analysis of such cables.

A copper cable was used as a structural element in about 700 B.C. (Costello, 1978). In spite of this long history of usage of cables, the history of developing theoretical models for cables, particularly those made of helically wrapped wires, is rather short. This is partly due to the complex mechanical behavior of such cables. Since cables are mainly used to support large axial loads with comparatively small bending or torsional stiffness, theoretical models for cables under axial loads developed first. Hruska (1951) developed a simple model to calculate the wire stress of cables under axial loading. In his model, wires are assumed to be subjected to pure tensile forces and friction between wires is neglected. Including the effect of wire bending and twisting, Philips and Costello (1973) developed a more advanced model based on Love's equation for the equilibrium of a curved rod (Love, 1944). Friction and slippage between wires were neglected in their model. An orthotropic sheet model was developed by Hobbs and Raoof (1982), where each layer of wires was replaced with an orthotropic layer. Friction between wires was included in this model, so that it can account for the cable deformation evolving gradually from a no-slip to a full-slip state.

Even though cables are primarily used to support axial loads, gravity, wind, water or inertia forces generated by ground motion induce transverse loads on cables. For analysis of cables

under such transverse loads, it is necessary to develop a model for the cable, which considers both bending and axial deformations. Models for cable bending are much more complex than for axial loading, since the axial symmetry assumed for the layers cannot be held for a cable under bending. Lutchansky (1969) proposed that the location of wires in a bent cable be represented mathematically by lines drawn on a torus surface. These lines are the mathematical extension of a *helix* line. Costello and Buston (1982) proposed a model, where wires were treated as curved rods without contact restraint. In their work, Love's wire equilibrium equations (Love 1944) were used to calculate internal forces on the wire assuming it had a deformed helix shape. Knapp (1988) calculated the bending and twisting strains from the kinematics of the deformed and undeformed wire, where the deformed wire centerline is assumed to be a deformed helix and two extreme conditions, no-slip and zero friction, were considered. Lanteigne (1985) determined the bending moment of a cable from the wire axial forces, calculated using the Bernoulli-Euler-Navier kinematic beam assumption, and also from independent wire bending. He showed a stepwise transition of the bending stiffness of the cable from the stick to the slip state of wires based on his model. According to his model, the slip starts with wires lying farthest from the neutral axis. This is in contradiction with test observations made by Raoof (1989), where the interlayer slippage was seen to start around the neutral axis. Papailiou (1997) proposed a model, where the wire tension force in the stick state was determined by the Bernoulli-Euler-Navier kinematic beam assumption and the wire tension force in the slip state was determined by a first-order differential equation that was derived from the relation between the radial normal force (or the friction force) on the wires and the tension force in the wire. Consistent with Raoof's test observations, the wire slippage in Papailiou's model starts near the neutral axis. A smooth transition of bending stiffness from a stick to a slip state of wires was shown by his model. A good summary of comparisons between the existing cable models is presented by Cardou and Jolicoeur (1997). Finally, two texts on cables are noteworthy. One by Irvine (1981) describes the classical theory for the static response of cables and the linear theory of free vibration of taut cables. The text by Costello (1997) describes various theories of wire rope, mostly based on research conducted by Costello and his colleagues. Neither of these texts addresses the issue of wire slippage in cables.

In the present study, an improved version of the model by Papailiou (1997) is developed to describe the behavior of the helically wrapped cable under the combined action of bending

and tension. Specific improvements to Papailiou's model are described in the development of the model in Chapter 2.

The improved model is implemented in a finite element formulation, where full account is made of the elasto-plastic behavior in bending, representing the effect of wire slippage, and the large displacements and rotations of the cable as it responds to dynamic loads. For this development, use is made of the geometrically exact elastic rod model developed by Simo and Vu-Quoc (1986a,b), which accounts for the highly nonlinear geometry of the cable. Simo *et al.* (1995) later extended this elastic rod model for 3-dimensional problems. The original development of this theory goes back to Cosserat brothers (1967). In the present study, the formulation by Simo and Vu-Quoc (1986a,b) is extended to account for the nonlinear bending behavior of the cable.

In order to guarantee an unconditionally stable numerical solution in time-history dynamic analysis with the elastic rod, Simo *et al.* (1995) suggested to use the energy-conserving algorithm for time integration. In our previous study with an elastic model of the cable (Der Kiureghian *et al.*, 2000, Hong *et al.* 2001), we used a modified version of this energy-conserving algorithm for time-integration. The modification introduced numerical damping in the algorithm to stabilize the computations, while slightly compromising on the conservation of energy.

Since the cable model developed in this study has an elasto-plastic constitutive law for cable bending, the energy-conserving algorithm, which was designed for elastic problems, cannot be used. To the author's knowledge, there is no time-stepping algorithm that has been proven to be unconditionally stable for the cable dynamic problem, where both geometric nonlinearity and plastic behavior are present. Therefore, as a trial, we selected to use the HHT algorithm (Hilber, Hughes and Taylor, 1977), which was designed to solve nonlinear dynamic problems. Our experience shows that the HHT algorithm, with certain parameter values and time step, works well for the plasto-dynamic cable problem. The return-mapping algorithm (Simo and Hughes 1998) is used for determining the algorithmic tangent in the elasto-plastic cable model.

As mentioned earlier, the main interest in this study is in determining the effect of dynamic interaction in cable-connected equipment systems. Few experimental studies are available on the dynamic response of conductor cables under large displacements and rotations. Dastous and Pierre (1996) conducted experiments on two conductor cables by imposing harmonic displacements at both ends of a horizontal span. They observed large amplification of the cable ten-

sion force relative to the static tension force due to gravity alone. They also observed compression forces in the cable, which can be attributed to the effects of flexural stiffness and horizontal mass inertia of the cable. More recently, Filiatrault and Stearns (2002) conducted static and dynamic tests on several different conductor cables. In the static tests, they attempted to measure the bending moment versus curvature and load versus displacement relationships of the cable under cyclic loads. They also conducted shake table experiments on two model equipment items connected by a conductor cable. Later in this study, we compare our analytical predictions with the experimental results of Dastous and Pierre (1996) and Filiatrault and Stearns (2002).

In our own previous work, we have used two different models to study the dynamic response of cable-connected systems. In Der Kiureghian *et al.* (1999) and Hong *et al.* (2001), we used the catenary cable model to describe the highly nonlinear stiffness property of the conductor cable. This approach neglected the flexural stiffness of the cable as well as its inertia forces. In our more recent study, Der Kiureghian *et al.* (2000) and Hong *et al.* (2001), we used a finite element model of the cable, accounting for its flexural stiffness and mass inertia, as well as for its large displacements and rotations. However, the cable was assumed to have a purely elastic behavior. To approximately account for the effect of wire slippage, a reduced moment of inertia based on a simple formula suggested in the IEEE recommendations (IEEE 1999) was used. The present study improves on this formulation by fully accounting for the slippage of wires and the inelastic bending behavior of the cable.

1.3 Objectives and Scope

The main objectives of this study are as follows:

a) To develop a theoretical model to describe the nonlinear behavior of a cable made of helically wrapped wires under tension and bending loads by accounting for friction and slippage between wires in neighboring layers;
b) To develop a finite element model that accounts for the nonlinear bending behavior of the cable, as well as for its large displacements and rotations;
c) To compare predictions by the analytical model with static and dynamic tests conducted on cables by other investigators, with the objective of verifying the validity of the model and determining its parameters;

d) To investigate the effect of interaction in cable-connected equipment systems using the developed finite element model, and to develop a simple predictive formula to estimate this effect in practice.

Throughout this study, we restrict our attention to a cable moving in a vertical plane. Furthermore, the material of the cable is assumed to remain linear elastic at all times; nonlinearities considered are due to slippage of wires and large displacements and rotations of the cable. In investigating the effect of interaction in cable-connected equipment systems, the consideration is restricted to two equipment items with a single connecting cable. Furthermore, the equipment items are modeled as linear, single-degree-of-freedom oscillators. All energy dissipation mechanisms of the equipment items are idealized as viscous damping. In spite of these limitations and idealizations, we believe that the model developed in the present study is applicable to many real cable-connected equipment systems, and the results derived have important ramifications for practical design, particularly for electrical substation equipment.

1.4 Organization and Overview

In Chapter 2, we develop the theoretical model describing the flexural behavior of the helically wrapped cable situated in a vertical plane and subjected to axial and bending loads. First, the geometries of the wires in the undeformed (straight) and deformed (curved) cable are formulated. It is shown that, for the range of cable curvatures of interest, the curvature of a helical wire in the undeformed straight cable can be taken as a good approximation of its curvature in the curved cable. Using this approximation, a simple expression is derived for the normal and friction forces acting on the wire for a given axial strain and curvature of the cable. This leads to a simple first-order differential inequality condition for slippage of the wire under bending stresses. According to this condition, a wire remains stuck when the unbalanced tension force caused by bending in a differential wire element does not exceed the maximum friction force that is the sum of all friction forces that can be generated on the wire element. The wire slips, or is in a state of impending slippage, when the unbalanced tension force equals the maximum friction force. According to this model, the secant bending stiffness, which depends on the curvature and tension force of the cable, varies between two extreme limits. These limits correspond to the extreme cases of fully slipping and fully stuck wires.

Chapter 3 describes the development of a finite element model for dynamic analysis of the cable, which accounts for the nonlinear moment-curvature relation as well as for geometric nonlinearity arising from large displacements and rotations of the cable. The formulation given by Simo and Vu-Quoc (1986a,b) for elastic rods is extended to account for the nonlinear bending behavior of the cable, where the geometric nonlinearity is fully accounted for. The nonlinear moment-curvature-tension relation of the cable is fitted by a bilinear elasto-plastic constitutive model with kinematic hardening, with the yield moment depending on the tension force. This bilinear elasto-plastic model is implemented as a bending constitutive law in place of the elastic constitution law in the formulation given by Simo and Vu-Quoc. For dynamic analysis, the HHT algorithm by Hilber, Hughes and Taylor (1977) is used for time integration, and the return-mapping algorithm by Simo and Hughes (1998) is used for determining the algorithmic tangent in the elasto-plastic model.

In Chapter 4, we make comparisons between predictions by the finite element model developed in this study and the results of monotonic and cyclic static tests conducted by Filiatrault and Stearns (2002) and Dastous and Pierre (1996). The former conducted tests on two different conductor cables laid in the vertical position and subjected to tension and to transverse loads at 1/3 span points. Comparisons are made with both moment-curvature and load-displacement relations under various tension loads. Dastous and Pierre (1996) conducted tests on two conductor cables laid in a horizontal position with one end fixed and the other end subjected to horizontal displacement motion. Comparisons are made for the cable-force versus end-displacement relationship.

Chapter 5 describes comparisons between predictions by the finite element model developed in this study and the results of dynamic tests conducted by Filiatrault and Stearns (2002) and Dastous and Pierre (1996) for cable-connected idealized equipment items or conductor cables. Filiatrault and Stearns (2002) experimented with two idealized equipment items (fixed base poles with mass on top) connected by a conductor cable on a shake table. The shake table was subjected to earthquake-type motions. We make comparisons for three different systems with varying cable slackness. Comparisons are made between the measured and predicted equipment displacements and cable forces. Dastous and Pierre (1996) subjected a horizontal conductor cable to out-of-phase harmonic displacements at both ends of the cable. Comparisons are made between the measured and predicted time history of the cable force at one end.

In Chapter 6, we use the finite element model developed in this study to investigate the effect of dynamic interaction between two idealized equipment items connected by a conductor cable. The equipment items are modeled as single-degree-of-freedom oscillators with prescribed natural frequencies, masses and damping ratios. In our previous study (Der Kiureghian *et al.* 1999), we introduced the *response ratio* as a measure of interaction between two connected equipment items. This is the ratio of the maximum response of an equipment item in the connected system to its maximum response in the stand-alone configuration. Obviously, if this ratio is greater than unity, the interaction results in amplification of the equipment response (relative to its stand-alone response), and if it is less than unity, the interaction results in de-amplification of the equipment response. In the same study, we also introduced an *interaction parameter* as a predictive measure of the magnitude of the interaction effect. This parameter depends only on the geometry of the connecting cable and the relative displacement between the equipment items, in their stand-alone configuration, when subjected to a specified ground motion. A simple response spectrum method for computing the latter quantity was presented in our earlier study (Der Kiureghian *et al.* 1999). In the present study, we use the improved finite element model to generate a large sample of "observed" responses of cable-connected equipment systems with varying equipment, conductor cable, and ground motion characteristics. This sample is then used in conjunction with well-established statistical methods to generate a simple predictive model for the response ratio in terms of the interaction parameter and the equipment and cable characteristics. This predictive formula is then recast in a form appropriate for determining the necessary cable slackness to reduce the interaction effect to an acceptable level. Additional investigations related to the effect of energy dissipation due to slippage of wires in the cable are contained in this chapter.

Chapter 7 presents a summary of the study and its main findings. Areas where further study would be beneficial are identified.

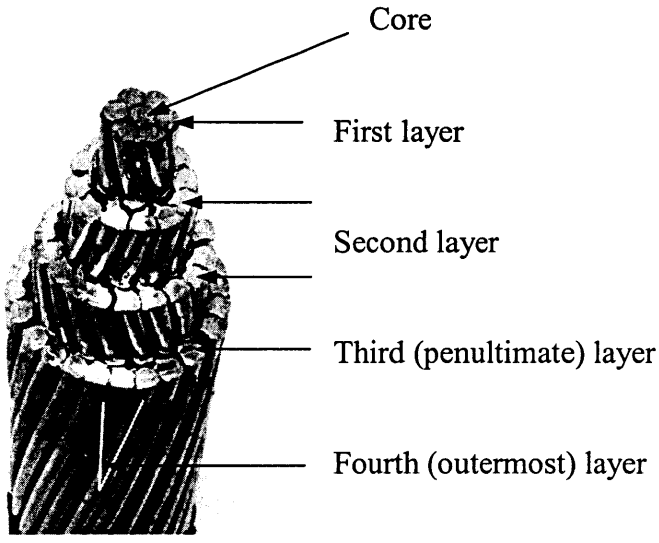

Figure 1.1 Typical helically wrapped flexible conductor.

2 MECHANICAL MODEL OF CONDUCTOR CABLE

2.1 Introduction

Conductor cables used for power transmission lines or in electrical substations are typically made of helically wrapped aluminum wires. In this chapter, a theoretical model is developed to describe the nonlinear moment-curvature relationship of such a cable by accounting for the friction and slippage between wires in neighboring layers. This friction is referred to as *interlayer friction* (Papailiou 1997). The model developed herein does not account for friction between wires in the same layer, which is assumed to be negligible compared to interlayer friction.

According to this model, the bending stiffness of the cable, which depends on the tension force in, and the curvature of, the cable, varies between two extreme limits. These limits correspond to the extreme cases of fully slipping wires and fully stuck wires, respectively leading to bending stiffnesses $EI_{\min}$ and $EI_{\max}$. The quantity E is Young's modulus for the material of the cable, $I_{\max}$ is the second moment of area of the cross-section of the cable about the centroidal axis based on the state where all the wires are stuck together, and $I_{\min}$ is the second moment of area based on the state where all the wires are slipping For typical conductor cables, $I_{\max}$ can be more than two orders of magnitude greater than $I_{\min}$. The theoretical model developed in this study is an improvement of Papailiou's model (1997). Specific differences between the two models are described when they appear in the derivation presented in this chapter.

In computing the normal force in each wire, the wire curvature is approximated by its value for the straight cable. This gives a simple first-order differential condition for slippage of a wire. According to this condition, a wire remains stuck when the unbalanced tension force, which is caused by bending, in a differential element is less than the maximum friction force, which is the sum of all friction forces that can be generated, on the wire. The wire can slip when the unbalanced tension force equals the maximum friction force. The condition of impending slippage is described by equality between the unbalanced tension force on the wire and the maximum friction force that can be generated.

In each cross section of the cable, two regions are identified: a "stick" region, where wires are stuck, and a "slip" region, where wires are slipping. The well-known Bernoulli-Euler-

Navier kinematic beam assumption is applied in the stick region, while equality holds between the unbalanced tension forces and the maximum friction forces for the wires in the slip region. The continuity in internal tension forces of the wires is satisfied at the boundaries between the two regions, and the elastic constitutive law for the tension forces of the wires is assumed.

In Section 2.2, the geometries of helically wrapped wires in undeformed and deformed cables are addressed. An exact expression for the curvature of a single wire in the deformed cable is derived in Section 2.3. Using this expression, numerical comparisons are made between the exact wire curvature in the bent cable and the wire curvature in the straight cable. The comparison shows that, for all practical purposes, the curvature of the wire in the straight cable can be used as an approximation of the wire curvature in the deformed cable.

Section 2.4 describes the unbalanced forces that cause slippage of wires. Due to the helical geometry of the wires, the two ends of a differential wire element have differences in elevation from the neutral axis of the cable. This generates the unbalanced tension force on the wire element caused by bending moment. To study the static equilibrium of a typical differential element of the wire, it is necessary to also determine the friction forces acting on the wire. These friction forces are determined from knowledge of the normal forces acting on the differential element of the wire and the friction coefficient between wires.

A simple formula for the normal force on a wire in a given layer is derived in Section 2.5 using the wire curvature in the undeformed cable as an approximation. For multi-layer cables, this normal force is a consequence not only that arising from the tension in the wire and the curvature of the wire itself, but also due to the contributions of wires in all layers above the layer being considered.

The relationship between the unbalanced tension force and the normal force is the key to the determination of whether a wire is in the stick or slip state. In Sections 2.6 and 2.7, the expressions governing the stick and slip states, respectively, are derived. In the stick region, the continuity of axial strain in each wire along with the Bernoulli-Euler-Navier kinematic beam assumption is used to determine the axial force in the wire. In the slip region, the condition for the slippage of the wire is used to determine the axial force in the wire.

In Section 2.8, the boundary between stick and slip regions is determined by imposing the requirement of continuity of internal tension forces along the length of the wire. As shown in

Section 2.9, the resultant forces acting on a cable cross-section are readily computed for a prescribed curvature and axial strain of the cable. In Section 2.10, a numerical example is presented for the determination of the nonlinear moment-curvature relationship and secant bending stiffness for the Jessamine cable (Division of Aluminum Company of America 1974), which is a typical conductor used in electrical substations.

2.2 Geometry of Cable and Wire

The behavior of a cable made of helically wrapped wires subjected to tension and bending loads is the subject of this study. This behavior is complicated because of the complex geometry of the wires and the friction and slippage that occurs between the wires in different layers when the cable is deformed.

Herein, we consider a cable that is initially straight, undeformed and unstressed. This configuration will be referred to as the *reference configuration* of the cable. In this configuration, the wires have helix geometry. If now the cable is uniformly extended in such a way that it remains straight, then, provided no slippage between the wires occurs, the stretched wires will still have helix geometry (Huang and Vinogradov 1993). In this configuration, each wire has constant curvature and tortuosity (Love 1944, Nutbourne and Martin 1988) that depends on its lay angle (the angle between the wire and a line parallel to the centerline of the core of the cable) and its distance from the centerline of the core of the cable (herein referred to as the centerline of the cable).

As we bend the cable, the wire configuration is no longer a helix but a mathematical extension of a helix, since the curvature and tortuosity now vary along the length of the wire. To be a helix, the curvature and tortuosity should be constant along the centerline of the wire. In the literature, this configuration of the wire has been called "a helix embedded in a bent cable" (Huang and Vinogradov 1993). For brevity, we call it a "helix-like" configuration. On the other hand, if there is no friction between the wires so that the wires freely slide, the wire has a *geodesic* configuration (Out and Morgen 1997). The actual configuration of the wire in the bent cable is somewhere between these two limiting cases.

Figure 2.1 shows the geometry of a helically wrapped conductor cable in its deformed configuration. The bent cylinder represents the cable, which consists of several layers of wires

wrapped around a core. The core is an initially single straight wire about which the other wires are helically wrapped, layer-by-layer. As mentioned above, the reference configuration coincides with a straight, undeformed and unstressed cable. In what follows, we restrict our attention to the case where the deformation of the cable takes place in a vertical plane. The thick line on the bent cylinder represents a single wire in a typical layer. At the selected cross section, tangents to the wire and the projection of the cable centerline on the surface of the cylinder (the dotted line in Figure 2.1) make the angle α. This is known as the lay angle of the wire. In the deformed configuration, the lay angle varies along the length of the wire. In the undeformed (straight) configuration of the cable, the lay angle for each wire is a constant and we denote it by α_0. Usually, all wires in a given layer have the same lay angle in the undeformed configuration. Furthermore, wires in neighboring layers typically have opposite lay angles. This is to prevent unwrapping of the wires when the cable is put in tension.

To describe the geometry of the wire in the deformed cable, we define a referential coordinate system by use of the right-handed orthonormal set of basis vectors $(\mathbf{E}_1, \mathbf{E}_2, \mathbf{E}_3)$. The vectors $\mathbf{E}_2$ and $\mathbf{E}_3$ define the plane in which the centerline of the cable bends. Similarly, a local coordinate system $(\mathbf{e}_1, \mathbf{e}_2, \mathbf{e}_3)$ is attached to the cross section of the cable, and, when the cable is in the reference configuration, coincides with $(\mathbf{E}_1, \mathbf{E}_2, \mathbf{E}_3)$. From an arbitrary origin O_z on the centerline of the cable, the distance measured along the centerline of the cable is indicated by the symbol z_c. The positive direction of z_c is taken to coincide with $\mathbf{e}_3$. In the same way, from an arbitrary origin O_s on the centerline of a typical wire, the distance measured along the centerline of that wire is indicated by the symbol s. The positive direction of s is chosen such that the scalar product between the tangent to the curve of the centerline of the wire, in the direction of increasing s, and $\mathbf{e}_3$ is positive.

The local coordinate system $(\mathbf{e}_1, \mathbf{e}_2, \mathbf{e}_3)$ is used to define the location of the center of a wire with respect to the center of the cross section O_c of the cable. The vector $\mathbf{e}_3$ is selected to be tangent to the centerline of the cable, and we note that $\mathbf{e}_2$ is normal to the cable centerline. If the cable centerline is concave up (down) with respect to $(\mathbf{E}_2, \mathbf{E}_3)$, then $\mathbf{e}_2$ $(-\mathbf{e}_2)$ is in the direction of the center of curvature of the cable centerline. Let θ_c denote the angle between $\mathbf{E}_2$ and

$\mathbf{e}_2$, as $\mathbf{E}_2$ rotates counterclockwise into $\mathbf{e}_2$. Then, the orthonormal basis $(\mathbf{e}_1, \mathbf{e}_2, \mathbf{e}_3)$ can be expressed as components on the reference basis $(\mathbf{E}_1, \mathbf{E}_2, \mathbf{E}_3)$ as

$$\mathbf{e}_1 = \begin{Bmatrix} 1 \\ 0 \\ 0 \end{Bmatrix}, \ \mathbf{e}_2 = \begin{Bmatrix} 0 \\ \cos(\theta_c) \\ \sin(\theta_c) \end{Bmatrix}, \ \mathbf{e}_3 = \begin{Bmatrix} 0 \\ -\sin(\theta_c) \\ \cos(\theta_c) \end{Bmatrix} \tag{2.1}$$

With respect to the reference coordinate system, the location of the center of the wire W in the cable cross-section, as shown in Figure 2.1, is defined by the vector

$$\mathbf{x} = \mathbf{x}_\rho + \mathbf{x}_c + \mathbf{x}_w \tag{2.2}$$

where $\mathbf{x}_\rho$ is the vector from the reference origin O to the instantaneous center of curvature O_ρ of the cable, $\mathbf{x}_c$ is the vector from the instantaneous center of curvature of the cable to the center of the cable cross-section O_c, and $\mathbf{x}_w$ is the vector from the center of the cable cross-section to the center of the wire in the cable cross-section.

At this point we assume that the cable is deformed into a curve with constant curvature. The geometric relations that are obtained will prove to be useful for a cable deformed into a planar shape with slowly varying curvature along its length. By this assumption, $\mathbf{x}_\rho$ is a constant. Considering the curve to be concave down, as shown in Figure 2.1, for a given radius of curvature of the cable, ρ_c, we have

$$\mathbf{x}_c = \rho_c \mathbf{e}_2 \tag{2.3}$$

since $\mathbf{x}_c$ is in the same direction as $\mathbf{e}_2$. The vector $\mathbf{x}_w$ is represented in a polar coordinate system as

$$\begin{aligned} \mathbf{x}_w &= r\cos(\varphi)\mathbf{e}_1 + r\sin(\varphi)\mathbf{e}_2 \\ &= \begin{Bmatrix} r\cos(\varphi) \\ r\cos(\theta_c)\sin(\varphi) \\ r\sin(\theta_c)\sin(\varphi) \end{Bmatrix} \end{aligned} \tag{2.4}$$

where r is the distance from the center of the cable to the center of the wire, a constant for a given layer, and φ is the polar angle from $\mathbf{e}_1$ to $\mathbf{x}_w$, both defined on the cable cross-section as shown in Figure 2.2. Using (2.3) and (2.4) in (2.2), the location of the center of the wire is derived as

$$\mathbf{x} = \mathbf{x}_\rho + \begin{Bmatrix} r\cos(\varphi) \\ [\rho_c + r\sin(\varphi)]\cos(\theta_c) \\ [\rho_c + r\sin(\varphi)]\sin(\theta_c) \end{Bmatrix} \tag{2.5}$$

2.3 Curvature of a Wire

To derive an expression for the curvature of the wire, we introduce a set of *directors* embedded in the cross-section of the wire and defined as a right-handed orthonormal basis ($\mathbf{t}_1$, $\mathbf{t}_2$, $\mathbf{t}_3$), as shown in Figure 2.3. $\mathbf{t}_1$, $\mathbf{t}_2$ and $\mathbf{t}_3$ are unit vectors binormal, normal and tangent, respectively, to the centerline of the wire. The mathematical definition of this right-handed orthonormal basis is

$$\mathbf{t}_3 = \frac{d\mathbf{x}}{ds}, \tag{2.6a}$$

$$\mathbf{t}_2 = \frac{d^2\mathbf{x}/ds^2}{\left\|d^2\mathbf{x}/ds^2\right\|} = \frac{d\mathbf{t}_3/ds}{\left\|d\mathbf{t}_3/ds\right\|}, \tag{2.6b}$$

$$\mathbf{t}_1 = \mathbf{t}_2 \times \mathbf{t}_3 \tag{2.6c}$$

where s is the distance measured along the centerline of the wire from an arbitrary origin O_s on the centerline of the wire, as shown in Figure 2.1.

The rate of change of the tangential unit vector, $\mathbf{t}_3$, along the length of the wire defines the wire curvature. The curvature vector, $\boldsymbol{\kappa}_w$, is defined as

$$\boldsymbol{\kappa}_w = \frac{d\mathbf{t}_3}{ds} = \kappa_w \mathbf{t}_2 \tag{2.7}$$

where (2.6b) is used and

$$\kappa_w = \left\|\frac{d\mathbf{t}_3}{ds}\right\| = \left\|\frac{d^2\mathbf{x}}{ds^2}\right\| \tag{2.8}$$

is the magnitude of the curvature. As (2.7) shows, with respect to the directors ($\mathbf{t}_1$, $\mathbf{t}_2$, $\mathbf{t}_3$), the curvature vector has a component only in the osculating, $\mathbf{t}_2$-$\mathbf{t}_3$, plane (Nutbourne and Martin 1988) and, in particular, only in the $\mathbf{t}_2$ direction.

The *tortuosity*, τ_w (Love 1944), sometimes referred to as *torsion* (Nutbourne and Martin 1988), which defines the rate of change of the orientation of the binormal $\mathbf{t}_1$ about the tangential unit vector $\mathbf{t}_3$, is defined as

$$\tau_w = -\mathbf{t}_2 \cdot \frac{d\mathbf{t}_1}{ds} \tag{2.9}$$

It should be noted that the tortuosity is different from what is commonly called "the twist" of the wire. This is because the twist is a measure of material deformation due to a torque, whereas the tortuosity is a geometric property of a space curve and has nothing to do with the wire material (McIver 1995). The effect of wire twist on the friction and slippage of the wires is not considered in this study, because we assume that the axial behavior of the wire is the main source of the friction between wires.

We now derive an expression for the curvature of the wire for a given axial strain ε_c and curvature $\kappa_c (= 1/\rho_c)$ of the cable, and for a given lay angle α and radial and angular coordinates (r, φ) of the wire on the cable cross-section. In Figure 2.4a, the bent cylinder indicates the differential cable element in the deformed configuration for a given axial strain and curvature of the cable. The thick line indicates the differential wire element in the cable. In Figure 2.4b, the view of the differential wire element is magnified. From this figure, for the differential wire element in the deformed cable, we have

$$dz = ds\cos(\alpha) \tag{2.10a}$$

$$r\,d\varphi = ds\sin(\alpha) \tag{2.10b}$$

$$r\,d\varphi = dz\tan(\alpha) \tag{2.10c}$$

where ds is the differential length of the wire and dz is the projection of ds on the centerline of the cable. The same relations hold for the undeformed (straight) cable:

$$dz_0 = ds_0\cos(\alpha_0) \tag{2.11a}$$

$$r\,d\varphi = ds_0\sin(\alpha_0) \tag{2.11b}$$

$$r\,d\varphi = dz_0\tan(\alpha_0) \tag{2.11c}$$

In the above, the subscript 0 indicates variables of the undeformed (straight) cable. The differential elongated length at the centerline of the cable is $dz_c = \rho_c d\theta_c$, which has the following relation with the axial strain of the cable and the initial length of the differential cable element dz_0:

$$dz_c = \rho_c d\theta_c = (1+\varepsilon_c)dz_0 \tag{2.12}$$

Using $\rho_c = 1/\kappa_c$ and (2.11c) in the above, we have

$$\begin{aligned} \frac{d\theta_c}{d\varphi} &= (1+\varepsilon_c)\kappa_c \frac{dz_0}{d\varphi} \\ &= (1+\varepsilon_c)\frac{\kappa_c r}{\tan(\alpha_0)} \end{aligned} \tag{2.13}$$

Since (2.13) is independent of φ, its second derivative respect φ is zero.

As shown in Appendix A, the differential length of the wire in the deformed cable can be determined by taking the norm of the differential of $\mathbf{x}$ and using (2.11b) and (2.13). The result is

$$ds = ds_0\sqrt{\sin^2(\alpha_0)+\cos^2(\alpha_0)(1+\varepsilon_c)^2\left[1+\kappa_c r\sin(\varphi)\right]^2} \tag{2.14}$$

This result is consistent with an earlier derivation by Knapp (1988), where he only accounted for bending deformation with no axial deformation and he assumed that the plane section of the cable remains plane after deformation under full friction between wires. As also shown in Appendix A, using (2.8) and (2.11b), the curvature vector of the wire in the deformed cable can be expressed as

$$\begin{aligned} \boldsymbol{\kappa}_w &= \frac{d}{ds}\left(\frac{d\mathbf{x}}{ds}\right) \\ &= \left(\frac{\sin(\alpha_0)}{r}\right)^2 \cdot \frac{ds_0}{ds} \cdot \left[-\kappa_c B\frac{d\mathbf{x}}{d\varphi} + \frac{ds_0}{ds}\cdot\frac{d}{d\varphi}\left(\frac{d\mathbf{x}}{d\varphi}\right)\right] \end{aligned} \tag{2.15}$$

where

$$B = \frac{r\cos(\varphi)\cos^2(\alpha_0)(1+\varepsilon_c)^2\left[1+\kappa_c r\sin(\varphi)\right]}{\left\{\sin^2(\alpha_0)+\cos^2(\alpha_0)(1+\varepsilon_c)^2\left[1+\kappa_c r\sin(\varphi)\right]^2\right\}^{3/2}} \tag{2.16}$$

$$\frac{d\mathbf{x}}{d\varphi} = \begin{Bmatrix} -r\sin(\varphi) \\ r\cos(\varphi)\cos(\theta_c) - [\rho_c + r\sin(\varphi)]\sin(\theta_c)\dfrac{d\theta_c}{d\varphi} \\ r\cos(\varphi)\sin(\theta_c) + [\rho_c + r\sin(\varphi)]\cos(\theta_c)\dfrac{d\theta_c}{d\varphi} \end{Bmatrix} \tag{2.17}$$

$$\frac{d^2\mathbf{x}}{d\varphi^2} = \begin{Bmatrix} -r\cos(\varphi) \\ -\cos(\theta_c)\left[r\sin(\varphi) + [\rho_c + r\sin(\varphi)]\left(\dfrac{d\theta_c}{d\varphi}\right)^2 \right] - 2r\cos(\varphi)\sin(\theta_c)\dfrac{d\theta_c}{d\varphi} \\ -\sin(\theta_c)\left[r\sin(\varphi) + [\rho_c + r\sin(\varphi)]\left(\dfrac{d\theta_c}{d\varphi}\right)^2 \right] + 2r\cos(\varphi)\cos(\theta_c)\dfrac{d\theta_c}{d\varphi} \end{Bmatrix} \tag{2.18}$$

where $d\theta_c / d\varphi$ is given by (2.13), $d^2\theta_c / d\varphi^2 = 0$, as mentioned earlier, and ds_0 / ds is given by (2.14). By substituting $\kappa_c = 0$, $\varepsilon_c = 0$ and $\theta_c = 0$ into (2.15)-(2.18), the curvature vector of the wire in the undeformed (straight) cable becomes

$$\boldsymbol{\kappa}_{w0} = -\frac{\sin^2(\alpha_0)}{r}\begin{Bmatrix} \cos(\varphi) \\ \sin(\varphi) \\ 0 \end{Bmatrix} \tag{2.19}$$

In order to determine the normal force on the wire in the radial direction (see Section 2.5), we need to know the radial component of the curvature vector $\boldsymbol{\kappa}_w$ on the cable cross-section. The magnitude of this component, denoted κ_{wr}, is obtained by taking the inner product of the curvature vector and the unit radial vector $(-\mathbf{x}_w / \|\mathbf{x}_w\|)$. The negative sign is necessary to make κ_{wr} positive in the undeformed configuration. Using (2.4) and (2.15), we obtain

$$\begin{aligned} \kappa_{wr} &= \boldsymbol{\kappa}_w \cdot \left(-\frac{\mathbf{x}_w}{\|\mathbf{x}_w\|} \right) \\ &= -\boldsymbol{\kappa}_w \cdot \begin{Bmatrix} \cos(\varphi) \\ \cos(\theta_c)\sin(\varphi) \\ \sin(\theta_c)\sin(\varphi) \end{Bmatrix} \end{aligned} \tag{2.20}$$

The corresponding curvature in the undeformed (straight) cable, denoted κ_{w0}, is obtained by substituting (2.19) into (2.20) in place of κ_w, which yields

$$\kappa_{w0} = \frac{\sin^2(\alpha_0)}{r} \tag{2.21}$$

Figure 2.5 shows a comparison between the magnitudes of the radial components of the wire curvature in the undeformed and deformed configurations for the Jessamine conductor cable. This cable has 4 layers of wire; each wire and the core has a diameter of 4.30mm and all the wires except the core are assumed to have a 12 degree lay angle. The properties of this cable are listed in Table 2.1. The axial strain of the cable is assumed to be 10^{-6}. Each plot shows the radial component of the curvature κ_{wr} for the wires in each layer as a function of the cable curvature. The horizontal dashed lines indicate the wire curvature in the undeformed (straight) cable, which is constant. The solid lines in each plot are the curvature of wires in each layer in the deformed cable. Because of the symmetry of the cable cross-section, only half of wires in each layer need be shown. Shaded gray circles indicate the wires considered. In each plot, the top solid line indicates the curvature of the top wire in each layer, the bottom solid line indicates the curvature of the bottom wire and so on. The curvature of the middle wires, which are located exactly on the axis of the cable centerline, in the deformed cable coincides with the curvature of wires in the undeformed cable in Figure 2.5a and c. It is seen that, for cable curvatures up to about κ_c=1/m, the wire curvatures in the deformed cable are essentially equal to those in the undeformed cable. For larger cable curvatures, the wire curvatures on the upper half of the cable are larger relative to the wire curvatures in the undeformed state of the cable. This is the side where wires experience increased tension due to bending. On the bottom half of the cross section, where the tension in the wires is decreased due to bending, the wire curvatures are smaller in relation to the wire curvatures in the undeformed cable. For very large values of the cable curvature, the curvatures of some of these wires may in fact become negative (see curves for the lower wires in Figures 2.5b, c and d). These wires experience reverse bending. Knapp (1988) also observed this effect.

Due to high axial stiffness of conductor cables, the axial strain ε_c is expected to be small and any reasonable changes in its value will have negligible effect on κ_{wr}. This observation and the results in Figure 2.5 lead us to conclude that the radial component of the wire curvature in the

deformed cable can be closely approximated by its curvature in the undeformed cable for cable curvatures up to nearly κ_c=1/m. Conductor cables with curvature near or greater than 1/m are not typical in practice. Furthermore, when a straight cable is bent, we believe that most wires in the cable start slipping well before the curvature reaches κ_c=1/m. It follows that, for all practical purposes, we can approximate κ_{wr} with the wire curvature in the undeformed cable, κ_{w0}, as given by (2.21). This greatly simplifies the analysis for determining the normal force on the wire. This approximation is sufficiently accurate for determining the stick/slip states of the wires in the cable, since full slippage of wires occurs at cable curvatures much smaller than 1/m. Numerical results in Section 2.10 support this assertion. Papailiou (1997) also used this approximation of the wire curvature of the deformed cable. In this study, it is clearly verified to be a reasonable assumption.

2.4 Unbalanced Force on a Wire

Consider a segment of the cable under axial tension T and bending moment M, as shown in Figure 2.6a. The thick gray line indicates a typical differential wire element. The tension forces acting on the two ends of this wire element are also shown in the figure. There is a difference dT_w between the two end forces of the wire element. This unbalanced force arises because of the unequal distances of the two ends of the wire element from the neutral axis of the cable, which is caused by a non-zero lay angle. The difference between these distances of the two ends of the wire is denoted by Δy. Note that, if the wire were laid parallel to the centerline of the cable, there would be no differential tension force.

The unbalanced tension force dT_w tends to slide the wire along its axis. In the stick state, this force is smaller than the maximum friction force μdN acting on the wire, which is caused by the normal force dN on the wire as shown in Figure 2.6b, where μ is the friction coefficient between the wire and wires in the neighboring inner layer. The wire in the figure is located in the outermost layer of the cable. Of course, when the wire is located in any inner layer, there is friction force from wires in layers above that wire as well as below it. When the unbalanced force dT_w equals the maximum friction force, the wire can slide along its axis. If sliding occurs, this causes a redistribution of forces acting on the wire, and slippage continues until equilibrium is

reached. The magnitude of dT_w clearly depends on the state of the wire. In the following section, we determine this unbalanced force and the maximum friction forces on each wire in the stick and slip states.

2.5 Normal and Friction Forces on a Wire

When a wire wrapped on the neighboring inner layer of wires is subjected to tension, normal forces develop along the radial direction. These normal forces give rise to friction forces acting in the interface between the wires and the inner wires on which it rests. For the wires in the outermost layer, friction forces develop only on the inner surface of the wire. For wires in inner layers, friction forces develop on both inner and outer surfaces of the wire. Furthermore, normal forces from the outer layers accumulate on the inner layers. In this section, analytical expressions are derived for the normal forces and maximum friction forces in the wires.

To our knowledge, no experiments have been conducted to determine the friction coefficient between the wires in a conductor cable. Tests for measuring the friction coefficients between wires in the cable are necessary to have a more exact model for cable bending. In this study, we assumed that all friction coefficients between wires are the same.

2.5.1 Normal Force on a Wire in the Outermost Layer

Consider a small differential element of the wire in the outermost layer resting on the penultimate layer. Figure 2.7 shows the differential wire element projected into the plane defined by the unit radial vector $\mathbf{x}_w / \|\mathbf{x}_w\|$ and the unit tangential vector $\mathbf{t}_3$ (see Figures 2.2 and 2.3 for the definitions of these vectors). In this figure, T_w is the tension force in the wire, $\rho_{wr} = 1/\kappa_{wr}$ is the radius of curvature in the plane, $d\theta_{wr}$ is the differential angle of the wire element in the plane, and p is the intensity of the distributed normal force on the wire coming from the penultimate layer in the radial direction. Equilibrium of the wire in the radial direction requires that

$$p\rho_{wr} d\theta_{wr} = 2T_w \sin\left(\frac{d\theta_{wr}}{2}\right) \tag{2.22a}$$

or

$$p = \frac{T_w}{\rho_{wr}} \tag{2.22b}$$

The differential normal force on the wire element is the product of the distributed force intensity p and the absolute value of the differential length, $|ds|$. The differential length ds of the wire changes its sign according to the sign of its lay angle because of (2.10b). Note that the radial distance r to the wire from the center of the cable is always positive and $d\varphi$ is chosen to be positive in Figure 2.4. Therefore, we can define the absolute value of the differential length as

$$|ds| = \frac{r\, d\varphi}{\sin|\alpha|} \tag{2.23}$$

Consequently, the differential normal force, dN, on the wire element is given by

$$dN = p|ds| = \frac{T_w}{\rho_{wr}} \frac{r\, d\varphi}{\sin|\alpha|} \tag{2.24}$$

Of course, the above applies when T_w is positive, i.e., the wire is in tension. When the wire is subjected to compression, there is no normal force on the wire from the penultimate layer and dN is zero.

In Section 2.3, we derived an exact expression (2.20) for the curvature of the wire in the radial direction, $\kappa_{wr} = 1/\rho_{wr}$, in the deformed configuration of the cable. If this result is used in (2.24), we can obtain an exact expression for the normal force on the wire in terms of the given axial strain and curvature of the cable. However, this expression turns out to be too complicated for use in the derivation for the relations between the unbalanced force and the friction forces on the wire. For this reason, in the following analysis, the curvature of the wire in the undeformed straight cable is used as an approximation of the curvature of the wire in the deformed cable. The justification for this approximation was presented in Section 2.3. To further simplify the expression, the lay angle, α_0, of the wire in the undeformed cable is used as an approximation of the lay angle, α, in the deformed cable. This approximation is reasonable, since for operating values of the axial strain and curvature of the cable, the change in the lay angle is negligible. We have performed calculations for the Jessamine cable and found that for cable curvatures even up to about $\kappa_c = 1/\text{m}$ the worst deviation of the lay angle in the deformed configuration (which occurs

in the outermost layer, on that wire which experiences the greatest increment of compression), as compared to the lay angle in the undeformed straight configuration, was less than 1.7%.

Thus, substituting (2.21) for $\kappa_{wr} = 1/\rho_{wr}$ and α_0 for α, in (2.24), the differential normal force on the wire becomes

$$dN \approx T_w \sin|\alpha_0|\, d\varphi \tag{2.25}$$

This is the normal force on the inner surface of the wire caused from the tension force in that wire. This expression was also derived by Papailiou (1997) but he did not use the absolute value of the lay angle in the sine function.

2.5.2 Normal Force on a Wire in an Inner Layer

In deriving an expression for the normal force acting on a wire of an inner layer, two important considerations should be made: First, normal forces accumulate from the outermost layer to the core, so that the normal force on a wire of an inner layer is larger than that of an outer layer. Second, for most multi-layered conductor cables, the wires in neighboring layers have alternating algebraic signs of the lay angle. This is to prevent cables from unwinding under tensile or torsional loads.

To determine the normal force of a wire in an inner layer, we begin by considering two differential wire elements in different layers with different lay angle, as shown in Figure 2.8. The two cylinder segments in Figure 2.8a, which have the same length $|dz|$ in $\mathbf{e}_3$ direction, indicate the positions of the j-th (outer) and the l-th (inner) layers of wires in the cable. The thick lines on the surface of those cylinders indicate the differential wire elements in the corresponding layers. Figure 2.8b is a cross-sectional view of the cable. Since the two cylinder segments have the same length $|dz|$, using (2.10c), from this figure, we have

$$|dz| = \frac{r_j d\varphi_j}{\tan|\alpha_j|} = \frac{r_l d\varphi_l}{\tan|\alpha_l|} \quad \text{for} \quad j,l = 1,\ldots,NL \tag{2.26}$$

where the subscripts j and l indicate the layer numbers and NL denotes the total number of layers in the cable. For use in the subsequent analysis, we define n_j as the number of wires in the j-th layer.

Figure 2.9 shows the wires of the j-th and the l-th layers. In Figure 2.9a, the gray thick lines on the outer cylinder segment indicate the wire elements in the j-th (outer) layer, from which normal forces are transferred to the wire element in the l-th (inner) layer, which is shown as a black thick line on the inner cylinder segment. The black thick line on the outer cylinder segment indicates the radial projection of the wire element in the inner layer to the outer layer. The differential angle of this projected line is $d\varphi_l$.

Figure 2.9b is a view of the wires of the j-th and l-th layers from a point inside both layers. There are

$$\frac{n_j}{2\pi} d\varphi_l \tag{2.27}$$

wires in the j-th layer that cross the projected line, which has the differential angle $d\varphi_l$. Each of these crossing wires in the j-th (outer) layer applies a radial normal force on the wire in the l-th (inner) layer (shaded wire in Figure 2.9b) equal to

$$dN_{j,l}^{\text{single}} = \frac{dN_j}{d\varphi_j} \frac{2\pi}{n_l} \tag{2.28}$$

where the superscript 'single' indicates that the normal force comes from a single wire in the j-th layer. The factor $2\pi / n_l$ is the angle associated with a single wire in l-th layer as shown in Figure 2.9b. Therefore, the total normal force on the wire in the l-th layer from the wires in the j-th layer, $dN_{j,l}$, is simply the product of (2.27) and (2.28), i.e.

$$\begin{aligned} dN_{j,l} &= \left(\frac{dN_j}{d\varphi_j} \frac{2\pi}{n_l} \right) \times \left(\frac{n_j}{2\pi} d\varphi_l \right) \\ &= \sin|\alpha_j| T_{wj} \frac{n_j}{n_l} \frac{r_l}{r_j} \frac{\tan|\alpha_j|}{\tan|\alpha_l|} d\varphi_l \quad \text{for } j > l \end{aligned} \tag{2.29}$$

where we have used (2.25) and (2.26), and where, for convenience, we have dropped the subscript '0' from the lay angles. Also, note that (2.29) is applicable to all inner layers except the core in the cable since the core does not have a helix configuration.

As a special case, if all wires in the cable have the same diameter, then we have

$$\frac{n_j}{n_l} \frac{r_l}{r_j} = 1 \tag{2.30}$$

since, if d is the common diameter of the wires, and assuming there are no gaps between wires in a layer, we must have

$$d = \frac{2\pi r_j}{n_j} = \frac{2\pi r_l}{n_l} \tag{2.31}$$

In this case, (2.29) can be simplified by using the identity (2.30).

It should be noted that the expression for the normal force on the wire utilized by Papailiou (1997) is not general and applies only for the special case when the diameters, and the absolute values of the lay angles, of all the wires are the same. He used the expression for this special case in a numerical determination of the secant bending stiffness for a particular cable (ACSR Cardinal), even though the diameters and the lay angles of the wires in this cable are not the same for all layers.

2.5.3 Accumulation of Normal Forces

In calculating the normal force on a wire in an inner layer, we need to account for the accumulation of normal force from the wires in all outer layers. Each wire has normal forces on its inner and outer surfaces, where it is in contact with the wires in the neghiboring inner and outer layers, respectively. Of course, a wire in the outermost layer only has normal forces on its inner surface. The normal force on the outer surface of a wire can be calculated by adding all the normal forces from the outer layers. The normal force on the inner surface of a wire is equal to the normal force on the outer surface plus the normal force from the current layer. Figure 2.10 shows the normal forces acting on a wire in the l-th layer, where NL denotes the total number of layers. The normal force on the inner surface of the wire has one more term than the normal force on the outer surface to account for the normal force caused by the tension in the wire itself.

2.5.4 Maximum Friction Force

The normal forces on the inner and outer surfaces of the wire generate friction forces on these surfaces. The maximum friction force that can be generated is equal to the normal force times the friction coefficient of the contact surface. Figure 2.11 shows the maximum friction forces on the inner and outer surfaces of the wire in the l-th layer. In this figure, $\mu_{l+1,l}$ and $\mu_{l,l-1}$ are the friction coefficients between the wires in the (l+1)-th and l-th layers and between the wires in the l-th and (l-1)-th layers, respectively. The maximum friction forces are simply products of these

friction coefficients and the corresponding normal forces. The direction of each friction force is opposite to the unbalanced tension force in the wire, and both are in the axial direction of the wire. Note that, by neglecting the effect of torsion on the wire, we have assumed that the wire moves only in the axial direction.

2.6 Wires in Stick State

In the stick state, the unbalanced tension force of the wire is smaller than the maximum friction force that can be generated on the wire. Thus, the condition for the stick state for a wire in the outermost layer is

$$dT_{w(NL)} < \mu_{NL,(NL-1)} dN_{NL,NL} \tag{2.32}$$

where $dT_{w(NL)}$ is the unbalanced tension force in the wire element in the (NL)-th (outermost) layer. Note that there is no friction force on the outer surface of the wire but there is a friction force on the inner surface caused by the tension of the wire itself. Substituting (2.29) into (2.32), we have

$$dT_{w(NL)} < \mu_{NL,(NL-1)} \sin|\alpha_{NL}| T_{w(NL)} d\varphi_{NL} \tag{2.33}$$

as the condition for a wire in the outermost layer to be in stick state. The condition for a wire in an inner layer is

$$dT_{wl} < \mu_{l+1,l} \sum_{j=l+1}^{NL} dN_{j,l} + \mu_{l,l-1} \sum_{j=l}^{NL} dN_{j,l} \quad \text{for } l = 1,\ldots,(NL-1) \tag{2.34}$$

where dT_{wl} is the unbalanced tension force in the wire element in the l-th layer. The first and second terms on the right-hand side in the above equation represent the friction forces on the outer and inner surfaces, respectively. Substituting (2.29) into (2.34), we have

$$\begin{aligned} dT_{wl} <& \mu_{l+1,l} \sum_{j=l+1}^{NL} \sin|\alpha_j| T_{wj} \frac{n_j}{n_l} \frac{r_l}{r_j} \frac{\tan|\alpha_j|}{\tan|\alpha_l|} d\varphi_l \\ &+ \mu_{l,l-1} \sum_{j=l}^{NL} \sin|\alpha_j| T_{wj} \frac{n_j}{n_l} \frac{r_l}{r_j} \frac{\tan|\alpha_j|}{\tan|\alpha_l|} d\varphi_l \quad \text{for } l = 1,\ldots,(NL-1) \end{aligned} \tag{2.35}$$

2.6.1 Fully Stick State

It is useful to investigate the fully stick state of the cable because this will allow us to make proper assumptions for the stick region in the cable. A cable in the fully stick state has all its

wires stuck together so that it can be assumed that the wires in the cable have a helix-like configuration, as we discussed in Section 2.2. The axial deformation of each wire can be defined simply by using the differential length of the deformed configuration of the wire in (2.14), which yields

$$\varepsilon_w^{stick}(\varphi, r) = \sqrt{\sin^2(\alpha_0) + \cos^2(\alpha_0)(1+\varepsilon_c)^2\{1+\kappa_c r\sin(\varphi)\}^2} - 1 \qquad (2.36)$$

This equation gives the exact axial strain of the wire when the cable is in a fully stick state and the wire has a helix-like configuration in the deformed cable.

Since the wires in the cable are stuck together we can assume that the cable cross-section behaves like a solid cross-section satisfying Bernoulli-Euler-Navier kinematic assumption for the bending of beam. This assumption provides us with another way to define the axial deformation of the wire. By this kinematic assumption, the cross-section of the cable, which is plane and perpendicular to the cable centerline before deformation, remains plane and perpendicular to the cable centerline after deformation if the wires in the cable are fully stuck together. Therefore, for a given axial strain, ε_c, and curvature, κ_c, of the cable, the strain of a wire in the longitudinal direction of the cable ($\mathbf{e}_3$ direction in Figure 2.1), $\varepsilon_z^{stick}(\varphi, r)$, is given by

$$\varepsilon_z^{stick}(\varphi, r) = \varepsilon_c + \kappa_c r\sin(\varphi) \qquad (2.37)$$

where φ and r are the polar coordinates, on the cable cross-section, of the wire relative to the center of the cable. When the cable is subjected to axial and pure moment loadings, this strain term is the only non-zero component of the strain tensor of the wire. By transforming the strain tensor into the axial direction of the wire, we can determine the axial and shear strains of the wire. Since wires helically wrapped in conductor cables generally have small lay angle (around 10 degrees) and the shear strain of the wire with small lay angle is small compared to the axial strain of the wire, the shear strain is neglected in the following analysis. Hence, an alternative expression for the axial strain of the wire is obtained as

$$\varepsilon_w^{stick}(\varphi, r) = \cos^2(\alpha_0)\{\varepsilon_c + \kappa_c r\sin(\varphi)\} \qquad (2.38)$$

The above expression can be obtained by linearization of (2.36) for small axial strain and curvature of the cable (see Appendix A). The tension in the wire in the fully stick state, $T_w^{stick}(\varphi, r)$, is calculated by multiplying $\varepsilon_w^{stick}(\varphi, r)$ by the elastic modulus of the material and the cross-sectional area of the wire.

2.6.2 Partially Stick State

Suppose that the cable is subjected to tension loading only. In this case, all wires in the cable are in stick state where we neglect slipping due to torsion of wires. If a pure bending moment loading is added to the cable and gradually increased, then some wires having larger unbalanced tension will start to slip while other wires will remain stuck. To define the axial deformation of the wire in the stick region, we use the Bernoulli-Euler-Navier kinematic assumption for the bending of cable in the same way as we did for the cable in the fully stick state. However, we need to account for the continuity of the axial displacement and internal force of the wires at the boundaries between the stick and slip regions. Since we assumed that wires in the deformed cable have a continuous helix-like configuration, there is no break or overlapping point on the wires. The continuity of the axial displacement of the wires is thus automatically satisfied. The continuity of the tension force in the wires must be satisfied at the boundaries between the stick and slip regions. We are restricting attention to cables in which the material and geometric property of each wire does not change along its length. Then, the axial strain in the wire will also be continuous along the entire length of the wire. Through this continuity condition, the axial strain of the wire in the stick region is coupled with the axial strain of the wire in the slip region. The solution for the axial strain of the wire in the stick region will be presented in Section 2.8, after determining the strain of wires in the slip region in the following section.

2.7 Wires in Slip State

As we discussed in the previous section, when the cable is subjected to tension and bending moment, in general, some wires in the cable will be in the stick state and others will be in the slip state. The unbalanced tension force of a wire in the slip state is equal to the maximum friction force that can be generated on the wire. This condition gives us a set of first-order differential equations for the unbalanced tension forces of wires in the slip state. The solutions for this set of equations are derived for the wires in the outermost, penultimate, and then inner layers, sequentially. In order to determine arbitrary coefficients in the solutions of the differential equation, we need to use appropriate boundary conditions for the wires.

Let ε_c denote the average strain in the cable. The definition of this average strain in terms of the resultant tension force in the cable will be shown in Section 2.9. Suppose this level of strain, ε_c, occurs along a horizontal axis of the cross section with vertical distance y from the

horizontal centroidal axis of the cross section. When there is no slippage of wires, obviously we have $y = 0$. Initially, we make the assumption that, after slippage of wires, y is not very different from zero. Hence, as a first approximation, we determine the forces acting on the wires in both the stick and slip states based on the assumption that $y = 0$. This approximation can be checked and improved, if necessary, through an iterative procedure. It is noted that Papailiou (1997) assumed $y = 0$ without discussing the approximation involved.

2.7.1 Outermost layer

The condition for a wire in the outermost layer to be in the slip state is

$$dT^{slip}_{w(NL)} = \mu_{NL,(NL-1)} \sin|\alpha_{NL}| T_{w(NL)} d\varphi_{NL} \tag{2.39}$$

Dividing by $d\varphi_{NL}$, we have

$$\frac{dT^{slip}_{w(NL)}}{d\varphi_{NL}} = \mu_{NL,(NL-1)} \sin|\alpha_{NL}| T^{slip}_{w(NL)} \tag{2.40}$$

where we have used the superscript "slip" for the tension force in the wire to indicate that it is in the slip state.

The solution of the above differential equation is

$$T^{slip}_{w(NL)} = C^{h}_{NL} \exp\left(\mu_{NL,(NL-1)} \sin|\alpha_{NL}| \varphi_{NL}\right) \tag{2.41}$$

where the arbitrary constant C^{h}_{NL} must be determined by satisfying a boundary condition on $T^{slip}_{w(NL)}$. As mentioned above, we assume that ε_c occurs at $y = 0$. Under this assumption, the axial tension force of wires located at $y = 0$ is

$$\begin{aligned} T^{slip}_{w(NL)}(y = 0) &= T^{slip}_{w(NL)}(\varphi = 0) \\ &= (EA)_{NL}\, \varepsilon_{w(NL)} \\ &= (EA)_{NL} \cos^2(\alpha_{NL})\, \varepsilon_c \end{aligned} \tag{2.42}$$

where $(EA)_{NL}$ is the product of the Young's modulus and the cross-section area of the wire in the outermost layer. The cosine term comes from the tensor transformation from longitudinal direction of the cable to the axial direction of the wire in the cable. The above boundary value is used to find the constant C^{h}_{NL} in (2.41), which is

$$C_{NL}^{h} = (EA)_{NL} \cos^2(\alpha_{NL})\, \varepsilon_c \tag{2.43}$$

2.7.2 Penultimate layer

A wire in the penultimate layer has friction forces acting on its inner and outer surfaces. The friction force on the outer surface is caused by the tension forces of the wires in the outermost layer, and the friction force on the inner surface is caused by the tension forces of the wires in the outermost and penultimate layers. The condition for a wire in the penultimate layer to be in the slip state is

$$\begin{aligned} dT_{w(NL-1)}^{slip} &= \mu_{(NL-1),(NL-2)} \sin|\alpha_{NL-1}| T_{w(NL-1)}^{slip}\, d\varphi_{NL-1} \\ &\quad + (\mu_{NL,(NL-1)} + \mu_{(NL-1),(NL-2)}) \sin|\alpha_{NL}| T_{w(NL)} \frac{n_{NL}}{n_{NL-1}} \frac{r_{NL-1}}{r_{NL}} \frac{\tan|\alpha_{NL}|}{\tan|\alpha_{NL-1}|}\, d\varphi_{NL-1} \end{aligned} \tag{2.44}$$

Dividing by $d\varphi_{NL-1}$, we have

$$\begin{aligned} \frac{dT_{w(NL-1)}^{slip}}{d\varphi_{NL-1}} &= \mu_{(NL-1),(NL-2)} \sin|\alpha_{NL-1}| T_{w(NL-1)}^{slip} \\ &\quad + (\mu_{NL,(NL-1)} + \mu_{(NL-1),(NL-2)}) \sin|\alpha_{NL}| T_{w(NL)} \frac{n_{NL}}{n_{NL-1}} \frac{r_{NL-1}}{r_{NL}} \frac{\tan|\alpha_{NL}|}{\tan|\alpha_{NL-1}|} \end{aligned} \tag{2.45}$$

At this point, we assume that the wires in the outermost layer, from which normal forces are transferred to the wire in the penultimate layer, are in the slip state. Then, by replacing $T_{w(NL)}$ with $T_{w(NL)}^{slip}$, (2.45) becomes

$$\begin{aligned} \frac{dT_{w(NL-1)}^{slip}}{d\varphi_{NL-1}} &= \mu_{(NL-1),(NL-2)} \sin|\alpha_{NL-1}| T_{w(NL-1)}^{slip} \\ &\quad + (\mu_{NL,(NL-1)} + \mu_{(NL-1),(NL-2)}) \sin|\alpha_{NL}| T_{w(NL)}^{slip} \frac{n_{NL}}{n_{NL-1}} \frac{r_{NL-1}}{r_{NL}} \frac{\tan|\alpha_{NL}|}{\tan|\alpha_{NL-1}|} \end{aligned} \tag{2.46}$$

This assumption, that the wires in the outer layers slip first, is reasonable, since the wires in the outer layers are subjected to smaller normal forces and, therefore, smaller friction forces. A numerical example in Section 2.10 verifies this assumption.

Equation (2.46) is a first-order differential equation for $T_{w(NL-1)}^{slip}$ where $T_{w(NL)}^{slip}$ was already determined for the outermost layer. The solution of this equation is the sum of the homogeneous and the particular solutions,

$$T^{slip}_{w(NL-1)} = T^{h}_{w(NL-1)} + T^{p}_{w(NL-1)} \tag{2.47}$$

The homogeneous solution, $T^{h}_{w(NL-1)}$, is given by

$$T^{h}_{w(NL-1)} = C^{h}_{NL-1} \exp\left(\mu_{(NL-1),(NL-2)} \sin|\alpha_{NL-1}| \varphi_{NL-1}\right) \tag{2.48}$$

where the arbitrary constant C^{h}_{NL-1} must be determined by satisfying a boundary condition on $T^{slip}_{w(NL-1)}$. The particular solution, $T^{p}_{w(NL-1)}$, is given by

$$T^{p}_{w(NL-1)} = C^{p}_{NL(NL-1)} \exp(\mu_{NL,(NL-1)} \sin|\alpha_{NL}| \varphi_{NL-1}) \tag{2.49}$$

where the constant $C^{p}_{NL(NL-1)}$ is determined by requiring that the particular solution satisfy the differential equation (2.46). In the above case, the quantities $\mu_{NL,(NL-1)} \sin|\alpha_{NL}|$ and $\mu_{(NL-1),(NL-2)} \sin|\alpha_{NL-1}|$ are different. On the other hand, if these quantities are the same, e.g. if all wires have the same friction coefficient and lay angle, the expression for the particular solution is

$$T^{p}_{w(NL-1)} = C^{p}_{NL(NL-1)} \exp(\mu \sin|\alpha| \varphi_{NL-1}) \varphi_{NL-1} \tag{2.50}$$

where μ and α are the common friction coefficient and lay angle, respectively.

The particular solutions, (2.49) and (2.50), must satisfy (2.46), i.e.

$$\begin{aligned} \frac{dT^{p}_{w(NL-1)}}{d\varphi_{NL-1}} &= \mu_{(NL-1),(NL-2)} \sin|\alpha_{NL-1}| T^{p}_{w(NL-1)} \\ &+ (\mu_{NL,(NL-1)} + \mu_{(NL-1),(NL-2)}) \sum_{j=l+1}^{NL} \sin|\alpha_{NL}| T^{slip}_{w(NL)} \frac{n_{NL}}{n_{NL-1}} \frac{r_{NL-1}}{r_{NL}} \frac{\tan|\alpha_{NL}|}{\tan|\alpha_{NL-1}|} \end{aligned} \tag{2.51}$$

By this equation, we determine the coefficient $C^{p}_{NL(NL-1)}$ in (2.49) or (2.50).

Let us examine the case where (2.49) is the particular solution. The derivative of $T^{p}_{w(NL-1)}$ with respect to φ_{NL-1} is

$$\frac{dT^{p}_{w(NL-1)}}{d\varphi_{NL-1}} = C^{p}_{NL(NL-1)} \mu_{NL,(NL-1)} \sin|\alpha_{NL}| \exp\left(\mu_{NL,(NL-1)} \sin|\alpha_{NL}| \varphi_{NL-1}\right) \tag{2.52}$$

By replacing φ_{NL} with φ_{NL-1}, the expression for the tension of the wire in the outermost layer (2.41) can be rewritten as a function of φ_{NL-1}

$$T^{slip}_{w(NL)} = C^{h}_{NL} \exp\left(\mu_{NL,(NL-1)} \sin|\alpha_{NL}| \varphi_{NL-1}\right) \tag{2.53}$$

Substituting (2.49), (2.52) and (2.53) into (2.51), we have

$$
\begin{aligned}
& C^{p}_{NL(NL-1)}\ \mu_{NL,(NL-1)} \sin|\alpha_{NL}| \exp\left(\mu_{NL,(NL-1)} \sin|\alpha_{NL}|\ \varphi_{NL-1}\right) \\
&= \mu_{(NL-1),(NL-2)} \sin|\alpha_{NL-1}|\ C^{p}_{NL(NL-1)} \exp\left(\mu_{NL,(NL-1)} \sin|\alpha_{NL}|\ \varphi_{NL-1}\right) \\
&+ \left(\mu_{NL,(NL-1)} + \mu_{(NL-1),(NL-2)}\right) \sin|\alpha_{NL}| \frac{n_{NL}}{n_{NL-1}} \frac{r_{NL-1}}{r_{NL}} \frac{\tan|\alpha_{NL}|}{\tan|\alpha_{NL-1}|} \\
&\times C^{h}_{NL} \exp\left(\mu_{NL,NL-1} \sin|\alpha_{NL}|\ \varphi_{NL-1}\right)
\end{aligned}
\tag{2.54}
$$

Now, we can determine $C^{p}_{NL(NL-1)}$ from (2.54)

$$
C^{p}_{NL(NL-1)} = \frac{\left(\mu_{NL,(NL-1)} + \mu_{(NL-1),(NL-2)}\right) \sin|\alpha_{NL}| \frac{n_{NL}}{n_{NL-1}} \frac{r_{NL-1}}{r_{NL}} \frac{\tan|\alpha_{NL}|}{\tan|\alpha_{NL-1}|} C^{h}_{NL}}{\mu_{NL,(NL-1)} \sin|\alpha_{NL}| - \mu_{(NL-1),(NL-2)} \sin|\alpha_{NL-1}|}
\tag{2.55}
$$

where C^{h}_{NL} is readily determined by (2.41) and (2.42). This completely determines the particular solution of the case where the quantities $\mu_{NL,(NL-1)} \sin|\alpha_{NL}|$ and $\mu_{(NL-1),(NL-2)} \sin|\alpha_{NL-1}|$ are different.

Next, we look at the case where all layers have the same friction coefficient and lay angle. Then, the particular solution is assumed by (2.50). The derivative of $T^{p}_{w(NL-1)}$ with respect to φ_{NL-1} is

$$
\begin{aligned}
\frac{dT^{p}_{w(NL-1)}}{d\varphi_{NL-1}} &= \mu \sin|\alpha| \exp\left(\mu \sin|\alpha| \varphi_{NL-1}\right) C^{p}_{NL(NL-1)} \varphi_{NL-1} \\
&+ \exp\left(\mu \sin|\alpha| \varphi_{NL-1}\right) C^{p}_{NL(NL-1)}
\end{aligned}
\tag{2.56}
$$

where μ and α are the same friction coefficient and lay angle, respectively. We rewrite the solution for the outermost layer, which was determined already, as a function of φ_{NL-1}

$$
T^{slip}_{w(NL)} = C^{h}_{NL} \exp\left(\mu \sin|\alpha|\ \varphi_{NL-1}\right)
\tag{2.57}
$$

Substituting (2.56) and (2.57) into (2.51), we have

$$
\begin{aligned}
& \mu \sin|\alpha| C^{p}_{NL(NL-1)}\ \varphi_{NL-1} + C^{p}_{NL(NL-1)} \\
&= \mu \sin|\alpha| C^{p}_{NL(NL-1)}\ \varphi_{NL-1} \\
&+ 2\mu \sin|\alpha| \frac{n_{NL}}{n_{NL-1}} \frac{r_{NL-1}}{r_{NL}} C^{h}_{NL}
\end{aligned}
\tag{2.58}
$$

$C^{p}_{NL(NL-1)}$ can be determined from (2.58).

$$C^{p}_{NL(NL-1)} = 2\mu \sin|\alpha| \frac{n_{NL}}{n_{NL-1}} \frac{r_{NL-1}}{r_{NL}} C^{h}_{NL} \tag{2.59}$$

This completely determines the particular solution for the case where all layers have the same friction coefficient and lay angle.

The coefficient in the homogeneous solution, C^{h}_{NL-1}, is determined by the boundary condition on $T^{slip}_{w(NL-1)}$. We again assume that ε_c occurs at $y = 0$. Under this assumption, the axial tension force of wires located at y =0 is

$$\begin{aligned} T^{slip}_{w(NL-1)}(y=0) &= T^{slip}_{w(NL-1)}(\varphi = 0) \\ &= (EA)_{NL-1} \cdot \varepsilon_{w(NL-1)} \\ &= (EA)_{NL-1} \cdot \cos^2(\alpha_{NL-1}) \varepsilon_c \end{aligned} \tag{2.60}$$

where $(EA)_{NL-1}$ is the product of the Young's modulus and the cross-section area of the wire in the penultimate layer.

In order to determine C^{h}_{NL-1}, let us consider the two cases mentioned above again: the case where the quantities $\mu_{NL,(NL-1)} \sin|\alpha_{NL}|$ and $\mu_{(NL-1),(NL-2)} \sin|\alpha_{NL-1}|$ are different and the case where all wires have the same friction coefficient and lay angle. In the first case, the solution for $T^{slip}_{w(NL-1)}$ is given by the sum of (2.48) and (2.49). Then, the boundary condition (2.60) gives

$$C^{h}_{NL-1} = \cos^2(\alpha_{NL-1}) \cdot (EA)_{NL-1} \varepsilon_c - C^{p}_{NL(NL-1)} \tag{2.61}$$

In the second case, the solution for $T^{slip}_{w(NL-1)}$ is given by the sum of (2.48) and (2.50). Then, the boundary condition (2.60) gives

$$C^{h}_{NL-1} = \cos^2(\alpha) \cdot (EA)_{NL-1} \varepsilon_c \tag{2.62}$$

The above completes the solution for the tension force in the wires in the penultimate layer for two cases: 1) the quantities $\mu_{NL,(NL-1)} \sin|\alpha_{NL}|$ and $\mu_{(NL-1),(NL-2)} \sin|\alpha_{NL-1}|$ are different and 2) all wires have the same friction coefficient and lay angle.

2.7.3 Inner layer

Consider a wire in an inner layer in the slip state. To determine the tension force in that wire, we assume that the tension forces in all of the wires in the outer layers are already known. The wire

in the current layer has friction forces acting on its inner and outer surfaces. The friction force on the outer surface is caused by the tension forces in the wires in the outer layers, and the friction force on the inner surface by the tension forces in the wires in the outer layers as well as in the current layer. The condition for the wire in the current layer to be in the slip state is

$$dT_{wl}^{slip} = \mu_{l+1,l} \sum_{j=l+1}^{NL} \sin|\alpha_j| T_{wj} \frac{n_j}{n_l} \frac{r_l}{r_j} \frac{\tan|\alpha_j|}{\tan|\alpha_l|} d\varphi_l + \mu_{l,l-1} \sum_{j=l}^{NL} \sin|\alpha_j| T_{wj} \frac{n_j}{n_l} \frac{r_l}{r_j} \frac{\tan|\alpha_j|}{\tan|\alpha_l|} d\varphi_l \tag{2.63}$$

where l is the layer index that varies from 1 to $NL-2$, i.e. from the first layer to $(NL-2)$-th layer (just under the penultimate layer). Dividing (2.63) by $d\varphi_l$, and rearranging terms, we have

$$\frac{dT_{wl}^{slip}}{d\varphi_l} = \mu_{l,l-1} \sin|\alpha_l| T_{wl}^{slip} + (\mu_{l+1,l} + \mu_{l,l-1}) \sum_{j=l+1}^{NL} \sin|\alpha_j| T_{wj} \frac{n_j}{n_l} \frac{r_l}{r_j} \frac{\tan|\alpha_j|}{\tan|\alpha_l|} \tag{2.64}$$

As we did for the case of the penultimate layer, assume that the wires in the outer layers, (l+1)-th to NL-th layers, from which normal forces are transferred to the wire in the l-th layer, are in the slip state. Then, by replacing T_{wj} with T_{wj}^{slip} for $j = (l+1),\ldots,NL$, (2.64) becomes

$$\frac{dT_{wl}^{slip}}{d\varphi_l} = \mu_{l,l-1} \sin|\alpha_l| T_{wl}^{slip} + (\mu_{l+1,l} + \mu_{l,l-1}) \sum_{j=l+1}^{NL} \sin|\alpha_j| T_{wj}^{slip} \frac{n_j}{n_l} \frac{r_l}{r_j} \frac{\tan|\alpha_j|}{\tan|\alpha_l|} \tag{2.65}$$

This assumption is reasonable, since the wires in the outer layers are subject to smaller normal and, therefore, smaller friction forces. This is verified through a numerical example in Section 2.10.

The solution of this equation is the sum of the homogeneous and the particular solutions,

$$T_{wl}^{slip} = T_{wl}^{h} + T_{wl}^{p} \tag{2.66}$$

The homogeneous solution, T_{wl}^{h}, is simply

$$T_{wl}^{h} = C_l^{h} \exp(\mu_{l,l-1} \sin|\alpha_l| \varphi_l) \tag{2.67}$$

where C_l^{h} can be determined by a given boundary condition for T_{wl}^{h}. The particular solution, T_{wl}^{p}, is

$$T_{wl}^{p} = \sum_{j=l+1}^{NL} C_{jl}^{p} \exp(\mu_{j,j-1} \sin|\alpha_j| \varphi_l) \tag{2.68}$$

where the constant C_{jl}^{p} is determined by requiring that the particular solution satisfy the differential equation (2.65). In the above case, the quantities $\mu_{j,j-1}\sin|\alpha_j|$ are different for different j. On the other hand, if these quantities are the same, where all wires have the same friction coefficient and lay angle, the expression for the particular solution is

$$T_{wl}^{p} = \exp(\mu \sin|\alpha|\, \varphi_l) \sum_{j=l+1}^{NL} C_{jl}^{p}\, \varphi_l^{NL-j+1} \tag{2.69}$$

where μ and α are the common friction coefficient and lay angle, respectively. These assumed particular solutions (2.68) and (2.69) must satisfy (2.65), i.e.,

$$\frac{dT_{wl}^{p}}{d\varphi_l} = \mu_{l,l-1}\sin|\alpha_l| T_{wl}^{p} + (\mu_{l+1,l} + \mu_{l,l-1}) \sum_{j=l+1}^{NL} \sin|\alpha_j| T_{wj}^{slip} \frac{n_j}{n_l}\frac{r_l}{r_j}\frac{\tan|\alpha_j|}{\tan|\alpha_l|} \tag{2.70}$$

Using this equation, we can determine the coefficients C_{jl}^{p} in (2.68) or (2.69).

Let us examine the first case where the quantities $\mu_{j,j-1}\sin|\alpha_j|$ are different for different layers (different j) and, therefore, (2.68) is the particular solution. The derivative of T_{wl}^{p} with respect to φ_l is

$$\frac{dT_{wl}^{p}}{d\varphi_l} = \sum_{j=l+1}^{NL} C_{jl}^{p}\, \mu_{j,j-1}\sin|\alpha_j| \exp\left(\mu_{j,j-1}\sin|\alpha_j|\varphi_l\right) \tag{2.71}$$

We rewrite the tension force of the wires in the outer layers, (l+1) to (NL-2), as a function of φ_l

$$\begin{aligned} T_{wj}^{slip} &= T_{wj}^{h} + T_{wj}^{p} \\ &= C_j^{h} \exp\left(\mu_{j,j-1}\sin|\alpha_j|\varphi_l\right) + \sum_{i=j+1}^{NL} C_{ij}^{p} \exp\left(\mu_{i,i-1}\sin|\alpha_j|\varphi_l\right) \end{aligned} \tag{2.72}$$

$$\text{for } j = l+1, \ldots, NL-2$$

The tension force of the wires in the outermost and penultimate layers, when j equals NL-1 and NL, are determined by (2.41), (2.43), (2.48), (2.49), (2.55) and (2.61). Substituting these equations together with (2.71) and (2.72) into (2.70), we have

$$\sum_{j=l+1}^{NL} C_{jl}^{p}\ \mu_{j,j-1}\sin|\alpha_j|\exp\left(\mu_{j,j-1}\sin|\alpha_j|\varphi_l\right)$$
$$= \mu_{l,l-1}\sin|\alpha_l|\sum_{j=l+1}^{NL} C_{jl}^{p}\exp\left(\mu_{j,j-1}\sin|\alpha_j|\varphi_l\right)$$
$$+(\mu_{l+1,l}+\mu_{l,l-1})\sum_{j=l+1}^{NL}\sin|\alpha_j|\frac{n_j}{n_l}\frac{r_l}{r_j}\frac{\tan|\alpha_j|}{\tan|\alpha_l|}C_j^{h}\exp\left(\mu_{j,j-1}\sin|\alpha_j|\varphi_l\right) \tag{2.73}$$
$$+(\mu_{l+1,l}+\mu_{l,l-1})\sum_{j=l+1}^{NL}\sum_{i=j+1}^{NL}\sin|\alpha_j|\frac{n_j}{n_l}\frac{r_l}{r_j}\frac{\tan|\alpha_j|}{\tan|\alpha_l|}C_{ij}^{p}\exp\left(\mu_{i,i-1}\sin|\alpha_i|\varphi_l\right)$$

Changing the order of summation and exchanging the notation of the dummy indices, the double summation term can be rewritten as

$$\sum_{j=l+1}^{NL}\sum_{i=j+1}^{NL}\sin|\alpha_j|\frac{n_j}{n_l}\frac{r_l}{r_j}\frac{\tan|\alpha_j|}{\tan|\alpha_l|}C_{ij}^{p}\exp\left(\mu_{i,i-1}\sin|\alpha_i|\varphi_l\right)$$
$$=\sum_{j=l+2}^{NL}\sum_{i=l+1}^{j-1}\sin|\alpha_i|\frac{n_i}{n_l}\frac{r_l}{r_i}\frac{\tan|\alpha_i|}{\tan|\alpha_l|}C_{ji}^{p}\exp\left(\mu_{j,j-1}\sin|\alpha_j|\varphi_l\right) \tag{2.74}$$

Now, we can determine C_{jl}^{p} by substituting (2.74) into (2.73) and equating summation terms on the two sides of the equation. The result is

$$C_{(l+1)l}^{p}=\frac{(\mu_{l+1,l}+\mu_{l,l-1})\sin|\alpha_{l+1}|\frac{n_{l+1}}{n_l}\frac{r_l}{r_{l+1}}\frac{\tan|\alpha_{l+1}|}{\tan|\alpha_l|}C_{l+1}^{h}}{\mu_{l+1,l}\sin|\alpha_{l+1}|-\mu_{l,l-1}\sin|\alpha_l|} \tag{2.75a}$$

$$C_{jl}^{p}=\frac{(\mu_{l+1,l}+\mu_{l,l-1})\left[\sin|\alpha_j|\frac{n_j}{n_l}\frac{r_l}{r_j}\frac{\tan|\alpha_j|}{\tan|\alpha_l|}C_j^{h}+\sum_{i=l+1}^{j-1}\sin|\alpha_i|\frac{n_i}{n_l}\frac{r_i}{r_l}\frac{\tan|\alpha_i|}{\tan|\alpha_l|}C_{ji}^{p}\right]}{\mu_{j,j-1}\sin|\alpha_j|-\mu_{l,l-1}\sin|\alpha_i|} \tag{2.75b}$$

$$\text{for } j=l+2,\ldots,NL$$

where C_{l+1}^{h}, C_j^{h} and C_{ji}^{p} are known since we already determined the tension force of the wires in the outer layers previously. This completely determines the particular solution of the case where the quantities $\mu_{j,j-1}\sin|\alpha_j|$ are different for different layers (different j).

Next, we consider the case where all layers have the same friction coefficient and lay angle. Then, the particular solution is assumed by (2.69). The derivative of T_{wl}^{p} with respect to φ_l is

$$\frac{dT_{wl}^{p}}{d\varphi_l} = \mu \sin|\alpha| \exp\left(\mu \sin|\alpha| \varphi_l\right) \sum_{j=l+1}^{NL} C_{jl}^{p} \varphi_l^{NL-j+1} + \exp\left(\mu \sin|\alpha| \varphi_l\right) \sum_{j=l+1}^{NL} C_{jl}^{p} (NL-j+1) \varphi_l^{NL-j} \tag{2.76}$$

We rewrite the tension force of the wires in the outer layers, (l+1) to (NL-2)-th layers, as a function of φ_l

$$\begin{aligned} T_{wj}^{slip} &= T_{wj}^{h} + T_{wj}^{p} \\ &= C_j^{h} \exp\left(\mu \sin|\alpha| \varphi_l\right) + \exp\left(\mu \sin|\alpha| \varphi_l\right) \sum_{i=j+1}^{NL} C_{ij}^{p} \varphi_l^{NL=j+1} \quad \text{for } j=l+1,\ldots,NL-2 \end{aligned} \tag{2.77}$$

The tension force of the wires in the outermost and penultimate layers, when j equals NL-1 and NL, are provided in (2.41), (2.43), (2.48), (2.50), (2.59) and (2.62). Substituting these together with (2.76) and (2.77) into (2.70), we have

$$\begin{aligned} &\mu|\sin(\alpha)| \sum_{j=l+1}^{NL} C_{jl}^{p} \varphi_l^{NL-j+1} + \sum_{j=l+1}^{NL} C_{jl}^{p} (NL-j+1) \varphi_l^{NL-j} \\ &= \mu|\sin(\alpha)| \sum_{j=l+1}^{NL} C_{jl}^{p} \varphi_l^{NL-j+1} + 2\mu \sum_{j=l+1}^{NL} |\sin(\alpha)| \frac{n_j}{n_l} \frac{r_l}{r_j} C_j^{h} \\ &+ 2\mu \sum_{j=l+1}^{NL} \sum_{i=j+1}^{NL} |\sin(\alpha)| \frac{n_j}{n_l} \frac{r_l}{r_j} C_{ij}^{p} \varphi_l^{NL-i+1} \end{aligned} \tag{2.78}$$

The double summation term can be rewritten as

$$\begin{aligned} &\sum_{j=l+1}^{NL} \sum_{i=j+1}^{NL} |\sin(\alpha)| \frac{n_j}{n_l} \frac{r_l}{r_j} C_{ij}^{p} \varphi^{NL-i+1} \\ &= \sum_{j=l+2}^{NL} \sum_{i=l+1}^{j-1} |\sin(\alpha)| \frac{n_i}{n_l} \frac{r_l}{r_i} C_{ji}^{p} \varphi^{NL-j+1} \end{aligned} \tag{2.79}$$

C_{jl}^{p} is determined by substituting (2.79) into (2.78).

$$C_{NL\,l}^{p} = 2\mu \sum_{j=l+1}^{NL} |\sin(\alpha)| \frac{n_j}{n_l} \frac{r_l}{r_j} C_j^{h} \tag{2.80a}$$

$$C_{(j-1)l}^{p} = \frac{2\mu \sum_{i=l+1}^{j-1} |\sin(\alpha)| \frac{n_i}{n_l} \frac{r_l}{r_i} C_{ji}^{p}}{NL-j+2} \quad \text{for } j=l+2,\ldots,NL \tag{2.80b}$$

This completely determines the particular solution of the case where all layers have the same friction coefficient and lay angle.

The coefficient in the homogeneous solution, C_l^h, is determined by the boundary condition on T_{wl}^{slip}. We again assume that ε_c occurs at $y = 0$. Under this assumption, the axial tension force of wires located at y=0 is

$$\begin{aligned} T_{wl}^{slip}(y=0) &= T_{wl}^{slip}(\varphi=0) \\ &= (EA)_l \cdot \varepsilon_{wl} \\ &= (EA)_l \cdot \cos^2(\alpha_l)\, \varepsilon_c \end{aligned} \tag{2.81}$$

where $(EA)_l$ is the product of the Young's modulus and the cross-section area of the wire in the l-th layer.

In order to determine C_l^h, let us consider the two cases mentioned above again. In the first case, where the quantities $\mu_{j,j-1}\sin|\alpha_j|$ are different for different layers (different j) so that the sum of (2.67) and (2.68) is the solution of T_{wl}^{slip}, the boundary condition (2.81) gives

$$C_l^h = \cos^2(\alpha_l)\cdot(EA)_l\, \varepsilon_c - \sum_{j=l+1}^{NL} C_{jl}^p \tag{2.82}$$

In the second case, where all wires have the same friction coefficient and lay angle so that the sum of (2.67) and (2.69) is the solution of T_{wl}^{slip},

$$C_l^h = \cos^2(\alpha_l)\cdot(EA)_l\, \varepsilon_c \tag{2.83}$$

The above completely determine the solution of T_{wl}^{slip} for two cases: 1) the quantities $\mu_{j,j-1}\sin|\alpha_j|$ are different for different j and 2) all wires have the same friction coefficient and lay angle.

In his derivation, Papailiou (1997) assumed that the terms corresponding to the friction force caused from the outer wires, the second terms on the right-hand side of (2.65), could be approximated by a constant independent of φ, so that he could derive simplified solutions. In the present solution, we do not apply this approximation. Therefore, the solution derived here is more accurate, but also more complicated.

Of course, there are several other possible cases where some layers have the same friction coefficient and lay angle and the others have different values. The ingredients for the solution of these cases are contained in the above equations.

2.8 Boundary between Stick and Slip Regions

The cable under tension and moment loads has some wires in the stick state and the others in the slip state. In each layer, the unbalanced tension force is the maximum for that wire which is located at the neutral axis because that differential wire element has the largest difference in the elevation between its end points. Furthermore, the smaller the normal force on the wire, the smaller the corresponding friction force. Therefore, as we increase the curvature of the cable, the wire in the outermost layer (where the normal force on the wire is minimum among all layers) near the neutral axis (where the difference in the elevation between the end points of the element is maximum) on the side of smaller tension, is the one to slide first. In Section 2.10, a numerical example shows this effect. Raoof (1989) made the same observation in his experiments. It should be recognized that the analysis in this study explains well the reason for this observation. More wires in inner layers or farther from the neutral axis start to slip later as we further increase the curvature of the cable. Therefore, the slip region of the wires on the cable cross-section increases as the curvature of the cable increases.

The tension force of the wires in the slip region can be determined by obtaining solutions of the first-order differential equations as we discussed in Section 2.7. For the known tension force of the wires in the slip region, the tension force of the wires in the stick region is to be determined based on the applications of the Bernoulli-Euler-Navier kinematic assumption, the elastic constitutive law for the wire tension force, and the continuity in the wire tension force. The latter two imply that the axial strain of the wire must be continuous. In particular, this continuity condition of the axial strain of the wire must be satisfied at the boundaries between the stick and slip regions. The continuity in the wire tension force follows from the observation that no concentrated axial force is applied on the wire. Of course, the axial strain of the wire in the slip region is readily determined from the tension force of that wire by application of the elastic constitutive law.

In order to determine the tension force of the wires in the stick region, it is necessary to determine the boundary between the stick and slip regions because the tension force of the wire in the stick region depends on the location of the boundaries, which is determined by use of the continuity condition. Figure 2.12 shows the wires in the cross-section of a 4-layer cable, where the unshaded wires are in the stick state and the wires in dark-gray and the light-gray shades are in the slip state. Specifically, the figure shows the boundary between the stick and the slip re-

gions in the third layer as an example, where the dark-gray wires are in the slip state. In general, the boundaries between the stick and slip regions in the l-th layer are φ_l^+ and φ_l^-, which are angular coordinates of the boundaries.

Due to the continuity of the axial strain of the wires at the boundaries and the Bernoulli-Euler-Navier kinematic assumption, the axial strain of the wire in the stick region is written as

$$\varepsilon_{wl}^{stick}(\varphi) = \varepsilon_{wl}^{slip}(\varphi_l^{\pm}) + \cos^2(\alpha_l)\kappa_c r_l\left[\sin(\varphi) - \sin(\varphi_l^{\pm})\right] \text{ for } \varphi \le \varphi_l^- \text{ or } \varphi \ge \varphi_l^+ \tag{2.84}$$

where φ_l^+ and φ_l^- are still unknowns to be determined.

Figure 2.13 is a side view of the location of wires, which are located on a vertical cross-section in the deformed cable, in the l-th layer, after slipping of some wires has occurred. Note that φ_l^+ and φ_l^- are the boundaries between the stick and slip regions. The wires in the stick region are located on the plane that, because of the Bernoulli-Euler-Navier kinematic assumption, is orthogonal to the centroidal axis of the cable after deformation. The wires in the slip region form the serrated side view as shown in Figure 2.13 because of the slipping. Papailiou (1997) neglected this continuity condition of the axial strain of wires at the boundaries between the stick and slip regions in his derivation. Specifically, he used (2.38) instead of (2.84) for the axial strain of wire in the stick region.

The axial force in the wire in the stick region is simply the product of the axial strain of the wire in this region with Young's modulus and the cross-sectional area of the wire, i.e.,

$$T_{wl}^{stick}(\varphi) = (EA)_l\left\{\varepsilon_{wl}^{slip}(\varphi_l^{\pm}) + \cos^2(\alpha_l)\kappa_c r_l\left[\sin(\varphi) - \sin(\varphi_l^{\pm})\right]\right\}$$
$$\text{for } \varphi \le \varphi_l^- \text{ or } \varphi \ge \varphi_l^+ \tag{2.85}$$

In order to determine the boundaries between the stick and slip regions, we make use of the fact that the axial strain of the wire in both the stick and the slip regions must satisfy the slip conditions, (2.40) for the outermost layer, (2.46) for the penultimate layer and (2.65) for the inner layers, at the boundaries. Of course, the axial strain of the wire in the slip region automatically satisfies the above slip conditions since the axial strain is calculated from these conditions. Therefore, we make use of the fact that the tension force of the wire in the stick region must satisfy the above slip conditions at the boundaries, i.e.,

$$\frac{dT_{w(NL)}^{stick}}{d\varphi_{NL}} = \mu_{NL,(NL-1)}\sin|\alpha_{NL}|T_{w(NL)}^{stick} \quad \text{when } \varphi_{NL} = \varphi_{NL}^{\pm} \tag{2.86}$$

$$\frac{dT^{stick}_{w(NL-1)}}{d\varphi_{NL-1}} = \mu_{(NL-1),(NL-2)} \sin|\alpha_{NL-1}| T^{stick}_{w(NL-1)}$$

$$+ (\mu_{NL,(NL-1)} + \mu_{(NL-1),(NL-2)}) \sin|\alpha_{NL}| T^{slip}_{w(NL)} \frac{n_{NL}}{n_{NL-1}} \frac{r_{NL-1}}{r_{NL}} \frac{\tan|\alpha_{NL}|}{\tan|\alpha_{NL-1}|}$$

$$\text{when } \varphi_{NL-1} = \varphi^{\pm}_{NL-1} \tag{2.87}$$

$$\frac{dT^{stick}_{wl}}{d\varphi_l} = \mu_{l,l-1} \sin|\alpha_l| T^{stick}_{wl} + (\mu_{l+1,l} + \mu_{l,l-1}) \sum_{j=l+1}^{NL} \sin|\alpha_j| T^{slip}_{wj} \frac{n_j}{n_l} \frac{r_l}{r_j}$$

$$\text{when } \varphi_l = \varphi^{\pm}_l \text{ for } l=1,\ldots,NL-2 \tag{2.88}$$

The above is a set of nonlinear equations that is solved for the boundary coordinates $\varphi^{\pm}_j$ j=1,...,NL numerically using a Newton iteration scheme. The calculated values of the boundaries $\varphi^{\pm}_j$ are substituted in (2.85) to determine the axial force in the wire in the stick region. Hence, by utilizing the analysis presented in Sections 2.6-2.8, we have completely determined all the wire forces in the cable.

With all the wire forces known, one can now determine the location of the neutral axis i.e., the distance y from the centroid of the cross-section to the horizontal line where the stress is equal to the average stress due to the tension force. When wires slip, this neutral axis might be different from the previously assumed value $y = 0$. Using this new neutral axis, one can update the wire forces following the procedure described above. By iteratively updating the location of the neutral axis and the wire forces, a more exact solution can be obtained. Our investigations indicate that the first approximation provides sufficiently accurate results for all practical cases encountered in engineering practice.

2.9 Resultant Forces on a Cable

In the previous sections, for a given axial strain and curvature of the cable, we have determined the axial forces in all wires in the cable. The resultant tension force of the cable, T, is calculated by summing up the components, in the axial direction of the cable, of the tension forces of all wires in the cable, i.e.,

$$
\begin{aligned}
T &= \sum_{\text{all wires}} T_w \cos(\alpha) \\
&= \sum_{\text{all wires}} EA\varepsilon_w \cos(\alpha) \\
&= \sum_{\text{all wires}} EA\cos^3(\alpha)\varepsilon_z
\end{aligned}
\tag{2.89}
$$

where the axial strain of each wire is, $\varepsilon_w = \varepsilon_z \cos^2(\alpha)$, obtained by tensor transformation. From this expression, we can define the average strain in terms of the tension force in the cable as

$$
\varepsilon_c = \frac{T}{\sum_{\text{all wires}} EA\cos^3(\alpha)} \tag{2.90}
$$

where E is Young's modulus, A is the cross-sectional area and α is the lay angle, of each wire or the core.

The resultant bending moment in the cable is calculated as

$$
M = \sum_{\text{all wires}} EI_w\kappa_c + \sum_{\text{all wires}} T_w(\varepsilon_c,\kappa_c)\cdot\cos(\alpha)\cdot r\sin(\varphi) \tag{2.91}
$$

where $I_w = \pi d_w^{\,4}/64$ is the moment of inertia for each wire or the core. The first term on the right-hand side in this equation accounts for the bending stiffness of each individual wire or the core. The second term represents the moment due to the axial forces of all wires. The resultant bending moment of the cable as calculated from the above equation has a nonlinear relationship with the curvature of the cable, κ_c, and depends on the axial strain of the cable, ε_c. This is so because T_w is a nonlinear function of κ_c and ε_c, as discussed in previous sections. In the next section, this nonlinearity of the moment-curvature relationship will be exhibited through a numerical example.

2.10 Example Application

We choose the Jessamine cable as a numerical example and calculate the resultant forces on the cable for a given axial strain and curvature of the cable. As described in Section 2.3, the Jessamine cable has 4 layers of aluminum wires and a core. Each wire and the core in the cable has 4.30mm diameter and all the wires except the core are assumed to have 12 degree lay angles. The Young's modulus of each wire is E=70×10^9. The properties of the Jessamine cable are listed in Table 2.1. The coefficient of friction between wires in adjacent layers in the cable is as-

sumed to be 0.3. Since the friction coefficients and lay angles of all wires are the same, we use the formulations in (2.41) for the outermost layer, (2.48) and (2.50) for the penultimate layer, and (2.67) and (2.69) for the inner layers. Furthermore, since all wires in the cable have the same diameter, we can use the identity (2.30).

For the fixed axial strain in the cable $\varepsilon_c=10^{-6}$, Figure 2.14 shows the angular coordinates of the boundaries between the stick and slip regions, $\varphi_l^{\pm}$, as a function of the cable curvature, κ_c. The wires start to slip from the outermost layer to inner layers. If a wire in an inner layer is in the slip state, then we can see from the figure that the wires in the outer layers, which have the same angular coordinate as the wire in the inner layer, are also in the slip state. This observation is consistent with the assumption we made in Section 2.7. In addition, the wires near the neutral axis on the side of smaller tension start to slip first in each layer, which is consistent with the test results obtained by Raoof (1989) as described in Section 2.8.

The resultant tension force in the cable as a function of curvature of the cable is shown in Figure 2.15 for different axial strains of the cable. The resultant tension force is almost constant even if wires in the cable are slipping. Therefore, the initially applied average axial strain in the cable basically does not change as the cable curvature is increased. Figure 2.16 shows the nonlinear moment-curvature relationship of the cable for different axial strains (or axial forces) in the cable. For the larger axial strain, it is noted that the transition region from the fully stick state to the fully slip state becomes wider. Also, the initial yielding moment and the initial yielding curvature of the cable are larger for a larger axial strain of the cable. These results are due to the fact that the friction forces on the wires in the cable are larger when the axial strain (or axial forces) of the cable is larger.

The moment of the cable divided by the curvature, M/κ_c, is the secant bending stiffness of the cable. This measure is plotted versus the curvature of the cable in Figure 2.17 for different axial strains of the cable. The secant bending stiffness reduces from $EI_{\max}$ (=5361.0 N·m^2) to $EI_{\min}$ (=70.3 N·m^2) as the curvature of the cable increases, where $EI_{\max}$ and $EI_{\min}$ are the bending stiffnesses of the cable in the fully stick state and in the fully slip state, respectively. For small axial strain of the cable, the transition zone from $EI_{\max}$ to $EI_{\min}$ is very rapid so that $EI_{\min}$ essentially governs the bending behavior of the cable.

It is interesting to compare the relationship between the secant bending stiffness and the curvature of the cable with that calculated based on Papailiou's model (see equations (24)-(42) in Papailiou 1997). Figure 2.18 shows the relationship between the secant bending stiffness and the curvature of the cable for different axial strains. Papailiou's cable model has a smaller secant bending stiffness than that of the improved cable model in this study. The discrepancy between these two model occurred from the facts that the improved model uses a more exact expression for the normal forces on the wire as shown in (2.29), that Papailiou's model does not satisfy continuity of axial strain of the wires between the stick and slip regions but the improved model does, and that Papailiou approximated the terms corresponding to the friction force caused from the outer wires, the second terms on the right-hand side of (2.64), with a constant independent of φ but the improved model uses the exact expression. Certainly, it is expected that the improved model would provide more accurate results. The discrepancy between the two models, as exhibited in Figure 2.18, could be significant when the curvature of the cable is between the initial-slip curvature and the full-slip curvature and closer to the full-slip curvature. For example, each of the two circled points on the vertical dotted line indicates the calculated secant bending stiffness, for a given curvature of the cable, based on each model. The secant bending moment of the upper point, which corresponds to the improved model, is about two times larger than that of the lower point, which corresponds to the Papailiou's model.

The model developed for cable bending in this chapter accounts only for the case of monotonic loading. For cyclic bending behavior of the cable, we assume that the cable behaves as if it were an elastic-plastic material with kinematic hardening, since the nonlinear bending behavior of the cable is due to slipping between wires. This slipping is similar to slip in crystalline metallic materials undergoing plastic flow, for which it has been shown that kinematic hardening is the appropriate model (Flouriot *et al.*, 2003). The nonlinear moment-curvature relationship of the cable in this chapter can be treated as an elasto-plastic constitutive model in a finite element analysis. The development of the finite element model accounting for nonlinear geometry and nonlinear bending behavior of the cable is discussed in the next chapter.

Table 2.1 Properties of the Jessamine cable

Property	Jessamine
Young's modulus	70×10^{9} N/m^2
number of layers except core	4
number of strands	61
strand diameter	4.303 mm
overall conductor diameter	38.73 mm
cross section area	831 mm^2
mass per unit length	2.253 kg/m
lay angle	12 degree
I_{min}	1,004 mm^4
I_{max}	76,585 mm^4

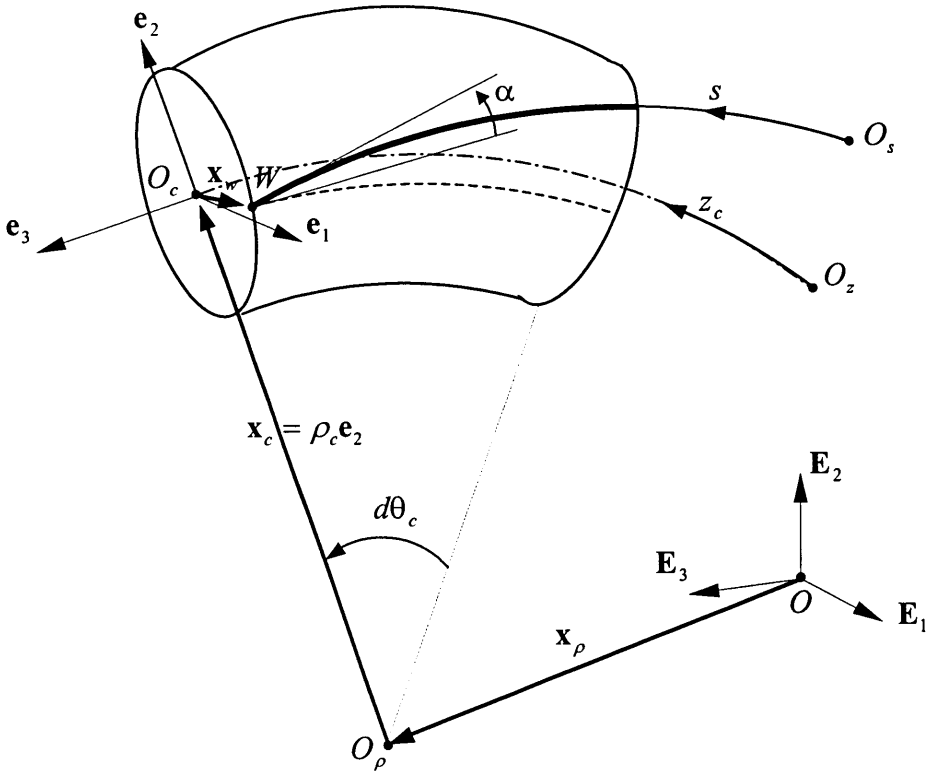

Figure 2.1 Helix-like configuration of a wire wrapped around a bent cable

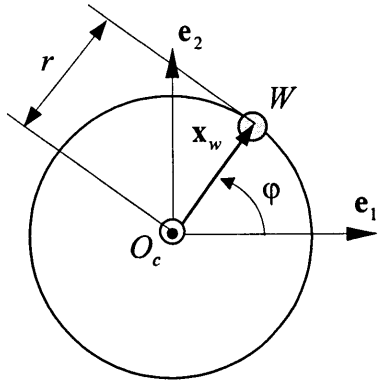

Figure 2.2 Local coordinate system in a cross-section of the cable

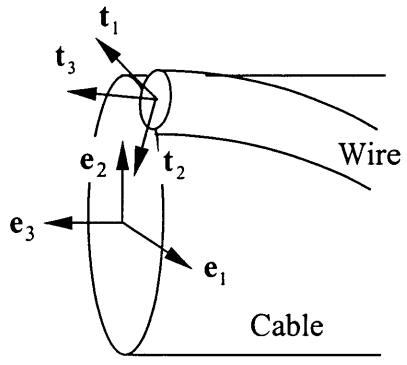

Figure 2.3 Orthonormal bases on the cross-sections of the cable and the wire

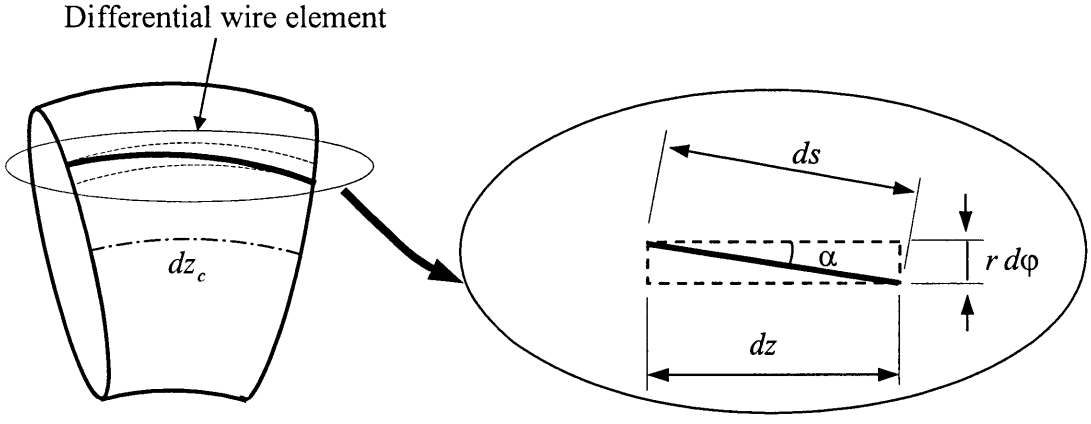

Figure 2.4 Differential wire element in the deformed cable

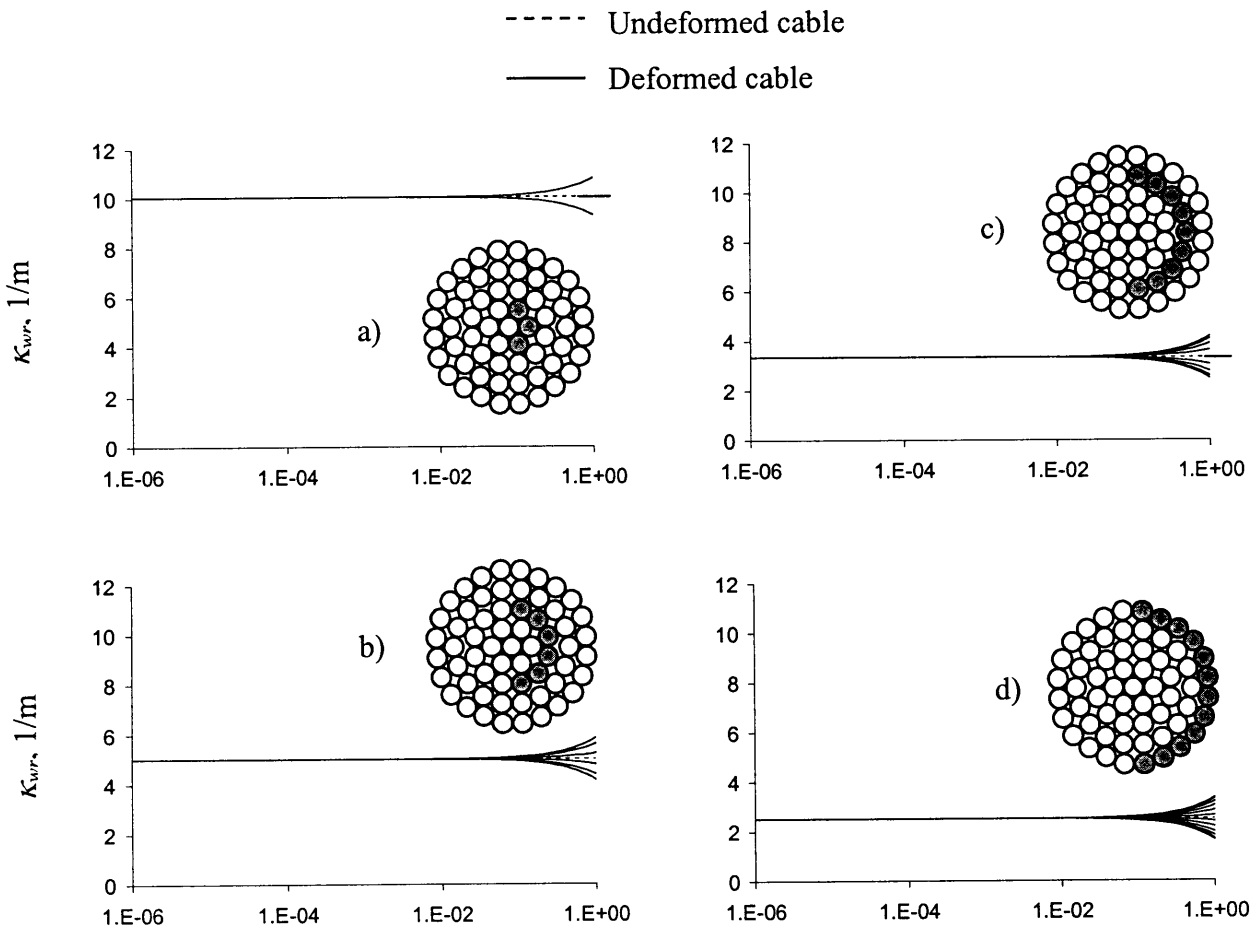

Figure 2.5 Comparison between radial components of wire curvatures in deformed and undeformed cable: a) wires in first layer, b) wires in second layer, c) wires in third layer, d) wires in fourth layer

a)

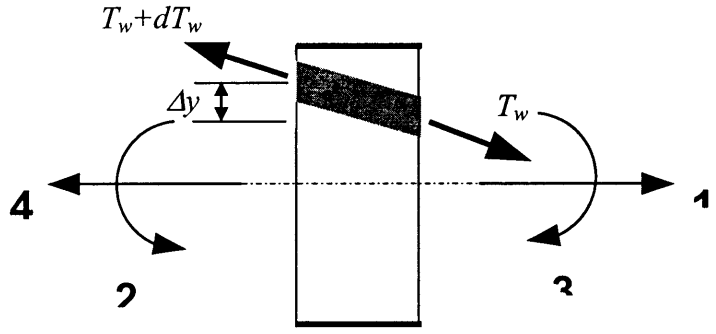

b)

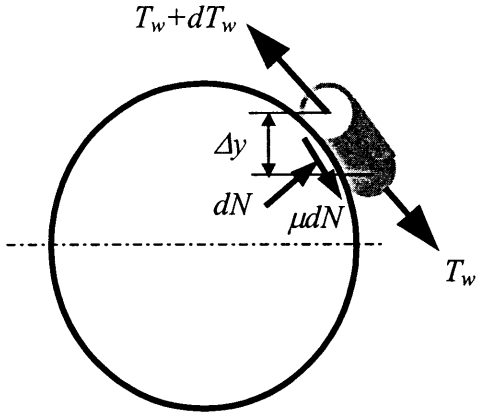

Figure 2.6 Forces on a wire helically wrapped in a cable: a) side view, b) cross-sectional view

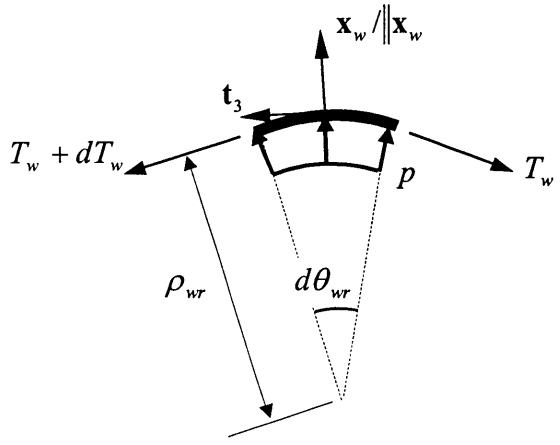

Figure 2.7 Normal pressure on a wire in the outermost layer

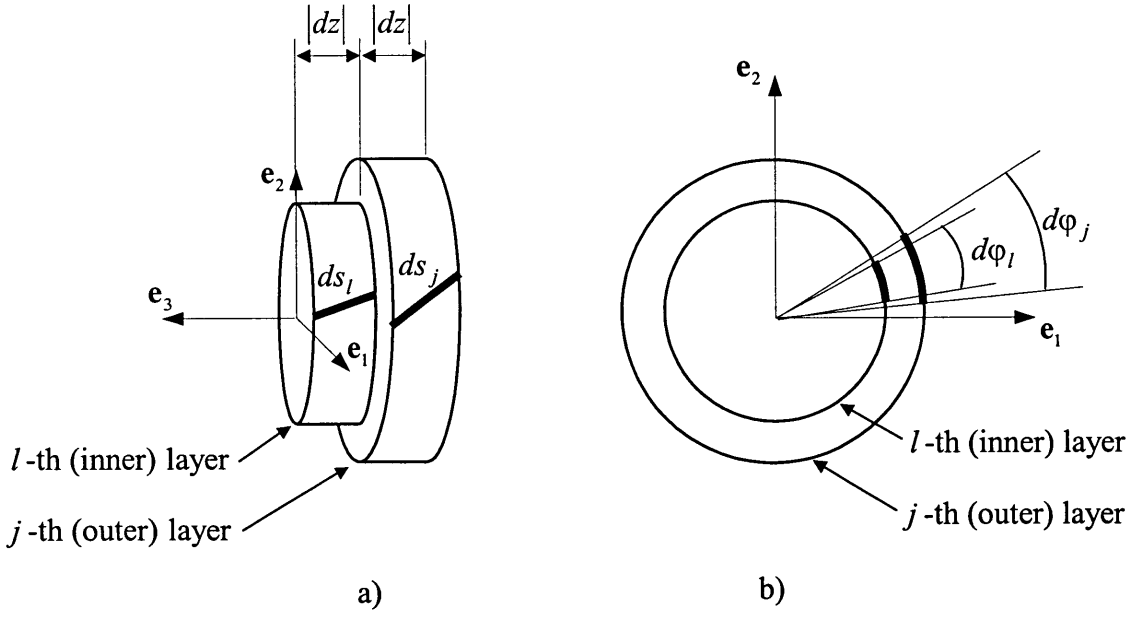

Figure 2.8 Differential wire elements in j-th and l-th layers with different lay angles

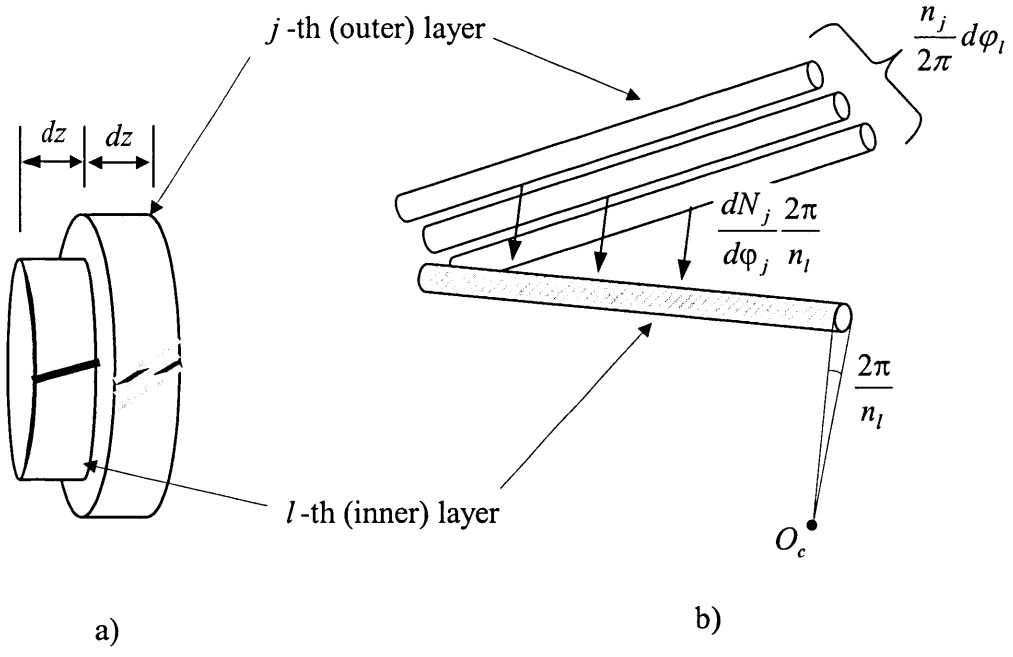

Figure 2.9 Wires in two different layers

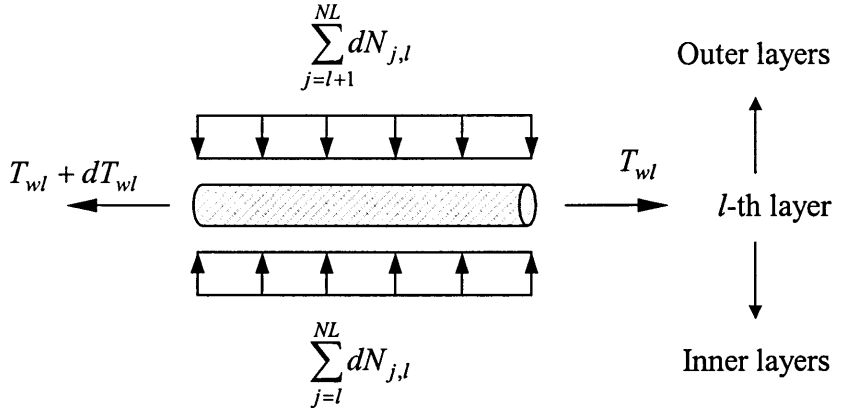

Figure 2.10 Normal forces acting on a single wire in the *l*-th layer

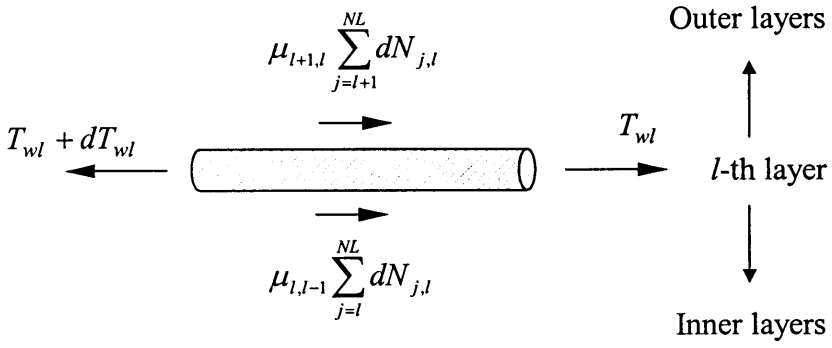

Figure 2.11 Friction forces acting on a single wire in the l-th layer

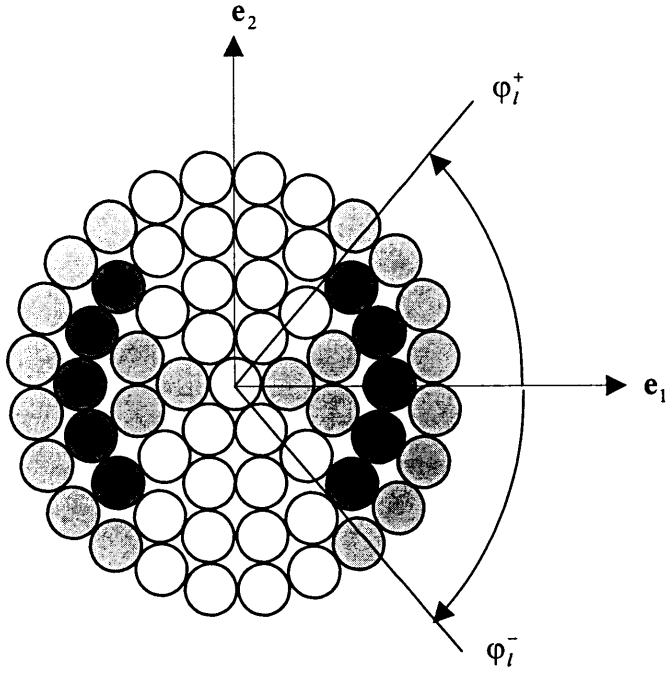

Figure 2.12 Wires in stick (unshaded) and slip region (dark and light-gray shades)

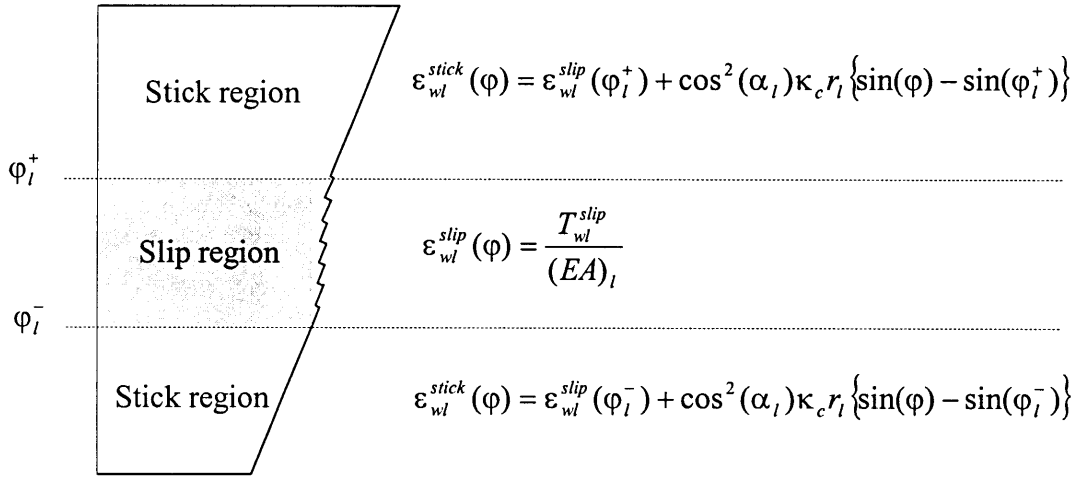

Figure 2.13 Side view of the location of wires in *l*-th layer of the cable after deformation under bending and tension loads

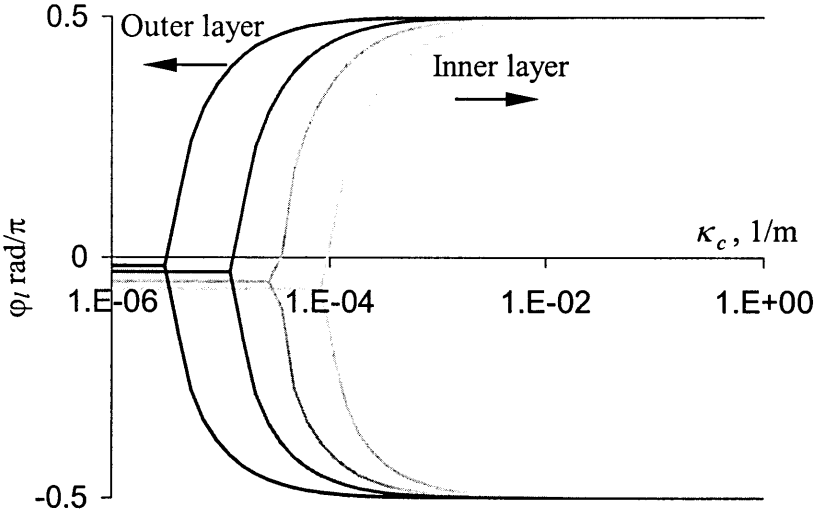

Figure 2.14 Boundaries between the stick and slip regions on a cross-section of the Jessamine cable vs. the curvature of the cable for ε_c=1.0E-6

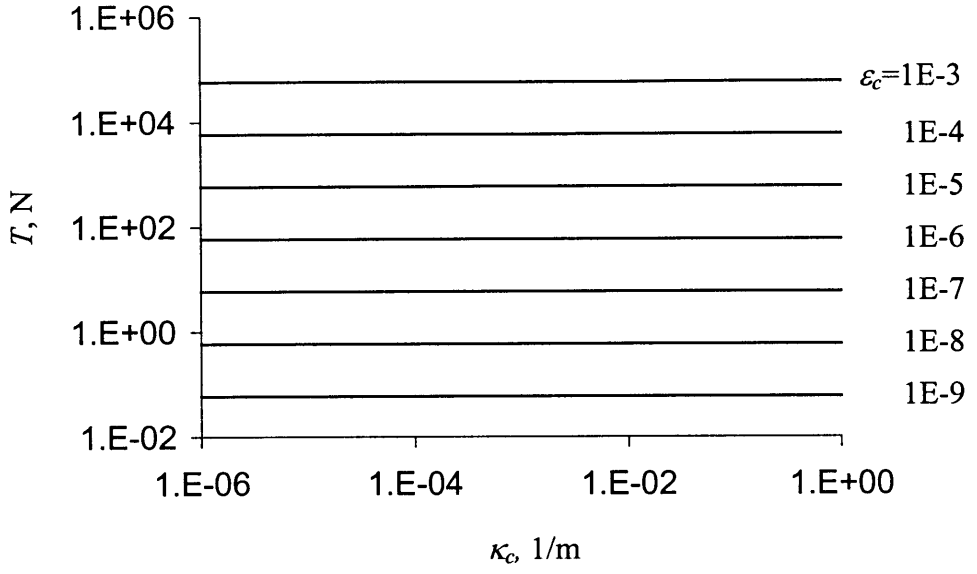

Figure 2.15 Tension in the Jessamine cable vs. the cable curvature for different axial strains of the cable

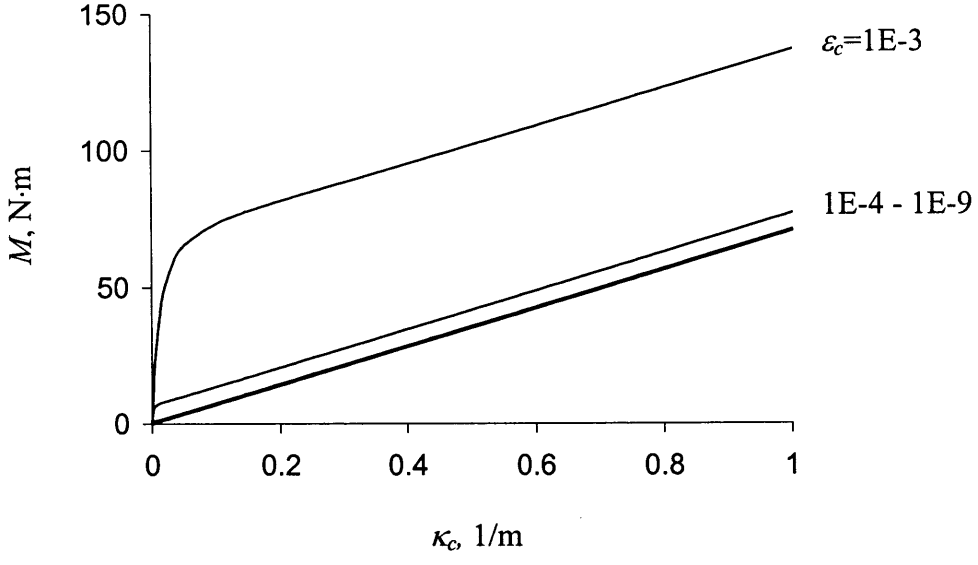

Figure 2.16 Moment-curvature relations of the Jessamine cable for different axial strains of the cable

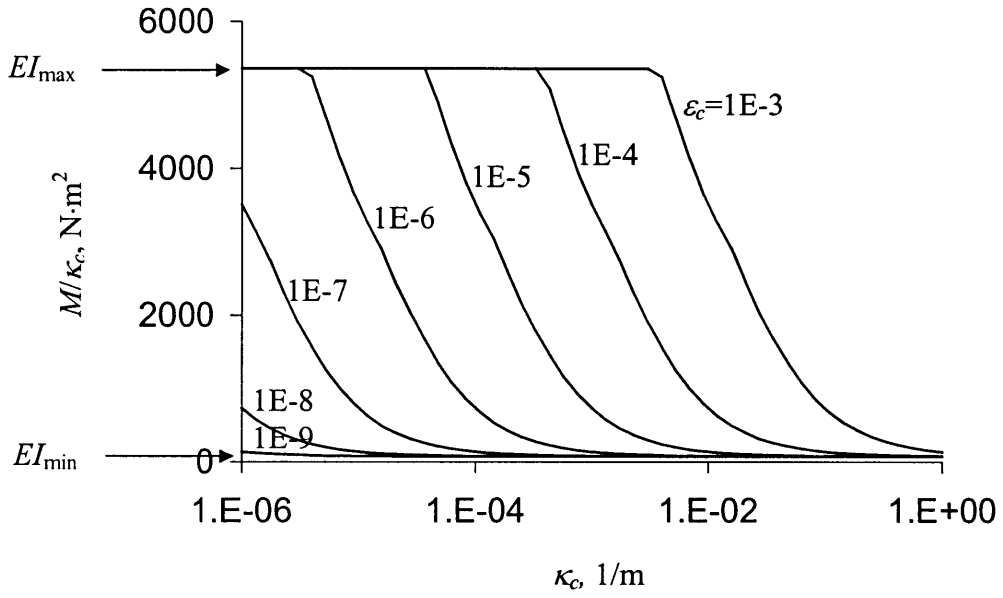

Figure 2.17 Secant bending stiffness of the Jessamine cable vs. the cable curvature for different axial strains of the cable

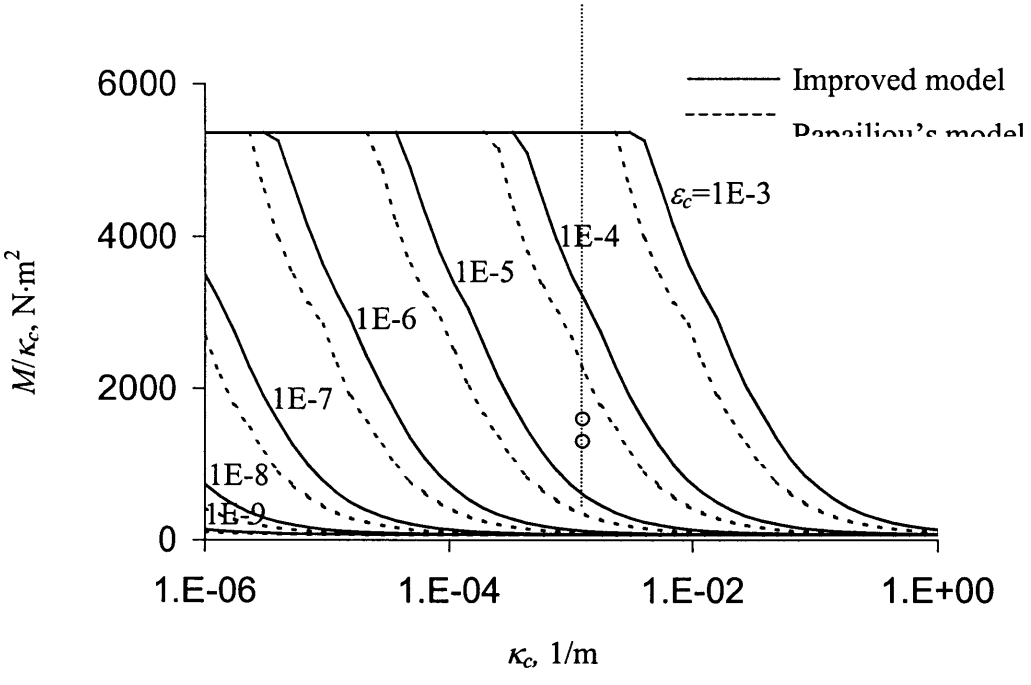

Figure 2.18 Comparison of the relationship between the secant bending stiffness of the Jessamine cable and the curvature of the cable calculated by the improved model and Papailiou's model for different axial strains

3 FINITE ELEMENT MODEL FOR CONDUCTOR CABLES

3.1 Introduction

From the previous chapter, we know that the cable has a nonlinear moment-curvature relationship due to the slippage of wires in the cable. This moment-curvature relationship also depends on the tension force (or axial strain) in the cable. Furthermore, geometric nonlinearity in the behavior of the cable is important because the cable, having small flexural stiffness, can have significantly large rotations and displacements.

Both the nonlinear moment-curvature relationship and the geometric nonlinearity should be considered in static or dynamic analyses of the cable. To deal with the nonlinear geometry, it is convenient to utilize the general theory of elastic rods developed by Cosserat brothers (1967). This leads to a highly nonlinear problem that will have to be solved numerically. An effective way to accomplish this is to use the finite element method. To that end, it is convenient to employ the formulation given by Simo and Vu-Quoc (1986a,b) for elastic rods. The Simo and Vu-Quoc formulation is based on the work of the Cosserat brothers, but develops it in a form appropriate for application to the finite element method.

To deal with the nonlinear dissipative moment-curvature relationship, we model the cable as if it were a solid rod made of an elastic-plastic material that replicates the hysteretic behavior of the cable that is actually caused by slipping of wires. In the present study, this material model is incorporated into the Simo and Vu-Quoc formulation to obtain a finite element formulation that accounts for both the nonlinear moment-curvature relationship and the geometrical nonlinearity of the cable, and that is in a form convenient for numerical computation.

For simplicity, we consider the case where the motion of the cable is in a given, fixed vertical plane. The geometrically exact rod theory that models this 2-dimensional problem of the cable is described in Section 3.2. The elasto-plastic constitutive law used to mimic the nonlinear dissipative behavior of the cable is described in Section 3.3. In Section 3.4, we summarize the section properties of the cable used in the finite element model.

3.2 Geometrically exact rod model

In this section, we focus on the dynamics of a flexible cable subjected to large motions taking place in a given vertical plane. It is to be noted that the theory we employ is fully invariant under superposed rigid body motions, and can accommodate finite deformations in stretch, shear and bending, as well as account for large rotations. When deformations are small, this model reduces to the well-known Timoshenko beam theory (Gere and Timoshenko 1997). For completeness of presentation, the Simo and Vu-Quoc (1986a, b) formulation of the rod model in the context of the finite element method is described below.

3.2.1 Basic Kinematics

The cable under investigation, which undergoes motion in a single plane, is depicted in Figure 3.1. The initial undeformed, unstressed, straight configuration of the cable, denoted as the *reference configuration*, is indicated by the dotted lines. The unit normal basis vectors $\{\mathbf{E}_1, \mathbf{E}_2\}$, with the origin $\mathbf{O}$, constitute an inertial frame attached to the fixed undeformed configuration that is used to locate material points in the reference configuration. The basis vector $\mathbf{E}_1$ is in the direction of the centroidal axis and $\mathbf{E}_2$ is in the plane of the cross-section of the undisturbed cable. The deformed configuration, referred to as the *current configuration*, is indicated by solid lines.

The basic kinematic assumption is that plane sections normal to the axis of the beam in the undeformed configuration remain plane in the deformed configuration. In addition, it is assumed that the shape of the cross-section of the cable remains unchanged and that no twisting of the cross-section takes place around the centroidal axis of the cable. A set of unit orthonormal basis vectors, $\{\mathbf{d}_1, \mathbf{d}_2\}$, associated with each cross-section of the cable, is introduced. These vectors, often referred to as *directors*, are used to track the rigid-body motion of each cross-section. The vector $\mathbf{d}_1$ is taken normal to the cross-section so that $\mathbf{d}_2$ lies in the plane of the cross-section.

The location of a material point of the cable cross-section at time $t = 0$ is given by the coordinates (X_1, X_2). At time t in the deformed configuration, the location of this material point is given by the position vector, $\mathbf{x}(X_1, X_2, t)$ where

$$\mathbf{x}(X_1, X_2, t) = \mathbf{x}_0(X_1, t) + X_2 \cdot \mathbf{d}_2(X_1, t) \tag{3.1}$$

and where $\mathbf{x}_0$ is the position vector to the centroid of the cross-section in the current configuration.

$$\mathbf{x}_0(X_1,t) = [X_1 + u_1(X_1,t)]\mathbf{E}_1 + u_2(X_1,t)\mathbf{E}_2 \tag{3.2}$$

where u_1 and u_2 are the displacements of the centroid of the cross-section in the directions of $\mathbf{E}_1$ and $\mathbf{E}_2$, respectively. The vectors $\{\mathbf{d}_1,\mathbf{d}_2\}$ are given in terms of the basis vectors of the reference configuration as

$$\mathbf{d}_1(X_1,t) = \cos\vartheta(X_1,t)\mathbf{E}_1 + \sin\vartheta(X_1,t)\mathbf{E}_2 \tag{3.3a}$$

$$\mathbf{d}_2(X_1,t) = -\sin\vartheta(X_1,t)\mathbf{E}_1 + \cos\vartheta(X_1,t)\mathbf{E}_2 \tag{3.3b}$$

where $\vartheta(X_1,t)$ is the rotation of the cross-section from the initial configuration, considered positive counter-clockwise as shown in Figure 3.1.

It is to be noted that the directors $\{\mathbf{d}_1,\mathbf{d}_2\}$ remain orthonormal to one another but the cross sections are not necessarily orthogonal to the centerline of the cable. To rule out the non-physical situation of infinite shear, the restriction

$$\mathbf{x}_0' \cdot \mathbf{d}_1 > 0 \tag{3.4}$$

is imposed on the set of admissible configurations, where the vector $\mathbf{x}_0'(X_1,t)$ is tangent to the centerline, and where $(\cdot)' = d(\cdot)/dX_1$. For compactness, we introduce the matrix, $\mathbf{\Lambda}$, which describes the rotation between the basis vectors in the reference configuration and the directors. This rotation matrix is given by

$$\mathbf{\Lambda} = [\mathbf{d}_1 \quad \mathbf{d}_2] = \begin{bmatrix} \cos(\vartheta) & -\sin(\vartheta) \\ \sin(\vartheta) & \cos(\vartheta) \end{bmatrix} \tag{3.5}$$

3.2.2 Strain and Stress

The following strain measures are employed:

$$\mathbf{\Gamma} = \begin{Bmatrix} \Gamma_1 \\ \Gamma_2 \end{Bmatrix} = \mathbf{\Lambda}^T(\mathbf{x}_0' - \mathbf{d}_1) \tag{3.6a}$$

$$K = \vartheta' \tag{3.6b}$$

The components of the vector $\mathbf{\Gamma}$, Γ_1 and Γ_2, are identified with the axial and shear strains, respectively, and K, the curvature of the centerline of the cable, with the bending strain. The strain

vector $\boldsymbol{\Gamma}$ defines the nonlinear strain measure in the reference configuration. The counterpart of $\boldsymbol{\Gamma}$ in the current configuration is the strain measure $\boldsymbol{\gamma}$:

$$\boldsymbol{\gamma} = \begin{Bmatrix} \gamma_1 \\ \gamma_2 \end{Bmatrix} = \mathbf{x}_0' - \mathbf{d}_1 \tag{3.7}$$

The expression of the curvature in the current configuration, κ, is the same as the curvature K in the reference configuration, because the rotation of the cable is restrained to the plane $\{\mathbf{E}_1, \mathbf{E}_2\}$.

The internal forces corresponding to the strains need to be defined. As was discussed in Chapter 2, the bending moment M in the reference configuration is a nonlinear function of the curvature and axial strain of the cable so that,

$$M = M(\mathrm{K}, \Gamma_1) = \hat{M}(\kappa_c, \varepsilon_c) \tag{3.8}$$

Note that, in Chapter 2, the curvature K and the axial strain Γ_1 of the cable were denoted by $\kappa_c(1+\varepsilon_c)$ and ε_c, respectively.

We can use a bilinear elasto-plastic model to represent the moment-curvature relationship (3.8). The detailed description of the bilinear elasto-plastic model is prescribed in Section 3.3. The axial and shear forces, $\mathbf{N}$, in the reference configuration are assumed to be related to the corresponding strains, $\boldsymbol{\Gamma}$, through an linear elastic law such that

$$\mathbf{N} = \begin{Bmatrix} N_1 \\ N_2 \end{Bmatrix} = \begin{bmatrix} EA & 0 \\ 0 & GA_S \end{bmatrix} \boldsymbol{\Gamma} \tag{3.9}$$

where E and G are the Young's and shear moduli of the cable material, respectively. A is the area of the cross section and A_s is the effective shear area. The internal force vector in the current configuration, $\mathbf{n}$, is obtained by transforming $\mathbf{N}$ to the current configuration,

$$\mathbf{n} = \boldsymbol{\Lambda}\mathbf{N} \tag{3.10}$$

The expression of the bending moment in the current configuration, m, is the same as in (3.8) because the motion of the cable is restricted to the plane $\{\mathbf{E}_1, \mathbf{E}_2\}$.

3.2.3 Equations of Motion

As given in Simo and Vu-Quoc (1986a), the spatial form of the local balance law for the thin rod is

$$A_\rho \ddot{\mathbf{u}} = \frac{d\mathbf{n}}{dX_1} + \bar{\mathbf{n}} \tag{3.11a}$$

$$I_\rho \ddot{\vartheta} = \frac{dm}{dX_1} + (1 + \frac{du_1}{dX_1}) n_2 - \frac{du_2}{dX_1} n_1 + \bar{m} \tag{3.11b}$$

where A_ρ and I_ρ are the mass and the rotational inertia constants of the cable per unit length in the reference configuration, respectively, $\mathbf{u} = (u_1 \quad u_2)^T$ is the displacement vector of the center-line of the cable, $\mathbf{n} = (n_1 \quad n_2)^T$ is the internal force vector acting on a typical cross-section of the rod in the current configuration, $\bar{\mathbf{n}}$ is the distributed external loading vector, m is the bending moment in the current configuration, and $\bar{m}$ is the distributed external moment loading. Let the material of the cable have density ρ_0 per unit of undeformed volume. Then, A_ρ and I_ρ are given as

$$A_\rho = \int_A \rho_0 dA \tag{3.12a}$$

$$I_\rho = \int_A \rho_0 X_2^{\,2} dA \tag{3.12b}$$

3.2.4 The Weak Form

Define the following quantities

$$\mathbf{I} = \mathrm{Diag}\lfloor A_\rho \quad A_\rho \quad I_\rho \rfloor,$$

$$\phi(X_1,t) = \begin{Bmatrix} X_1 + u_1(X_1,t) \\ u_2(X_1,t) \\ \vartheta(X_1,t) \end{Bmatrix}, \quad \mathbf{f}(X_1,t) = \begin{Bmatrix} \bar{n}_1(X_1,t) \\ \bar{n}_2(X_1,t) \\ \bar{m}(X_1,t) \end{Bmatrix} \tag{3.13}$$

where $\phi(X_1,t)$ defines the configuration of the cable and $\mathbf{f}(X_1,t)$ is the external distributed load acting on the cable.

The weak form of the equations of motion (3.11) is obtained by integrating the scalar product (indicated by the dot symbol) of (3.11) with an arbitrary weight function η over the domain $[0, S]$

$$G_{dyn}(\phi,\eta) = \int_{[0,S]} \eta \cdot \mathbf{I}\, \ddot{\phi}\, dX_1 + G_{stat}(\phi,\eta) = 0, \quad \forall\, \eta \tag{3.14}$$

where S is the length of the cable in the reference configuration and $G_{stat}(\phi,\eta)$ denotes the weak form of the PDE's when inertia terms are dropped, and where

$$G_{stat}(\phi,\eta) = -\int_{[0,S]} \eta \cdot \begin{Bmatrix} n_1' \\ n_2' \\ m'+(1+u_1')n_2 - u_2'n_1 \end{Bmatrix} dX_1 - \int_{[0,S]} \eta \cdot \mathbf{f}\, dX_1 \tag{3.15}$$

with

$$\eta = \begin{Bmatrix} \eta_1 \\ \eta_2 \\ \eta_3 \end{Bmatrix} \tag{3.16}$$

The weight function η is the set of all admissible variations that satisfy the boundary conditions.

$$\eta \cdot \{n_1 \quad n_2 \quad m\}\Big|_{X_1=0}^{X_1=S} = 0 \tag{3.17}$$

Then, by integrating the first term in (3.15) by parts, we obtain

$$G_{stat}(\phi,\eta) = \int_{[0,S]} \Xi(\phi)\eta \cdot \begin{Bmatrix} n_1 \\ n_2 \\ m \end{Bmatrix} dX_1 - \int_{[0,S]} \eta \cdot \mathbf{f}\, dX_1 \tag{3.18}$$

where $\Xi(\phi)$ denotes the differential operator defined by

$$\Xi(\phi) = \begin{bmatrix} \dfrac{d}{dX_1} & 0 & u_2' \\ 0 & \dfrac{d}{dX_1} & -(1+u_1') \\ 0 & 0 & \dfrac{d}{dX_1} \end{bmatrix} \tag{3.19}$$

3.2.5 Time-Stepping Scheme

After extensive numerical investigation using several different time-stepping algorithms, it was found that the most appropriate one for the dynamic analysis of the cable was the HHT algorithm (Hilber, Hughes and Taylor 1977). This algorithm, which is widely used in nonlinear structural dynamics, was found to be a stable one for the problem under investigation.

Let $\phi_n(s)$ denote the approximate solution to $\phi(X_1,t_n)$ at time t_n. Similarly, let $\mathbf{v}_n(s) \cong \dot{\phi}(X_1,t_n)$ and $\mathbf{a}_n(s) \cong \ddot{\phi}(X_1,t_n)$, respectively, represent the approximate velocity and acceleration at time t_n. Assume that $(\phi_n, \mathbf{v}_n, \mathbf{a}_n)$ completely satisfy the temporal discrete version of the weak form (3.14) at time t_n. The solution $(\phi_{n+1}, \mathbf{v}_{n+1}, \mathbf{a}_{n+1})$ at the next time step t_{n+1} is to be determined so that

$$G_{dyn}(\boldsymbol{\phi}_{n+\alpha}, \mathbf{v}_{n+\alpha}, \boldsymbol{\eta}) = \int_{[0,S]} \boldsymbol{\eta} \cdot \mathbf{I}\, \mathbf{a}_{n+\alpha}\, dX_1 + G_{stat}(\boldsymbol{\phi}_{n+\alpha}, \mathbf{v}_{n+\alpha}, \boldsymbol{\eta}) = 0, \quad \forall \boldsymbol{\eta} \tag{3.20}$$

where

$$\boldsymbol{\phi}_{n+\alpha} = (1-\alpha)\boldsymbol{\phi}_n + \alpha\boldsymbol{\phi}_{n+1} \tag{3.21a}$$

$$\mathbf{v}_{n+\alpha} = (1-\alpha)\mathbf{v}_n + \alpha\mathbf{v}_{n+1} \tag{3.21b}$$

$$\mathbf{a}_{n+\alpha} = \mathbf{a}_{n+1} \tag{3.21c}$$

and where the values of the parameter α and the additional parameters β and γ, introduced in (3.22), are chosen to produce sufficient numerical damping to have stable numerical solutions, see Taylor (1998).

The quantities $\boldsymbol{\phi}_{n+1}$, $\mathbf{v}_{n+1}$ and $\mathbf{a}_{n+1}$ are calculated using the well-known Newmark time-integration formula

$$\boldsymbol{\phi}_{n+1} = \boldsymbol{\phi}_n + \Delta t \mathbf{v}_n + \Delta t^2 \left[(0.5-\beta)\mathbf{a}_n + \beta \mathbf{a}_{n+1}\right] \tag{3.22a}$$

$$\mathbf{v}_{n+1} = \mathbf{v}_n + \Delta t\left[(1-\gamma)\mathbf{a}_n + \gamma \mathbf{a}_{n+1}\right] \tag{3.22b}$$

where $\Delta t = t_{n+1} - t_n$ denotes the time step.

3.2.6 Linearization of the Weak Form

We employ the Newton iteration scheme to calculate the solution of the weak form (3.20) at time t_{n+1}. Let $\Delta\boldsymbol{\varphi} = \left[\Delta u_1 \quad \Delta u_2 \quad \Delta\vartheta\right]^T$ denote the incremental displacement field. Consider a known configuration $\hat{\boldsymbol{\phi}}_{n+1}(X_1)$, and let $\boldsymbol{\phi}_{n+1,\varepsilon}(X_1)$ represent the perturbed configuration in the direction of $\Delta\boldsymbol{\varphi}_{n+1}$, defined as

$$\boldsymbol{\phi}_{n+1,\epsilon} = \hat{\boldsymbol{\phi}}_{n+1} + \varepsilon\, \Delta\boldsymbol{\varphi}_{n+1} \tag{3.23}$$

Using the above expression, we also define a perturbed configuration of $\boldsymbol{\phi}_{n+\alpha}(X_1)$ as

$$\begin{aligned} \boldsymbol{\phi}_{n+\alpha,\epsilon} &= (1-\alpha)\boldsymbol{\phi}_n + \alpha\boldsymbol{\phi}_{n+1,\varepsilon} \\ &= (1-\alpha)\boldsymbol{\phi}_n + \alpha\left[\hat{\boldsymbol{\phi}}_{n+1} + \varepsilon\, \Delta\boldsymbol{\varphi}_{n+1}\right] \\ &= \hat{\boldsymbol{\phi}}_{n+\alpha} + \alpha\varepsilon\, \Delta\boldsymbol{\varphi}_{n+1} \end{aligned} \tag{3.24}$$

where

$$\hat{\boldsymbol{\phi}}_{n+\alpha} = (1-\alpha)\boldsymbol{\phi}_n + \alpha\hat{\boldsymbol{\phi}}_{n+1} \tag{3.25}$$

The weak form $G_{dyn}(\phi_{n+\alpha}, \mathbf{v}_{n+\alpha}, \eta)$ in (3.20) is to be linearized in the direction of $\Delta\varphi_{n+1}$. Note that this weak form is a function of the unknown vector, ϕ_{n+1}, due to the relations (3.21) and (3.22), and the velocity terms can be dropped since there is no internal viscous damping in the cable. The linearization of this weak form about the known configuration $\hat{\phi}_{n+\alpha}$ can be put in the following form

$$L\left[G_{dyn}(\hat{\phi}_{n+\alpha}, \eta)\right] = G_{dyn}(\hat{\phi}_{n+\alpha}, \eta) + DG_{dyn}(\hat{\phi}_{n+\alpha}, \eta) \cdot \Delta\varphi_{n+1} = 0 \tag{3.26}$$

for all admissible variations η that satisfy (3.17). In the above, $G_{dyn}(\hat{\phi}_{n+\alpha}, \eta)$ represents the dynamic residual at configuration $\hat{\phi}_{n+\alpha}$. The directional derivative of $G_{dyn}(\hat{\phi}_{n+\alpha}, \eta)$ in the direction $\Delta\varphi_{n+1}$, *i.e.*, $DG_{dyn}(\hat{\phi}_{n+\alpha}, \eta) \cdot \Delta\varphi_{n+1}$, is given by

$$DG_{dyn}(\hat{\phi}_{n+\alpha}, \eta) \cdot \Delta\varphi_{n+1} = \frac{d}{d\varepsilon} G_{dyn}(\hat{\phi}_{n+\alpha,\varepsilon}, \eta)\Big|_{\varepsilon=0} \tag{3.27}$$

The linearization of each term in the weak form $G_{dyn}(\phi_{n+\alpha}, \eta)$ given in (3.20) is determined below.

3.2.6.1 Tangent Inertia Operator

Consider the first term in (3.20), which involves the acceleration $\mathbf{a}_{n+1}(s)$. Its linearized form is easily obtained by use of the Newmark formula (3.22) and the perturbed configuration (3.23) as

$$D_M G_{dyn}(\hat{\phi}_{n+\alpha}, \eta) \cdot \Delta\varphi_{n+1} = \frac{1}{\beta\Delta t^2} \int_0^S \eta \cdot \mathbf{I}\, \Delta\varphi_{n+1} dX_1 \tag{3.28}$$

where $D_M G_{dyn} \cdot \Delta\varphi_{n+1}$ is the tangent inertia operator.

3.2.6.2 Tangent Material Stiffness Operator

We obtain the linear part of the weak form $G_{stat}(\phi_{n+\alpha}, \eta)$ in (3.20) as the sum of the tangent material stiffness operator and the tangent geometric stiffness operator. Below, we determine the tangent stiffness operator. To this end, we introduce several quantities and their linearized forms.

Rewrite the spatial internal forces in terms of their form in the reference configuration by using the "enlarged" rotation matrix, i.e.,

$$\begin{Bmatrix} n_1(\phi_{n+\alpha}) \\ n_2(\phi_{n+\alpha}) \\ m(\phi_{n+\alpha}) \end{Bmatrix} = \Lambda_3(\vartheta_{n+\alpha}) \begin{Bmatrix} N_1(\phi_{n+\alpha}) \\ N_2(\phi_{n+\alpha}) \\ M(\phi_{n+\alpha}) \end{Bmatrix} \tag{3.29}$$

where the material internal forces are defined by

$$\begin{Bmatrix} N_1(\phi_{n+\alpha}) \\ N_2(\phi_{n+\alpha}) \\ M(\phi_{n+\alpha}) \end{Bmatrix} = \begin{bmatrix} EA & 0 & 0 \\ 0 & GA & 0 \\ 0 & 0 & 1 \end{bmatrix} \begin{Bmatrix} \Gamma_1(\phi_{n+\alpha}) \\ \Gamma_2(\phi_{n+\alpha}) \\ M(\mathrm{K}(\phi_{n+\alpha}), \Gamma_1(\phi_{n+\alpha})) \end{Bmatrix} \tag{3.30}$$

with

$$\begin{Bmatrix} \Gamma_1(\phi_{n+\alpha}) \\ \Gamma_2(\phi_{n+\alpha}) \\ M(\mathrm{K}(\phi_{n+\alpha}), \Gamma_1(\phi_{n+\alpha})) \end{Bmatrix} = \Lambda_3^{\mathrm{T}}(\vartheta_{n+\alpha}) \begin{Bmatrix} 1+u_{1,n+\alpha}' \\ u_{2,n+\alpha}' \\ M(\mathrm{K}(\phi_{n+\alpha}), \Gamma_1(\phi_{n+\alpha})) \end{Bmatrix} - \begin{Bmatrix} 1 \\ 0 \\ 0 \end{Bmatrix} \tag{3.31a}$$

$$\Lambda_3(\vartheta_{n+\alpha}) = \begin{bmatrix} \cos(\vartheta_{n+\alpha}) & -\sin(\vartheta_{n+\alpha}) & 0 \\ \sin(\vartheta_{n+\alpha}) & \cos(\vartheta_{n+\alpha}) & 0 \\ 0 & 0 & 1 \end{bmatrix} \tag{3.31b}$$

The following linearized quantities at $\hat{\phi}_{n+1}$ are also needed:

$$D\Lambda_3(\hat{\vartheta}_{n+\alpha}) \cdot \Delta\vartheta = \frac{d}{d\varepsilon} \Lambda_3(\hat{\vartheta}_{n+\alpha} + \alpha\varepsilon\Delta\vartheta)\Big|_{\varepsilon=0} = \alpha \begin{bmatrix} 0 & -\Delta\vartheta & 0 \\ \Delta\vartheta & 0 & 0 \\ 0 & 0 & 0 \end{bmatrix} \Lambda_3(\hat{\vartheta}_{n+1}) \tag{3.32a}$$

$$\begin{aligned} D\begin{Bmatrix} N_1 \\ N_2 \\ M \end{Bmatrix}(\hat{\phi}_{n+\alpha}) \cdot \Delta\phi &= \frac{d}{d\varepsilon} \begin{Bmatrix} N_1 \\ N_2 \\ M \end{Bmatrix}(\hat{\phi}_{n+\alpha} + \alpha\varepsilon\Delta\phi) \\ &= \alpha \begin{bmatrix} EA & 0 & 0 \\ 0 & GA & 0 \\ \dfrac{\partial M}{\partial \Gamma_1} & 0 & \dfrac{\partial M}{\partial \mathrm{K}} \end{bmatrix} \Lambda_3^{\mathrm{T}}\, \Xi(\hat{\phi})\, \Delta\phi \end{aligned} \tag{3.32b}$$

$$\frac{d}{d\varepsilon} \Xi(\hat{\phi}_{n+\alpha} + \alpha\varepsilon\Delta\phi)\Big|_{\varepsilon=0} = \alpha \begin{bmatrix} 0 & 0 & \Delta u_2' \\ 0 & 0 & -\Delta u_1' \\ 0 & 0 & 0 \end{bmatrix} \tag{3.32c}$$

From the definition of the material internal forces (3.30) and its linearized form (3.32b), the tangent material stiffness operator, $D_S G_{dyn} \cdot \Delta\varphi_{n+1}$, becomes

$$\begin{aligned} &D_S G_{dyn}(\hat{\phi}_{n+1}, \eta) \cdot \Delta\varphi_{n+1} \\ &= \int_0^S \Xi(\hat{\phi}_{n+\alpha}) \eta \cdot \Lambda_3(\hat{\vartheta}_{n+\alpha})\, \mathrm{C}(\hat{\phi}_{n+\alpha})\, \alpha \left[\Lambda_3^{\mathrm{T}}(\hat{\vartheta}_{n+\alpha})\, \Xi(\hat{\phi}_{n+\alpha})\right]_{\alpha=1} \Delta\varphi_{n+1} dX_1 \end{aligned} \tag{3.33}$$

where

$$\mathbf{C}(\hat{\boldsymbol{\phi}}_{n+\alpha}) = \begin{bmatrix} EA & 0 & 0 \\ 0 & GA_s & 0 \\ \dfrac{\partial M}{\partial \Gamma_1}(\hat{\boldsymbol{\phi}}_{n+\alpha}) & 0 & \dfrac{\partial M}{\partial \mathrm{K}}(\hat{\boldsymbol{\phi}}_{n+\alpha}) \end{bmatrix} \tag{3.34}$$

The terms involved with the plastic behavior of the cable, $\partial M / \partial \Gamma_1$ and $\partial M / \partial \mathrm{K}$, in this expression will be described in Section 3.3 in detail.

3.2.6.3 Tangent Geometric Stiffness Operator

The tangent geometric stiffness operator, $D_G G_{dyn} \cdot \Delta\boldsymbol{\varphi}_{n+1}$, is the remainder of the linearization of (3.20) corresponding to the linearization of $\boldsymbol{\Xi}$ and $\boldsymbol{\Lambda}$ with the material internal forces fixed. Making use of (3.32a) and (3.32c) with some re-arrangement, the expression becomes

$$D_G G_{dyn}(\hat{\boldsymbol{\phi}}_{n+\alpha}, \boldsymbol{\eta}) \cdot \Delta\boldsymbol{\varphi}_{n+1} = \int_0^S \mathbf{T}\,\boldsymbol{\eta} \cdot \mathbf{B}(\hat{\boldsymbol{\phi}}_{n+\alpha})\ \alpha\, \mathbf{T}\,\Delta\boldsymbol{\varphi}_{n+1}\, dX_1 \tag{3.35}$$

where

$$\mathbf{T} = \begin{bmatrix} d/dX_1 & 0 & 0 \\ 0 & d/dX_1 & 0 \\ 0 & 0 & 1 \end{bmatrix} \tag{3.36a}$$

$$\mathbf{B}(\hat{\boldsymbol{\phi}}) = \begin{bmatrix} 0 & 0 & -n_2(\hat{\boldsymbol{\phi}}) \\ 0 & 0 & n_1(\hat{\boldsymbol{\phi}}) \\ -n_2(\hat{\boldsymbol{\phi}}) & n_1(\hat{\boldsymbol{\phi}}) & -\left[(1+\hat{u}_1')n_1(\hat{\boldsymbol{\phi}}) + \hat{u}_2' n_2(\hat{\boldsymbol{\phi}})\right] \end{bmatrix} \tag{3.36b}$$

Finally, the linear part of G_{dyn} at $\boldsymbol{\phi} = \hat{\boldsymbol{\phi}}_{n+\alpha}$ is the sum of the above operators

$$DG_{dyn}(\hat{\boldsymbol{\phi}}_{n+\alpha}, \boldsymbol{\eta}) \cdot \Delta\boldsymbol{\varphi}_{n+1} = (D_M + D_S + D_G)\, G_{dyn}(\hat{\boldsymbol{\phi}}_{n+\alpha}, \boldsymbol{\eta}) \cdot \Delta\boldsymbol{\varphi}_{n+1} \tag{3.37}$$

3.2.7 Spatial Discretization

To formulate the Galerkin approximation of the weak form (3.14), a mesh is defined which partitions the cable axis into a finite number of disjoint elements connected at N nodes. Then, the approximations of the configuration $\boldsymbol{\phi}(X_1)$ and its incremental displacement field $\Delta\boldsymbol{\phi}(X_1)$ are

$$\phi(X_1) \cong \sum_{I=1}^{N} N_I(X_1)\,\phi_I \tag{3.38a}$$

$$\Delta\phi(X_1) \cong \sum_{I=1}^{N} N_I(X_1)\,\Delta\phi_I \tag{3.38b}$$

where $N_I(X_1)$ denotes the standard one dimensional isoparametric shape functions, ϕ_I is the nodal value of the configuration, and $\Delta\phi_I$ is the nodal incremental displacement. Further, let the weight function $\eta(s)$ be interpolated in the same manner

$$\eta(s) \cong \sum_{I=1}^{N} N_I(X_1)\,\eta_I \tag{3.39}$$

where η_I denotes the nodal variation. Introducing the above approximations into (3.14) and (3.15), we obtain the spatially discrete counterpart of the weak form as

$$G_{dyn}(\phi,\eta) \cong \sum_{I=1}^{N} \eta_I \cdot \left[N_I(X_1)\,\mathbf{I}\,\ddot{\phi} - N_I(X_1)\,\mathbf{f} + \Xi^{\mathrm{T}} \cdot \begin{Bmatrix} n_1 \\ n_2 \\ m \end{Bmatrix} \right] \tag{3.40}$$

In the Newton iteration scheme, we linearize the weak form G_{dyn} at $\phi = \hat{\phi}_{n+\alpha}$

$$L\left[G_{dyn}(\hat{\phi}_{n+\alpha},\eta)\right] \cong \sum_{I=1}^{N} \eta_I \cdot \left[\mathbf{P}_I(\hat{\phi}_{n+\alpha}) + \sum_{J=1}^{N} \mathbf{K}_{IJ}(\hat{\phi}_{n+\alpha}) \cdot \Delta\boldsymbol{\varphi}_{n+1} \right] = 0 \tag{3.41}$$

for all admissible η_I, and solve for the incremental displacement field $\Delta\boldsymbol{\varphi}_{n+1}$. $\mathbf{P}_I(\hat{\phi}_{n+\alpha})$ denotes the discrete dynamic residual force in the Newton iteration scheme, and $\mathbf{K}_{IJ}(\hat{\phi}_{n+\alpha})$ denotes the discrete dynamic tangent operator such that

$$\mathbf{K}_{IJ}(\hat{\phi}_{n+\alpha}) \cdot = \mathbf{M}_{IJ} + \mathbf{S}_{IJ}(\hat{\phi}_{n+\alpha}) + \mathbf{G}_{IJ}(\hat{\phi}_{n+\alpha}) \tag{3.42}$$

where $\mathbf{M}_{IJ}$ is the tangent inertia matrix, $\mathbf{S}_{IJ}(\hat{\phi}_{n+\alpha})$ is the tangent material stiffness matrix, and $\mathbf{G}_{IJ}(\hat{\phi}_{n+\alpha})$ is the tangent geometric stiffness matrix.

3.2.7.1 Dynamic Residual Force

The expressions (3.20) together with the discretizations (3.38) and (3.39), yield

$$\mathbf{P}_I(\hat{\phi}_{n+\alpha}) \cong \int_0^S N_I(X_1)\mathbf{I}\,\mathbf{a}_{n+\alpha}dX_1 + \int_0^S \{\Xi(\hat{\phi}_{n+\alpha})[N_I(X_1)\mathbf{1}_3]\}^{\mathrm{T}} \begin{Bmatrix} n_1(\hat{\phi}_{n+\alpha}) \\ n_2(\hat{\phi}_{n+\alpha}) \\ m(\hat{\phi}_{n+\alpha}) \end{Bmatrix} dX_1 \qquad (3.43)$$

$$- \int N_I(s)\mathbf{f}(t_{n+1})dX_1$$

where the terms on the right-hand side respectively correspond to the inertia, material stiffness, and external applied forces. Ξ is defined in (3.19) and $\mathbf{1}_3 = \mathrm{Diag}[1, 1, 1]$.

3.2.7.2 Tangent Inertia Matrix

Substituting approximations (3.38) and (3.39) in the expression of $D_M G_{dyn}$ in (3.28), we obtain

$$\mathbf{M}_{IJ} = \frac{1}{\beta\Delta t^2}\int_0^S N_I(X_1)\,\mathbf{I}\,N_J(X_1)dX_1 \qquad (3.44)$$

Note that in the plane problem $\mathbf{M}_{IJ}$ is symmetric and constant. Therefore, it needs to be evaluated only once throughout the computation.

3.2.7.3 Tangent Material Stiffness Matrix

It follows from (3.33), (3.38) and (3.39) that

$$\mathbf{S}_{IJ}(\hat{\phi}_{n+\alpha})$$
$$= \alpha\int_0^S \{\Xi(\hat{\phi}_{n+\alpha})[N_I(X_1)\mathbf{1}_3]\}^{\mathrm{T}}\,\Lambda_3(\hat{\vartheta}_{n+\alpha})\mathbf{C}(\hat{\phi}_{n+\alpha})\left[\Lambda_3{}^{\mathrm{T}}(\hat{\vartheta}_{n+\alpha})\,\Xi(\hat{\phi}_{n+\alpha})\right]_{\alpha=1}[N_J(X_1)\mathbf{1}_3]dX_1 \qquad (3.45)$$

with Ξ, Λ_3 and $\mathbf{C}$ defined in (3.19), (3.31b) and (3.34), respectively.

3.2.7.4 Tangent Geometric Stiffness Matrix

Substitution of (3.38) and (3.39) into (3.35) gives

$$\mathbf{G}_{IJ}(\hat{\phi}_{n+1}) = \alpha\int_0^S \{\mathbf{T}[N_I(X_1)\mathbf{1}_3]\}^{\mathrm{T}}\cdot\mathbf{B}(\hat{\phi}_{n+1})\,\mathbf{T}[N_I(X_1)\mathbf{1}_3]dX_1 \qquad (3.46)$$

with $\mathbf{T}$ and $\mathbf{B}$ defined in (3.36a) and (3.36b), respectively.

In the following section, we present detailed descriptions of the derivative terms, which appear in (3.34).

3.3 Plastic Bending Model for Cables

In the previous section, a summary of the geometrically exact frame element model was presented in the context of the finite element method. The only thing left to be determined is a definition of the expression (3.8), which represents the nonlinear bending behavior of the cable discussed in Chapter 2. This nonlinear bending behavior can be represented by a time-rate independent elasto-plastic model, because the slippage between wires in the cable, which is time-rate independent, is the main source of the nonlinear behavior of the cable in bending.

The simplest model for the plastic bending of the cable is a bilinear elasto-plastic model. Furthermore, since the nonlinear behavior occurs only in bending, the model is essentially one-dimensional. Simo and Hughes (1997) described the theoretical foundations of inelasticity and the corresponding computational methods. In their book, a detailed description of the one-dimensional bilinear plastic model can be found. The following review is based on that book.

We saw in Chapter 2 that the range of elastic behavior in the bending of the cable is increased with increasing tension force. This indicates that the yield function in the elasto-plastic bending model should be a function of the axial strain as well as the curvature of the cable.

Coefficients in the elasto-plastic bending model of the cable can be determined by fitting the model to the nonlinear moment-curvature relation of the cable determined by the theoretical model developed in Chapter 2. The elasto-plastic bending model is then implemented in the finite element code using the return-mapping algorithm (Simo and Hughes 1997). In describing the elasto-plastic bending model under cyclic loading, we only consider kinematic hardening since the nonlinear behavior in bending of the cable comes mainly from the slipping between wires in the cable. This slipping is similar to slip in crystalline metallic materials undergoing plastic flow, for which it has been shown that kinematic hardening is the appropriate model (Flouriot *et al.*, 2003).

3.3.1 Basic Definitions

We assume that the nonlinear bending response of the cable can be represented by the one-dimensional frictional device illustrated in Figure 3.2. The device consists of two springs and a Coulomb friction element as shown in Figure 3.2. We assume that the applied moment M acts like the force, and the total curvature K is represented by the displacement in the device. The maximum friction that can be developed in the Coulomb element, at which slipping can occur, is

represented by the yield moment, $M_Y(\Gamma_1)$, which depends on the axial strain in the cable. The spring constant $k_1 = EI_{\max}$ represents the elastic bending response of the cable. The spring constant $k_2 = EI_{\max}EI_{\min}/(EI_{\max} - EI_{\min})$ is the plastic modulus and it is chosen so that the elasto-plastic tension modulus is $EI_{\min}$.

The total curvature K splits into a part K^e, referred to as the elastic part, and a curvature K^p, referred to as the plastic part, that is

$$\mathrm{K} = \mathrm{K}^e + \mathrm{K}^p \tag{3.47}$$

By equilibrium, the force on the right spring in Figure 3.2 with stiffness $EI_{\max}$ is M, and we have the elastic relationship

$$M = EI_{\max}\mathrm{K}^e = EI_{\max}(\mathrm{K} - \mathrm{K}^p) \tag{3.48}$$

Since the nonlinear bending behavior of the cable occurs from the slippage between wires in the cable, we assume kinematic hardening behavior of the cable in bending, i.e. the center of the yield surface of bending experiences a motion in the direction of the plastic flow. This phenomenon known as the Bauschinger effect can be captured by introducing an internal variable, denoted by Q (which we call the back moment, similar to the back stress in plasticity theory), that defines the location of the center of the yield surface. We further assume that the absolute value of the difference between the moment and the back moment in the frictional device cannot be greater in absolute value than M_Y. This leads to the definition of the yield function f

$$f(M, Q, \Gamma_1) = |M - Q| - M_Y(\Gamma_1) \le 0 \tag{3.49}$$

where the flow moment M_Y is a function of the axial strain Γ_1 of the cable. As mentioned earlier, the larger the axial strain, the larger the size of the elastic range in the bending of the cable. We postpone the definition of the flow moment function to the next section, where we fit the theoretical results derived in Chapter 2 with the current bilinear elasto-plastic model.

If the yield function becomes negative, no change in K^p takes place, i.e. $\dot{\mathrm{K}}^p = 0$ and the device is elastic with spring stiffness $EI_{\max}$. A change in K^p can take place only when the yield function equals zero. In this condition, the frictional device experiences slip in the direction of the applied moment, with a constant slip rate. Let $\gamma \ge 0$ be the absolute value of the slip rate. Then,

$$\dot{\mathrm{K}}^{p} = \gamma \, \mathrm{sign}(M - Q) \text{ iff } f(M, Q, \Gamma_1) = 0 \tag{3.50}$$

This is called the flow rule. The evolution of the back moment is defined as

$$\dot{Q} = H \, \dot{\mathrm{K}}^{p} = \gamma \, H \, \mathrm{sign}(M - Q) \tag{3.51}$$

where γ is called the consistency parameter and H is the kinematic hardening modulus.

Based on the assumptions made above, we observe that

$$\gamma \geq 0 \text{ and } f(M, Q, \Gamma_1) \leq 0 \tag{3.52}$$

Furthermore, observe that $\gamma = 0$ if $f(M, Q, \Gamma_1) < 0$, and $\gamma > 0$ only if $f(M, Q, \Gamma_1) = 0$. These observations imply

$$\gamma \, f(M, Q, \Gamma_1) = 0 \tag{3.53}$$

The conditions in (3.52) and (3.53) are known as the Kuhn-Tucker conditions.

Consider the case where $\hat{f}(t) = f[M(t), Q(t), \Gamma_1(t)] = 0$ at time t. Then, it is easy to show that $\dot{\hat{f}}(t) \leq 0$, since should $\dot{\hat{f}}(t)$ be positive it would imply that $\hat{f}(t + \Delta t) > 0$ for some $\Delta t > 0$, which violates the admissibility condition $f \leq 0$. Further, we specify that $\gamma > 0$ only if $\dot{\hat{f}}(t) = 0$, and set $\gamma = 0$ if $\dot{\hat{f}}(t) < 0$; that is (dropping the hat to simplify the notation) we set

$$\gamma \, \dot{f}(M, Q, \Gamma_1) = 0 \text{ if } f(M, Q, \Gamma_1) = 0 \tag{3.54}$$

This condition enables us to determine the actual value of $\gamma \geq 0$ at any given time t and is referred to as the consistency condition.

3.3.2 Fitting with Elasto-Plastic Model

For the elasto-plastic model, the definition of the yield moment $M_Y(\Gamma_1)$ in the yield function (3.49) has to be determined. $M_Y(\Gamma_1)$ must be chosen to properly represent the nonlinear bending behavior of the cable. In order to gain insight for the definition of $M_Y(\Gamma_1)$, we re-examine the nonlinear moment-curvature relationship of the Jessamine cable shown in Figure 2.17-18. We redraw Figure 2.18, which shows the plot of M/K vs. K for the Jessamine cable, in Figure 3.3, where we indicate the initial slipping curvatures K_{init} (indicated by circles) and the fully slipped curvatures K_{full} (indicated by diamonds). For a given axial strain in the cable, Γ_1, wires in the cable start to slip when the curvature of the cable, K, reaches K_{init}, and all wires have slipped

when K reaches K_{full}. We observe in Figure 3.3 that the difference between $\log_{10}(K_{init})$ and $\log_{10}(K_{full})$ is almost independent of the axial strain in the cable. Let C_{full} denote this difference, i.e.

$$C_{full} = \log_{10}(K_{full}) - \log_{10}(K_{init}) \tag{3.55a}$$

so that

$$K_{full} = 10^{C_{full}} K_{init} \tag{3.55b}$$

From Figure 3.3, we see that C_{full} is approximately 3 for the Jessamine cable.

It is easy to see in Figure 3.3 that the initial slipping curvature of the cable, K_{init}, is a function of the axial strain Γ_1 (or axial force) in the cable. The larger the axial strain in the cable, the larger the initial slipping curvature. Figure 3.4 shows the relation between the initial slipping curvature K_{init} and the axial strain Γ_1 for the cable under consideration. It is clear that $\log_{10}(K_{init})$ and $\log_{10}(\Gamma_1)$ have a linear relationship such that

$$\log_{10}(K_{init}) - \log_{10}(K_0) = C_{init} \cdot \left[\log_{10}(\Gamma_1) - \log_{10}(\Gamma_{1,0})\right] \tag{3.56a}$$

so that

$$K_{init}(\Gamma_1) = K_0 \left(\frac{\Gamma_1}{\Gamma_{1,0}}\right)^{C_{init}} \tag{3.56b}$$

where $(\Gamma_{1,0}, K_0)$ is the coordinate of a convenient reference point on the line and C_{init} is the slope of the line in Figure 3.4. From Figure 3.4, we see that $C_{init} \cong 1$, and we choose to use as the reference point $(\Gamma_{1,0}, K_0)$ the point (1E-3, 4E-3). Then, K_{init} is completely defined by the expression (3.56) as a function of Γ_1.

Let us define the normalized curvature

$$\overline{K} = \frac{K - K_{init}}{K_{full} - K_{init}} \tag{3.57}$$

and the normalized moment

$$\overline{M} = \frac{M}{EI_{\max} K_{init}} \tag{3.58}$$

When $\overline{\mathrm{K}} < 0$, all wires in the cable are in the stick state so that the cable has elastic bending behavior with the bending stiffness being $EI_{\max}$. When $0 \le \overline{\mathrm{K}} < 1$, some wires in the cable are in the slip state so that the cable has undergone nonlinear bending. When $1 \le \overline{\mathrm{K}}$, all wires in the cable are in the slip state and the cable has the elasto-plastic bending stiffness $EI_{\min}$. The solid line in Figure 3.5 shows the relation between the normalized moment, $\overline{M}$, and the normalized curvature, $\overline{\mathrm{K}}$, for the Jessamine cable for all the strain levels shown in Figure 3.3. Interestingly, all the curves for the different strain levels in Figure 2.17 essentially coincide when they are normalized according to (3.57) and (3.58).

We employ the following form to define the yield moment $M_Y(\Gamma_1)$.

$$M_Y(\Gamma_1) = C_Y \cdot EI_{\max} \mathrm{K}_{init}(\Gamma_1) \tag{3.59}$$

The coefficient C_Y is determined from Figure 3.5, and $\mathrm{K}_{init}(\Gamma_1)$ is as defined in (3.56b). Drawing the dotted line in Figure 3.5, we assume that this line represents the plastic behavior of the cable in the bilinear elasto-plastic model. Then, the yielding occurs when $\overline{M} \cong 3$. By accounting for (3.58) and (3.59), we determine $C_Y \cong 3$ for the Jessamine cable.

C_{full}, C_{init} and C_Y are the fitting coefficients for the nonlinear moment-curvature relationship of a cable. In the above, we determined these coefficients for the Jessamine cable. In general, we can determine the fitting coefficients by plotting the relationships between M/K vs. K, K_{init} vs. Γ_1, and $\overline{M}$ vs. $\overline{\mathrm{K}}$ for any given cable. The fitting coefficients for some other cables (Division of Aluminum Company of America 1974) used by industry are listed in Table 3.1. These coefficient values have been rounded to the nearest 0.5.

3.3.3 Return-Mapping Algorithm

Let $X_1 \in [0, S]$ be a given point along the centerline of the cable. Assume that the local state of the cable at point X_1 and current time, t_n, is completely known. This means that the values of

$$\left\{\mathrm{K}_n(X_1), \mathrm{K}_n^p(X_1), Q_n(X_1)\right\} \tag{3.60}$$

are known and, therefore, the moment state

$$M_n(X_1) = EI_{\max}\left[\mathrm{K}_n(X_1) - \mathrm{K}_n^p(X_1)\right] \tag{3.61}$$

is also known. The subscript 'n' refers to the current time, t_n. Suppose "increments" are given in the total curvature and in the axial strain of the cable at X_1, say $\Delta \mathrm{K}_n$ and $\Delta \Gamma_{1,n}$, respectively. Then, the total curvature and the axial strain of the cable at time $t_{n+1} = t_n + \Delta t$ are

$$\mathrm{K}_{n+1} = \mathrm{K}_n + \Delta \mathrm{K}_n \tag{3.62a}$$

$$\Gamma_{1,n+1} = \Gamma_{1,n} + \Delta \Gamma_{1,n} \tag{3.62b}$$

The basic problem we are concerned with is the update of the basic variables (3.60) and (3.61) to time t_{n+1} in a manner consistent with the constitutive model we have developed.

From (3.50) and (3.51), by application of the backward-Euler method, we obtain

$$Q_{n+1} = Q_n + \Delta\gamma \, H \, \mathrm{sgn}(\mathrm{Z}_{n+1}) \tag{3.63a}$$

$$\mathrm{K}^p_{n+1} = \mathrm{K}^p_n + \Delta\gamma \, \mathrm{sgn}(\mathrm{Z}_{n+1}) \tag{3.63b}$$

where $\Delta\gamma = \gamma_{n+1} \Delta t \geq 0$ is the algorithmic counterpart of the consistency parameter $\gamma \geq 0$ and the relative moment is defined as

$$\mathrm{Z} = M - Q \tag{3.64}$$

From (3.48), we also have the moment state such that

$$M_{n+1} = EI_{\max}(\mathrm{K}_{n+1} - \mathrm{K}^p_{n+1}) \tag{3.65}$$

The variables (M_{n+1}, Q_{n+1}) along with $\Delta\gamma$ are constrained by the following discrete version of the Kuhn-Tucker conditions:

$$f_{n+1} = |Z_{n+1}| - M_Y(\Gamma_{1,n+1}) \leq 0, \tag{3.66a}$$

$$\Delta\gamma \geq 0, \tag{3.66b}$$

$$\Delta\gamma \, f_{n+1} = 0. \tag{3.66c}$$

where $\Gamma_{1,n+1}$ is defined in (3.62b) and M_Y is given in (3.59).

3.3.3.1 Trial elastic state

We consider an auxiliary state by freezing the plastic flow. In other words, first we consider a purely elastic (trial) step defined by the formulas

$$M^{trial}_{n+1} = EI_{\max}(\mathrm{K}_{n+1} - \mathrm{K}^p_n) \equiv M_n + EI_{\max} \Delta \mathrm{K}_n, \tag{3.67a}$$

$$Z^{trial}_{n+1} = M^{trial}_{n+1} - Q_n, \tag{3.67b}$$

$$\mathrm{K}^{p,trial}_{n+1} = \mathrm{K}^p_n, \tag{3.67c}$$

$$Q_{n+1}^{trial} = Q_n\,, \tag{3.67d}$$

$$f_{n+1}^{trial} = \left|Z_{n+1}^{trial}\right| - M_Y(\Gamma_{1,n+1})\,. \tag{3.67e}$$

We observe that the trial state is determined solely in terms of the initial conditions $\{K_n, K_n^p, Q_n\}$ and the given incremental curvature ΔK_n and incremental axial strain $\Delta\Gamma_{1,n+1}$. This state in general may not correspond to any actual, physically admissible state unless the incremental process is elastic. The conclusion that an incremental process for the given incremental curvature and axial strain is elastic or plastic is drawn solely on the basis of the trial state according to the criterion

$$f_{n+1}^{trial}\begin{cases} \le 0 & \text{elastic step} \quad \Delta\gamma = 0, \\ > 0 & \text{plastic step} \quad \Delta\gamma > 0. \end{cases} \tag{3.68}$$

If the step is elastic in the sense of (3.68), the trial state is the actual solution of the incremental problem associated with the constitutive model of the cable. On the other hand, if the step is plastic, a closed form algorithm is constructed as follows:

3.3.3.2 Plastic State

Here we examine the algorithmic problem for an incrementally plastic process characterized by the condition

$$f_{n+1}^{trial} > 0 \Leftrightarrow f(M_{n+1}, Q_{n+1}) = 0 \quad \text{and} \quad \Delta\gamma = 0 \tag{3.69}$$

Our objective is to determine the solution $\{K_{n+1}^p, M_{n+1}, Q_{n+1}, \Delta\gamma\}$ to problem (3.62)-(3.66). The discrete algorithmic equations are obtained by applying an implicit backward-Euler difference scheme and using the final moment M_{n+1} in terms of M_{n+1}^{trial} and $\Delta\gamma$:

$$\begin{aligned} M_{n+1} &= EI_{\max}(K_{n+1} - K_{n+1}^p) \\ &= EI_{\max}(K_{n+1} - K_n^p) - EI_{\max}(K_{n+1}^p - K_n^p) \\ &= M_{n+1}^{trial} - EI_{\max}\Delta\gamma\ \mathrm{sgn}(Z_{n+1}) \end{aligned} \tag{3.70a}$$

$$K_{n+1}^p = K_n^p + \Delta\gamma\ \mathrm{sgn}(Z_{n+1}) \tag{3.70b}$$

$$Q_{n+1} = Q_n + \Delta\gamma\ H\ \mathrm{sgn}(Z_{n+1}) \tag{3.70c}$$

$$f_{n+1} = \left|Z_{n+1}\right| - M_Y(\Gamma_{1,n+1}) = 0 \tag{3.70d}$$

where

$$Z_{n+1} = M_{n+1} - Q_{n+1} \tag{3.71}$$

Now the problem posed by (3.70) and (3.71) is solved explicitly in terms of the trial elastic state by the following procedure: By subtracting (3.70c) from (3.70a) and using definition (3.71),

$$Z_{n+1} = (M_{n+1}^{trial} - Q_n) - \Delta\gamma\,(EI_{\max} + H)\,\mathrm{sgn}(Z_{n+1}) \tag{3.72}$$

Using the fact that $Z_{n+1}^{trial} = M_{n+1}^{trial} - Q_n$ and rearranging terms in (3.72), we obtain

$$\left[\left|Z_{n+1}\right| + \Delta\gamma\,(EI_{\max} + H)\right]\mathrm{sign}(Z_{n+1}) = \left|Z_{n+1}^{trial}\right|\mathrm{sgn}(Z_{n+1}^{trial}) \tag{3.73}$$

Since $\Delta\gamma > 0$ and $EI_{\max} + H > 0$ by assumption, it follows that the coefficient of $\mathrm{sign}(Z_{n+1})$ in (3.73) must be positive. Therefore, (3.73) implies the result

$$\mathrm{sgn}(Z_{n+1}) = \mathrm{sgn}(Z_{n+1}^{trial}) \tag{3.74}$$

along with the condition

$$\left|Z_{n+1}\right| + \Delta\gamma\,(EI_{\max} + H) = \left|Z_{n+1}^{trial}\right| \tag{3.75}$$

Now the incremental plastic consistency parameter $\Delta\gamma > 0$ is determined from the consistency requirement (3.70d) by using (3.75) and (3.67e):

$$\begin{aligned} f_{n+1} &= \left|Z_{n+1}^{trial}\right| - (EI_{\max} + H)\,\Delta\gamma - M_Y(\Gamma_{1,n+1}) \\ &= f_{n+1}^{trial} - (EI_{\max} + H)\,\Delta\gamma = 0 \end{aligned} \tag{3.76}$$

Solving the algebraic equation for $\Delta\gamma$ yields the result

$$\Delta\gamma = \frac{f_{n+1}^{trial}}{EI_{\max} + H} \tag{3.77}$$

Thus conditions (3.74) and (3.77) completely determine the unknown quantities appearing in (3.70).

3.3.3.3 Algorithmic Tangent Modulus

To complete the algorithmic procedure discussed above, explicit expressions for the derivatives in (3.78) must be determined, i.e.,

$$\frac{\partial M_{n+1}}{\partial K_{n+1}} \text{ and } \frac{\partial M_{n+1}}{\partial \Gamma_{1,n+1}} \tag{3.78}$$

Since K_n^p and Q_n are constants at time step n+1, from (3.67a) and (3.67b)

$$\frac{\partial M_{n+1}^{trial}}{\partial K_{n+1}} = EI_{\max} \tag{3.79a}$$

$$\frac{\partial M_{n+1}^{trial}}{\partial \Gamma_{1,n+1}} = 0 \tag{3.79b}$$

$$\frac{\partial Z_{n+1}^{trial}}{\partial \mathrm{K}_{n+1}} = \frac{\partial M_{n+1}^{trial}}{\partial \mathrm{K}_{n+1}} = EI_{\max} \tag{3.79c}$$

Using these result and differentiating (3.77) with respect to K_{n+1} and $\Gamma_{1,n+1}$, assuming that $f_{n+1}^{trial} > 0$, leads to

$$\begin{aligned}\frac{\partial(\Delta\gamma)}{\partial \mathrm{K}_{n+1}} &= \frac{1}{EI_{\max} + H}\frac{\partial f_{n+1}^{trial}}{\partial \mathrm{K}_{n+1}} \\ &= \frac{1}{EI_{\max} + H}\frac{\partial \left|\mathrm{Z}_{n+1}^{trial}\right|}{\partial \mathrm{Z}_{n+1}^{trial}}\frac{\partial \mathrm{Z}_{n+1}^{trial}}{\partial \mathrm{K}_{n+1}} \\ &= \frac{EI_{\max}}{EI_{\max} + H}\mathrm{sgn}(\mathrm{Z}_{n+1}^{trial})\end{aligned} \tag{3.80a}$$

$$\begin{aligned}\frac{\partial(\Delta\gamma)}{\partial \Gamma_{1,n+1}} &= \frac{1}{EI_{\max} + H}\frac{\partial f_{n+1}^{trial}}{\partial \Gamma_{1,n+1}} \\ &= \frac{-1}{EI_{\max} + H}\frac{\partial M_Y}{\partial \Gamma_{1,n+1}} \\ &= \frac{-EI_{\max}}{EI_{\max} + H} C_Y C_{init}\frac{\mathrm{K}_0}{\Gamma_{1,0}}\left(\frac{\Gamma_{1,n+1}}{\Gamma_{1,0}}\right)^{C_{init}-1}\end{aligned} \tag{3.80b}$$

Next, we rearrange (3.70a) as follows:

$$\begin{aligned}M_{n+1} &= (M_{n+1}^{trial} - Q_n) + Q_n - EI_{\max}\Delta\gamma\ \mathrm{sgn}(\mathrm{Z}_{n+1}) \\ &= Q_n + \mathrm{Z}_{n+1}^{trial} - EI_{\max}\Delta\gamma\ \mathrm{sgn}(\mathrm{Z}_{n+1}) \\ &= Q_n + \left[1 - \frac{EI_{\max}\Delta\gamma}{\left|\mathrm{Z}_{n+1}^{trial}\right|}\right]\mathrm{Z}_{n+1}^{trial}\end{aligned} \tag{3.81}$$

Finally, we differentiate the algorithmic constitutive equation (3.81) with respect to K_{n+1} and $\Gamma_{1,n+1}$ by using the chain rule along with relationships (3.79) and (3.80). Then, we obtain

$$\frac{\partial M_{n+1}}{\partial \mathrm{K}_{n+1}} = \frac{EI_{\max} H}{EI_{\max} + H} \tag{3.82a}$$

(3.82b)

$$\frac{\partial M_{n+1}}{\partial \Gamma_{1,n+1}} = \mathrm{sgn}(\mathrm{Z}_{n+1}^{trial}) \frac{EI_{\max}{}^2}{EI_{\max} + H} C_Y C_{init} \frac{\mathrm{K}_0}{\Gamma_{1,0}} \left(\frac{\Gamma_1}{\Gamma_{1,0}} \right)^{C_{ini}-1}$$

for $f_{n+1}^{trial} > 0$. Since $M_{n+1} = M_{n+1}^{trial}$ for $f_{n+1}^{trial} \le 0$, from (3.79) and (3.82),

$$\frac{\partial M_{n+1}}{\partial \mathrm{K}_{n+1}} = \begin{cases} EI_{\max} & \text{iff } f_{n+1}^{trial} \le 0 \\ \dfrac{EI_{\max} H}{EI_{\max} + H} & \text{iff } f_{n+1}^{trial} > 0 \end{cases} \tag{3.83a}$$

$$\frac{\partial M_{n+1}}{\partial \Gamma_{1,n+1}} = \begin{cases} 0 & \text{iff } f_{n+1}^{trial} \le 0 \\ \mathrm{sgn}(\mathrm{Z}_{n+1}^{trial}) \dfrac{EI_{\max}{}^2}{EI_{\max} + H} C_Y C_{init} \dfrac{\mathrm{K}_0}{\Gamma_{1,0}} \left(\dfrac{\Gamma_1}{\Gamma_{1,0}} \right)^{C_{ini}-1} & \text{iff } f_{n+1}^{trial} > 0 \end{cases} \tag{3.83b}$$

As we discussed in Chapter 2, the bending stiffness of the cable quickly approaches the minimum bending stiffness $EI_{\min}$ of the cable when the wires in the cable start to slip. Based on this observation, we set $\partial M_{n+1} / \partial \mathrm{K}_{n+1} = EI_{\min}$ when the cable is in plastic bending. Then, we obtain the kinematic hardening modulus as

$$H = \frac{EI_{\max} EI_{\min}}{EI_{\max} - EI_{\min}} \tag{3.84}$$

Note that this kinematic hardening modulus is represented by the spring constant k_2 in Figure 3.2. Finally, (3.83) and (3.84) are substituted into the constitutive relation (3.34).

The model described above has been implemented in the finite element code FEAP developed by Taylor (1998). For this purpose, the bilinear elasto-plastic bending model for the geometrically exact frame element had to be implemented in the code. The analyses in the subsequent chapters of this dissertation are carried out along this code.

3.4 Section Properties of Cables

In using the above finite element model for conductor cables, section properties of the cables are necessary to determine the axial, shear, and flexural rigidities. In this section, we summarize the definitions of these section properties. As mentioned earlier, the flexible conductor is typically made of wrapped strands of aluminum wire. For the following discussion, we let NL denote the number of layers, nl denote the number of strands in layer l, d_i denote the diameter of the i-th strand and α_i denote the layangle of the i-th strand in layer l.

As mentioned in our previous study (Der Kiureghian *et al.*, 2000), when the cable is subjected to a small tension force or to a large compression force, its axial stiffness can be smaller than the sum of the axial stiffnesses of the individual strands due to tightening or opening of the braids. We are not aware of any experiments that have investigated these effects. For the sake of simplicity, in the following analysis we ignore these effects and assume that the effective cross-sectional area, A, of the cable throughout its length is a constant and is equal to the sum of the cross-sectional areas of the strands, i.e.,

$$A = \sum_{l=0}^{NL} \sum_{i=1}^{nl} \frac{\pi d_i^{\,2}}{4} \cos^3(\alpha_i) \tag{3.85}$$

where the cosine term takes into account the direction of the wires in the cable. This is derived from (2.89).

The flexural rigidity of the cable at a cross section is given by the product EI, where E denotes the Young's modulus of the cable and I denotes the section moment of inertia. The value of I depends on whether the strands at the cross section remain stuck together or slide with respect to one another as the cable is bent. The minimum value of the moment of inertia, denoted $I_{\min}$, is obtained by assuming that the strands freely slide against one another. In that case the moment of inertia is simply the sum of the moments of inertia of the individual strands and is given by

$$I_{\min} = \sum_{l=0}^{NL} \sum_{i=1}^{nl} \frac{\pi d_i^{\,4}}{64} \cos(\alpha_i) \tag{3.86}$$

See equations (6), (17) and (19) in Papailiou (1997) for the derivation of (3.86).

In the actual system, significant friction forces may develop between the strands, particularly at locations where the cable is under high tension. These friction forces may prevent sliding of some of the strands and, hence, a larger effective moment of inertia may develop. The maximum value of I is obtained when all strands remain stuck together and is given by

$$\begin{aligned} I_{\max} &= \sum_{l=0}^{NL} \sum_{i=1}^{nl} \frac{\pi d_i^{\,2}}{4} \left(\frac{d_i^{\,2}}{16} \cos(\alpha_i) + r_i^2 \sin^2(\varphi_i) \cos^3(\alpha_l) \right) \\ &= \sum_{l=0}^{NL} \left[\sum_{i=1}^{nl} \frac{\pi d_i^{\,2}}{4} \left(\frac{d_i^{\,2}}{16} \cos(\alpha_i) \right) + \frac{nl}{2} A_l r_l^2 \cos^3(\alpha_l) \right] \end{aligned} \tag{3.87}$$

where r_i and r_l is the radial distance from the center of the cable to the center of wire i and to the center of any wire located in layer l, respectively, and φ_i is the angular coordinate of layer i, A_l is the cross-section area of the wire located in layer l, as shown in Figure 3.6 where wires in gray shade are the wires in layer l. See EPRI (1979), and equations (6), (7), (17) and (20) in Papailiou (1997) for derivation of (3.86). The moment of inertia would tend to vary along the cable depending on the cable curvature and the magnitude of the tension force. Unfortunately the two bounding values in (3.86) and (3.87) are widely apart for typical cables used in the power industry. For example, for a 1796MCM cable consisting of 61 strands in 4 layers and a core, the upper bound in (3.87) is about 80 times the lower bound in (3.86). Based on experiments conducted by BC Hydro in the 1990's, the IEEE guideline (IEEE 1999) recommends the use of the approximation

$$I \cong (1+N)I_{\min} \tag{3.88}$$

for short length aluminum conductors, where N denotes the number of layers of strand. This approximation was employed in a previous study (Der Kiureghian *et al.* 2000, Hong *et al.* 2001) assuming that the moment of inertia remains constant throughout the length of the cable at all times. In contrast, in the finite element model in this study, the flexural rigidity is changing from $EI_{\max}$ to $EI_{\min}$ depending on the tension force and curvature at each cross-section of the cable.

For the analyses in the subsequent chapters, it is also necessary to assign values to the Young's modulus, E, the Poisson's ratio, ν, and the ratio of reduced shear area, $\kappa_s = A_s / A$. The Young's modulus E=70GPa (=10,000ksi), Poisson's ratio ν=0.33 for pure aluminum, and the ratio of reduced shear area, $\kappa_s = 3/4$, for a circular cross-section are used. For given Poisson's ratio and Young's modulus, the shear modulus G is given by

$$G = \frac{E}{2(1+\nu)} \tag{3.89}$$

In order to account for the inertia effect and dead weight of the cable, the mass density 2,711 kg/m^3 of pure aluminum is used.

Table 3.1 Fitting parameters for several types of conductor cables

Type of cable	C_{full}	C_{init}	C_Y	K_0	$\Gamma_{1,0}$
Peachbell	3	1	1	4E-2	1E-3
Valerian	3	1	2	1E-2	1E-3
Syringa	3	1	2.5	7E-3	1E-3
Jessamine	3	1	3	4E-3	1E-3
Flag	3	1	4	5E-3	1E-3
Cowslip	3	1	4.5	3E-3	1E-3
Lupine	3	1	5	2E-3	1E-3
Trillium	3	1	4.5	3E-3	1E-3
1113-MCM	3	1	3.5	4E-3	1E-3
1796-MCM	3	1	3	4E-3	1E-3
2300-MCM	3	1	3	3E-3	1E-3
4000-MCM	3	1	8	2E-3	1E-3

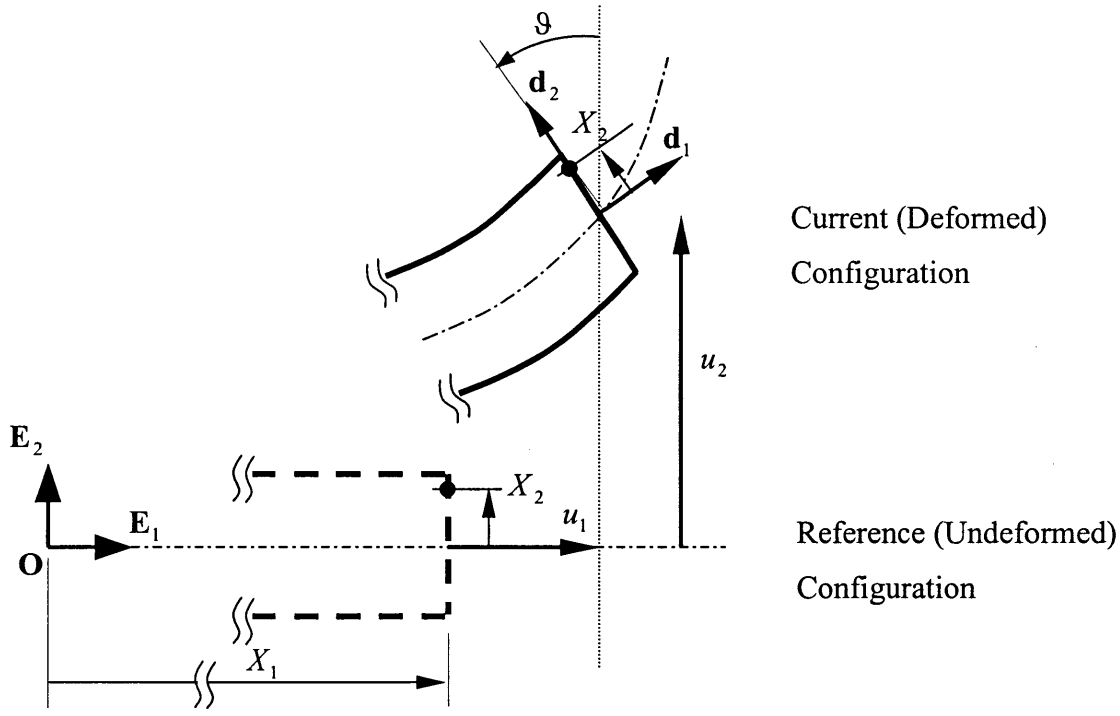

Figure 3.1 Basic kinematics. Undeformed and deformed configurations.

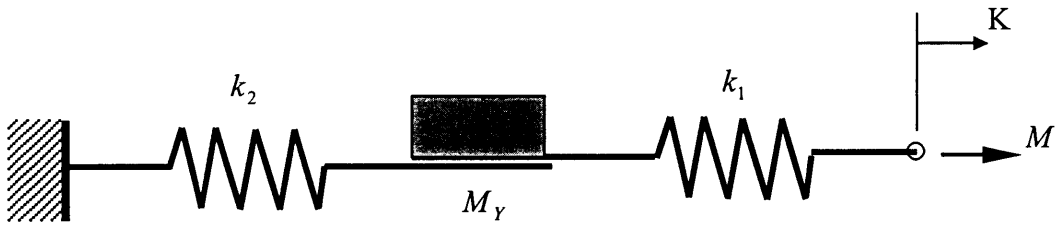

Figure 3.2 One-dimensional frictional device illustrating the nonlinear bending response of the cable

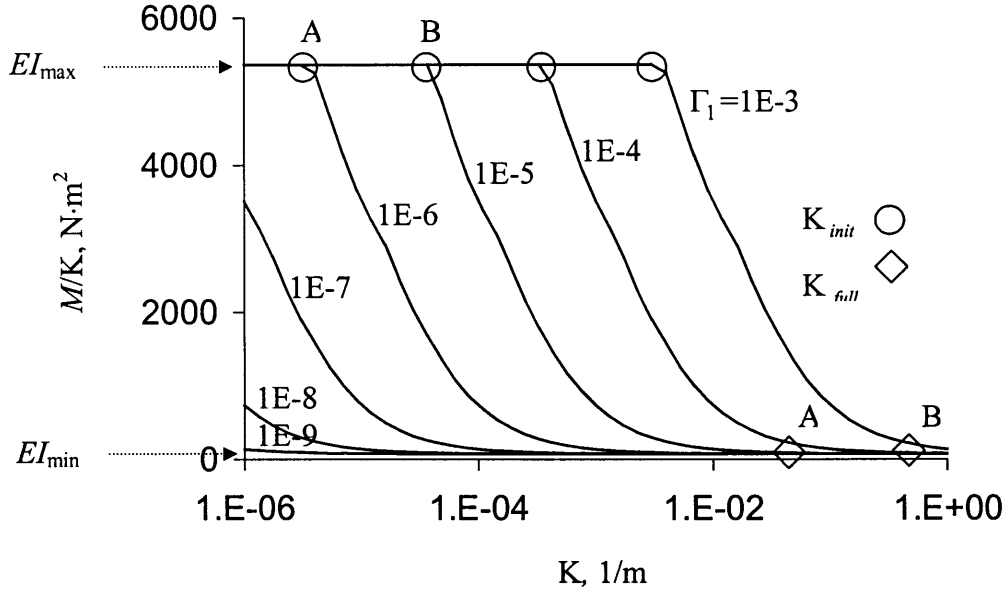

Figure 3.3 Secant bending stiffness in the Jessamine cable, *M*/K, vs. curvature of the cable, K, for different axial strains of the cable

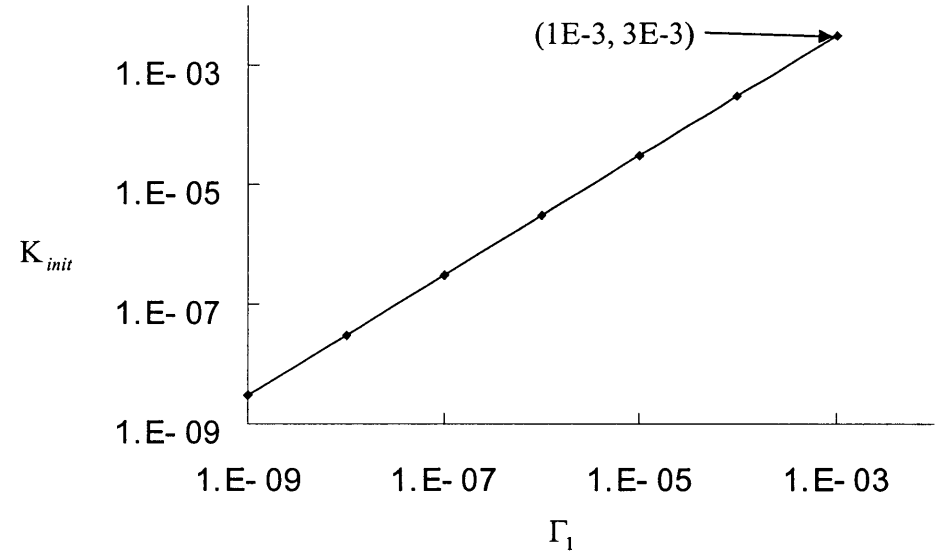

Figure 3.4 Initial slipping curvature, K_{init}, vs. axial strain, Γ_1, of the Jessamine cable

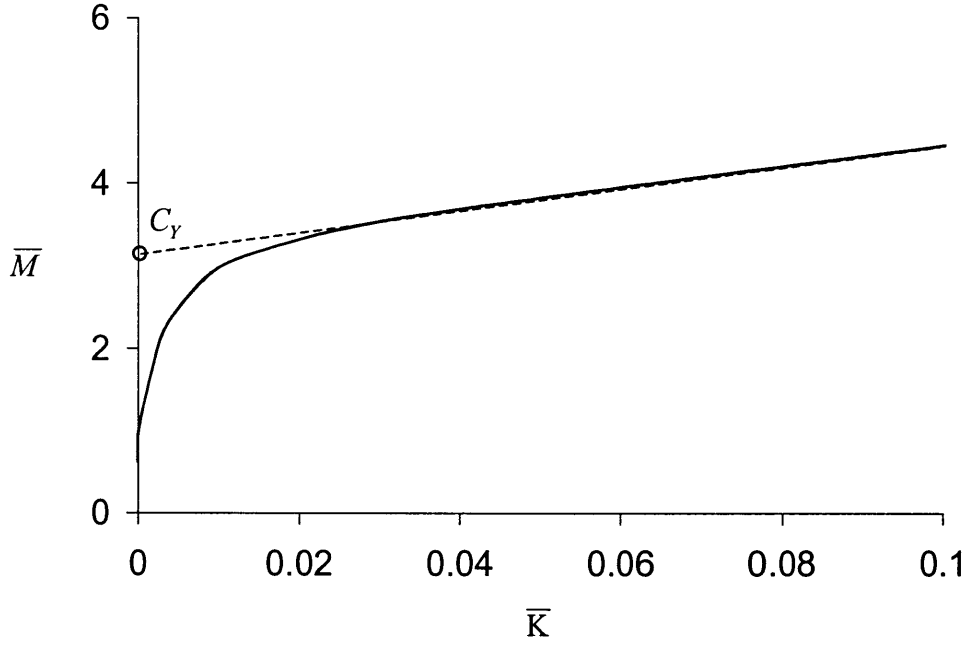

Figure 3.5 Normalized moment, $\overline{M}$, vs. normalized curvature, $\overline{K}$, of the Jessamine cable

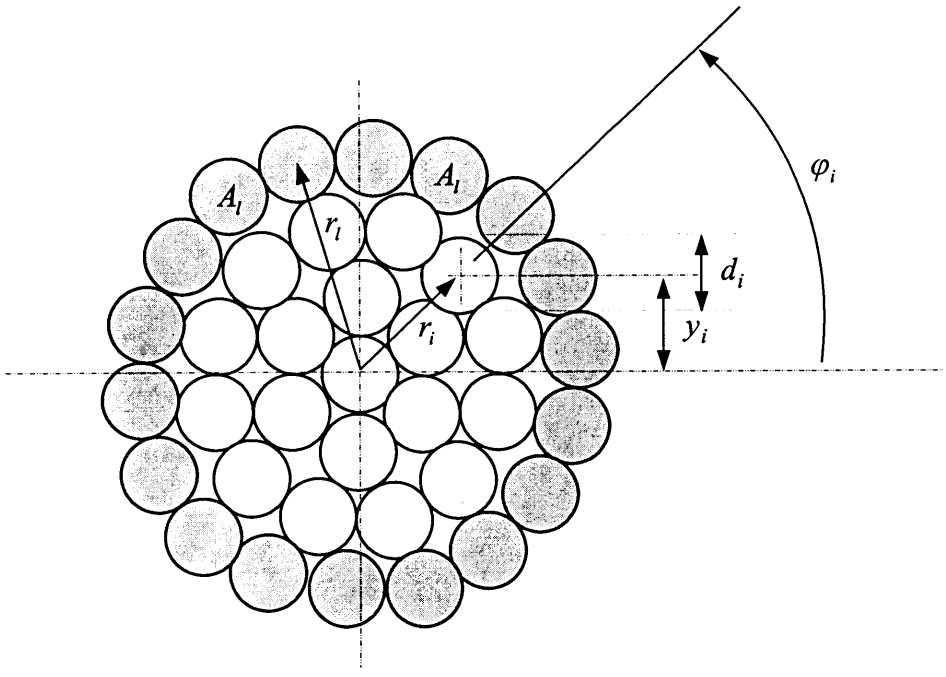

Figure 3.6 Cross-section of a conductor cable made of wrapped wires

4 STATIC ANALYSIS OF CONDUCTOR CABLES AND COMPARISON WITH EXPERIMENTAL RESULTS

4.1 Introduction

In this chapter, we use the finite element model developed in Chapters 2 and 3 to investigate the static response of flexible conductor cables under monotonic and cyclic loading, and compare the analytical predictions with experimental results obtained by other investigators. Specifically, comparisons are made with monotonic and cyclic tests performed by Filiatrault and Stearns (2002) on two cables subjected to 2-point transverse loading, and with tests performed by Dastous and Pierre (1996) on two cables subjected to cyclic end displacement loading. Filiatrault and Stearns used 1113MCM and 2300MCM conductor cables and Dastous and Pierre used 1796MCM and 4000MCM conductor cables. Important characteristics of these cables are summarized in Tables 4.1 and 4.2.

The finite element model developed in Chapters 2 and 3 accounts for the geometric nonlinearity due to large rotations and displacements of the cable, and for the material nonlinearity resulting from the slippage of wires in the cable. Using this model, an attempt is made to reproduce the experimental results of Filiatrault and Stearns (2002) and Dastous and Pierre (1996). This analysis is an improvement over our previous study (Der Kiureghian *et al.* 2000, Hong *et al.* 2001), where we assumed the moment of inertia of the cable is constant and given as in the IEEE guidelines (IEEE 1999). In contrast, the current analysis allows the moment of inertia of the cable to vary along the length of the cable and in time, depending on the curvature and tension force of the cable at each cross-section and time step. The variation is between I_{max} and I_{min}, where I_{max} is the moment of inertia of the cable when all the wires are in the stick state, and I_{min} is the moment of inertia when all wires are sliding. Recall that the ratio I_{max}/I_{min} can be as large as 100 or even larger.

For tests by Filiatrault and Stearns (2002), two types of comparisons are made. One is for the moment and curvature at one cross section of the cable for various values of the tension force, under both monotonic and cyclic loads. Unfortunately the experimental and analytical results for this case do not provide a good match, particularly when the tension force in the cable is high. The second type of comparison is for the force-displacement relationship for the entire system under cyclic loading. A fairly good match between the experimental and analytical results is achieved in this case. Possible sources of discrepancy between the analytical and experimental results are described. For the tests by Dastous and Pierre (1996), a fairly good match between the analytical and experimental results is achieved.

In Section 4.2, we describe the finite element model used for the analyses in this chapter. Also described is the nonlinear moment-curvature relationship for each tested cable and the assumed initial configuration of the cable for the analytical model. Comparisons with the experimental results of Filiatrault and Stearns (2002) are considered in Section 4.3. Section 4.4 describes the comparisons with the experimental results of Dastous and Pierre (1996).

4.2 Finite Element Model of the Cable

The cable is idealized with 100 frame elements, as described in Chapter 3, accounting for the elasto-plastic constitutive model that represents the nonlinear bending behavior of the cable, and for large rotations and displacements. As described in Section 3.3.2, the elasto-plastic constitutive model is determined by fitting to the nonlinear moment-curvature relationship of the cable that is determined according to the theory developed in Chapter 2. Figures 4.1 and 4.2 show the nonlinear bending behavior of the 1113MCM and 2300MCM conductor cables used in the tests conducted by Filiatrault and Stearns (2002), and Figures 4.3 and 4.4 show the nonlinear bending behavior of the 1796MCM and 4000MCM conductor cables used in the tests conducted by Dastous and Pierre (1996). The first plot in each figure shows the relationship between the secant bending stiffness and the curvature of the cable, and the second plot shows the relationship between the normalized bending moment and the normalized curvature. According to Figure 4.1a for the 1113MCM conductor cable, $C_{\text{full}} \cong 3$ and $C_{\text{init}} \cong 1$, and according to Figure 4.1b, $C_Y \cong 3.5$ for this cable. Definitions of these fitting parameters are given in Section 3.3.2 and Table 3.1 in Chapter 3 lists the values of the fitting parameters for all the tested cables. The section properties of the cables required for the finite element model are determined according to Section 3.4.

The initial shape of the cable specimen in the experiments and its previous deformation history causes uncertainty. A cable with flexural rigidity and fixed ends is a statically indeterminate system. As a result, response predictions depend on the assumed initial configuration. Since the cable is usually transported while rolled on a cylinder, it tends to have a natural curvature before installation. In the experiments, each cable was unrolled and installed manually, while making an attempt to approximately position it in a vertical plane. Unfortunately, it is not possible to numerically simulate the exact deformation history of the cable, since we do not have detailed information about the loading history before and during the installation process into the experimental setup. For this reason, in the present analysis, we assume a straight configuration as the initial undeformed shape of the cable. We then apply gravity loading and impose end displacements to achieve the initial static configuration of the cable with a specified span length in the experimental setup.

Before describing the comparisons with the experimental results, it is useful to recall the major approximating assumptions inherent in our theoretical model of the cable developed in Chapter 2. First, there is the assumption of constant bending or curvature. Specifically, we developed the model for the slippage of wires considering the unbalanced wire force only due to the variation in the distance from the neutral axis to the two ends of a differential wire element (see Figure 2.6). In the presence of a shear force, an additional unbalanced force will occur due to the variation in the bending moment. As we argued in Chapter 2, due to the small cross section of the cable relative to its length, the shear force in the cable is expected to be small. During the experiments, it was not possible to measure the shear force in the cable or the variation in the bending moment. As a result, the effect of this approximation could not be quantified.

A second assumption in the model developed in Chapter 2 is that the normal force acting between the wires is arising only from the tension force in the helically wrapped cable. However, normal forces between the wires may also result from transverse "pinching" forces, such as those resulting from reactions at the supports, or from external transverse forces acting on the cable. Such forces would tend to increase the friction between the wires and, hence, locally increase the moment of inertia of the cable. Real cables have long spans with no externally applied loads and their ends are typically fixed in rigid brackets. These end conditions are expected to have only local influences. In any case, it is important to recognize that the model developed in Chapter 2 cannot account for these local effects.

Another assumption inherent in our model is that the material of the cable remains elastic at all times. The modeled elasto-plastic bending behavior of the cable is due to slippage of the wires, but not inelastic deformation of the material. In real cables under dynamic loading, it is quite possible that some wires in cross sections with large curvature will yield. This is most likely to happen at the fixed end points and at points of application of transverse point loads. The mathematical model developed in Chapters 2 and 3 does not account for this effect. Our investigations with a number of example systems indicate that yielding of some wires in the cable is quite likely in typical cable systems under severe earthquake loading.

Several minor assumptions were also made in developing the moment-curvature relationship for the cable in Chapter 2. These included the assumption that the neutral axis of the cable cross section remains close to the neutral axis of the fully stuck state even after some wires slip; that the shear deformation in the cable is negligible; and that the curvature of each wire in the bent cable is well approximated by its curvature in the straight cable. We believe these assumptions have relatively minor influences on the predicted behavior of the cable under static and dynamic loads.

4.3 Comparison with Experimental Results of Filiatrault and Stearns

The present study and the experimental study by Filiatrault and Stearns (2002) were conducted as coordinated components of the Pacific Earthquake Engineering Research (PEER) Center's lifeline program on electrical substations. The two studies had similar objectives, i.e., to develop a better understanding of the behavior of conductor cables and to assess the effect of interaction between cable-connected electrical substation equipment. The two studies were coordinated with the idea that the experiments would provide a validation of the theory developed in this study. Furthermore, it would allow us to estimate the friction coefficient between the wires, which is the single unknown parameter in the theoretical model. However, as we will shortly see, the experiments with the flexible cable, and particularly the measuring of the cable curvature and bending moment, proved to be extremely difficult tasks. Large errors are present in the measured values of these quantities. Furthermore, the experimental setup involved unknown forces and conditions that could not be replicated by analysis. Thus, unfortunately, we cannot aim at validation of the theory through these experimental results. Nevertheless, fairly good agreement between the analytical and experimental results are obtained at the global level, as described below.

Figure 4.5 shows the experimental setup used by Filiatrault and Stearns (2002). The cable is laid out vertically with a dead load applied at the bottom to generate tension in the cable. Additional tension results from the weight of the cable itself. The top end of the cable is fixed in the horizontal and vertical directions, but is free to rotate. The cable is supported in the transverse direction at points A and D having distance $L = 2.74$ m from each other. At each point, a pair of cast wheels allows free movement of the cable in the vertical direction and in rotation, but it prevents movement of the cable in the horizontal direction. Pairs of wheels are also used to transfer the transverse displacement loads from the actuator at two points B and C on the cable, at L/3 and $2L/3$ points between the two supports. The actuator forces F at the two points B and C are measured. Under ideal conditions, and for small displacements, this setup would create constant bending in the cable between points B and C. This would be ideal for verification of the theoretical model developed in Chapter 2, which is based on the assumption of constant bending. However, as described below, several factors influence the forces acting on the cable so that the real situation is far from the above ideal condition.

As described above, the cast wheels at supports A and D and at points of application of the transverse loads at B and C were installed to allow free translation in the vertical direction and free rotation of the cable at these points. The gap between the grooves on each pair of wheels was made slightly wider than the diameter of the cable to allow these movements. However, three factors contradict these ideal conditions: (a) the journal bearing friction between the supporting wheels and their axles, (b) rolling friction between the cable and the supporting wheels, and (c) a moment couple applied on the cable by each pair of wheels, as the cable rotates and touches the two wheels at points not located along the line connecting the centers of the two wheels. As a result of these effects, the resultants of the external forces acting at each pair of wheels has a vertical component as well as a moment couple. The magnitudes of these forces remain unknown, but we can expect them to increase with increasing values of the actuator forces F.

Because of the vertical components of the forces at the wheels, and because of the weight of the cable itself, the tension force in the cable is not a constant. If we neglect the vertical forces at the wheels, the tension force at point C is equal to the dead weight hanging from the cable, plus the weight of the cable below point C. Let T denote this force. From the above discussion,

we can surmise that the actual tension force in the cable at point C is somewhat greater than T due to the horizontal components at the wheels, and that that difference is greater for larger values of the transverse load F.

As mentioned earlier, under small displacements, the bending moment in the cable between points B and C is nearly constant. However, for large displacements of the cable, the contribution from the tension force to the bending moment becomes significant. The bending moment in the middle of the span BC is given by

$$M = \frac{FL}{3} - T\delta \tag{4.1}$$

where δ is the horizontal displacement at midspan. This formula was used by Filiatrault and Stearns (2002) to compute the bending moment at the midspan. They actually controlled the displacement δ and measured the applied force F. It is clear that this estimate of the bending moment does not account for the moment couples and vertical components of forces potentially acting on the cable by the pairs of wheels. Since we expect the actual tension force at point C to be larger than T, it is likely that the actual bending moment in the cable is smaller than that computed using (4.1), particularly when the weight applied to the bottom of the cable is large.

To compute the curvature of the cable, Filiatrault and Stearns (2002) attached inclinometers on the cable. These devices measure the inclination of the cable and, therefore, the change in the slope as the cable undergoes deformation. The curvature at a point is approximately estimated as the total change in the slope measured at the two nearest inclinometers, divided by the distance between them. Using this approximate method, the curvature in the midspan was estimated by Filiatrault and Stearns (2002) by using two inclinometers situated 0.0653 m apart from the center point.

The analytical predictions of the bending moment and curvature of the cable are direct outputs from the finite element model. However, in order to be consistent with the curvatures computed in the experiment, instead of using the computed curvature in the midspan, we use the average of the curvatures computed at two points on the sides of the midspan at distance 0.0653 m. In the plots to be shown below, these estimates of the curvature are shown instead of the actual curvature at the midspan.

The finite element model of the cable is different from the experimental set up in two significant ways: (a) the pairs of wheels at the support points and at points of load application are assumed to be ideal, so that no vertical force or moment couple is acting at these points; (b) the additional normal force between the wires arising from the reaction forces at the wheels and the resulting increased friction between the wires, which would tend to prevent slippage of wires and increase the effective moment of inertia of the cable, are neglected. The effects of these additional forces are unknown and are presumed to be significant for large values of the cable tension T or applied loads F. They could be the source of the significant discrepancy observed between the experimental and analytical results.

In the following subsections, we present the comparisons between the experimental and analytical results for static monotonic and cyclic tests of the setup described above.

4.3.1 Monotonic Tests

Figures 4.6 and 4.7 compare the analytical and experimental estimates of the monotonic bending moment-curvature relationships for the 1113MCM and 2300MCM conductor cables, respectively, for 7 different tension forces. The curvature values shown are the averaged values computed over the two points 0.0653 m apart from the center point, as described in the preceding section. The plots on the left side of each figure have uniform scales; the plots on the right side are the same ones but individually scaled. For the analytical predictions, two values of the friction coefficient between the wires, $\mu = 0.3$ and $\mu = 0.5$, were assumed.

It is difficult to derive conclusions from the experimental results in Figure 4.6 for the 1113MCM conductor cable. This cable has a small cross section and, therefore, is highly flexible in bending. Obviously, there has been significant noise in measuring the curvature in the text. It also appears that the measured bending moments are affected by a non-zero initial value. We have concluded that the experimental results for this cable are too much affected by measurement errors and, therefore, cannot be used to derive conclusions vis-à-vis the analytical predictions.

For the 2300MCM conductor cable, the results in Figure 4.7 are somewhat better, particularly when the tension force in the cable is neither too small nor too large. For small tension forces, there appear to be large errors in measuring the bending moment. For large tension forces, the effect of friction at the wheels appears to become significant with the cable

forces, the effect of friction at the wheels appears to become significant with the cable showing much higher flexural stiffness in the experiment than in the analytical predictions. Overall, the trend predicted by the analytical model, i.e., an increase in the "yield" moment with increasing tension in the cable, appears to be born out by the experimental results. However, the resolution in the experiments is not sufficient to identify an appropriate value for the friction coefficient μ, which is the only parameter in the theoretical model. In the subsequent analysis, the value $\mu = 0.3$ is used.

4.3.2 Cyclic Test

For the displacement-controlled cyclic tests, Filiatrault and Stearns (2002) followed the ATC-24 loading protocol (Applied Technology Council, 1992). The displacement amplitude of the cycles was increased from the minimum 0.0063 m (0.25 in) to the maximum of 0.4064 m (16 in). Three load cycles were applied per amplitude. The resulting bending moment-curvature hysteresis loops for the 1113MCM and 2300MCM conductor cables are shown in Figures 4.8 and 4.9, respectively, for 7 different tension forces. Hysteresis loops based on the analytical predictions with the friction coefficient $\mu = 0.3$ are also shown. Again, the left set of plots in each figure has uniform scale, whereas the set on the right is individually scaled.

Figure 4.8 for the more flexible 1113MCM conductor cable again shows large measurement errors. Therefore, we consider the results for the 2300MCM conductor cable in Figure 4.9. The results in this figure show that when the tension force in the cable is small, say less than about 3,500N, the analytical predictions are in fairly good agreement with the test results for absolute curvature values less than about 0.16 m^{-1}. For larger values of the curvature, a sharp increase in the flexural stiffness of the cable is observed in the experiment. We believe this is due to the constraints provided by the wheels, and possibly the increased friction between the wires at the reaction points. This effect is evident in even lower curvatures as the tension force in the cable increases.

Figures 4.10 and 4.11 show the hysteretic relationships between the actuator force and the cable displacement at the midspan for the 1113MCM and 2300MCM conductor cables, respectively, for 7 different tension forces. These results provide an indication of the global force-deformation behavior of the cable. The finite element predictions and the test results are in close

agreement in terms of the overall stiffness. However, the test results show a higher amount of energy dissipation than the finite element predictions, particularly for large displacement loops. We believe a part of the energy dissipated in the test occurs due to friction at the wheels. Additional energy may be dissipated due to yielding of the wires at points of high curvature, a phenomenon that is not included in our theoretical model, or due to slippage of wires under large friction forces occurring at the wheels.

The above comparisons clearly show the difficulty in conducting experiments with cables, if the aim is to develop bending moment-curvature relationships. There is need for a method to accurately measure curvature. Furthermore, it appears that an alternative method of testing, which avoids applying concentrated transverse loads on the cable is preferable. As for the analytical model, the experimental results by Filiatrault and Stearns (2002) provide some support for its validity, but not a conclusive one due to lack of resolution in the measurements and non-ideal conditions in the experimental setup.

4.4 Comparison with Experimental Results of Dastous and Pierre

Dastous and Pierre (1996) used 1796MCM and 4000MCM conductor cables in quasi-static, displacement-controlled cyclic tests. The properties of these cables are listed in Table 4.2. The lay angles of the wires in the 1796MCM conductor cable are 18.6, 10.3, 12.6 and 13.8 degrees from the innermost to the outermost layer. However, for the sake of simplicity, in our analysis we have used a uniform lay angle of 12 degrees for all the wires. For the 4000MCM conductor cable, the lay angles were not reported. Based on observations of other similar cables, a uniform lay angle of 15 degrees was assumed for wire layers in this cable. Figures 4.3 and 4.4 show the bending moment-curvature relationships for the two cables, respectively.

The experimental setup used by these investigators is shown in Figure 4.12. Each cable was manually installed between two horizontal support points in a vertical plane. One end of the cable was fixed and the other end was horizontally moved by an actuator. The span length and the horizontal force at the moving support were measured.

As mentioned earlier, we do not have detailed information on the initial shape of the cable in each experiment. Therefore, we have used a straight undeformed configuration as the initial shape of the cable. The straight cable of specified length is modeled with both its ends fixed

and having no weight. The weight of the cable is then applied as dead load and the cable is allowed to deform. One end of the cable is then moved towards the other end until the specified initial span length used in the experiment is achieved. As described below, because of the uncertainty in the initial conditions of the cable in the experiments, the horizontal cable force as well as the cable sag in the theoretical initial state are somewhat different from the initial test values reported by Dastous and Pierre (1996).

In the first experiment, a 1796MCM conductor cable of initial length s_0=5.52m and initial span L_0= 5.51m was subjected to a displacement loading, u, at one end. The moving end of the cable statically and horizontally moved inwards by 1.2m and moved back to its original position. This movement was repeated twice. The horizontal actuator force, T, which is the same as the horizontal cable force at the moving support, is plotted in Figure 4.13 as a function of the measured span length, L. The analytical prediction of the T versus L hysteretic loop is also shown in the same figure. It is noted that the force in the cable becomes compressive when the span is made smaller than 5m. This is a clear indication of the flexural stiffness of the cable. The overall shapes of the experimental and analytical curves are similar. However, two major differences are observed. First, it appears that the initial tension force in the test cable is larger than that in the analysis. This is due to the unknown initial shape and deformation history of the test cable. Most probably the cable had an initial curvature due to being transported rolled on a cylinder and, therefore, it required a larger tension force to stretch to the initial span length of L_0= 5.51m. The second important difference is in the dissipation of energy. While the test shows a modest amount of energy dissipation, the theoretical hysteresis loop shows virtually no energy dissipation. One possible explanation for this is that the wires in the test cable may have experienced yielding, particularly near the end points, where the wires are compressed together by the end brackets and the cable experiences large curvatures. As discussed earlier, our model does not account for this effect. Another source of energy dissipation might be the experimental setup, i.e., friction in the moving support of the cable.

In the second experiment, a 4000MCM conductor cable of initial length s_0=5.64m and initial span length L_0=5.61m was used. One end of the cable was moved statically and horizontally inwards by 0.8m and then moved back to its original position. The cycle was repeated twice. Figure 4.14 compares the T versus L hysteretic loops obtained by the experiment and by

analysis. The agreement between the two sets of results is better here. However, again there is discrepancy in the initial cable force and in the amount of energy dissipated.

In summary, we can characterize the comparisons with the experimental results of Dastous and Pierre (1996) as being successful. These comparisons, as well as the comparisons with the global force-displacement test results of Filiatrault and Stearns (2002) show that the proposed analytical model correctly predicts the global response of cables. More precise experiments are needed to verify the theoretical model for the bending-moment versus curvature relationship.

Table 4.1 Properties of flexible conductors used in experiments by Filiatrault and Stearns (2002).

Property	1113MCM	2300MCM
Young's modulus	70×10^9 N/m^2	70×10^9 N/m^2
number of layers except core	4	4
number of strands	61	61
strand diameter	3.556 mm	4.928 mm
overall conductor diameter	32.00 mm	44.35 mm
cross section area	579 mm^2	1,112 mm^2
mass per unit length	1.570 kg/m	3.014 kg/m
lay angle	10 degree	10 degree
I_{min}	465 mm^4	1,739 mm^4
I_{max}	35,908 mm^4	134,420 mm^4

Table 4.2 Properties of flexible conductors used in experiments by Dastous and Pierre (1996).

Property	1796MCM	4000MCM
Young's modulus	70×10^9 N/m^2	70×10^9 N/m^2
number of layers except core	4	9
number of strands	61	271
strand diameter	4.358 mm	3.090 mm
overall conductor diameter	39.22 mm	58.71 mm
cross section area	853 mm^2	1,902 mm^2
mass per unit length	2.311 kg/m	5.157 kg/m
lay angle	12 degree	15 degree
I_{min}	1,057 mm^4	1,186 mm^4
I_{max}	80,609 mm^4	408,270 mm^4

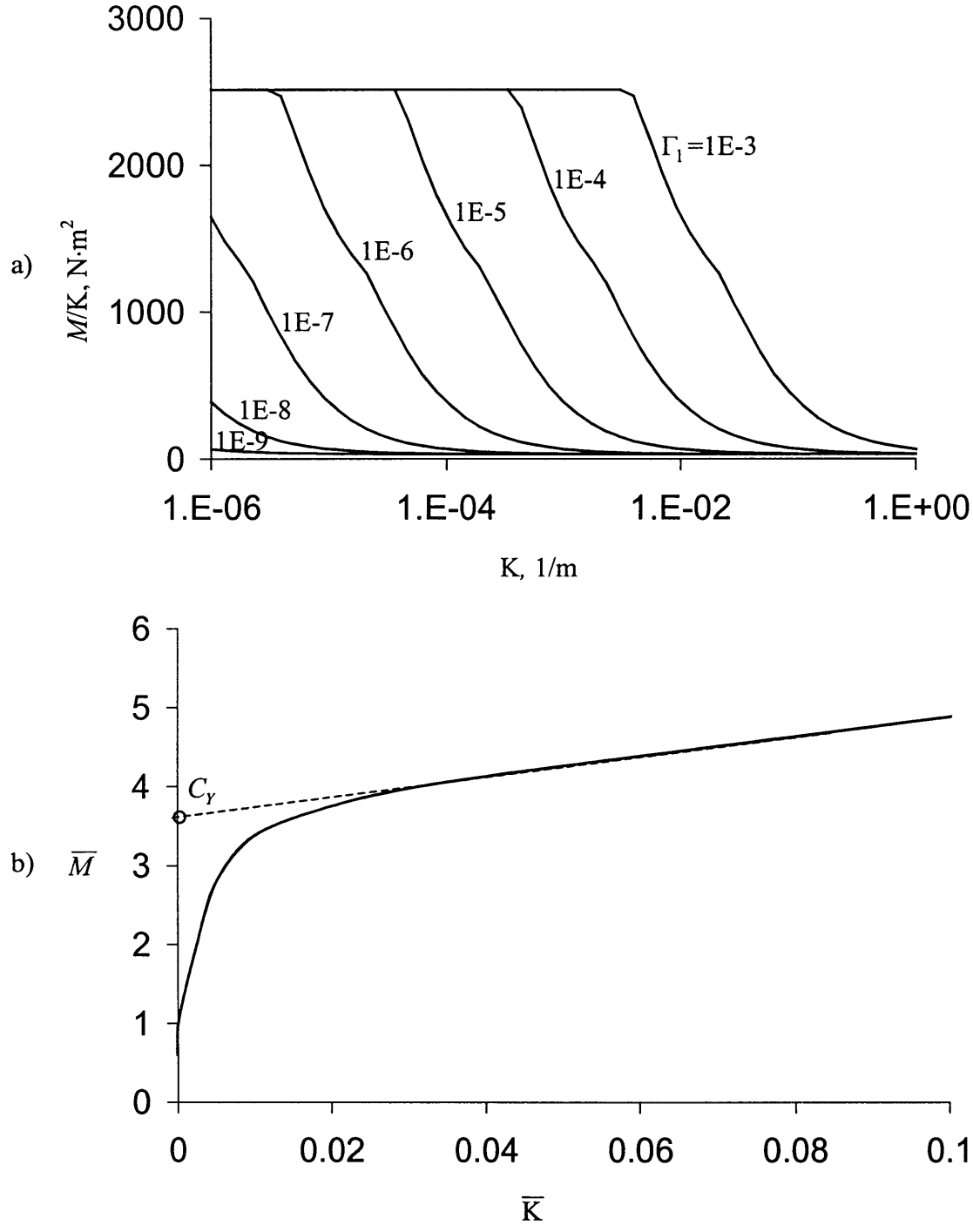

Figure 4.1 Nonlinear bending behavior of the 1113MCM conductor:

a) secant flexural stiffness vs. curvature for different axial strains

b) normalized moment vs. normalized curvature relation

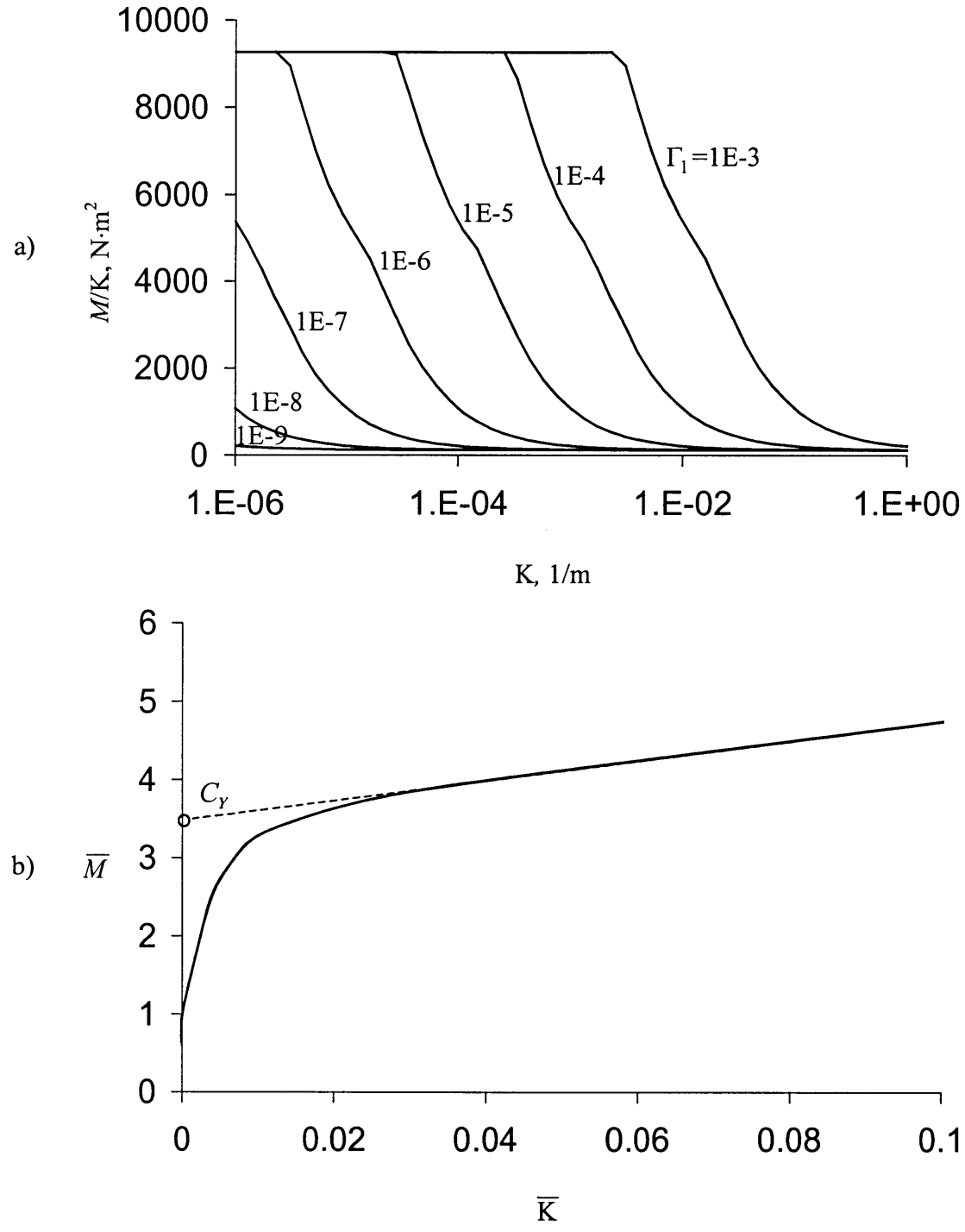

Figure 4.2 Nonlinear bending behavior of the 23003MCM conductor:

a) secant flexural stiffness vs. curvature for different axial strains

b) normalized moment vs. normalized curvature relation

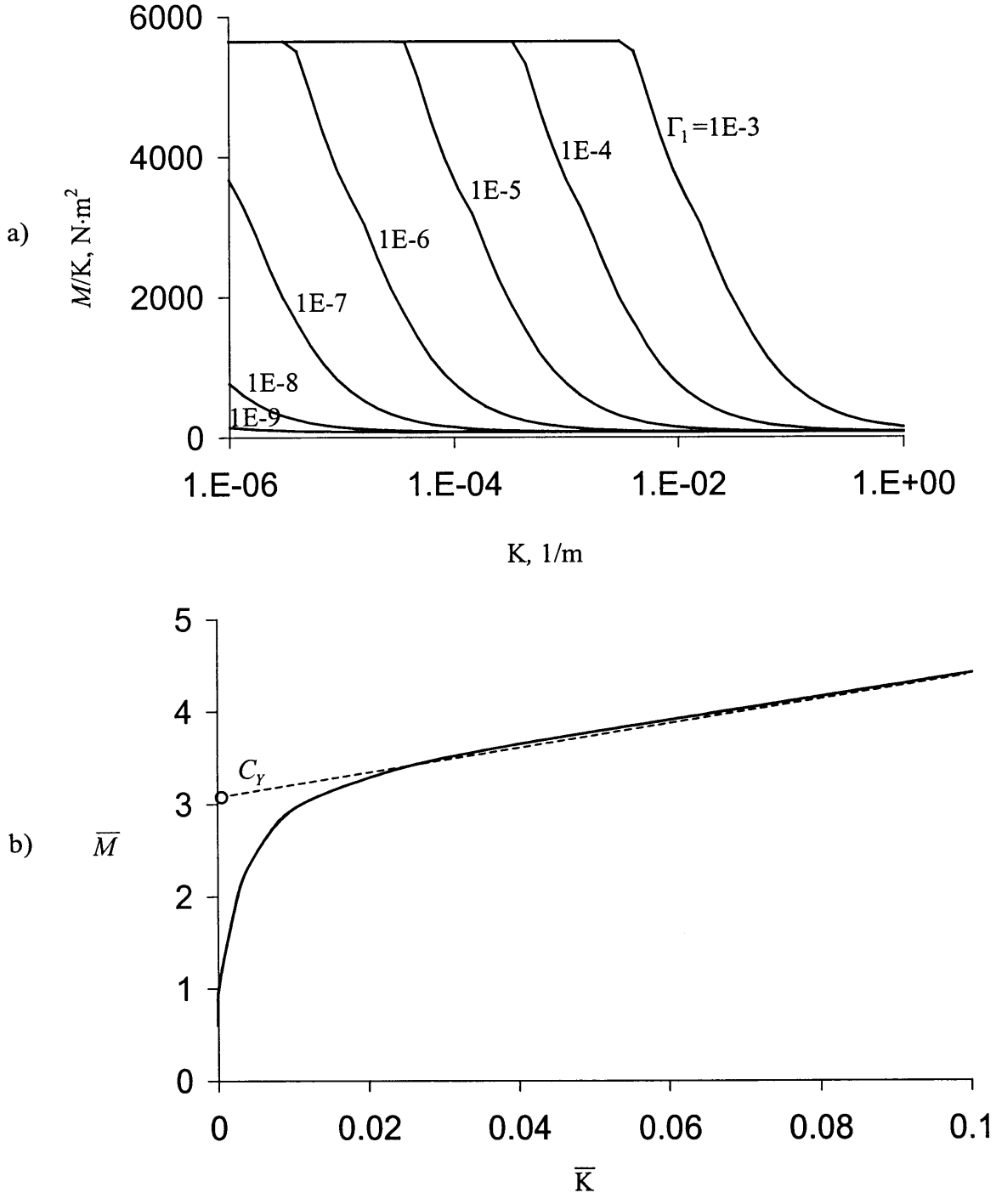

Figure 4.3 Nonlinear bending behavior of the 1796MCM conductor:

a) secant flexural stiffness vs. curvature for different axial strains,

b) normalized moment vs. normalized curvature relation

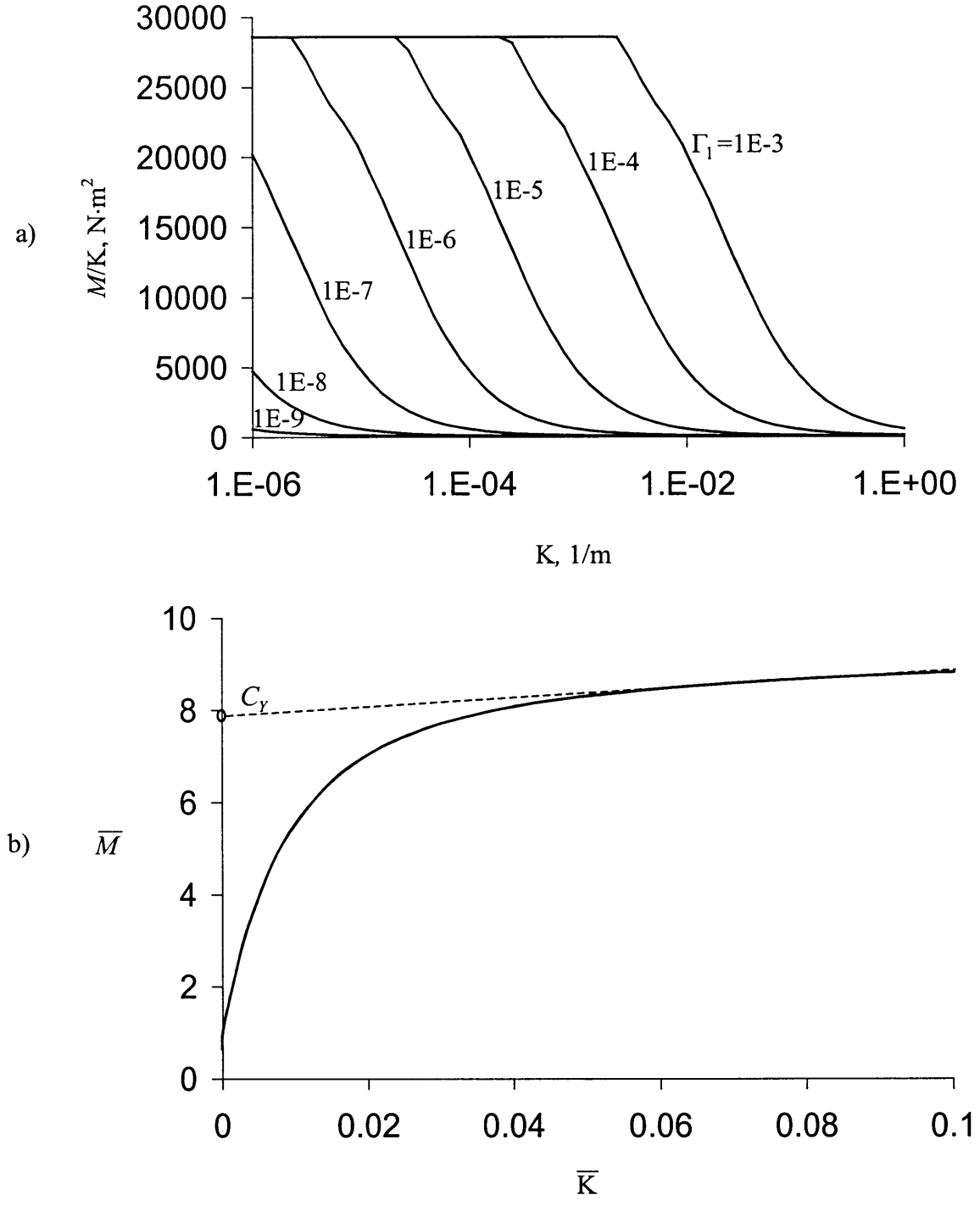

Figure 4.4 Nonlinear bending behavior of the 4000MCM conductor:

a) secant flexural stiffness vs. curvature for different axial strains

b) normalized moment vs. normalized curvature relation

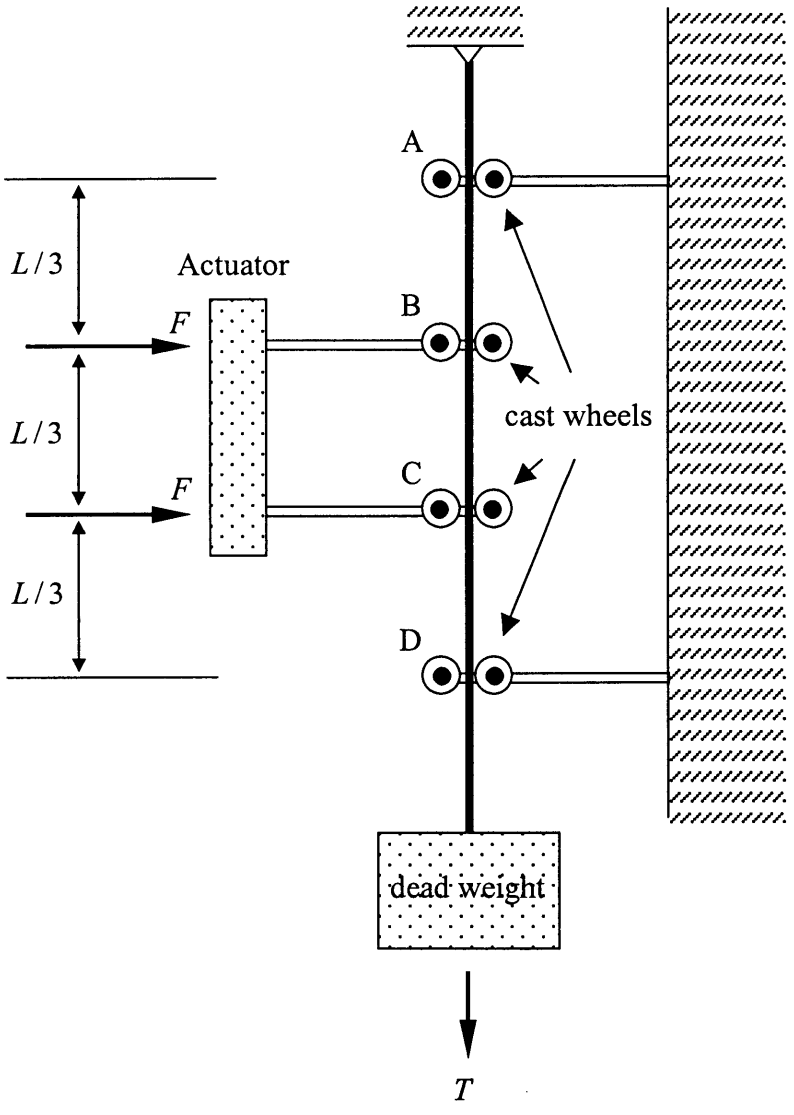

Figure 4.5 Two-point loading test conducted by Filiatrault and Stearns (2002)

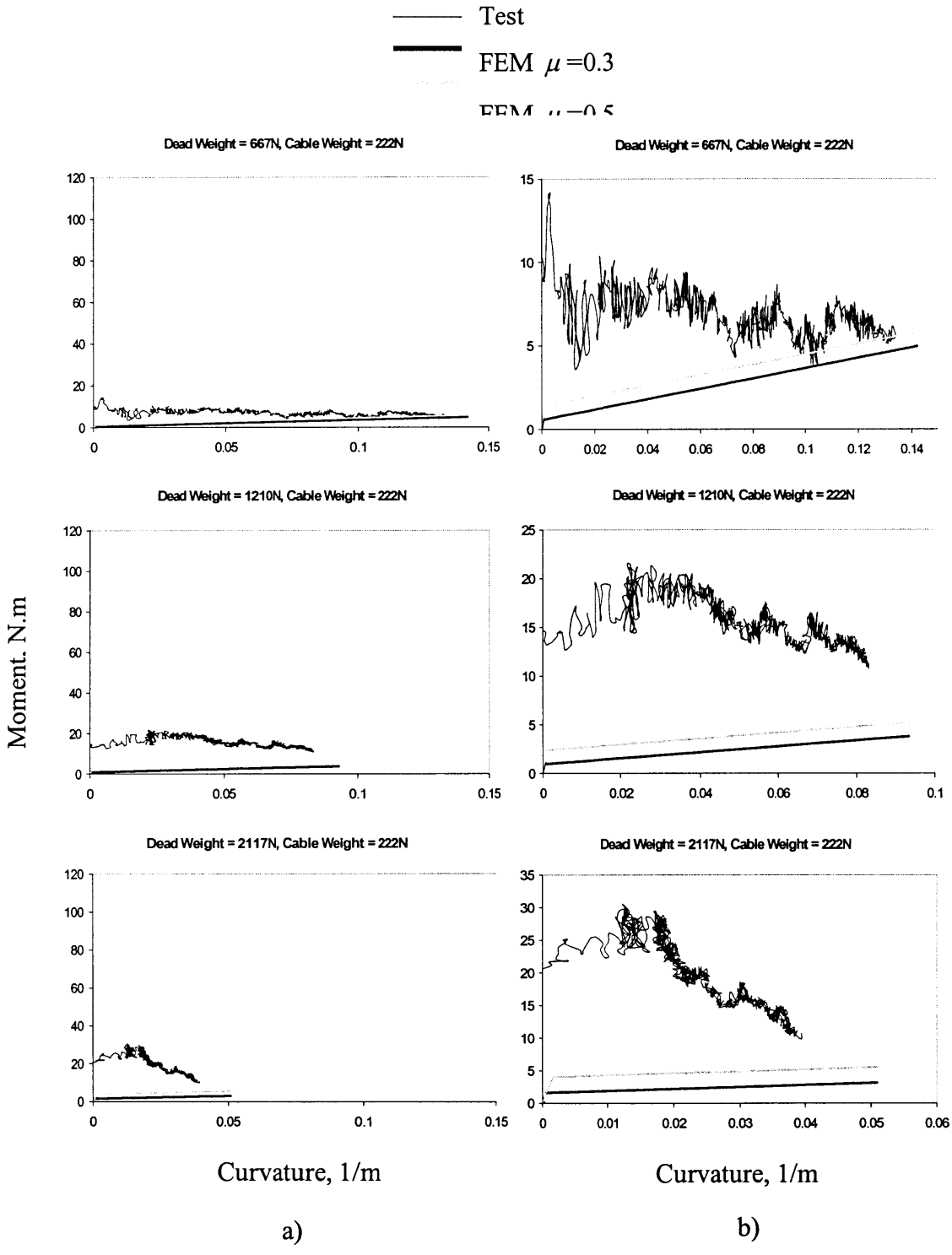

Figure 4.6 Moment-curvature relationship of the 1113MCM conductor in monotonic tests: a) consistent scale, b) magnified scale

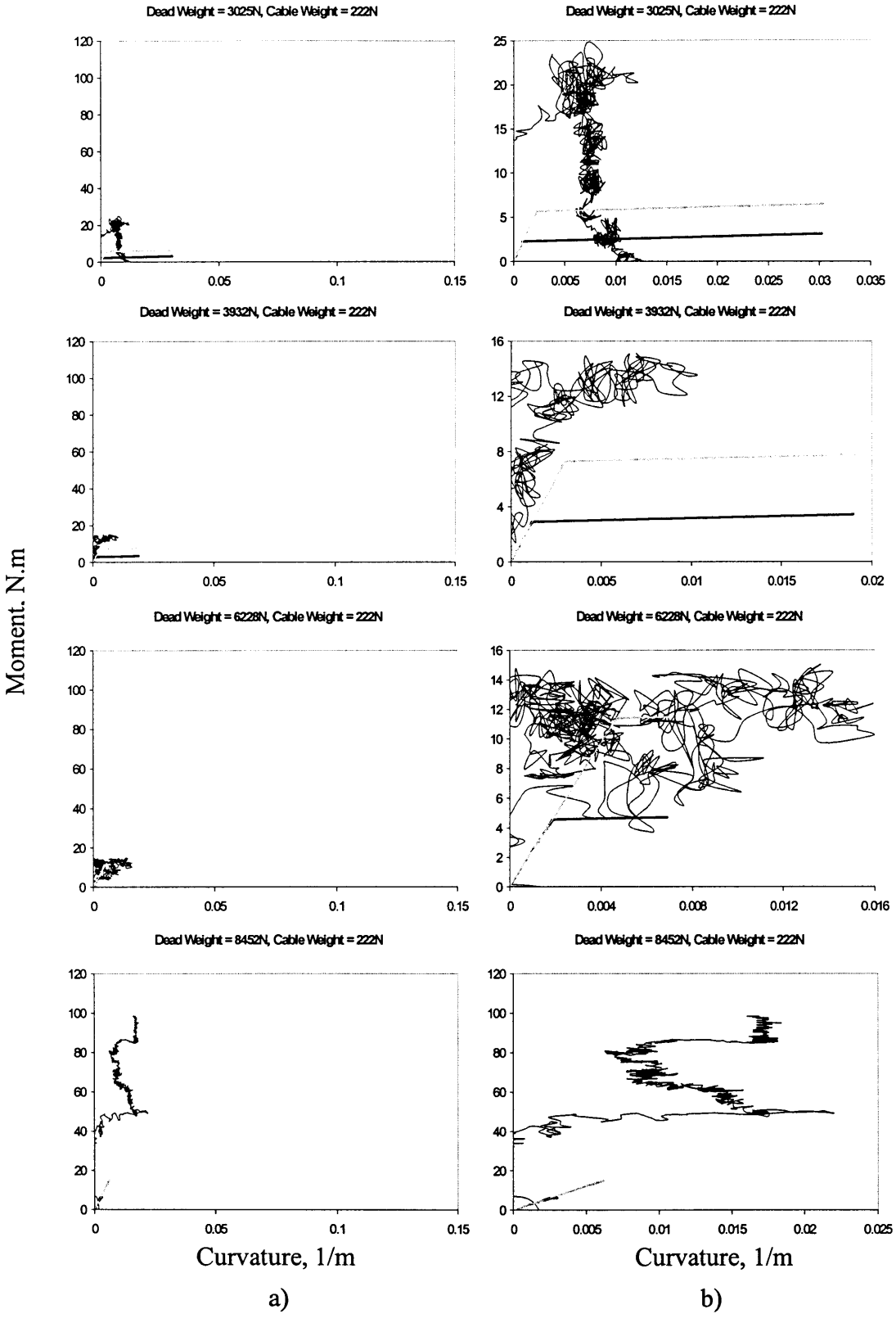

Figure 4.6 (continued) Moment-curvature relationship of the 1113MCM conductor in monotonic tests: a) consistent scale, b) magnified scale

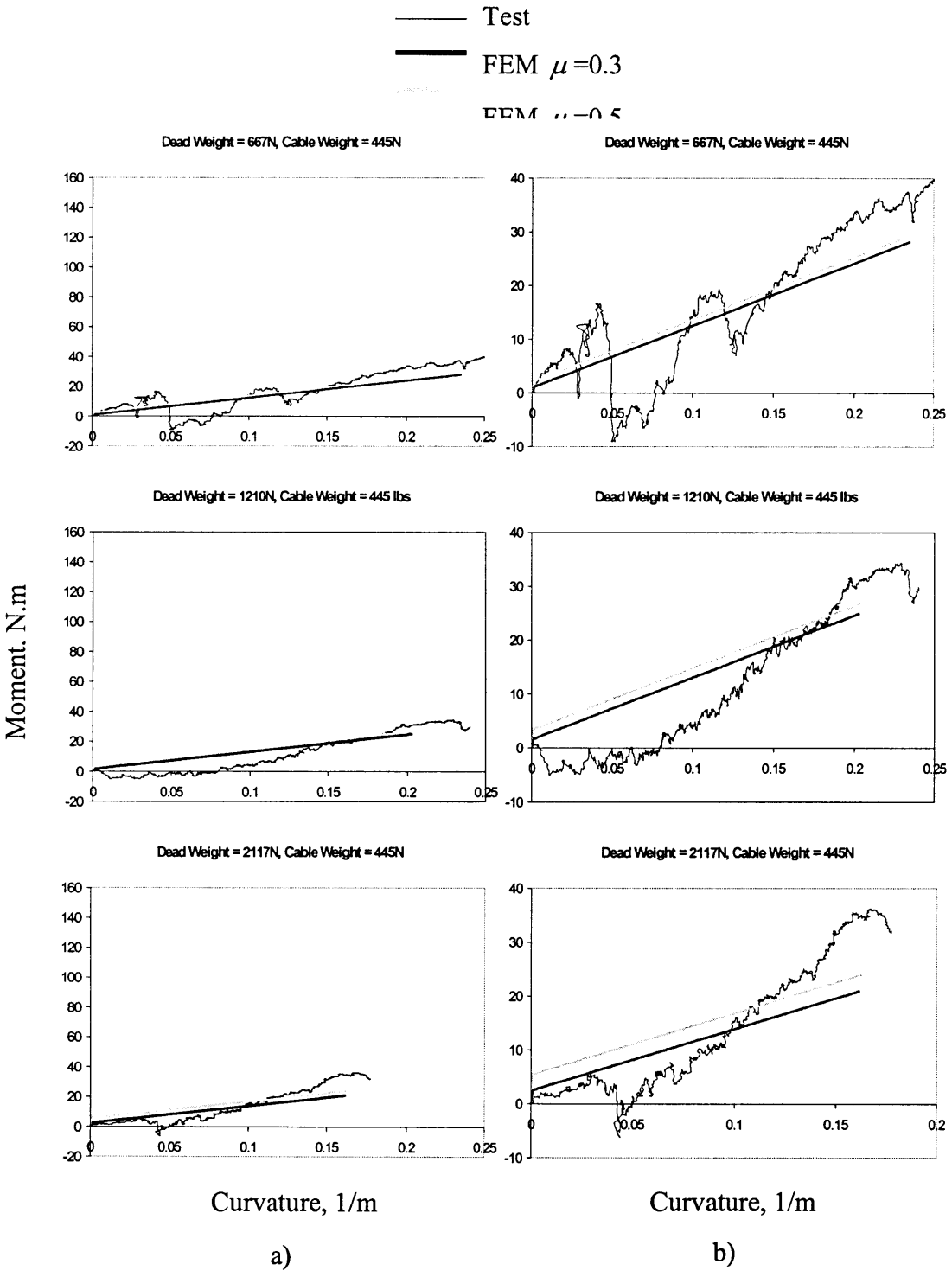

Figure 4.7 Moment-curvature relationship of the 2300MCM conductor in monotonic tests: a) consistent scale, b) magnified scale

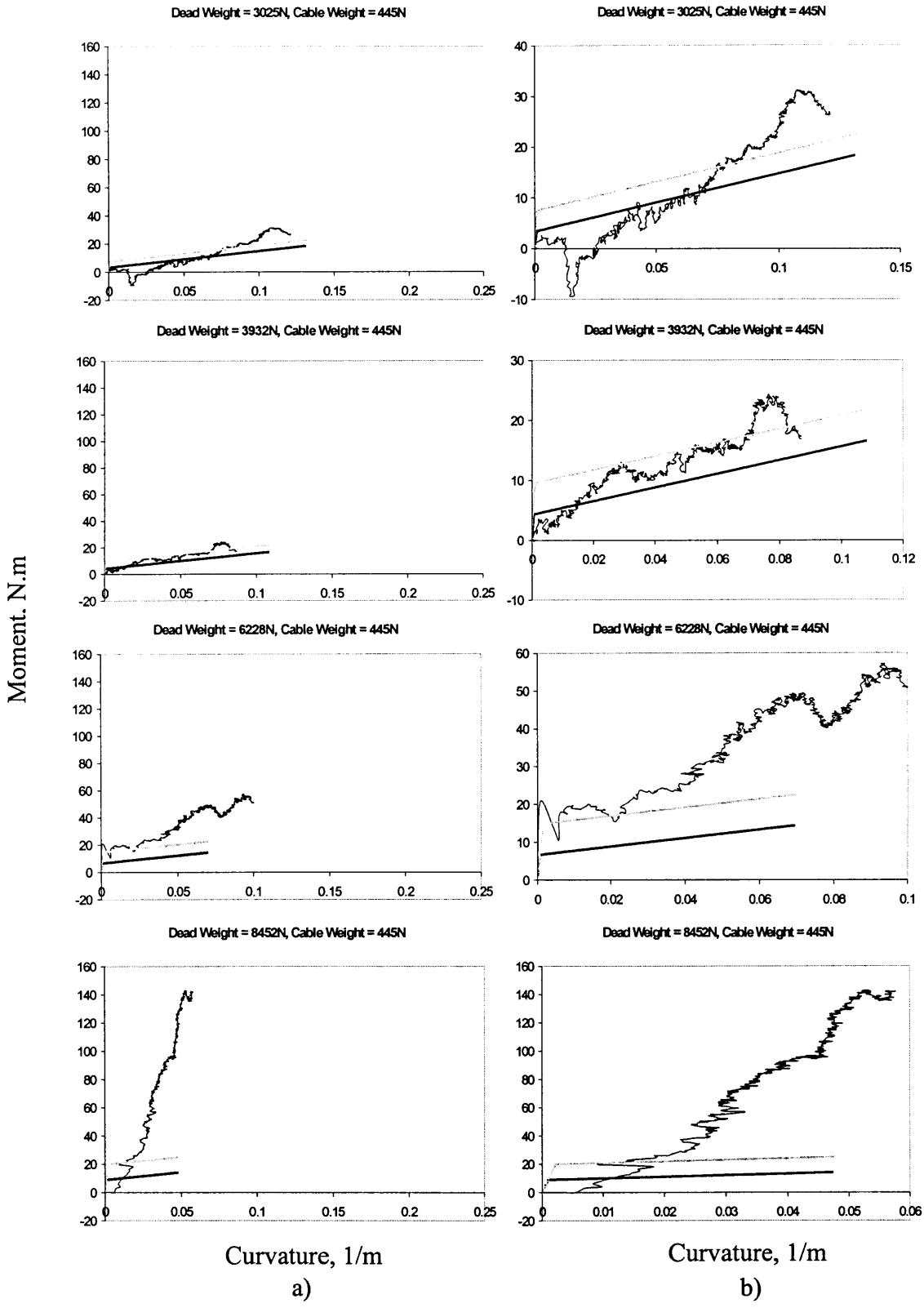

Figure 4.7 (continued) Moment-curvature relationship of the 2300MCM conductor in monotonic tests: a) consistent scale, b) magnified scale

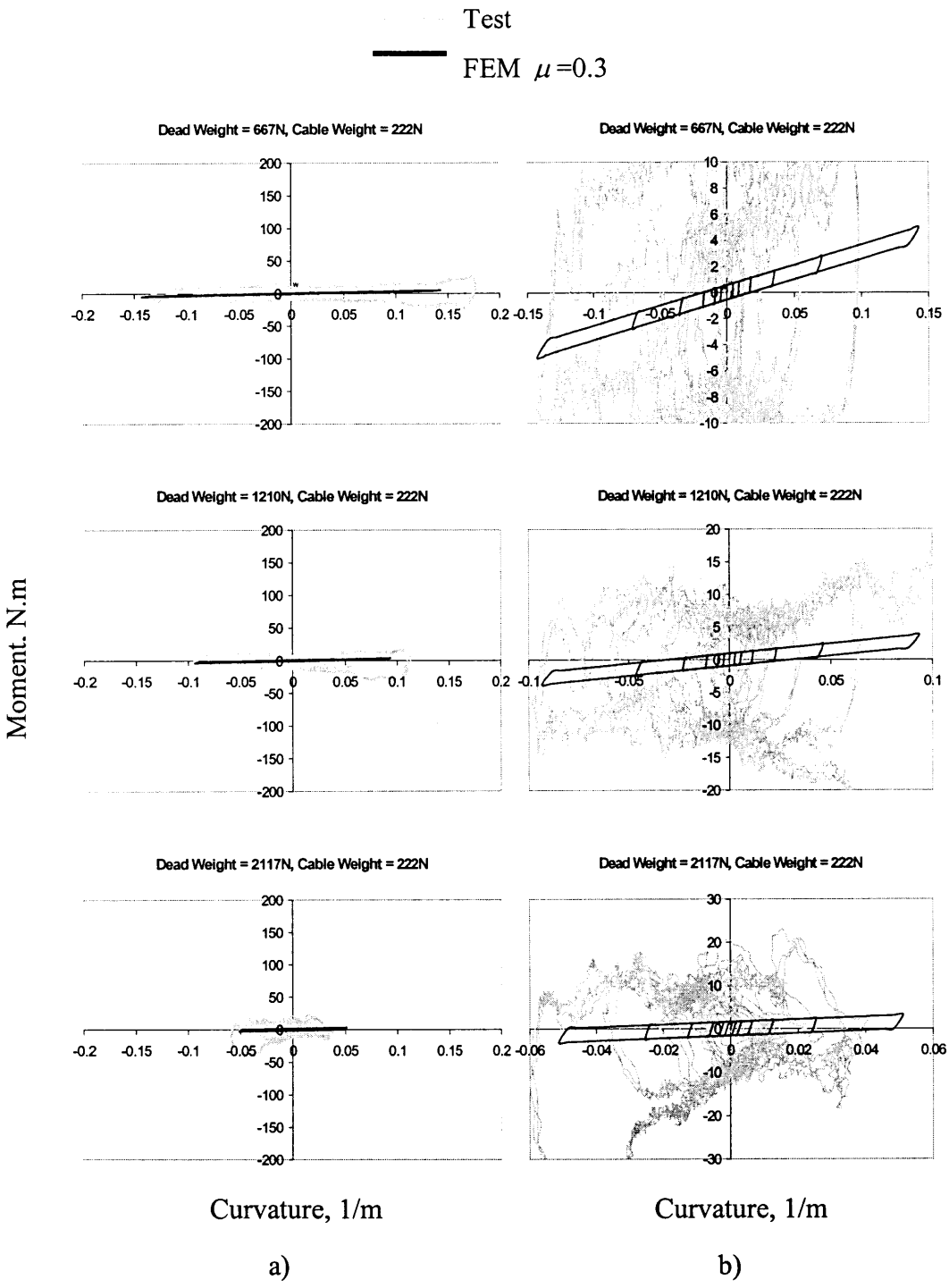

Figure 4.8 Moment-curvature relationship of the 1113MCM conductor in cyclic tests: a) consistent scale, b) magnified scale

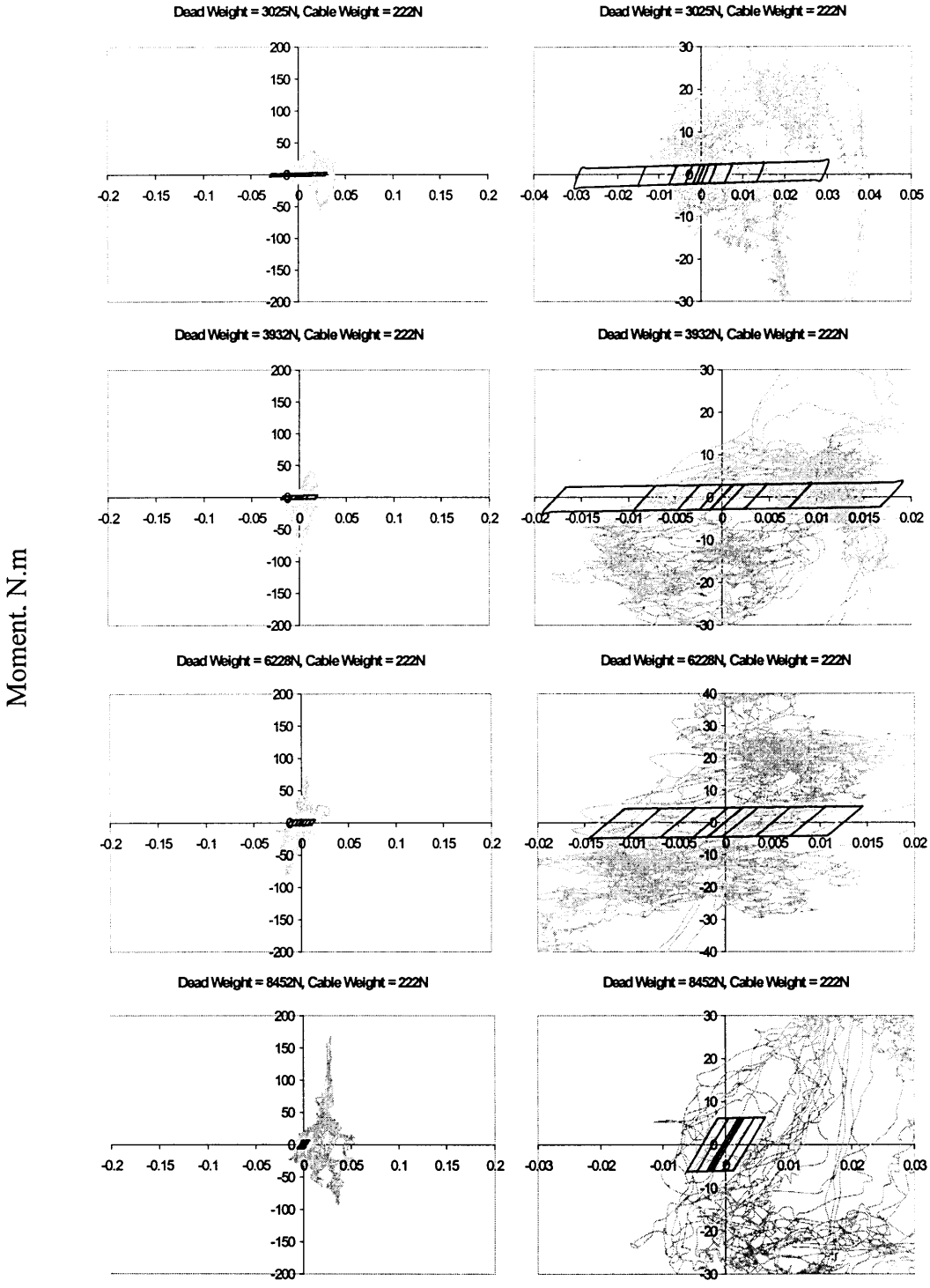

Figure 4.8 (continued) Moment-curvature relationship of the 1113MCM conductor in cyclic tests: a) consistent scale, b) magnified scale

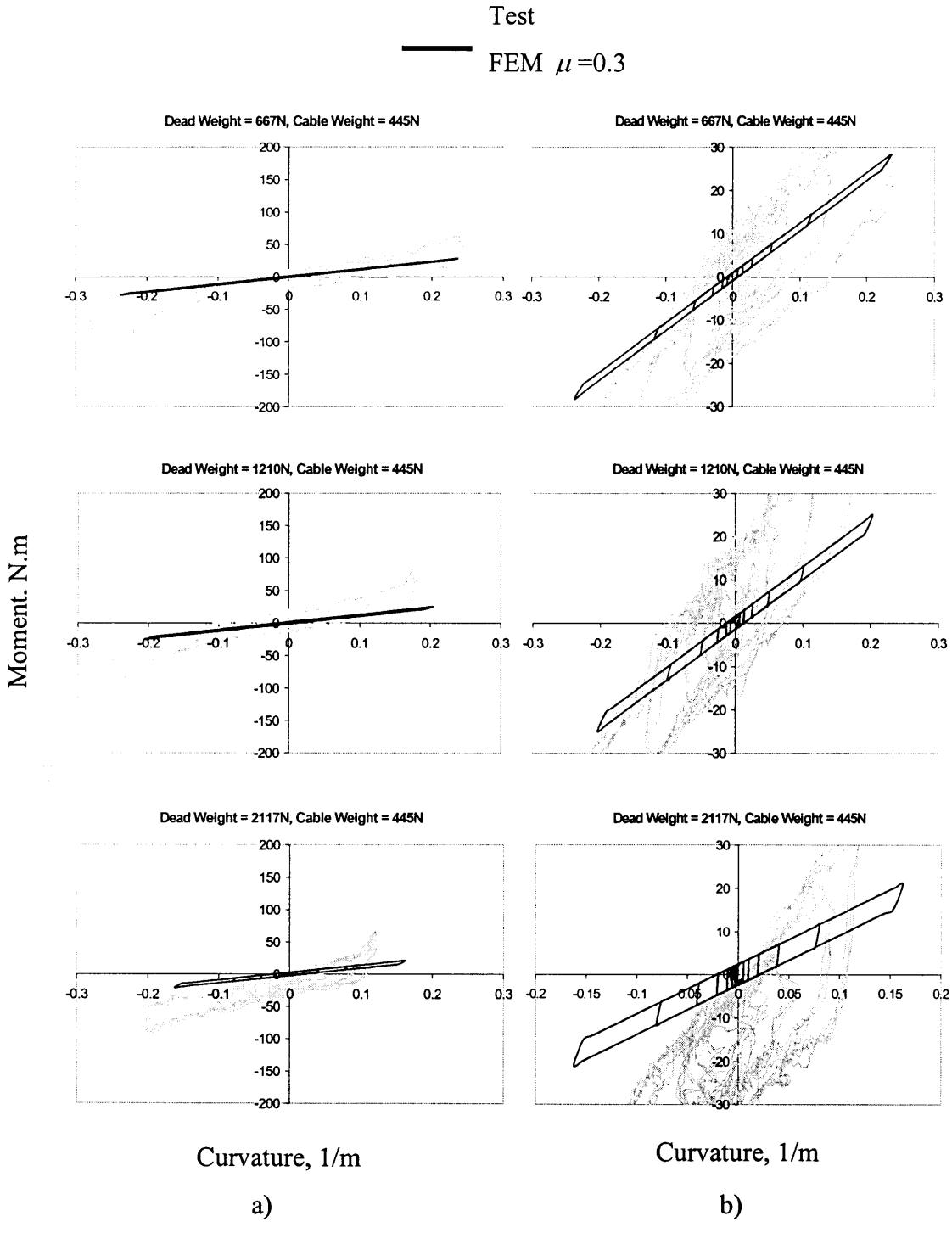

Figure 4.9 Moment-curvature relationship of the 2300MCM conductor in cyclic tests: a) consistent scale, b) magnified scale

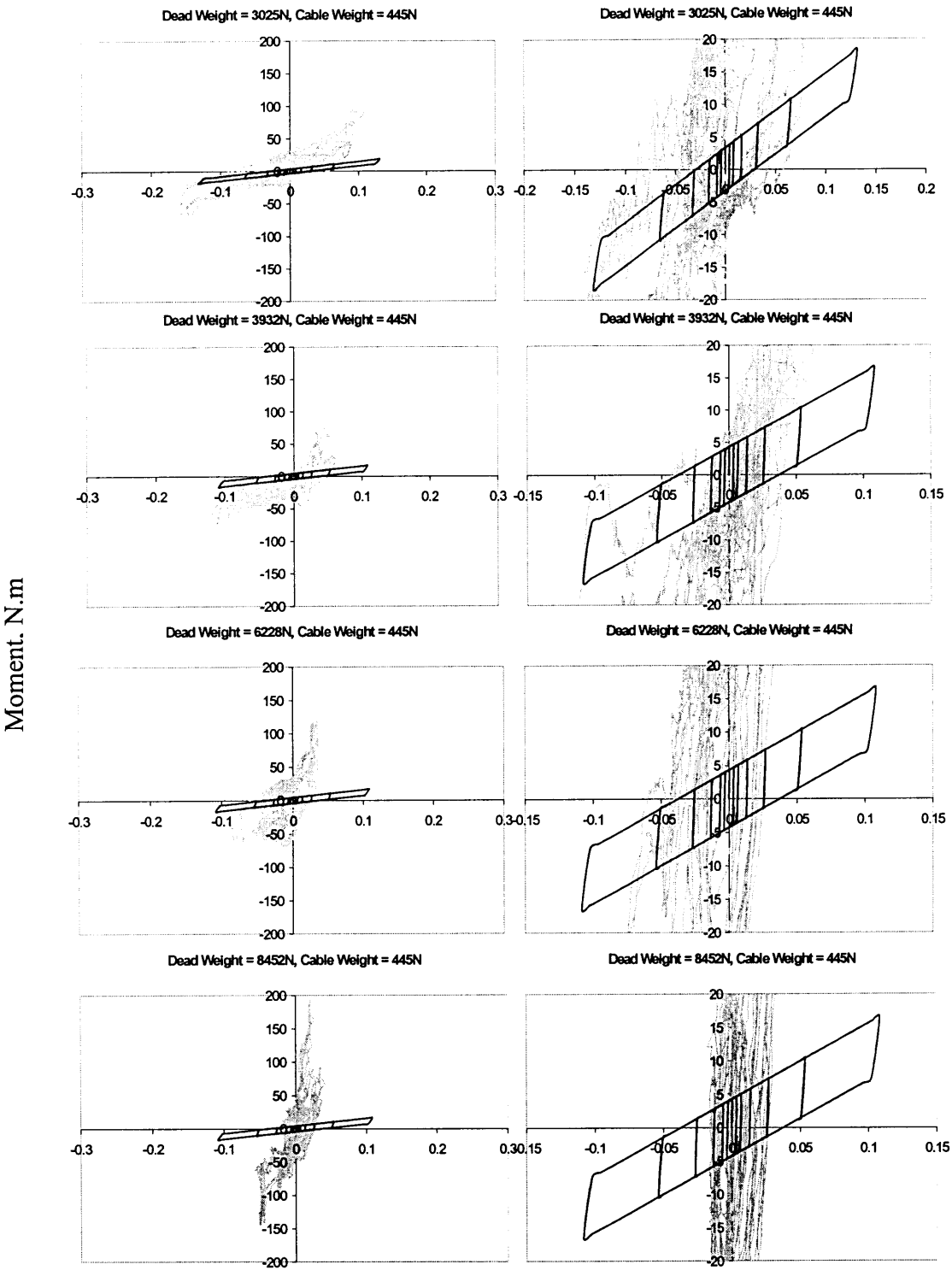

Figure 4.9 (continued) Moment-curvature relationship of the 2300MCM conductor in cyclic tests: a) consistent scale, b) magnified scale

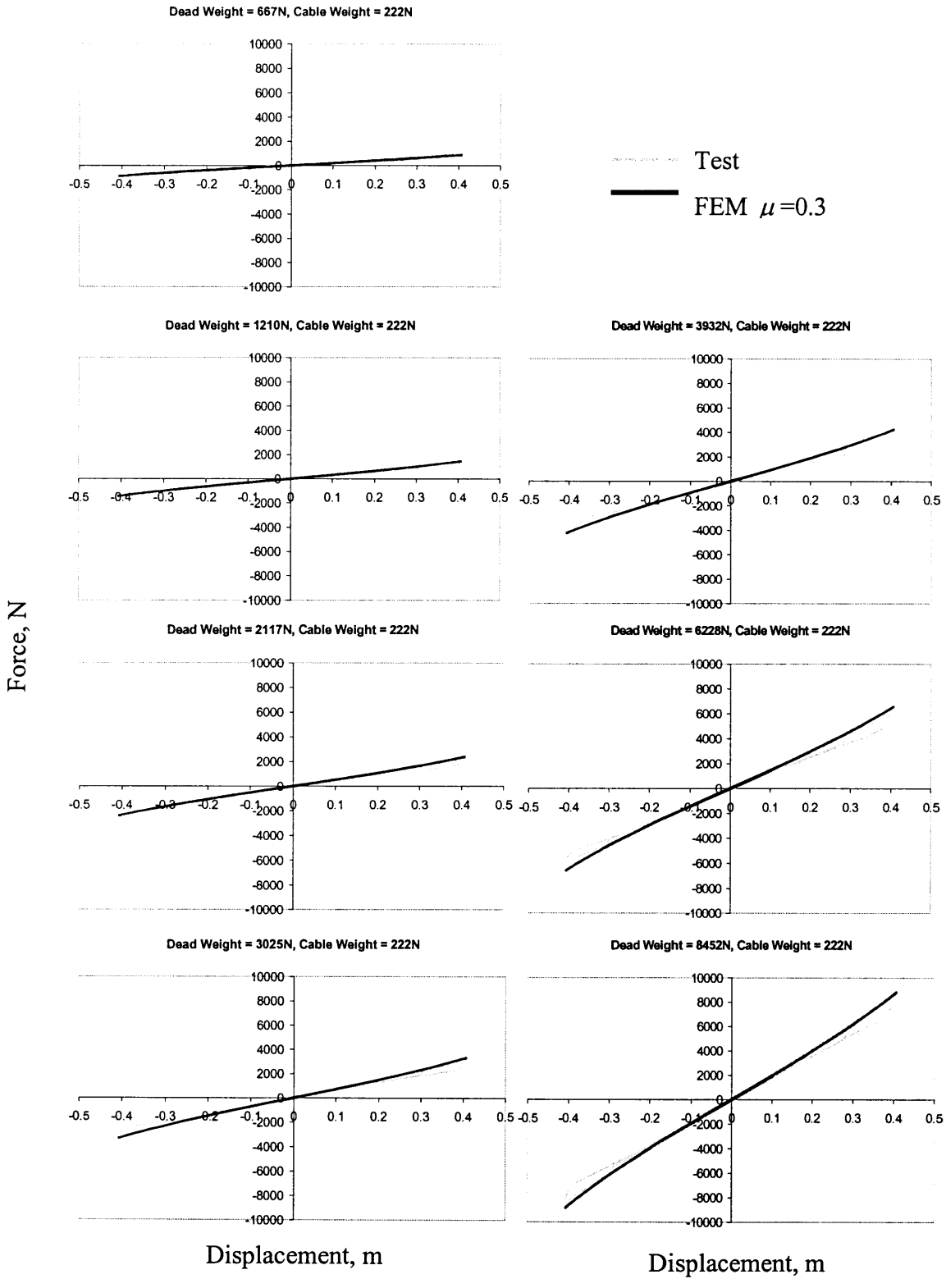

Figure 4.10 Actuator force-displacement relationship of the 1113MCM conductor in cyclic tests

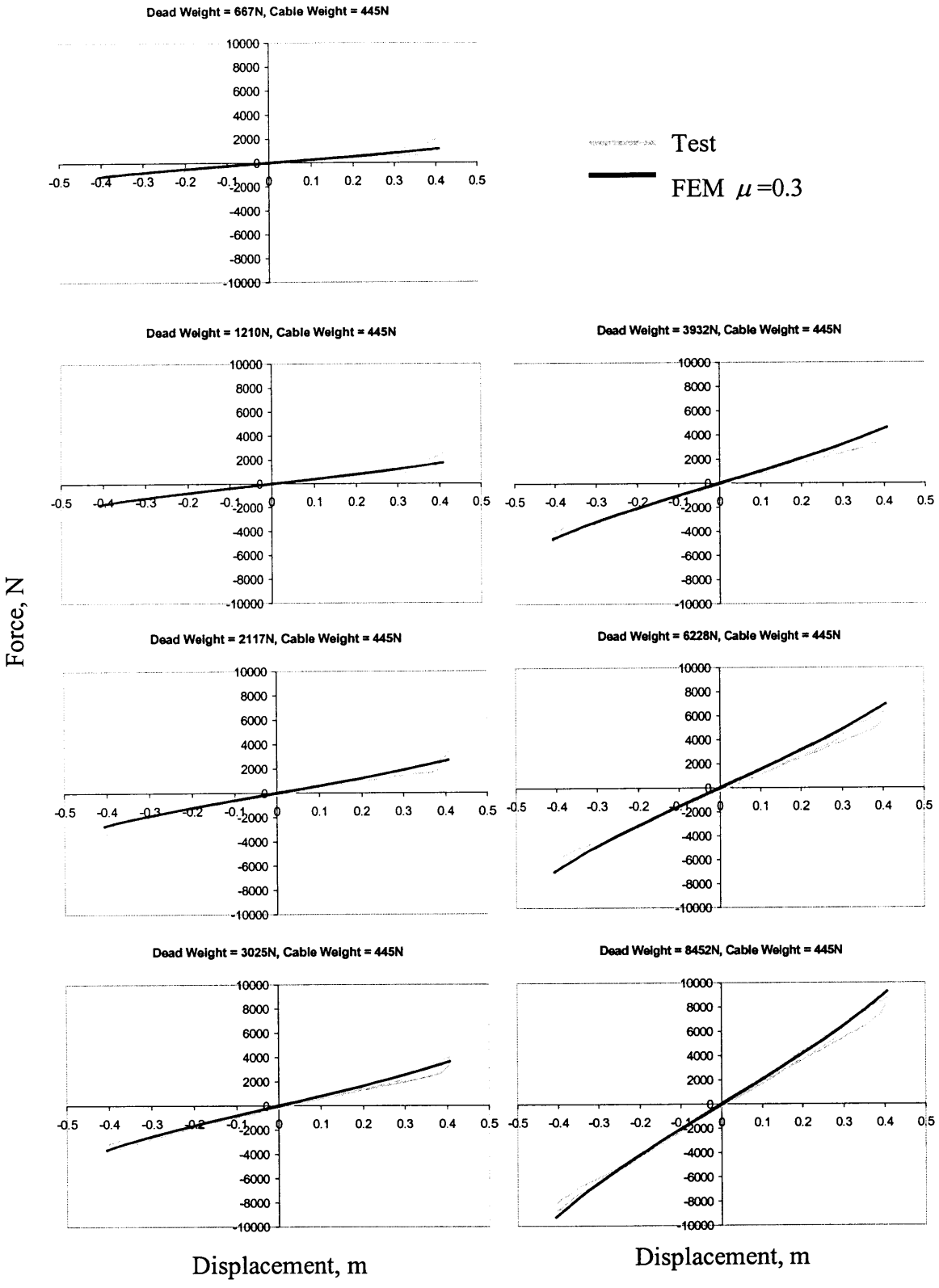

Figure 4.11 Actuator force-displacement relationship of the 2300MCM conductor in cyclic tests

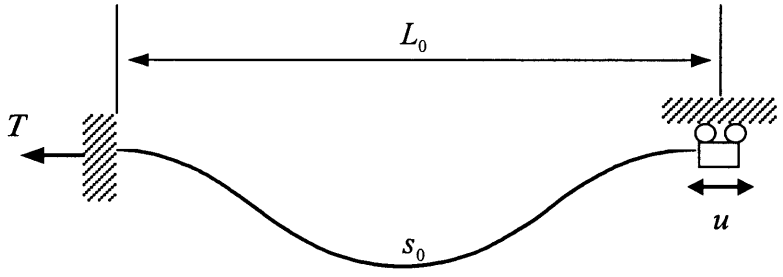

Figure 4.12 Static experiment conducted by Dastous and Pierre (1996)

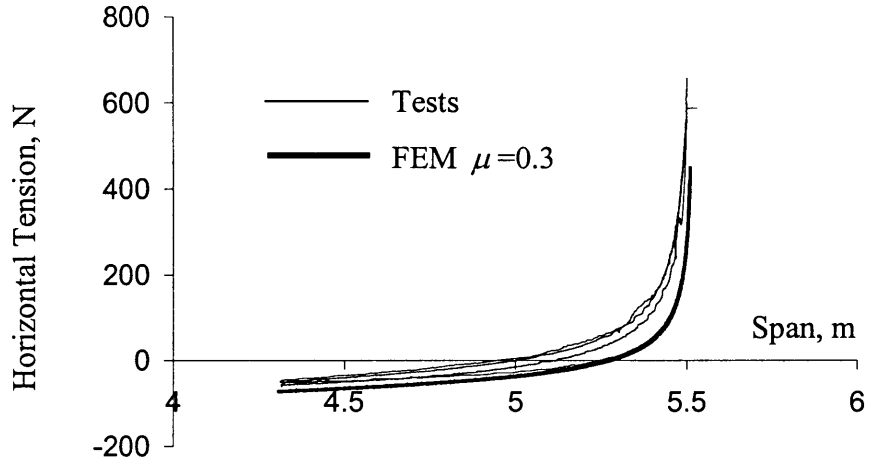

Figure 4.13 Horizontal tension vs. span length of the 1796MCM conductor

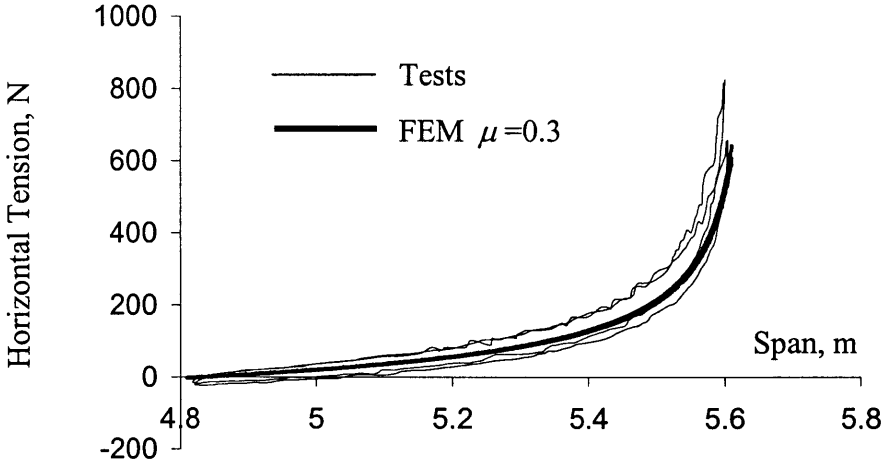

Figure 4.14 Horizontal tension vs. span length of the 4000MCM conductor

5 DYNAMIC ANALYSIS OF CONDUCTOR CABLES AND COMPARISON WITH EXPERIMENTAL RESULTS

5.1 Introduction

In this chapter, we use the finite element model developed in Chapter 3 to perform dynamic analysis of conductor cables or cable-connected equipment systems and compare such analytical predictions with the results of tests conducted by Filiatrault and Stearns (2002) and Dastous and Pierre (1996). The analysis method used in this study is an improvement over our previous study (Der Kiureghian *et al.*, 2000, Hong *et al.* 2001), where we assumed a constant but reduced value of the moment of inertia of the conductor cable (as recommended by IEEE 1999) to approximately account for the slippage of wires. In contrast, the current analysis explicitly considers the slippage of wires in the cable and allows the moment of inertia to vary along the cable and in time, depending on the curvature and tension force of the cable at each cross section. The variation is between the moment of inertia when all the wires are in the stick state and the moment of inertia when all the wires are sliding. Recall that the ratio of the maximum to minimum moments of inertia can be as large as 100 or even larger.

Filiatrault and Stearns (2002) conducted shake-table tests on cable-connected, idealized equipment items with varying characteristics. Comparisons are made for the equipment displacements and cable forces for three of their systems with varying cable slackness. Dastous and Pierre (1996) conducted tests on a horizontal conductor cable subjected to out-of-phase harmonic end displacements. For their test, comparisons are made between the measured and predicted time histories of the cable force at one end. Due to the complexity of the problem, close agreement between experimental observations and theoretical predictions cannot be expected and are not achieved. However, the general trends and response magnitudes are in fair agreement. Possible reasons for the discrepancy between the test results and analytical predictions are discussed.

The following section in this chapter describes the finite element model used in the dynamic analysis. Comparisons with the experimental results of Filiatrault and Stearns (2002) are described in Section 5.3. Section 5.4 describes the comparisons with the experimental results of Dastous and Pierre (1996).

5.2 Finite Element Model of the Cable

The conductor cable in each test is idealized with 100 frame elements, as described in Chapter 3, accounting for the elasto-plastic constitutive model that represents the nonlinear bending behavior of the cable, and for large rotations and displacements. As described in Section 3.3.2 of Chapter 3, the elasto-plastic constitutive model is determined by fitting to the nonlinear moment-curvature-tension relationship of the cable that is determined according to the theory developed in Chapter 2. Table 5.1 summarizes the properties of the Lupine conductor cable used by Filiatrault and Stearns (2002) in their tests. Figure 5.1 shows the nonlinear bending behavior of this cable. The top plot shows the relationship between the secant bending stiffness and the curvature of the cable for different axial strains, and the bottom plot shows the relationship between the normalized bending moment and the normalized curvature. The fitting parameters for this cable are listed in Table 3.1. Dastous and Pierre (1996) used the 1796MCM conductor cable in their dynamic tests. The moment-curvature relationships of this cable are shown in Figure 4.3 and the fitting parameters are listed in Table 3.1.

The dynamic analysis of a cable with large displacements and rotations is a highly nonlinear problem that has no known analytical solution. In our previous study with an elastic model of the cable (Der Kiureghian *et al.*, 2000, Hong *et al.* 2001), we used a modified version of the energy-conserving algorithm (Simo *et al.* 1995) for time-integration. The modification introduced numerical damping in the algorithm to stabilize the computations, while slightly compromising on the conservation of energy law. In the present study, the cable behavior in bending is inelastic, in account of consideration of the wire slippage, and this makes the numerical integration problem a lot harder. Unfortunately, the energy-conserving algorithm cannot be used for this problem, since it was designed for elastic problems. To the author's knowledge, there is no time-stepping algorithm that is proven to be unconditionally stable for the cable dynamic problem, where both geometric nonlinearity and plastic behavior are present. Therefore, as a trial, we selected to use the HHT algorithm (Hilber, Hughes and Taylor, 1977). This algorithm is widely used in nonlinear structural dynamics, but it does not guarantee an unconditionally stable solution. Our experience has shown that the HHT algorithm with parameter values $\alpha = 0.55$, $\beta = 0.5$ and $\gamma = 1$ (see Section 3.2.5 for the definitions of these parameters) and time step $\Delta t = 0.0005$s works well for computing the displacements in the plasto-dynamic cable problem. However,

when computing cable forces, instability was observed when the cable moment of inertia approached its minimum value, i.e., that corresponding to fully sliding wires. This was especially the case for relatively taut cables. In that state, there is a great mismatch between the bending and axial stiffnesses of the cable, and this, we believe may be the source of the instability. We note that the cable force is a derivative quantity and, therefore, is more sensitive to numerical instability than the displacement response.

To resolve the numerical instability in the computation of the cable force, we artificially increased the minimum moment of inertia of the cable. Thus, instead of $I_{\min}$, we used $mI_{\min}$ as the lower bound of the moment of inertia, where $1 \le m$. Starting with $m = 20$, repeated analyses were carried out while gradually decreasing the value of m. The smallest values of m that provided stable solutions for the cable force was used to determine the lower bound moment of inertia for the analysis reported later in this chapter. Our analysis showed that $m = 1$ was adequate for cables having 10% or more slackness, whereas $m = 5$ was necessary for cables with 5% slackness and $m = 10$ was necessary for cables with 2% slackness to achieve numerical stability in computing the cable force. (The definition of slackness is given below.) Recall that the ratio $I_{\max} / I_{\min}$ is of the order of 100. Thus, the adopted values of m still allow significant inelastic action in the cable. This modification was made only in computing the cable force. Displacement responses were all computed using $I_{\min}$ as the lower bound of the moment of inertia.

As described in Section 4.2, the initial state of the conductor cable in each test remains unknown. We have used the following steps to set the initial shape of the cable for the analyses in this chapter: A straight cable of the specified length is modeled with both ends fixed. The weight of the cable is applied as dead load and the cable is allowed to deform. One end of the cable is then moved towards the other end until the specified distance between the stand-alone equipment items or support points in the experiment is achieved. The deformed shape of the cable in this position is computed. This shape is considered to be the initial shape of the cable without any internal forces. The cable with this shape is now placed between the equipment items or the fixed supports and the reaction forces under the weight of the cable are computed. It is noted that, in the case of a cable connected between two equipment items, a small displacement of each equipment item under the cable weight occurs, so that the resulting initial span of the cable is slightly smaller than the initial distance between the stand-alone equipment items.

As we discussed in Section 4.2, there are several approximations inherent in our theoretical model of the cable, which may affect the accuracy of the predicted results. One is the neglect of the effect of shear force (variation in bending moment) on the slippage of wires. Another is the neglect of inelastic deformation in the wires, which may occur at points of high curvature, typically near the end points of the cable. No external transverse loads were applied on the cable in these experiments. However, unaccounted friction forces between the wires may have existed near the end points, where the cable is encased in a clamping bracket.

As a final consideration, it is noted that a slack cable has an extremely complex dynamic behavior. Small variations in the initial configuration, support conditions, or the input excitation may cause large changes in the response. For such a system, a close quantitative agreement between theoretical predictions and experimental results is inherently difficult to achieve. For such an agreement to occur, it is not only necessary to develop a highly accurate model and requisite numerical techniques, but also conduct extremely careful and well controlled experiments.

5.3 Comparison with Experimental Results of Filiatrault and Stearns

Figure 5.2 shows the test setup used by Filiatrault and Stearns (2002). Two poles were installed on the shake table and a lumped mass was loaded at the top of each pole. These represented "equipment" items. The top masses and pole stiffnesses were selected so as to achieve prescribed equipment natural frequencies and effective masses. A connecting conductor cable was installed between the two masses, as shown in Figure 5.2, such that the cable ends were at the same elevation. In the figure, $u_1(t)$ and $u_2(t)$ are the horizontal displacements of the two masses relative to the table, $T_1(t)$ and $T_2(t)$ are the forces in the cable at the connection points, and $x_g(t)$ is the displacement of the shake table during the test. The system was subjected to scaled versions of several recorded ground motions. Measurements were made of the displacement of each mass and the force in the cable at each connection point.

Among the several systems tested by Filiatrault and Stearns (2002), equipment combination 2 was selected for the comparison. The dynamic characteristics of the individual "equipment" items in this system, obtained by shaking them individually, are listed in Table 5.2. These include the fundamental frequency, the seismic mass, and the damping ratio. In the analytical model, each equipment item is modeled as a single-degree-of-freedom oscillator having the

characteristics listed in Table 5.2. It is noted that the equipment items have small damping ratios. The two masses were connected by a single Lupine conductor cable. The connected system was subjected to the Tabas (Iran 1978) accelerogram, scaled at 50%. Figure 5.3 shows the measured table motion for one of the tests. In the FEM analysis, the actual measured table motions were used as input. The single-degree-of-freedom models employed for the test equipment do not account for the effect of rotation at the top masses, which would tend to rotate the ends of the cable. We believe the contribution of this effect is negligible. No damping in the cable other than that resulting from the slippage of wires and represented by the elasto-plastic bending model is assumed.

The system described above was tested with connecting cables having 10%, 5% and 2% slackness, where slackness is defined as

$$\text{Slackness} = \frac{s_0 - c_0}{c_0} \tag{5.1}$$

with s_0 denoting the initial cable length and c_0 denoting the initial distance between the attachment points. In all three experiments, the cable length is $s_0 = 4.572$ m (=15 ft). The slackness is changed by adjusting the distance between the equipment items.

We first consider the test with the connecting cable having 10% slackness. Figures 5.4 and 5.5 compare the test and finite element (FEM) predictions of the displacement time histories of the lower and higher frequency equipment items, respectively. In Figure 5.4 for the lower frequency equipment item, the overall shape of the time histories as well as the peak responses are in fair agreement. The comparison is not as good for the higher frequency equipment item, shown in Figure 5.5, where the FEM predicted response has smaller peaks and higher frequency content. It is noted that the FEM predicted displacements start from small non-zero values. These are the initial displacements of equipment items due to the weight of the cable. These displacements are not included in the test measurements.

Figures 5.6 and 5.7 compare the test and FEM results for the horizontal components of the cable force at the attachment points to the lower and higher frequency items, respectively. The FEM predictions start from a non-zero value, indicating the tension force in the cable under static conditions. The test results do not include this initial force. Significant discrepancies between the test and FEM results are evident. Nevertheless, several noteworthy characteristics are

common to both the test results and the FEM predictions. For example, it is noted that the cable experiences significant compressive forces at both ends, with force magnitudes as large as in tension. This is attributed to the flexural stiffness and the horizontal mass inertia of the cable, since an ideal cable (i.e., one having zero flexural stiffness) with no horizontal inertia forces cannot take compression forces. The second noteworthy observation is the large difference in the magnitudes and frequency contents of the forces acting at the two ends of the cable. This again is attributed to the flexural stiffness and the horizontal mass inertia of the cable, since for an ideal cable under vertical loads, the horizontal component of the cable force is a constant at all points along the cable. The frequency content in the cable force at each end is clearly affected by the frequency of the attached equipment. This is an indication of the interaction occurring between each equipment item and the cable.

Next we consider the system with the connecting cable having 5% slackness. The test and FEM-predicted displacement responses of the lower and higher frequency equipment items are compared in Figures 5.8 and 5.9, respectively. Significant discrepancies between the test results and FEM predictions are evident in these figures. But again some common features can be observed. For example, compared to the system with 10% cable slackness, both test results and FEM predictions for the system with 5% cable slackness indicate a smaller displacement of the lower frequency equipment and a larger displacement of the higher frequency equipment. This is a consequence of the enhanced interaction between the equipment items as the cable slackness is reduced. Figures 5.10 and 5.11 compare the test and FEM predictions of the horizontal cable force at the attachment points to the lower and higher frequency equipment items, respectively.

As mentioned earlier, for taut cables, the calculation of the cable force becomes unstable when the flexural stiffness becomes too small in relation to the axial stiffness. To achieve numerical stability in computing the cable force for the case of 5% slackness, it was necessary to use $5I_{\min}$ as the lower bound of the moment of inertia. While the details of the force time histories in Figures 5.10 and 5.11 are quite different, the peak values predicted by FEM are in fair agreement with the test results. More importantly, both test results and FEM predictions indicate significantly larger forces as the cable slackness is reduced. This can be seen by comparing Figures 5.6 and 5.10 and Figures 5.7 and 5.11. It is important to note that, in case of small slackness, the cable force under dynamic loading can be extremely large. For example, in the case of 5%

cable slackness, the maximum dynamic tension force in both the experiment and FEM prediction is more than one order of magnitude greater than the static tension force, which is shown in the FEM predictions at time zero in Figures 5.10 and 5.11.

Next we consider the system with the connecting cable having 2% slackness. The test and FEM-predicted displacement responses of the lower and higher frequency equipment items are compared in Figures 5.12 and 5.13, respectively. Again significant discrepancies between the details of the test results and FEM predictions are evident, but common features can also be observed. One interesting common observation is that, for this small value of the cable slackness, the equipment items experience larger displacements towards the cable than away from the cable, so that the displacement time histories do not have zero averages. Obviously, with the taut cable, the equipment items are prevented from moving away from one another. When that happens, the cable is jerked and it exerts large tension forces on the equipment. This is evident in Figures 5.14 and 5.15, which compare the test results and FEM predictions of the horizontal cable force at the points of attachment to the lower and higher frequency equipment items, respectively. These were computed using $10I_{\min}$ as the lower bound of the moment of inertia. As can be seen in these figures, the jerking effect produces tension forces as large as 7 kN, as measured in the test, or 10 kN as predicted by the FEM model. These forces are much larger than the corresponding forces measured or predicted for the systems with 10% and 5% cable slackness, and represent nearly two orders of magnitude amplification relative to the static cable force. Another interesting observation, which is common to the test results and FEM predictions, is that the cable forces at the two ends are nearly identical when the cable is taut. This can be seen by comparing Figures 5.14 and 5.15. We believe this effect is due to a less prominent influence of the horizontal cable inertia, when the cable is taut.

Table 5.3 summarizes the peak values of the displacement and force responses for the three cases described above, as measured in the tests and predicted by FEM analyses. While close agreement between the numerical values cannot be observed, the trends between the test results and FEM predictions are in agreement. In particular, in both the test and FEM results, we see a reduction in the peak displacement of the lower frequency equipment item and an increase in the peak response of the higher frequency equipment item, as the cable slackness is reduced. This is an indication of enhanced interaction between the equipment items. We also see sharp

increases in the cable tension force in both the test and FEM results as the cable slackness is reduced.

Many factors may have contributed to the observed discrepancy between the test measurements and FEM predictions described above. As mentioned earlier, the dynamic response of a flexible cable is highly nonlinear and sensitive to model parameters and details of the excitation. Significant unknowns are present in the experiments, which we are unable to account for in our FEM predictions. Among these are the initial shape and condition of the cable, possible out-of-plane motions of the cable, uncounted sources of energy dissipation (e.g., in connections between the cable and equipment items, damping in the cable material other than that due to slippage of wires), and possible yielding of the wires. Undoubtedly, approximations inherent in our analytical model, including the modified lower bound moment of inertia, which was employed to avoid numerical instability in the calculation of the cable force, and the single-degree-of-freedom idealization of equipment items, have contributed to the discrepancy. Determining the relative importance of these factors would be a valuable lesson in planning future tests with conductor cables. However, the limited scope of this study prevents us from conducting such a sensitivity analysis at this time.

5.4 Comparison with Experimental Results of Dastous and Pierre

Dastous and Pierre (1996) conducted experiments with horizontal conductor cables subjected to out-of-phase, harmonic end motions. A schematic of their test setup is shown in Figure 5.16. A pair of actuators was used to impose prescribed horizontal harmonic motions at the two ends of the cable in opposing directions. The actuator forces, which are identical to the horizontal cable forces at each end, were measured during the displacement-controlled test. In some of their tests, Dastous and Pierre observed a "resonant" state, where the cable response was quite chaotic. In other cases, they observed a "dynamically stable" response state. For the comparison purposes in this study, we have selected one of the latter cases involving a 1796MCM conductor cable of length 5.52m and 5.19m span, which correspond to 6.4% slackness. The characteristics of this cable were presented in Table 4.2 and Figure 4.3. During the test, the cable was subjected to out-of-phase harmonic support motions of amplitude 0.02m and 3.5Hz frequency. Figure 5.17, taken from Dastous and Pierre (1996), shows the time history of the actuator force at one support measured during the experiment. Note that the actuator force at the other support is approxi-

mately the same since the boundary conditions on the cable are symmetric. It is noted that the initial cable force is around 40N in tension. During the test, the horizontal cable force at each support fluctuates, taking both positive (tension) and negative (compression) values.

In the finite element analysis, an out-of-phase, harmonic horizontal support displacements of the form

$$u(t) = \left[1 - \exp(-2\pi\alpha f t)\right] A \sin(2\pi f t) \tag{5.2}$$

is applied at each end, where $A = 0.02$ m is the amplitude and $f = 3.5$ Hz is the frequency. The term inside the square brackets is a loading ramp that is included to avoid numerical instability caused by non-zero initial conditions. For the present analysis, $\alpha = 0.1$ is used. Note that the term inside the square brackets approaches unity in a few cycles and the motion becomes purely harmonic.

In our previous study (Der Kiureghian *et al.* 2000, Hong *et al.* 2001), an elastic finite element model having the moment of inertia calculated by the IEEE guideline recommendation (IEEE 1999) was used to simulate the test. In the elastic model, it was assumed that the moment of inertia of the cable remained constant throughout the length of the cable at all times. In the present study, we use the elasto-plastic model developed in Chapters 2 and 3. It is interesting to compare the two analytical results obtained with the elastic and the elasto-plastic finite element models. In the elastic finite element model, a constant moment of inertia of $5I_{\min}$ was used, where the coefficient 5 was obtained from the IEEE guideline for the 1796MCM conductor cable with 4 layers of wires. In contrast, in the elasto-plastic finite element model, the moment of inertia varies from $5I_{\min}$ (the modified lower bound used to assure numerical stability in the tension force in the cable) to $I_{\max}$, depending on the curvature and tension force of the cable.

Figure 5.18 shows plots of the time history of the horizontal cable force, as predicted by the elastic (gray line) and elasto-plastic (black line) models. The two predicted results are nearly the same. This is because in the elasto-plastic cable the moment of inertia remains close to its lower bound most of the time, i.e., the cable is responding with its wires mostly in the fully slipping state. It appears, therefore, that elastic analysis with the lower bound moment of inertia can be used as an approximation to account for the effect of wire slippage. However, our investigations have shown that this approximation does not work well in cables under high tension or cables with large diameters and many layers of wires. In such cables, the yield bending moment

can be quite large and there can be significant dissipation of energy from slippage of wires under high friction forces. An example for such a case is investigated in Chapter 6.

Comparing Figures 5.17 and 5.18, we find the overall features of the predicted cable force to be in good agreement with the test results, though the peak force values are considerably different. Both test and theory indicate large amplifications of the cable force under dynamic conditions, relative to the initial static cable force. It is noteworthy that the cable experiences significant compression forces, as measured in the test and predicted by the FEM analysis. Reasons for the discrepancy between the experimental result and the FEM predictions may include differences in the assumed initial cable shape, non-ideal support conditions, yielding of wires in the test, and the approximating assumption inherent in the theoretical model.

Table 5.1 Properties of the Lupine cable used in experiments by Filiatrault and Stearns (2002).

Property	Lupine
Young's modulus	70×10^9 N/m^2
number of layers except core	5
number of strands	91
strand diameter	4.209 mm
overall conductor diameter	46.30 mm
cross section area	1,210 mm^2
mass per unit length	3.280 kg/m
lay angle	10 degree
I_{min}	1,381 mm^4
I_{max}	160,262 mm^4
length	15 ft

Table 5.2 Dynamic characteristics of idealized equipment models used by Filiatrault and Stearns (2002).

Property	Pole 1	Pole 2
damping ratio	0.01	0.006
seismic mass	453.4 kg	158.7 kg
natural frequency	1.60 Hz	7.38 Hz

Table 5.3 Comparison of test-measured and FEM-predicted peak responses of cable-connected equipment system.

Slackness	10%		5%		2%	
	Test	FEM	Test	FEM	Test	FEM
$\max(u_1)$, m	+0.188	+0.210	+0.136	+0.208	+0.140	+0.157
$\min(u_1)$, m	−0.194	−0.198	−0.152	−0.200	−0.097	−0.115
$\max(u_2)$, m	+0.016	+0.012	+0.014	+0.015	+0.027	+0.023
$\min(u_2)$, m	−0.015	−0.012	−0.018	−0.017	−0.040	−0.034
$\max(T_1)$, N	+800.2	+315.3	+1,165.5	+1,063	+5,859.7	+10,095
$\min(T_1)$, N	−823.8	−387.6	−1,089.5	−785.9	−1,512.6	−519.4
$\max(T_2)$, N	+735.5	+448.1	+1,327.5	+1,291.9	+6,771.9	+10,109
$\min(T_2)$, N	−757.9	−285.2	−575.3	−817.5	−1,698.0	−793.0

a)

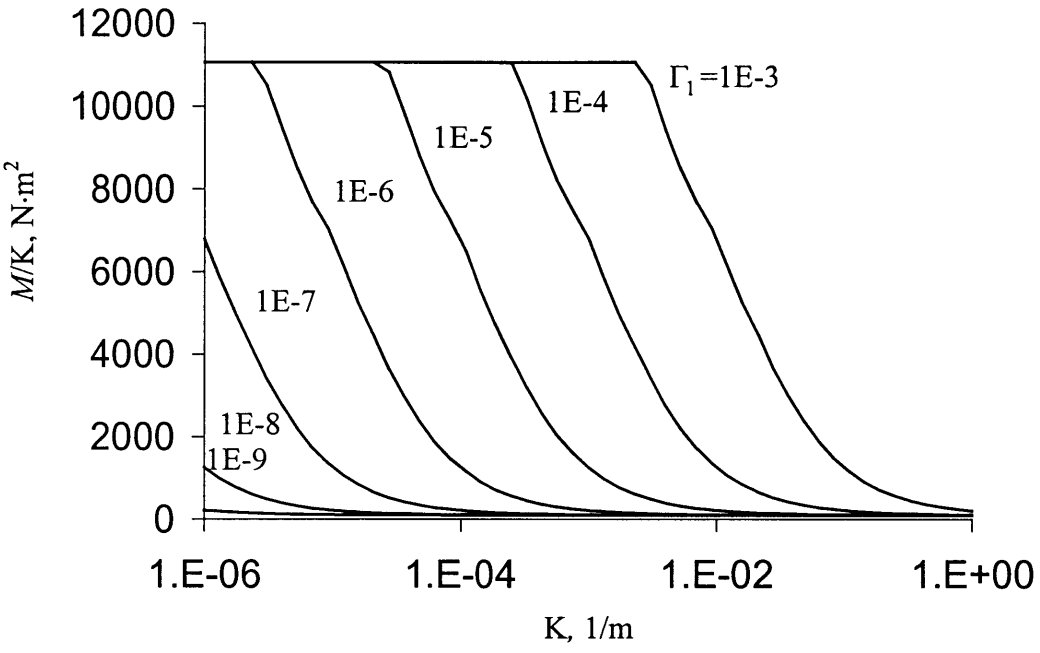

b)

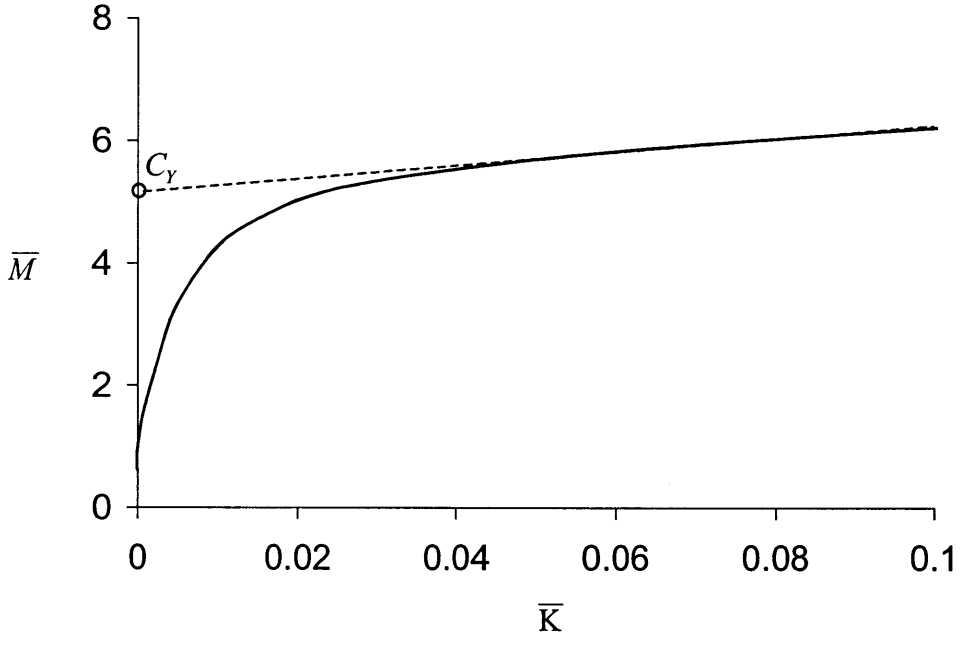

Figure 5.1 Nonlinear bending behavior of the Lupine conductor:

a) secant flexural stiffness vs. curvature for different axial strains

b) normalized moment vs. normalized curvature relation

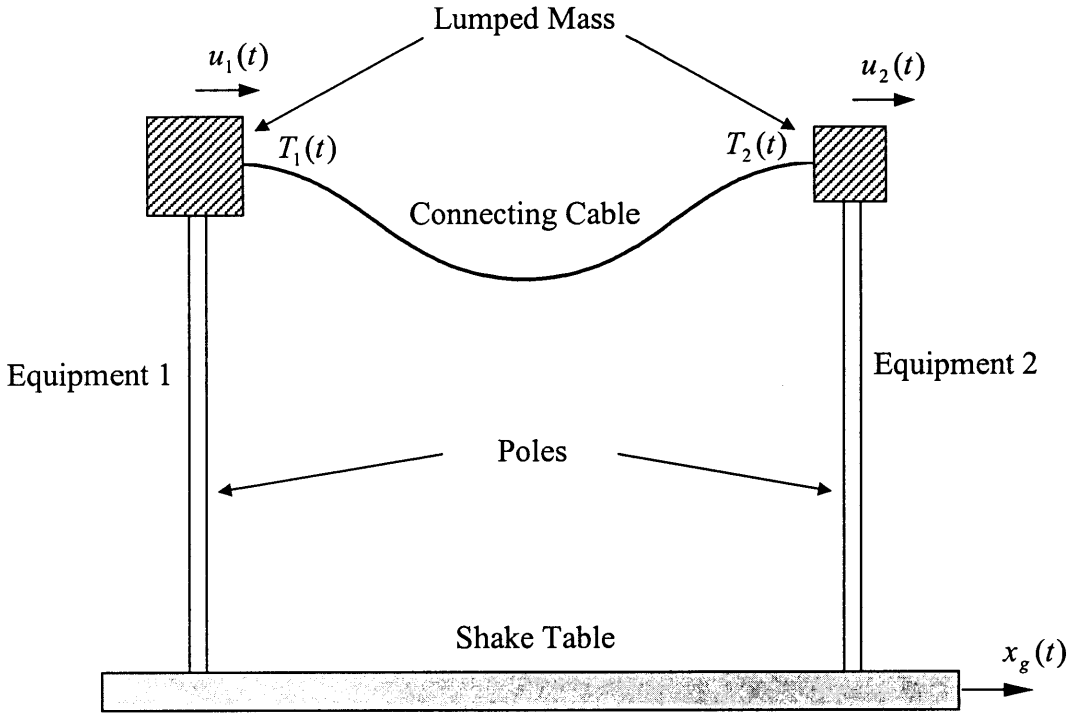

Figure 5.2 Schematic of test setup used by Filiatrault and Stearns (2002).

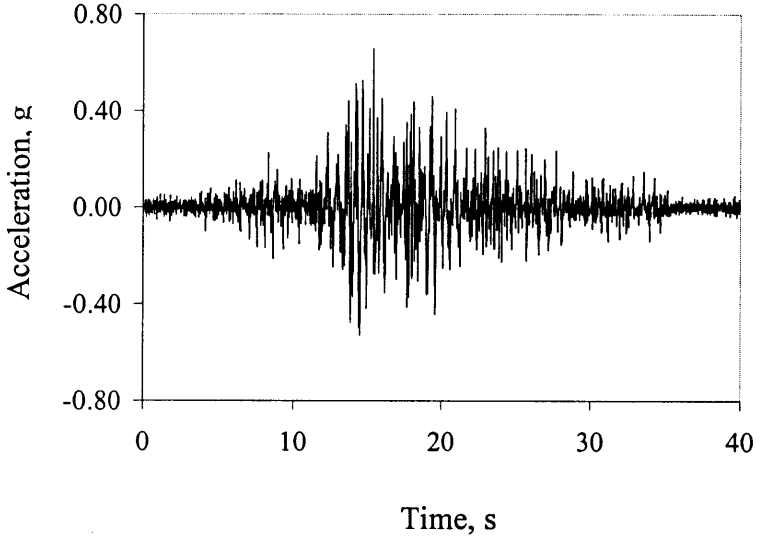

Figure 5.3 Measured table acceleration for test with 10% cable slackness

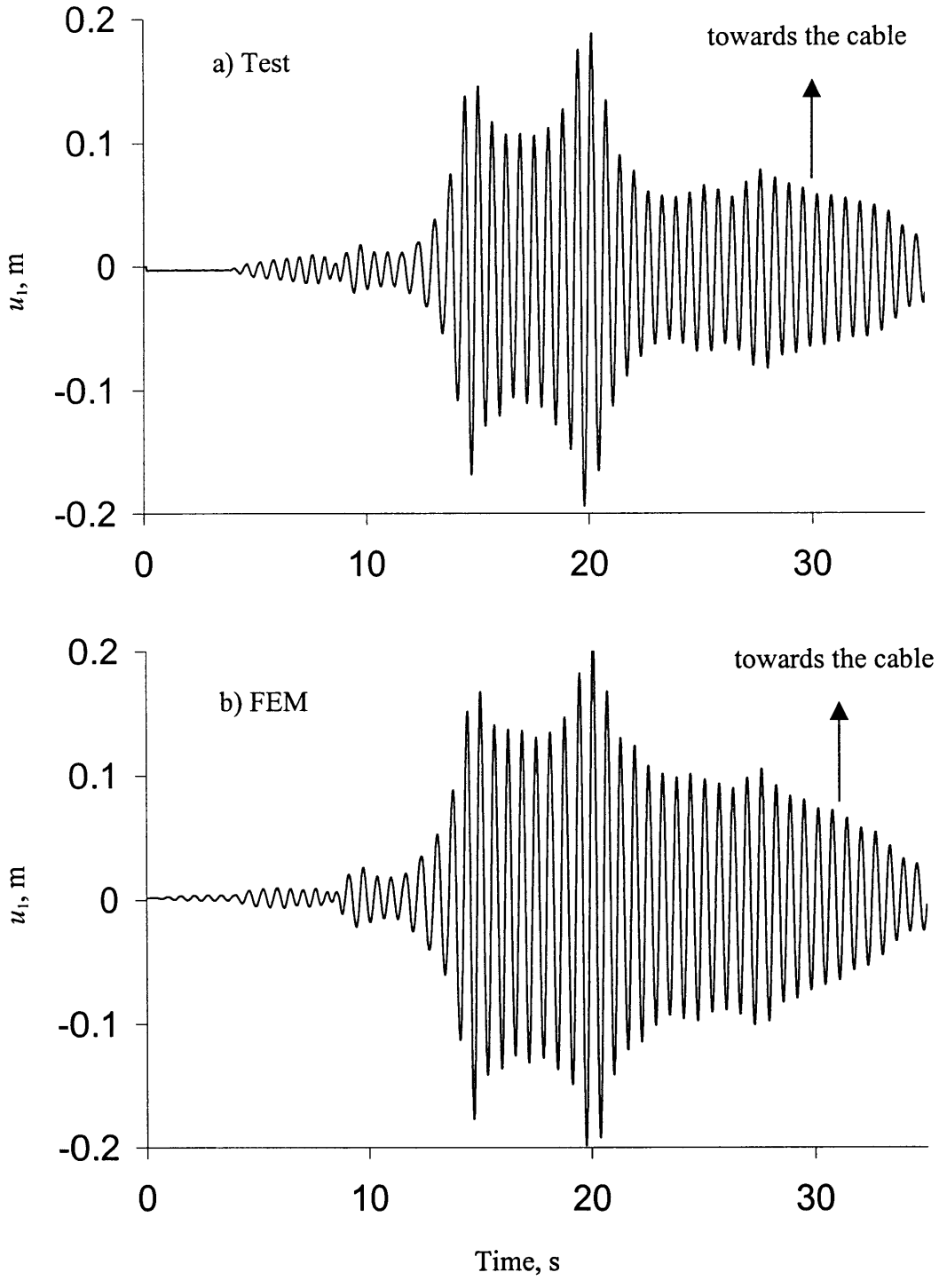

Figure 5.4 Displacement time histories of equipment 1 in system with 10% cable slackness: a) Test, b) FEM prediction.

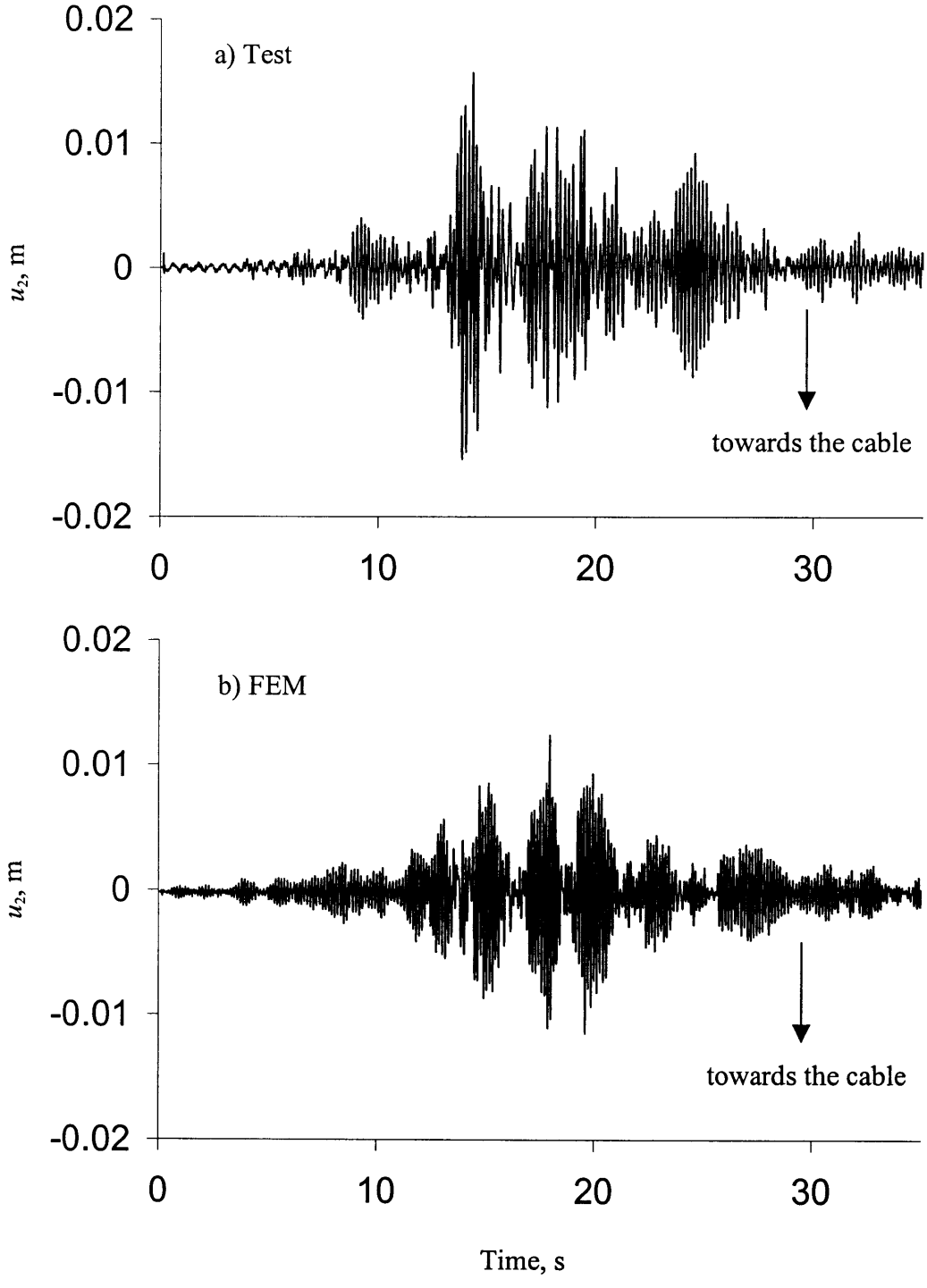

Figure 5.5 Displacement time histories of equipment 2 in system with 10% cable slackness: a) Test, b) FEM prediction.

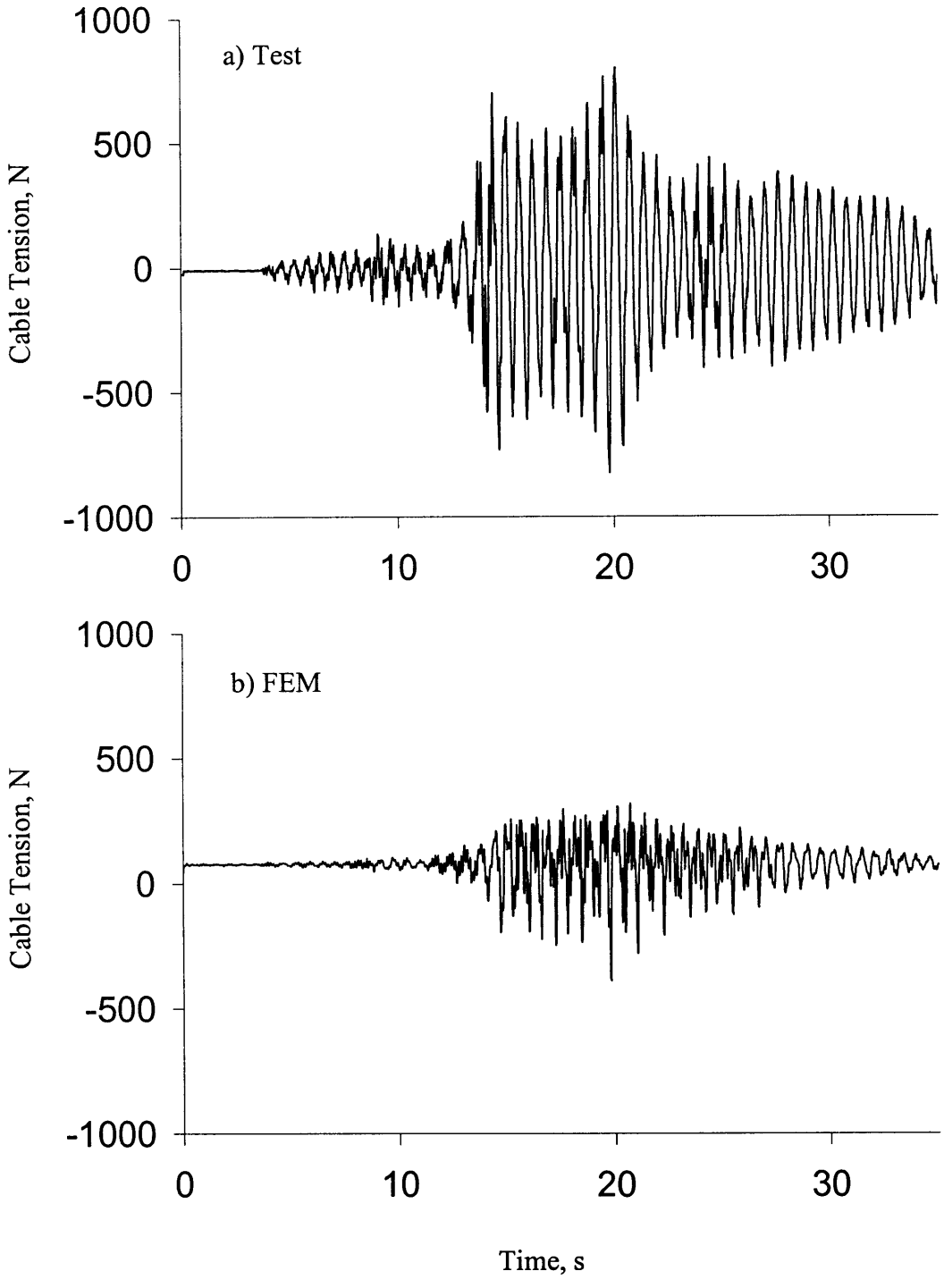

Figure 5.6 Time histories of horizontal cable force at connection to equipment 1 in system with 10% cable slackness: a) Test, b) FEM prediction

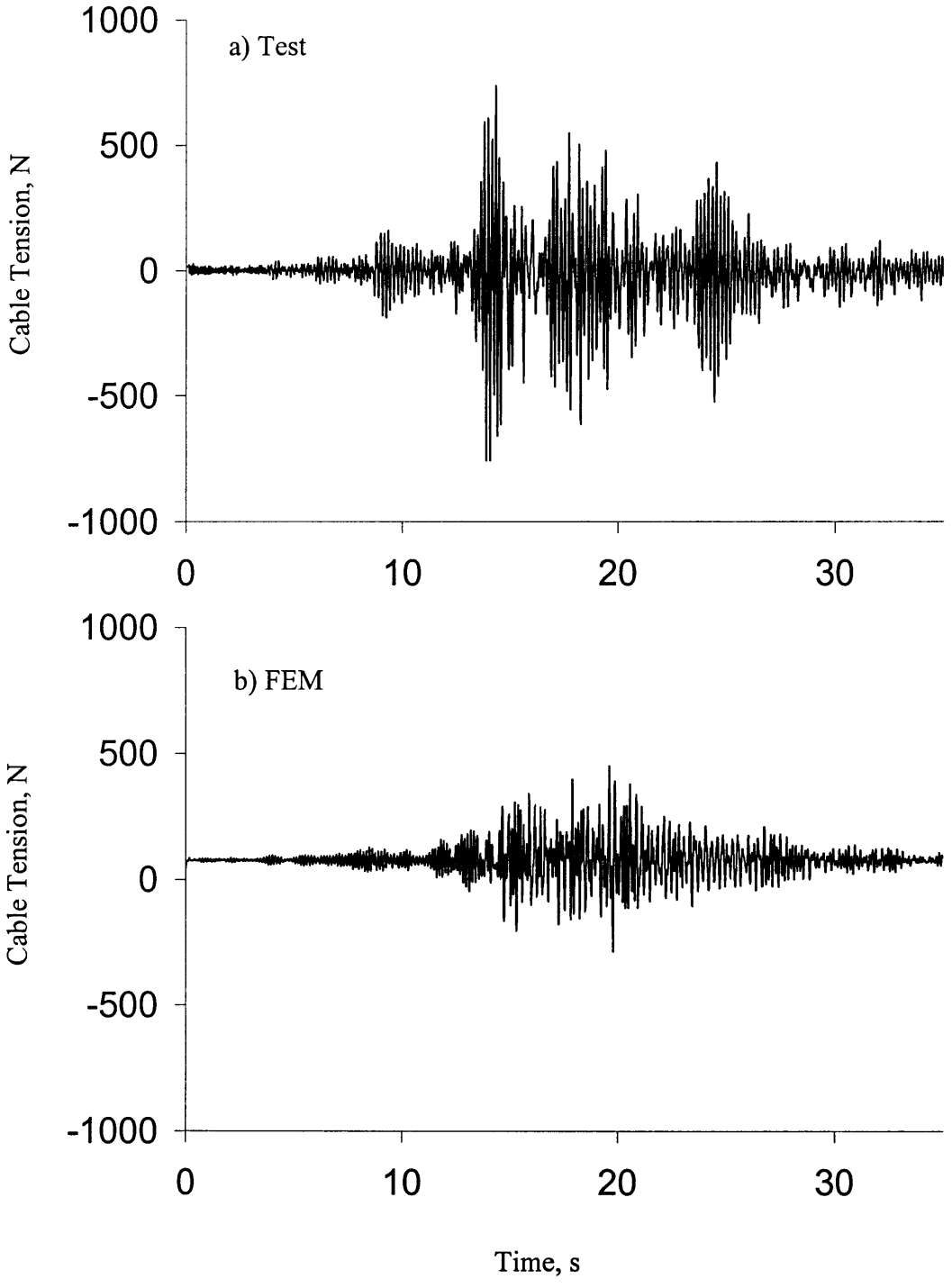

Figure 5.7 Time histories of horizontal cable force at connection to equipment 2 in system with 10% cable slackness: a) Test, b) FEM prediction

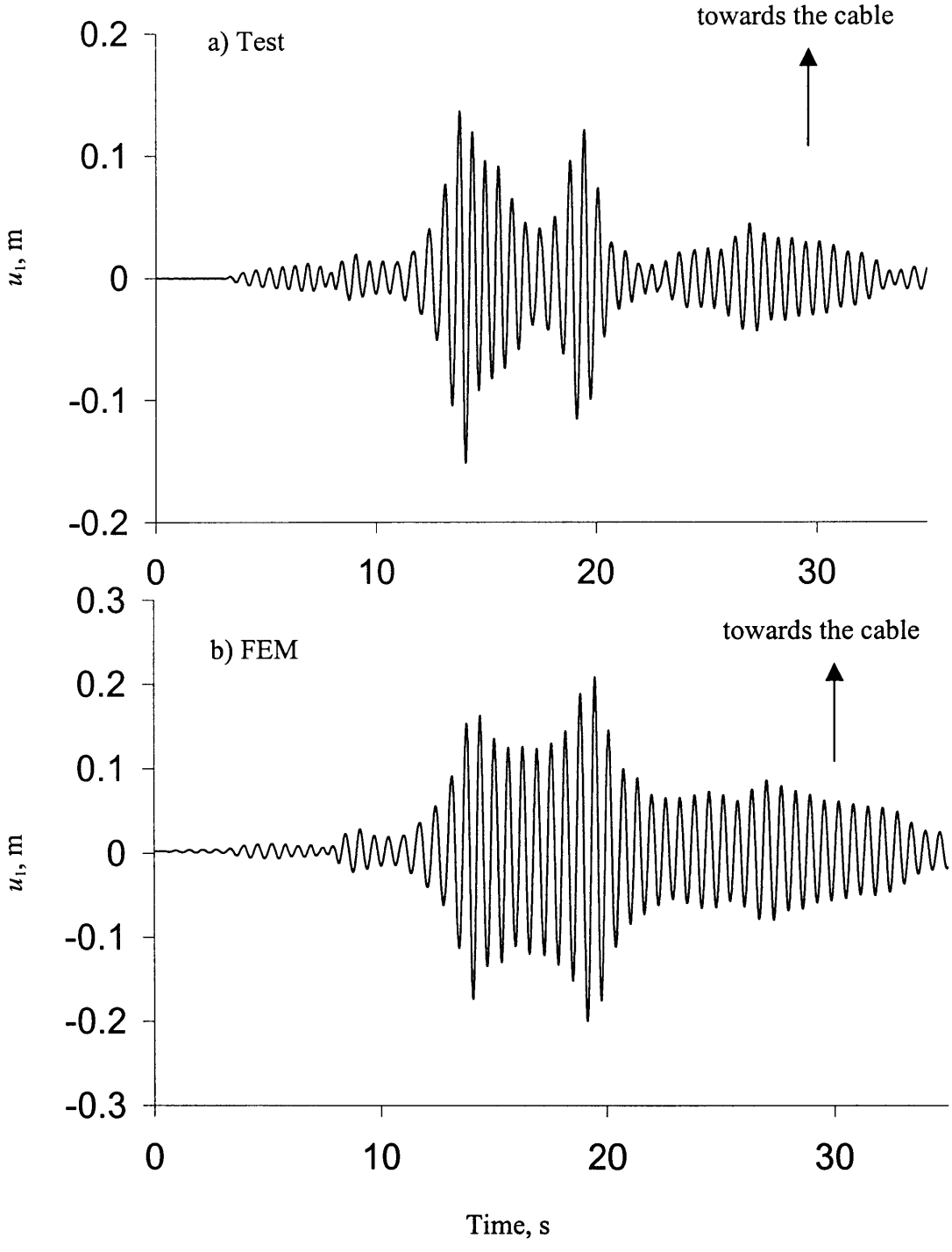

Figure 5.8 Displacement time histories of equipment 1 in system with 5% cable slackness: a) Test, b) FEM prediction.

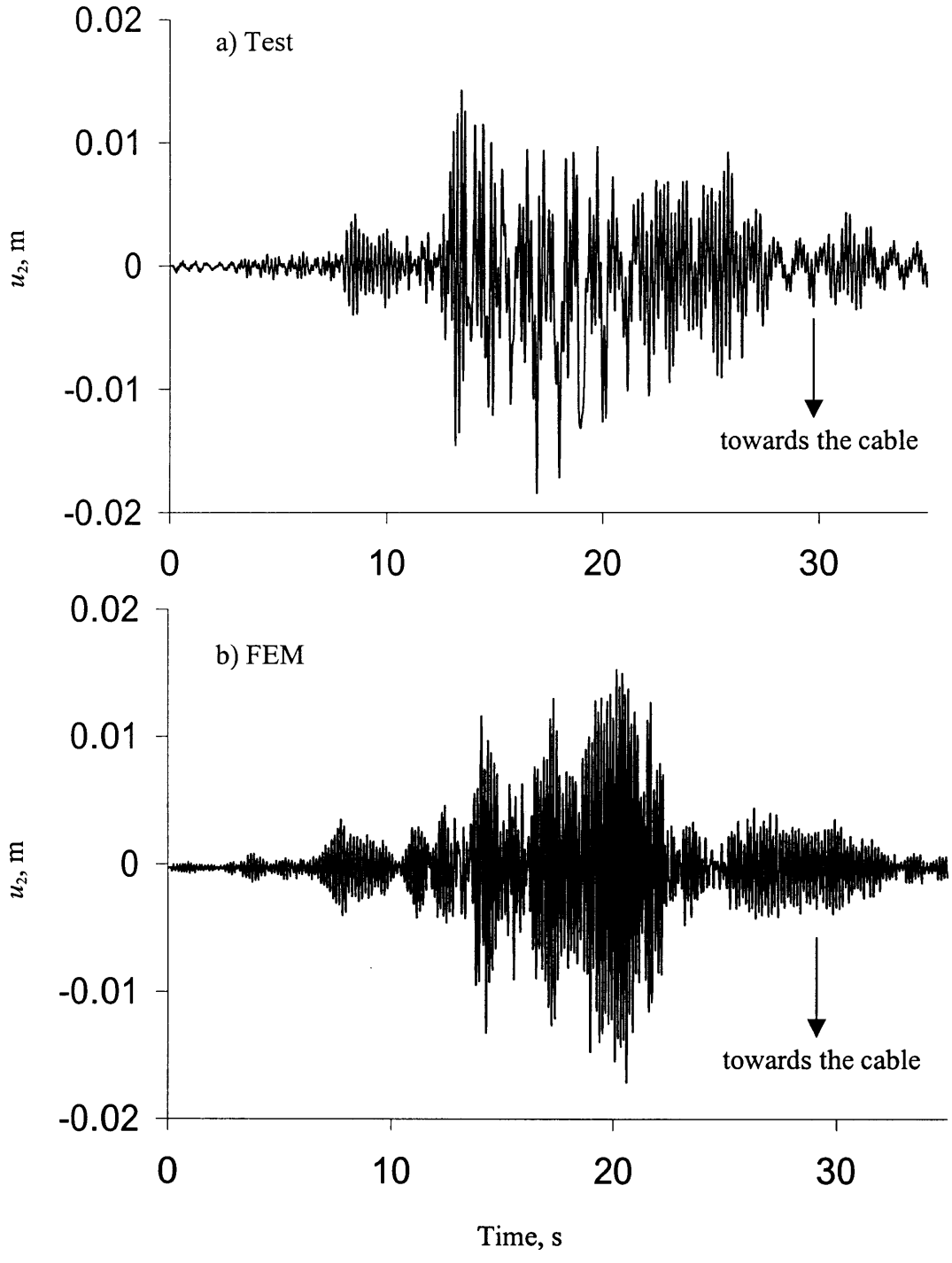

Figure 5.9 Displacement time histories of equipment 2 in system with 5% cable slackness: a) Test, b) FEM prediction.

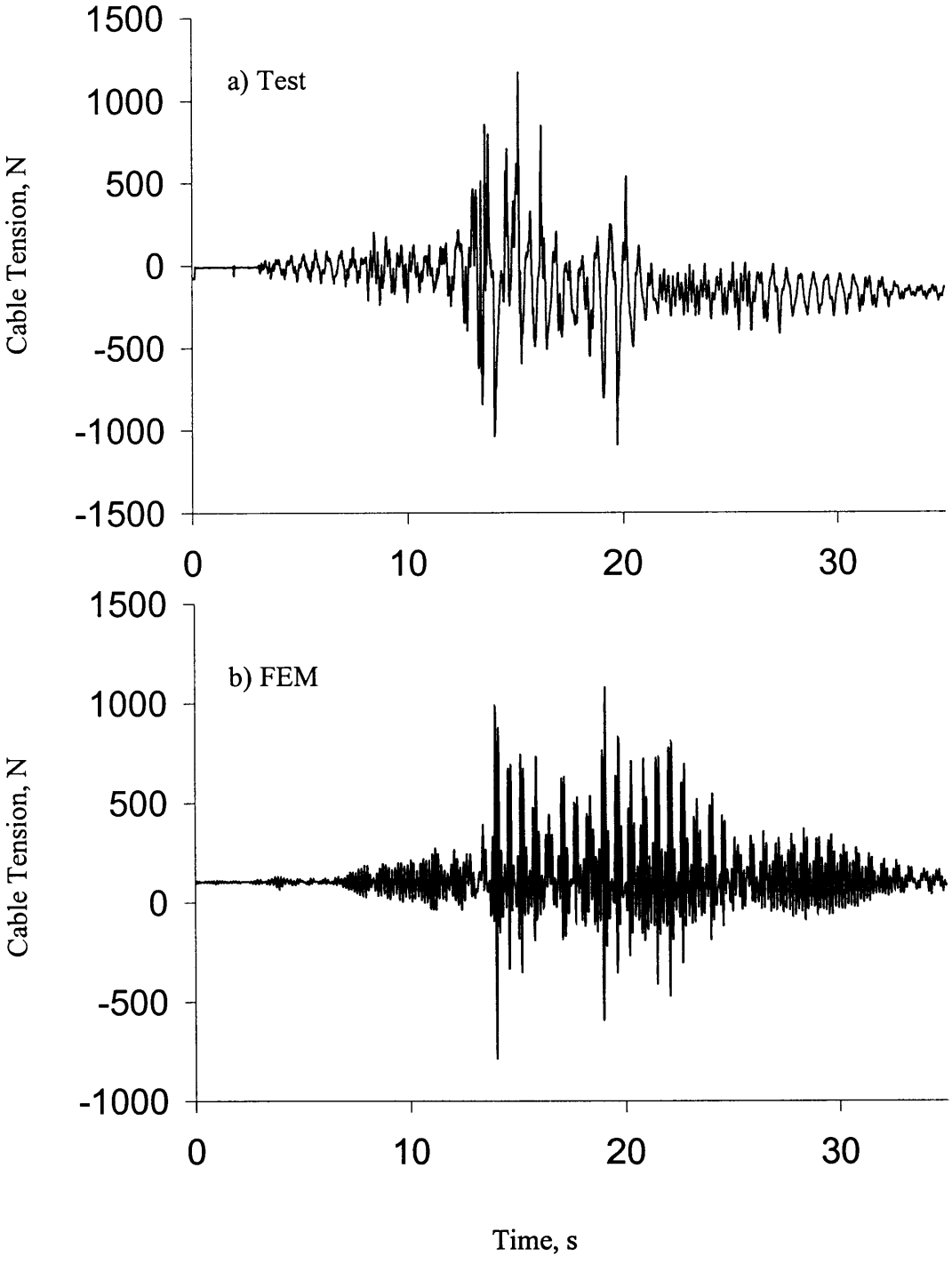

Figure 5.10 Time histories of horizontal cable force at connection to equipment 1 in system with 5% cable slackness: a) Test, b) FEM prediction

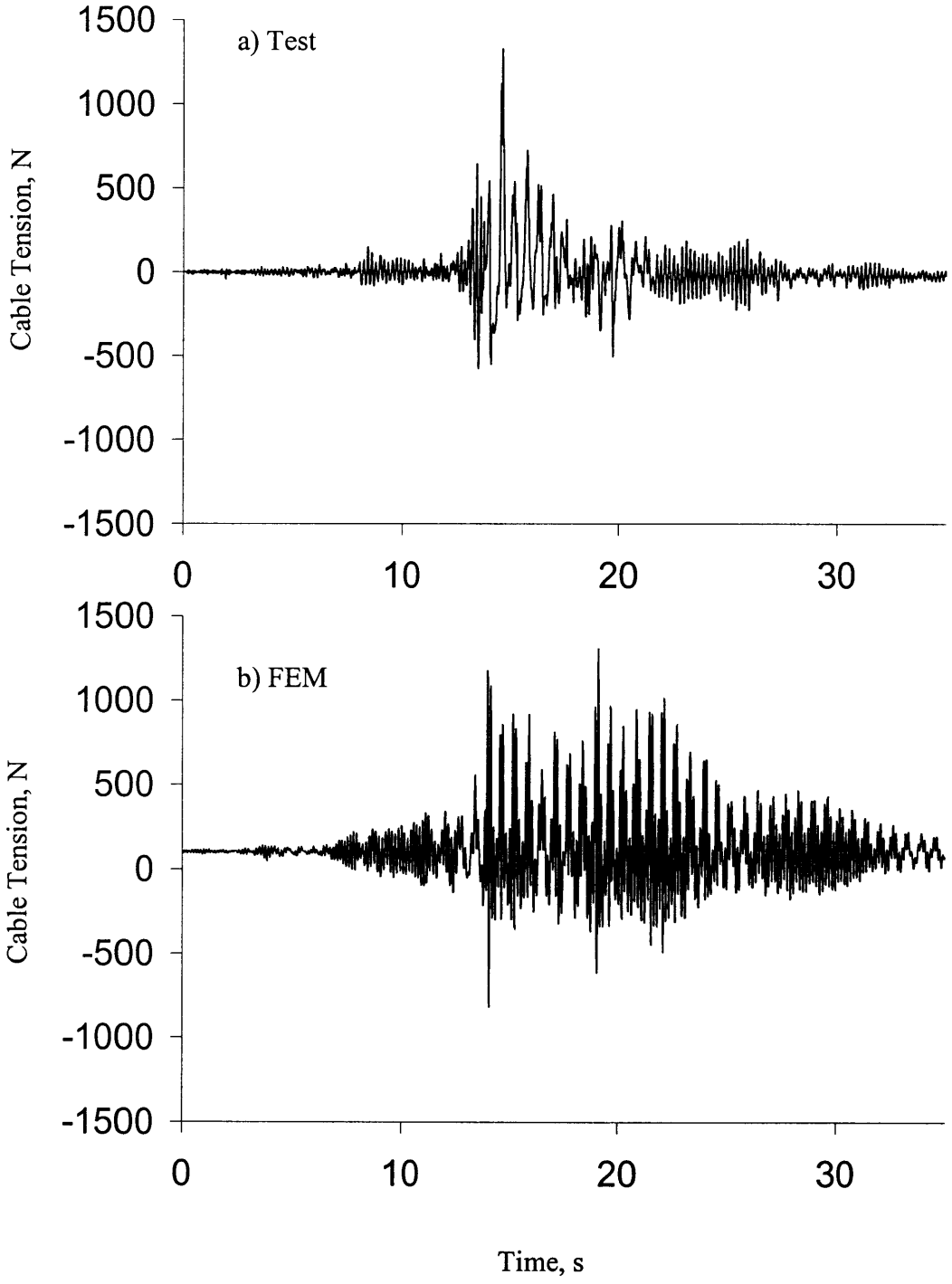

Figure 5.11 Time histories of horizontal cable force at connection to equipment 2 in system with 5% cable slackness: a) Test, b) FEM prediction

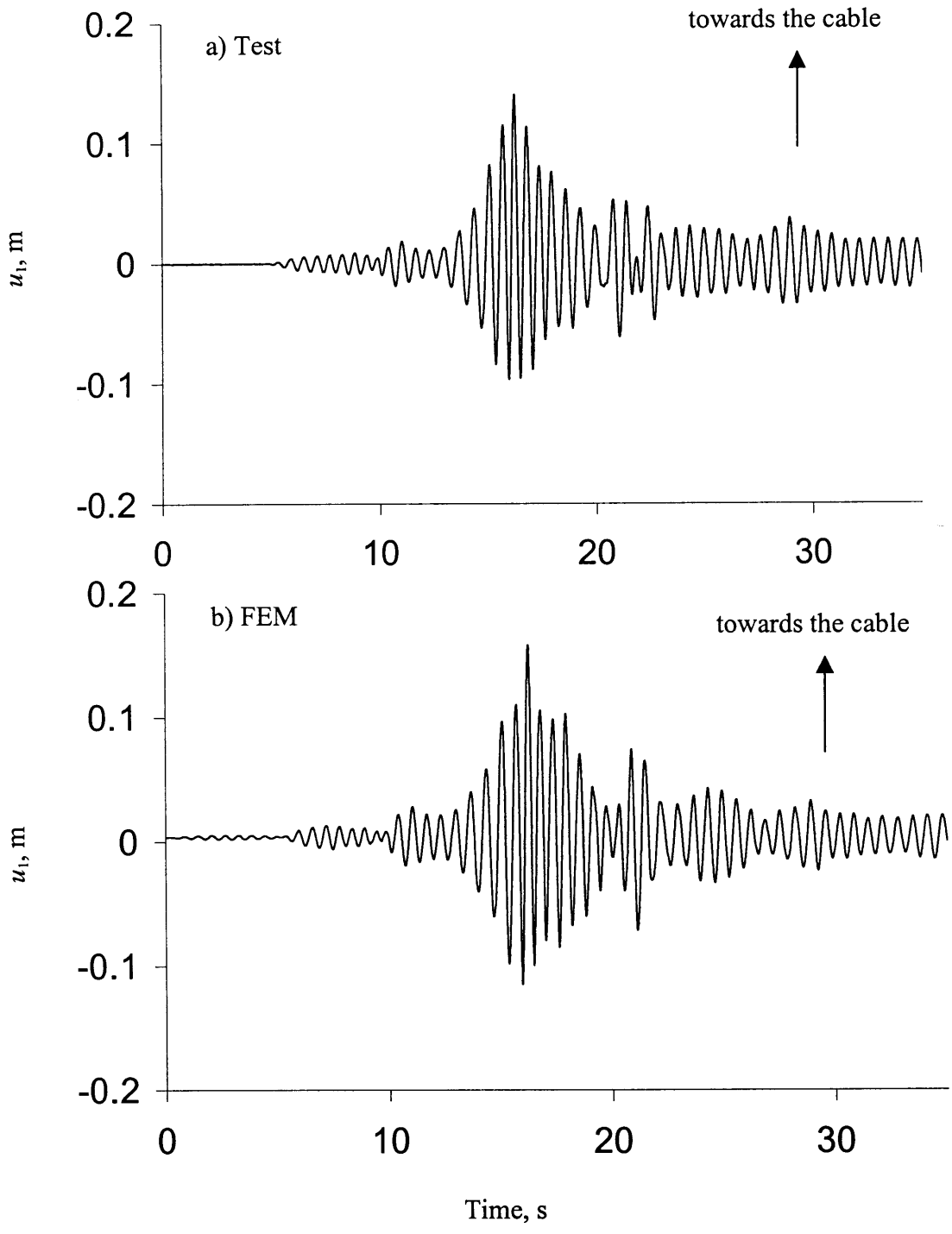

Figure 5.12 Displacement time histories of equipment 1 in system with 2% cable slackness: a) Test, b) FEM prediction.

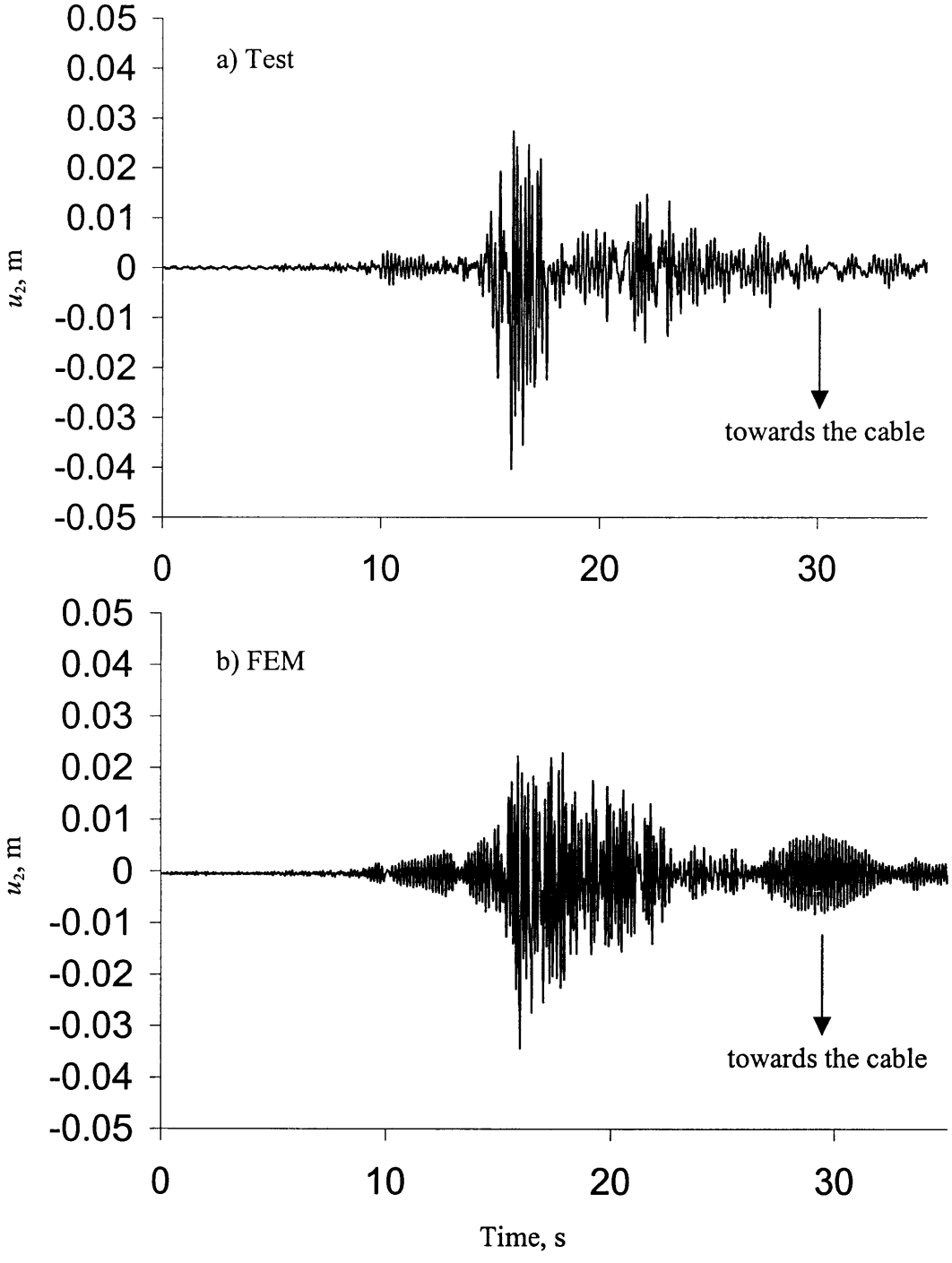

Figure 5.13 Displacement time histories of equipment 2 in system with 2% cable slackness: a) Test, b) FEM prediction.

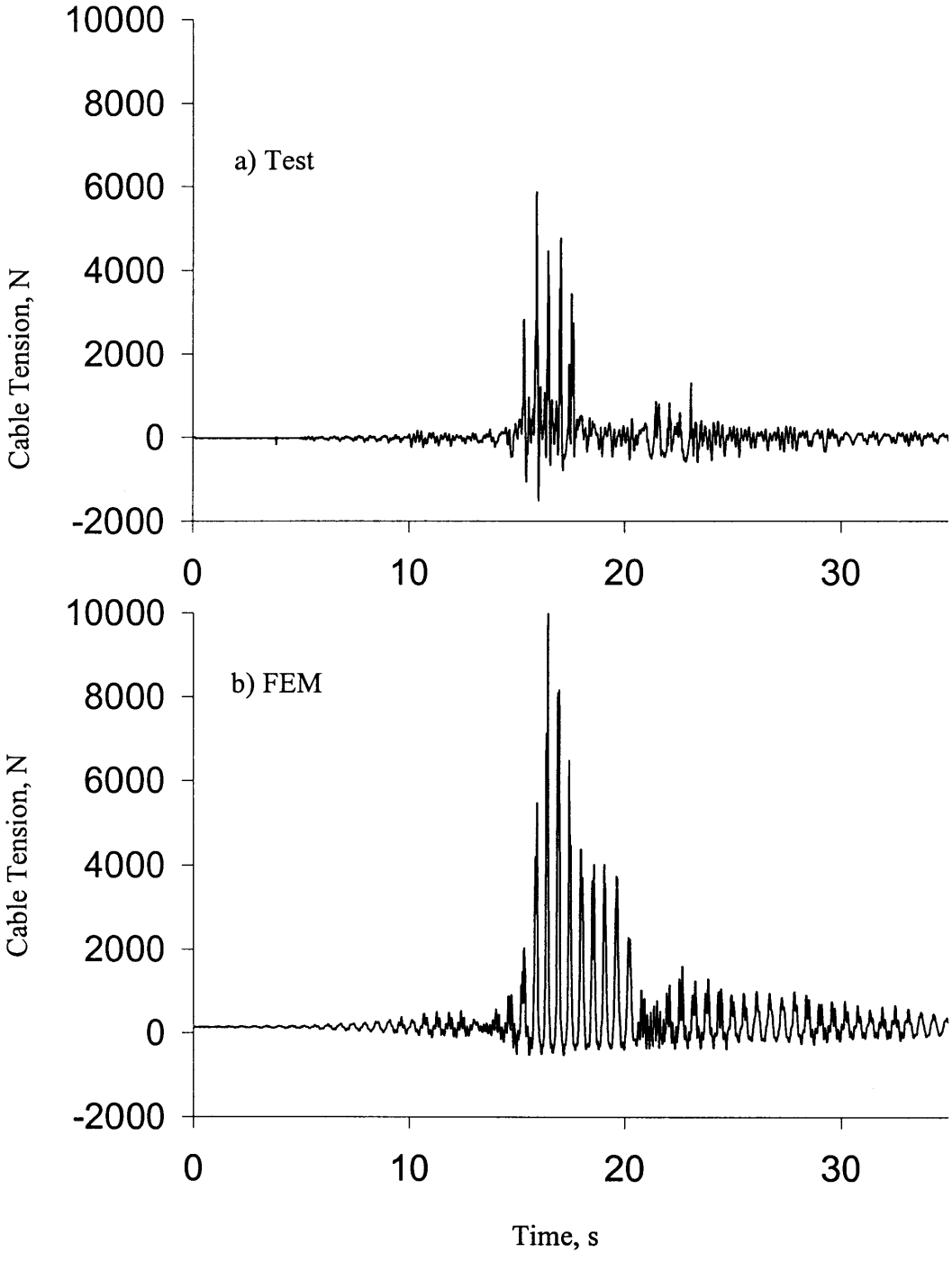

Figure 5.14 Time histories of horizontal cable force at connection to equipment 1 in system with 2% cable slackness: a) Test, b) FEM prediction.

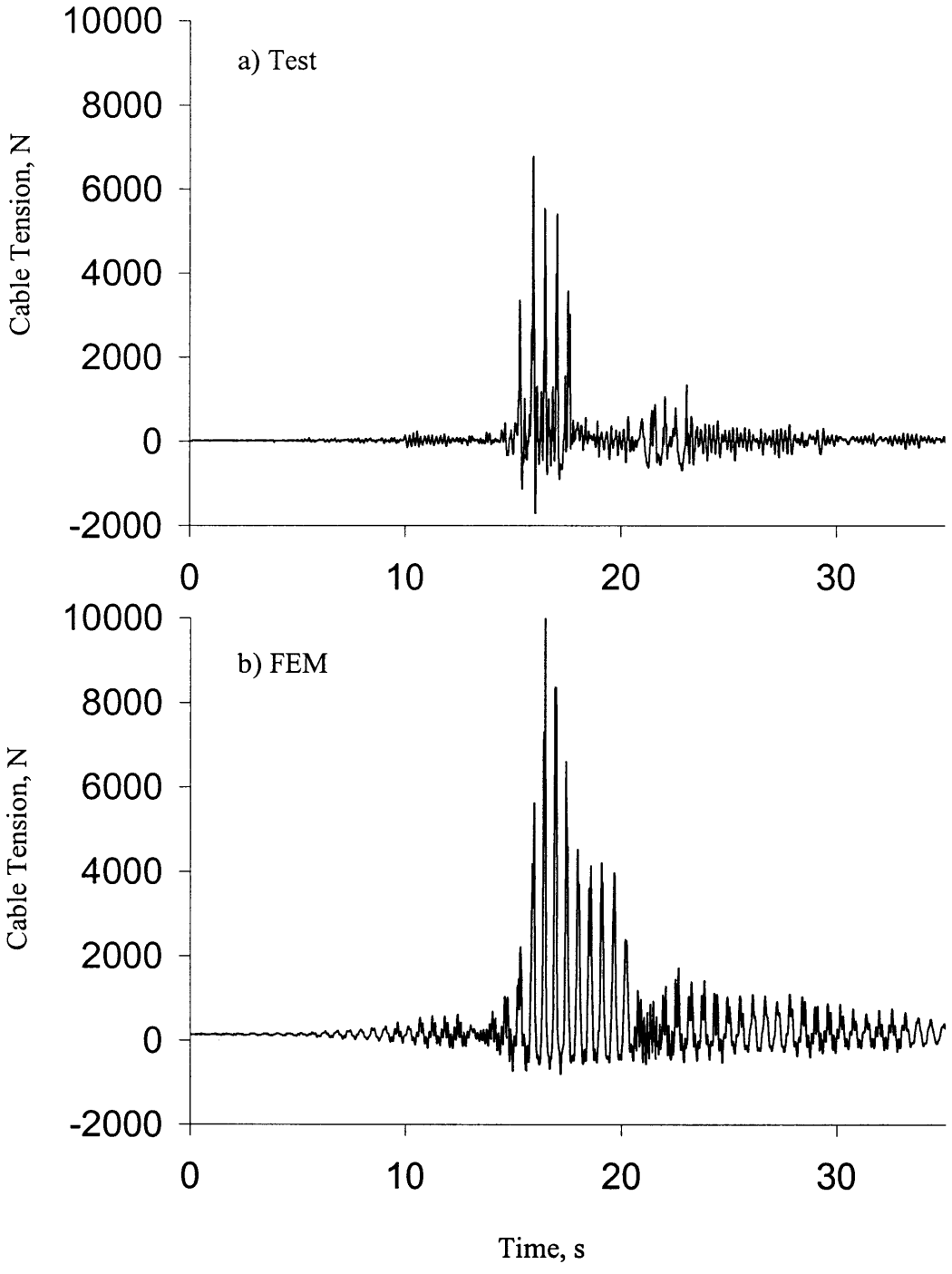

Figure 5.15 Time histories of horizontal cable force at connection to equipment 2 in system with 2% cable slackness: a) Test, b) FEM prediction.

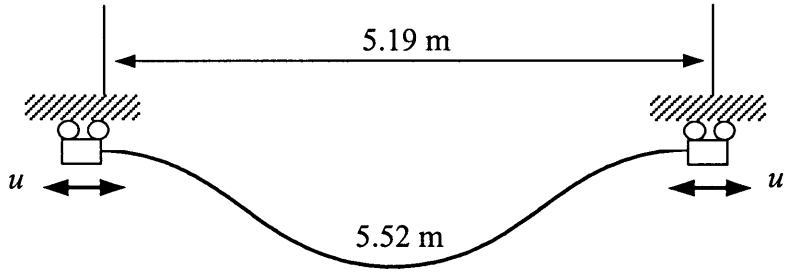

Figure 5.16 Schematic of test setup used by Dastous and Pierre (1996).

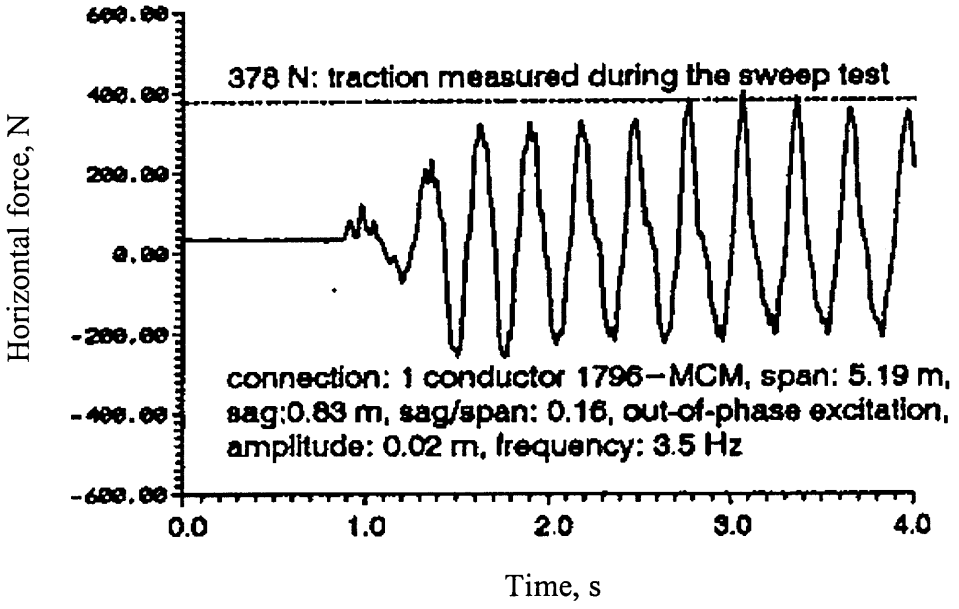

Figure 5.17 Time history of horizontal force at the cable support (after Dastous and Pierre 1996).

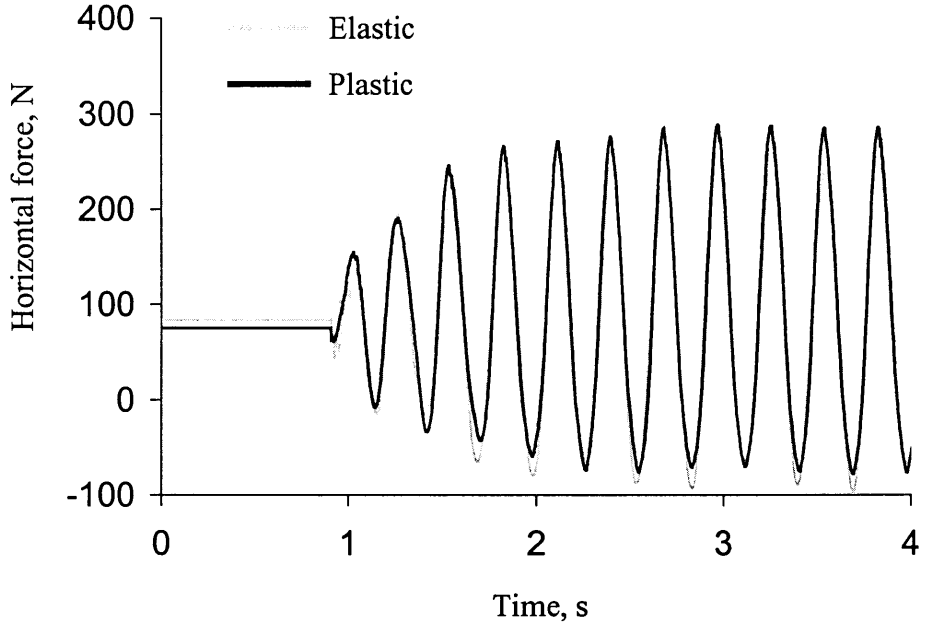

Figure 5.18 Time history of horizontal force at the cable support as predicted by the elastic and elasto-plastic finite element models.

6 EFFECT OF INTERACTION IN CABLE-CONNECTED EQUIPMENT SUBJECTED TO GROUND MOTION

6.1 Introduction

This chapter aims at investigating the effect of dynamic interaction on electrical substation equipment connected by a conductor cable and subjected to ground motions. As described in Section 1.1, under certain conditions, this interaction can lead to a strong amplification of the connected equipment response relative to its stand alone response. In this chapter, we first conduct a parametric study with the analytical model developed in Chapters 2 and 3 to gain a better understanding of this phenomenon. Consideration is restricted to two equipment items with a single connecting cable, where the equipment items are modeled as single degree of freedom oscillators. We then develop a simple predictive model to assess the interaction effect based on statistical analysis of a large data set of simulated systems. The statistical model is used to develop a simple design formula for the required cable slackness to reduce the interaction effect to a specified level.

The effect of interaction between cable-connected equipment items was investigated in our previous studies (Der Kiureghian *et al.*, 1999, 2000; Hong *et al.* 2001). In Der Kiureghian *et al.* (1999), we used a catenary model of the cable to investigate this effect. This model disregarded the flexural stiffness of the cable, as well as its mass inertia during the dynamic response. In Der Kiureghian *et al.* (2000) and Hong *et al.* (2001), we used a finite element model of the flexible conductor cable, which accounted for its large displacements and rotations, but used a linear elastic model of the cable. To approximately account for the effect of wire slippage, a reduced moment of inertia recommended by the IEEE guidelines (IEEE 1997) was used. The present study aims at refining this analysis by using the elasto-plastic bending model of the cable developed in Chapters 2 and 3, which properly accounts for the slippage of wires in the cable. Specifically, the flexural stiffness of the cable is allowed to vary along the cable and in time, depending on the curvature and tension force at each cross section of the cable. The effect of energy dissipation due to slippage of wires is investigated by comparing results based on the elastic and elasto-plastic models.

The finite element model developed in this study can be used in conjunction with appropriate models of equipment items to investigate the interaction effect for any given connected system and ground motion. However, the analysis, which properly accounts for the geometric and material nonlinearities, is time consuming and requires familiarity and access to an advanced finite element code. Given the plethora of equipment items in an electrical substation, such sophisticated and time-consuming analysis may not be possible or practical in practice. For this reason, there is interest in having a simple formula to predict the interaction effect without performing finite element dynamic analysis. Towards this end, using the finite element model developed in this study, we generate a large body of simulated interaction data for a variety of equipment items, conductor cables and ground motions. Consideration is again restricted to two equipment items with a single connecting cable, where the equipment items are modeled as single-degree-of-freedom oscillators. Using a statistical model assessment technique, and the simulated data, we develop an empirical formula relating a measure of the interaction effect to the equipment, cable and ground motion characteristics. This formula is then recast to give the required cable slackness to limit the interaction effect to a specified threshold.

6.2 Model of the Cable-Connected System

For the analysis in this chapter, we consider two equipment items with a single connecting cable, as shown in Figure 6.1. Using the method described in Der Kiureghian *et al.* (1999), each equipment item is idealized as a single degree of freedom system through the use of a displacement shape function. Thus, each equipment item i is described in terms of an effective mass, m_i, a natural frequency, ω_i, and a damping ratio, ζ_i, $i = 1, 2$. Given these parameters, the effective stiffness of the equipment can be obtained as $k_i = m_i\omega_i^2$. Let $u_1(t)$ and $u_2(t)$ denote the displacement responses of the two equipment items at their respective attachment points, as shown in Figure 6.1. The connecting cable is characterized by its compositional properties, i.e., the number of layers, the number of wires, the lay angles, wire and core diameters, the coefficient of friction between wires (assumed to be equal to 0.3), the elastic modulus of the material, the weight w per unit length, and its geometric properties, i.e., the initial length s_0, the initial span L_0, and the vertical offset H. The last three parameters are defined in the static equilibrium position of the system. In this position, the cable is stressed under its own weight. Therefore, s_0 is

slightly longer than the unstretched length of the cable, and L_0 is slightly smaller than the distance between the equipment items when they are not connected. The initial chord length is given by $c_0 = \sqrt{L_0^2 + H^2}$. The connected system is subjected to the horizontal base motion $x_g(t)$ in the plane of the cable.

The cable is modeled by 100 finite elements using the elasto-plastic bending model developed in Chapters 2 and 3. Five different conductor cables are used in the numerical investigations in this chapter. The properties of these cables are listed in Table 6.1. Note that these cover a wide range of properties. Specifically, the number of layers varies from 2 to 6, the number of strands (wires) varies from 19 to 127, and the cross-sectional area varies from 127 to 1,520 mm^2. Figures 6.2-6.6 show the nonlinear moment-curvature-tension relations for these five cables. These are computed according to the theory developed in Chapter 2, assuming a coefficient of friction of 0.3 between the wires. Following the procedure described in Section 3.3.2, the fitting parameters in the plastic model for each cable are determined. These are listed in Table 3.1.

6.3 Measures of Interaction

In order to quantify the effect of interaction, in Der Kiureghian *et al.* (1999) we introduced the *response ratio*. This is defined as the ratio of the maximum displacement response of an equipment item in the connected system to its maximum response in the stand alone configuration. Denoting the response of the i-th equipment in its stand-alone configuration as $u_{i0}(t)$, the response ratio is

$$R_i = \frac{\max|u_i(t)|}{\max|u_{i0}(t)|}, \quad i = 1, 2 \tag{6.1}$$

The response ratio provides a dimensionless measure of the interaction effect. A value greater than unity for the response ratio indicates that, on account of the interaction effect in the connected system, the response of the corresponding equipment is amplified relative to its response in the stand-alone configuration; also, a value smaller than unity for the response ratio indicates that the response of the corresponding equipment is deamplified relative to its response in the stand-alone configuration. It is noted that the internal forces in an equipment item, which is modeled as a single-degree-of-freedom system, are directly proportional to the displacement response. Hence, for the assumed model, the above ratios are equally applicable to force responses

in the two equipment items. Since equipment items are typically qualified in their stand-alone configurations, the response ratio provides the kind of information that an engineer would need in order to determine whether the equipment item can withstand the amplified seismic demand in the connected system.

While the response ratio provides a good measure of the interaction effect, it involves response quantities that require nonlinear dynamic analysis. For design purposes, it is important to identify simple predictive measures of the interaction effect. A quantity that strongly influences the degree of interaction between the cable-connected equipment items is the maximum distance that the two stand-alone equipment items move away from one another, when subjected to the same ground motion. This quantity is given by

$$\Delta = \max\left[u_{20}(t) - u_{10}(t)\right] \tag{6.2}$$

Obviously, the larger Δ is, the larger we expect the interaction effect to be. Another important measure is the amount of slack in the cable. This is measured in terms of the reserve cable length in excess of the chord length, i.e., $s_0 - c_0$. Now suppose one end of the cable is moved horizontally by the amount Δ, as shown in Figure 6.7. In this figure, the solid line indicates the initial position of the cable and the dashed line indicates the displaced position, with s denoting the current cable length. For Δ much smaller than the initial chord length, c_0, the chord length will increase approximately by the amount $\Delta L_0 / c_0$. One can regard this quantity as a measure of the seismic demand on the reserve cable length, $s_0 - c_0$, which can be regarded as the corresponding capacity. Obviously, if $\Delta L_0 / c_0$ is small in relation to $s_0 - c_0$, then there will be little interaction between the two equipment items. Conversely, if $\Delta L_0 / c_0$ is of the same magnitude or greater than $s_0 - c_0$, one can expect significant interaction. It follows that the dimensionless parameter

$$\beta = \frac{\Delta L_0 / c_0}{s_0 - c_0} \tag{6.3}$$

can serve as a predictive measure of the interaction effect, and we call it the *interaction parameter*. Other than Δ, the parameters in the above expression are readily available from the geometry of the cable. Since Δ is defined for the stand-alone equipment items, which by definition are linear and have single degrees of freedom, its determination requires relatively simple analysis.

In particular, as shown in Der Kiureghian *et al.* (1999), Δ can be conveniently computed by the response spectrum method.

In our previous study (Der Kiureghian *et al.* 19992000, Hong *et al.* 2001), we argued that there will be little interaction between the two equipment items if β is smaller than about 1. On that basis, and to account for a degree of conservatism, we provisionally recommended selecting the cable slackness such that β is no greater than 1. However, this simple rule does not account for the mechanical behavior of the cable, nor for the effect of the cable inertia. As a result, in many practical situations, one may encounter significant interaction for β values smaller than unity. Our next study (Der Kiureghian *et al.*, 2000, Hong *et al.* 2001), where we used the elastic frame element for the cable, showed that there could be significant interaction for β values smaller than unity due to the effect of the cable inertia. Based on this study, we recommended selecting the cable slackness such that β is no greater than 1 and designing the equipment items for forces slightly (about 50%) higher than the forces obtained for the stand-alone configuration. In any case, the interaction parameter β remains a good predictor of the interaction effect. Later in this chapter, we use this parameter in formulating a predictive model for the response ratio.

6.4 Numerical Studies with Example Cable-Connected Systems

In this section, we investigate the effect of interaction by performing nonlinear time-history analyses of example cable-connected systems subjected to selected ground motions. The systems are analyzed by both the elastic and the elasto-plastic finite element models of the cable. For the elastic analysis, $I_{\min}$ is used as the moment of inertia of the cable, i.e., the cable is assumed to be in a fully slipped state at all times. In both cases, geometric nonlinearities resulting from large displacements and rotations are accounted for. The comparison between the results from the elastic and elasto-plastic models reveals the influence of the variation in the flexural stiffness of the cable in the elasto-plastic model, as well as the dissipation of energy resulting from the slippage of wires. Next, we carry out parametric studies to better understand the relation between the response ratios and the interaction parameter β for different ground motions and conductor cables.

First consider two equipment items connected by the Valerian cable (see Table 6.1 and Figure 6.2) having an initial span $L_0 = 5\,\text{m}$ (under static equilibrium conditions), the vertical

separation $H = 0$, and the initial length $s_0 = 5.10\,\text{m}$. The initial slackness of this cable is $(s_0 - L_0)/L_0 = 0.02$. This is a rather taut cable and represents perhaps an extreme case. We select it to highlight the effect of interaction and the highly nonlinear nature of the response. Note that, among the conductor cables listed in Table 6.1, the Valerian is the most flexible having only two layers of strands and the smallest cross-sectional area and moment of inertia. Furthermore, for this cable the ratio of the maximum to minimum moment of inertia is $I_{\max}/I_{\min} = 22.7$, which is relatively small. The equipment items, modeled as single-degree-of-freedom oscillators, are assumed to have the effective masses $m_1 = 1000\,\text{kg}$ and $m_2 = 500\,\text{kg}$, natural frequencies $\omega_1 = 2\pi$ rad/s and $\omega_2 = 10\pi$ rad/s, and damping ratios $\zeta_1 = \zeta_2 = 0.02$.

We first examine the response of the cable-connected system to the N-S component of the Newhall record of the 1994 Northridge earthquake, which is shown in Figure 6.8. For this record, Figure 6.9 shows the stand-alone responses, $u_{10}(t)$ and $u_{20}(t)$, of the two equipment items calculated by the HHT algorithm. The calculated maximum stand-alone displacements are $\max|u_{10}(t)| = 0.3358\,\text{m}$ and $\max|u_{20}(t)| = 0.0159\,\text{m}$, respectively, and the maximum relative separation between the two stand-alone equipment items is $\Delta = \max[u_{20}(t) - u_{10}(t)] = 0.3163\,\text{m}$, yielding the interaction parameter value $\beta = 3.16$. The two stand-alone responses are significantly different because of the large separation between the equipment frequencies (1Hz and 5Hz, respectively). These time histories tend to have nearly symmetric peaks relative to the equilibrium positions with nearly zero averages over time.

Figure 6.10 shows the displacement time histories $u_1(t)$ and $u_2(t)$ of the two equipment items, which are connected by the Valerian cable, system calculated by the elastic (gray lines) and the elasto-plastic (black lines) finite element models of the cable. The latter model explicitly accounts for the slippage of wires in the cable by using the elasto-plastic bending model described in Chapters 2 and 3. The results of the analyses based on the two models are nearly identical for the lower frequency equipment item (equipment 1), as seen in the top plot in Figure 6.10. The results for the higher frequency equipment item are also similar for the most part, with slightly smaller peak values for the elasto-plastic predictions; see the bottom plot in Figure 6.10. These results imply that the moment of inertia in the elasto-plastic model remains close to its lower bound at most locations and times. Furthermore, the effect of energy dissipation due to the

slippage of wires is insignificant. These findings are not surprising. Recall that the yielding moment of the cable is given by $M_Y = C_Y EI_{\max} \mathrm{K}_{init}$, as shown in (3.59). For the Valerian cable, the $I_{\max}$ is relatively small, in fact the smallest among the five cables considered. As a result, the yield moment of the cable is quickly reached and little energy dissipation occurs. As we will see shortly, a different result is obtained for heavier conductor cables.

It is noted in Figure 6.10 that the displacement responses exhibit skewed peaks relative to the equilibrium positions, with non-zero averages over time and larger displacements accruing towards the side that slackens the cable. This is a clear indication of interaction between the two equipment items. We observe a decrease in the peak response of equipment 1 (the lower frequency equipment item) in the connected system relative to its stand-alone response, and a large increase in the peak response of equipment 2 (the higher frequency equipment item). The response ratios for the two equipment items, based on the elasto-plastic analyses, are $R_1 = 0.703$ and $R_2 = 3.71$, respectively. It is clear that the dynamic interaction adversely affects the higher frequency equipment item. Similar observations were reported in our previous studies (Der Kiureghian *et al.* 1999, 2000, Hong *et al.* 2000), where we used the catenary formulation or the elastic finite element model of the cable. As we will see later, it is possible that the lower frequency equipment item also experience amplification of its response due to the cable inertia.

The above analysis is now repeated with the Trillium cable connecting the two equipment items. The Trillium is the heaviest of the cables listed in Table 6 having six layers of wires and the largest cross-sectional area, moment of inertia, and weight per unit length. The ratio of the maximum to minimum moment of inertia for this cable is $I_{\max} / I_{\min} = 160$. In view of these properties, the plastic energy dissipation of the Trillium cable is expected to be much larger than that of the Valerian cable.

Figure 6.11 shows the displacement time histories $u_1(t)$ and $u_2(t)$ of the equipment items in the connected system calculated by the elastic (gray lines) and elasto-plastic (black lines) finite element models. The two predicted responses now are significantly different. In particular, the peaks in the response time history of the lower frequency equipment item are much smaller for the elasto-plastic predictions, though the extreme peak is nearly identical. Furthermore, the high frequency content in the response of the higher frequency equipment item has dis-

disappeared in the elasto-plastic prediction. These changes can be attributed to the significant energy dissipation that occurs in this cable due to slippage between the wires. Note that the maximum moment of inertia of the Trillium cable is 152 times larger than that of the Valerian cable as shown in Table 6.1 and, therefore, the yielding moment of the Trillium cable will be much larger than that of the Valerian cable. This indicates that the Trillium cable must have larger energy dissipation than the Valerian cable. The energy dissipation is at least partly responsible for reducing the response peaks and for damping out the higher-frequency components in the response of equipment 2. The response ratios for the two equipment items, based on the elasto-plastic analysis, are $R_1 = 0.466$ and $R_2 = 3.65$. Interestingly, these are not very different from the values observed for the more flexible Valerian cable.

To better understand the effect of interaction between the connected equipment items, we compute and plot the response ratios R_1 and R_2 for the above systems for the five different ground motions shown in Figure 6.12, while varying the interaction parameter β defined in (6.3). Since the vertical separation between the support points is zero, we have $c_0 = L_0$ and the interaction parameter for this case simplifies to

$$\beta = \frac{\Delta}{s_0 - L_0} \tag{6.4}$$

where $L_0 = 5\,\text{m}$ is the initial span and $\Delta = \max[u_{20}(t) - u_{10}(t)]$ is the maximum relative separation between the two stand-alone equipment items for the selected ground motion. All system parameters are kept constant, with the exception of the initial cable length s_0, which is varied to cover the range 0.1-2 of the interaction parameter β.

Figure 6.13 shows plots of the response ratios R_1 and R_2 as functions of the interaction parameter β for the system connected by the Valerian cable, as computed using the elastic finite element model. In this figure, there is virtually no amplification of the equipment responses for values of β less than 1. Based on this finding, in our previous study (Der Kiureghian *et al.* 2000, Hong *et al.* 2001), we provisionally recommended a cable length corresponding to $\beta = 1$ to avoid the interaction effect. Figure 6.14 shows the same plots, where the responses are calculated using the elasto-plastic finite element model. The plots in this figure are almost the same as those in Figure 6.13, indicating that the effect of plastic behavior in the cable is insignificant. As men-

tioned earlier, this is due to the small value of the yielding moment in this cable, as a result of which the wires are mostly in the fully slipped state.

Figures 6.15 and 6.16 show plots of the response ratios R_1 and R_2 versus the interaction parameter β for the system connected by the Trillium cable. Figure 6.15 is based on elastic analysis, whereas Figure 6.16 is based on elasto-plastic analysis. The result in Figure 6.15 is similar to what we observed for the Valerian cable: virtually no interaction occurs for β values smaller than unity. However, the result in Figure 6.16, where the responses are calculated by the elasto-plastic finite element model, are significantly different. Most importantly, in some cases the response ratios are significantly greater than unity for $\beta < 1$, particularly for the lower frequency equipment item. Given the complex nature of the cable behavior, it is hard to identify the exact factors that cause this difference. The higher bending stiffness of the cable, when the wires are not slipping, could be a reason. Possibly, resonance-type behavior in the cable is also causing some of the peaks in the R_1 and R_2 plots in Figure 6.16. However, it is clear from this finding that our previous provisional recommendation of determining the cable slackness based on $\beta = 1$ does not guarantee that there will not be an amplification of the response of either equipment.

It is clear from the above analyses that the interaction effect in cable-connected equipment items subjected to earthquake ground motions is a highly complex phenomenon. This effect depends not only on the equipment and cable characteristics, and this in a rather chaotic fashion, but also on the details of the ground motion. We note that, for a linear connected system, the response ratios are entirely independent of the scaling (intensity) of the ground motion. For a nonlinear system, such as the one under investigation, generally this would not be the case. Nevertheless, this observation suggests that the large variability observed in the response ratios in Figures 6.13-6.16 over the selected ground motions cannot all be attributed to the varying intensities of these motions (Figure 6.12). It appears that the interaction effect in the cable-connected system is highly sensitive to the details of the ground motion, such as the frequency content, the evolution of intensity in time, the existence of acceleration or velocity pulses, or other such characteristics. In a design situation, it is impossible to correctly predict such detailed characteristics of future earthquakes. Therefore, there is need to develop a method to predict the interaction effect in the cable-connected system, which does not require a detailed specification of the ground

motion, but which also accounts for the inevitable variability in the future ground motions. The development of such a method is the subject of the following section.

6.5 Statistical Model for Response Ratio

The finite element model developed for the cable-connected system offers us an opportunity to conduct a "virtual" experiment with any cable-connected system and earthquake ground motion. In this section, we develop a large sample of simulated response ratio data for pre-selected sets of equipment items, cables and ground motions. This "observed" data is then used to develop a statistical model for predicting the response ratio in terms of important characteristics of the equipment items, the cable and the ground motion. For this purpose, the Bayesian parameter estimation method is used. A recent description of this methodology can be found in Gardoni *et al.* (2002).

6.5.1 Numerical Simulations

To develop a representative sample of response ratios, numerical simulations are conducted for cable-connected systems with varying equipment, cable and ground motion characteristics. In all cases, the initial span $L_0 = 5\,\text{m}$ is used. Table 6.2 summarizes the variables selected for the numerical simulations. Each variable can have 5 different values: the ratio of equipment frequencies, ω_1/ω_2, varies from 0.2 to 1; the ratio of equipment masses, m_1/m_2, varies from 0.2 to 5; the inclination of the cable, H/L, varies from 0 to 1.0; the angles of the cable at the attachment points with respect to the chord line vary from $-\pi/4$ to $\pi/4$ radians; the initial cable slackness, $(s_0 - c_0)/c_0$, varies from 0.02 to 0.06; the conductor cable can be any of the five listed in Table 6.1; and the ratio of the total cable mass to the sum of equipment masses, $m_{\text{cable}}/(m_1 + m_2)$, varies from 0.01 to 0.2. Furthermore, ten recorded ground motions, shown in Figure 6.17, are selected.

If all combinations of the parameter values and the 10 ground motions were to be used, we would have 10×58=3,906,250 separate simulations. This is an unnecessarily large data set. Furthermore, many parameter combinations in this large set would yield unrealistic systems. For these reasons, certain parameter sets were grouped together, For example, for the case of horizontal cables, i.e. $H/L = 0$, the values for the parameters $(s_0 - c_0)/c_0$, cable type, and

$m_{cable}/(m_1+m_2)$ in each column in Table 6.2 were considered together, as were the values of the parameters ω_1/ω_2, and m_1/m_2. This procedure yielded 25 "realistic" systems, and each of the ten ground motions was applied to each system. Thus, we generated a data set of 250 systems and, therefore, 500 response ratios were obtained with each system having two response ratios.

For each simulated case, the responses of both equipment items in their connected as well as stand-alone configurations were calculated and the corresponding response ratios were determined. It turned out that in the majority of simulated cases, the response ratios were close to unity. In fact, of the 1000 simulated cases, 613 cases had response ratio values less than 1.2. If the entire data set is used, these cases will dominate the parameter estimation and the statistical model will not properly capture the trend for cases with large response ratios, which are of interest. For this reason, of these cases, only 13 cases were randomly selected for inclusion in the data set. Furthermore, of the remaining 387 cases, 11 cases had response ratio values greater than 10. These were also dropped, since they typically corresponded to unrealistic combinations of equipment characteristics. Thus, a total of 389 simulated cases were selected for the statistical analysis. It is believed that this set provides a broad representation of the characteristics of real connected equipment systems in electrical substations.

6.5.2 Statistical Model for the Response Ratio

Our interest is in developing a predictive model of the response ratio for a given equipment item, which is connected to another specified equipment item through a specified conductor cable. We use a statistical approach based on the simulated data described in the preceding section to develop this model. Considering the non-negative nature of the response ratio, it is convenient and appropriate to develop the model for the logarithm of the response ratio. Hence, following the approach suggested by Gardoni *et al.* (2002), we formulate the model as

$$y = \ln[R(\mathbf{x},\boldsymbol{\Theta})] = \sum_{i=1}^{m} \theta_i h_i(\mathbf{x}) + \sigma\varepsilon \qquad (6.5)$$

In this expression, $\mathbf{x} = (x_1, x_2, \ldots)$ denotes a set of measurable variables, $h_i(\mathbf{x})$, $i = 1, \ldots, m$, are a set of "explanatory" functions, ε is a normal random variable with zero mean and unit variance representing the model error, $\boldsymbol{\Theta} = (\boldsymbol{\theta}, \sigma)$ with $\boldsymbol{\theta} = (\theta_1, \ldots, \theta_m)$ is the set of unknown model parameters, and $y = \ln[R(\mathbf{x},\boldsymbol{\Theta})]$ is the logarithm of the response ratio for the equipment item under

consideration. Note that for given $\mathbf{x}$, θ and σ, we have $\mathrm{Var}\{\ln[R(\mathbf{x},\theta)]\} = \sigma^2$ as the variance of the model. The art in this type of modeling lies in the selection of the variables $\mathbf{x}$ and the explanatory functions $h_i(\mathbf{x})$. The experience gained from the analysis in this and our earlier studies guides us in the selection of these variables and explanatory functions, as described below.

To distinguish the properties of the two connected equipment items, we use the subscript "self" to denote the properties of the equipment item for which the response ratio is sought, and the subscript "other" to refer to the properties of the other connected equipment item. With this notation, the variables considered are: the equipment natural frequencies, ω_{self} and ω_{other}, the equipment masses, m_{self} and m_{other}, the interaction parameter, β, as defined in (6.3), the inclination of the chord line, H/L_0, the mass of the cable, m_{cable}, and the type of the conductor cable j, where $j = 1$ to 5 respectively denotes the Valerian, Syringa, Flag, Cowslip and Trillium cables, as listed in Table 6.1. Note that increasing j denotes increasing the thickness, and the number of layers, of the conductor cable. The variability in the ground motion is entirely allocated to the model error, $\sigma\varepsilon$.

To detect a constant bias in the logarithm of the response ratio, we select the first explanatory function as $h_1 = 1$. Since the response ratio is expected to be influenced by the ratio of equipment frequencies, we select $h_2 = \omega_{\text{other}}/\omega_{\text{self}}$. Similarly, $h_3 = m_{\text{other}}/m_{\text{self}}$ is selected in anticipation of an important influence from the ratio of equipment masses. The fourth explanatory function is selected as $h_4 = \mathrm{sgn}(\omega_{\text{self}} - \omega_{\text{other}})\beta$, where β is the interaction parameter and sgn(·) is the signum function, which is included because we anticipate the response ratio to increase with β when $\omega_{\text{other}} < \omega_{\text{self}}$, as can be seen in Figures 6.13-6.16. The fifth explanatory function is selected as $h_5 = m_{\text{cable}}/(m_{\text{self}} + m_{\text{other}})$ to explore possible dependence of the response ratio on the magnitude of the cable mass relative to the equipment masses. Finally, we select $h_6 = j$ to explore the dependence of the response ratio on the type of the conductor cable. It is noted that the above explanatory function are all dimensionless. As a result, the model parameters θ_i, $i = 1, \ldots, 6$, and σ are also dimensionless.

Before proceeding with estimation of the model parameters, exploratory plots are made to detect trends between the response ratio and each explanatory function. Figure 6.18 shows the scatter plot for the computed logarithms of the response ratios versus $h_2 = \omega_{other}/\omega_{self}$ for the 92 simulated cases. A clear trend is evident. Figure 6.19 shows the scatter plot of the logarithm of the response ratio versus $h_3 = m_{other}/m_{self}$, where again a clear trend is observed. Figure 6.20 shows the data for $h_4 = \text{sgn}(\omega_{self} - \omega_{other})\beta$, where the open diamonds indicate cases with $H/L = 0$, i.e., horizontal cables, and solid diamonds indicate cases with $H/L > 0$, i.e., cables with inclined chord lines. While both sets of data show clear increasing trends with h_4, the data points for inclined cables show a steeper trend. To approximately account for the influence of the cable inclination, h_4 is replaced by

$$\tilde{h}_4 = \text{sgn}(\omega_{self} - \omega_{other})\left(1 + a\frac{H}{L}\right)\beta \qquad (6.6)$$

where a is a parameter. By assigning a positive value to a, the solid data points in Figure 6.20 are shifted to the right so that their trend becomes similar to the trend of the data points for the horizontal cables. After several trails, we found a=0.5 to provide the best visual result. Figure 6.21 shows the scatter plot of the data points with respect to $\tilde{h}_4$ when a=0.5. It can be seen that the solid and open data points now have similar trends. Figure 6.22 shows the scatter plot of the logarithm of the response ratio versus $h_5 = m_{cable}/(m_{self} + m_{other})$ and Figure 6.23 shows the similar plot versus $h_6 = j$. No trend is evident in either of these plots, indicating that these explanatory functions are not informative. Additional investigations were carried out with explanatory functions involving the angles of the cable at the fixed ends. However, no trends were observed.

On the basis of the above exploratory investigation, and with a desire to have as simple a model as possible, the following model form is selected:

$$y = \ln[R(\mathbf{x},\boldsymbol{\theta})] = \theta_1 + \theta_2\frac{\omega_{other}}{\omega_{self}} + \theta_3\frac{m_{other}}{m_{self}} + \theta_4\,\text{sgn}(\omega_{self} - \omega_{other})\left(1 + 0.5\frac{H}{L}\right)\beta + \sigma\varepsilon \qquad (6.7)$$

where the first term corresponds to $h_1 = 1$. The Bayesian parameter estimation method is now used to estimate the parameters $\boldsymbol{\theta} = (\theta_1,\ldots,\theta_4)$ and σ of the model based on the 389 simulated data.

The $n = 389$ observations of the response ratio from the numerical simulations in the preceding section can be written in the matrix form

$$\mathbf{y} = \mathbf{H}\theta + \sigma\epsilon \tag{6.8}$$

where $\mathbf{y}$ is the $n \times 1$ vector of observations, $\mathbf{H}$ is an $n \times m$ matrix collecting the known values of the explanatory functions where $m = 4$, θ denotes the $m \times 1$ vector of unknown model parameters, ϵ is an $n \times 1$ vector of standard normal random variables, and σ represents the unknown standard deviation of the model error. Using the well-known Bayesian updating formula (Box and Tiao, 1992), the posterior distribution of the unknown parameters is computed from

$$f''(\theta,\sigma^2) = k\,L(\theta,\sigma^2) f'(\theta,\sigma^2) \tag{6.9}$$

where $f'(\theta,\sigma^2)$ is the prior distribution, $L(\theta,\sigma^2)$ is the likelihood function and k is a normalizing factor. Since no prior information on the model parameters is available, a non-informative prior in the form of a locally uniform distribution on θ and $\ln\sigma^2$ is used. This corresponds to $f'(\theta,\sigma^2) \propto \sigma^{-2}$. Under these conditions, and the assumption that the observations are statistically independent, Box and Tiao (1992) have shown that θ has the multivariate t distribution

$$f''(\theta) = \frac{\Gamma\left(\frac{\eta+m}{2}\right)\left|\mathbf{H}^{\mathrm{T}}\mathbf{H}\right|^{1/2} s^{-m}}{\left[\Gamma\left(\frac{1}{2}\right)\right]^m \Gamma\left(\frac{\eta}{2}\right)(\eta)^{m/2}} \left[1 + \frac{(\theta-\hat{\theta})^{\mathrm{T}}\mathbf{H}^{\mathrm{T}}\mathbf{H}(\theta-\hat{\theta})}{\eta s^2}\right]^{-(\eta+m)/2} \quad \begin{matrix} -\infty < \theta_i < \infty \\ i = 1,\ldots,m \end{matrix} \tag{6.10}$$

where

$$\hat{\theta} = (\mathbf{H}^{\mathrm{T}}\mathbf{H})^{-1}\mathbf{H}^{\mathrm{T}}\mathbf{y} \tag{6.11a}$$

$$s^2 = \frac{1}{\eta}(\mathbf{y}-\hat{\mathbf{y}})^{\mathrm{T}}(\mathbf{y}-\hat{\mathbf{y}}) \tag{6.11b}$$

$$\eta = n - m \tag{6.11c}$$

$$\hat{\mathbf{y}} = \mathbf{H}\hat{\theta} \tag{6.11d}$$

Furthermore, $\eta s^2/\sigma^2$ has the chi-square distribution with η degrees of freedom. We note that $\hat{\theta}$ is the mode as well as mean of θ, and its covariance matrix is $\eta s^2(\mathbf{H}^T\mathbf{H})^{-1}/(\eta-2)$. The mean of σ^2 is $\eta s^2/(\eta-2)$ and its variance is $2\eta^2 s^4/[(\eta-2)^2(\eta-4)]$.

Table 6.3 lists the posterior means, coefficients of variation (c.o.v.) and correlation coefficients of the model parameters computed using the 389 simulation data, as described above. Among the first four parameters, θ_4 has the smallest c.o.v. This implies that the corresponding explanatory function $\tilde{h}_4$, given in (6.6), is the most informative among the four explanatory functions considered. The second smallest c.o.v. belongs to θ_3, which is associated with $h_3 = m_{\text{other}}/m_{\text{self}}$. θ_1 and θ_2 have the largest c.o.v.'s, implying that $h_1 = 1$ and $h_2 = \omega_{\text{other}}/\omega_{\text{self}}$ are least informative among the four explanatory functions. It may appear counterintuitive that the ratio of equipment frequencies is not more informative. This is easily explained by noting that the interaction parameter β, which is present in $\tilde{h}_4$, implicitly includes information about the equipment frequencies through the parameter Δ, which is the maximum distance the two stand-alone equipment items move away from one another. Hence, $h_2 = \omega_{\text{other}}/\omega_{\text{self}}$ accounts for information about the equipment frequencies, which is not already contained in $\tilde{h}_4$. The above results suggest that there is little information in the equipment frequencies beyond that implicit in the interaction parameter.

Substituting the mean parameter values in (6.7), we arrive at the following predictive formula for the response ratio:

$$R = \exp\left[0.209 + 0.109\frac{\omega_{\text{other}}}{\omega_{\text{self}}} + 0.065\frac{m_{\text{other}}}{m_{\text{self}}} + 0.459\,\text{sgn}(\omega_{\text{self}} - \omega_{\text{other}})\left(1 + 0.5\frac{H}{L}\right)\beta + 0.351\varepsilon\right] \qquad (6.12)$$

Due to the presence of ε, which has the normal distribution, R in the above expression is a random variable having the lognormal distribution. The randomness in R comes from two sources: (a) inherent variability in the ground motion for the specified value of Δ, and (b) the random model error, arising from the vast simplification of the problem, i.e., from nonlinear dynamic analysis to a simple algebraic equation. The median value of R, denoted $\overline{R}$, is obtained by setting $\varepsilon = 0$, i.e.,

$$\overline{R} = \exp\left[0.209 + 0.109\frac{\omega_{other}}{\omega_{self}} + 0.065\frac{m_{other}}{m_{self}} + 0.459\,\mathrm{sgn}(\omega_{self} - \omega_{other})\left(1 + 0.5\frac{H}{L}\right)\beta\right] \qquad (6.13)$$

Figure 6.24 shows a plot of the median predicted values of the response ratios versus the measured response ratios in the data set. The scatter in this plot is indicative of the two sources of variability mentioned above. The dotted lines in this figure delimit the region within one standard deviation of the median. The response ratio thresholds for 90% and 10% probabilities of exceedance are obtained by setting $\varepsilon = -1.28$ and $\varepsilon = 1.28$, respectively. The results are $R_{0.90} = 0.558\overline{R}$ and $R_{0.10} = 1.79\overline{R}$, respectively. Thresholds for other probability values can be obtained by using the corresponding values of the standard normal variate in place of ε. As examples, Table 6.4 lists the median and the 90% and 10% exceedance probability thresholds of the response ratio for several selected connected equipment systems.

6.5.3 Required Cable Slackness

The model in (6.12) can be recast in a form convenient for determining the required slackness of the conductor cable for a pair of connected equipment items, so that the response ratio for the equipment under consideration does not exceed a prescribed threshold at a given exceedance probability. Substituting (6.3) for the interaction parameter in (6.12) and rearranging terms, one obtains

$$\frac{s_0 - c_0}{c_0} = \frac{0.459\,\mathrm{sgn}(1 - \omega_{other}/\omega_{self})}{\ln R - 0.209 - 0.109\dfrac{\omega_{other}}{\omega_{self}} - 0.065\dfrac{m_{other}}{m_{self}} - 0.351\varepsilon}\,\frac{1 + 0.5H/L_0}{1 + (H/L_0)^2}\,\frac{\Delta}{L_0} \qquad (6.14)$$

To use this expression, one needs to set an "acceptable" probability of exceeding a specified response ratio threshold, in addition to specifying the system properties and the seismic demand Δ. When designing for an extreme event, i.e., one with a small probability of occurrence during the service life of the equipment, it is appropriate to use the median required slackness, which is obtained by setting $\varepsilon = 0$ in the above expression, i.e.,

$$\overline{\frac{s_0 - c_0}{c_0}} = \frac{0.459\,\mathrm{sgn}(1 - \omega_{other}/\omega_{self})}{\ln R - 0.209 - 0.109\dfrac{\omega_{other}}{\omega_{self}} - 0.065\dfrac{m_{other}}{m_{self}}}\,\frac{1 + 0.5H/L_0}{1 + (H/L_0)^2}\,\frac{\Delta}{L_0} \qquad (6.15)$$

Table 6.5 lists the required median cable slackness for several example systems for $R = 2$. Note that the denominator in (6.14) or (6.15) can be negative for certain combinations of the parameters. This implies that no slackness value can satisfy the specified conditions. In that case, one needs to accommodate a larger threshold of the response ratio. For determining the required slackness, it is necessary to compute the value of Δ for the specified design earthquake. As mentioned earlier, a simple method to compute this value by response spectrum analysis is given in our earlier study, Der Kiureghian *et al.* (1999). It is important to note that the above determination of the required cable slackness properly accounts for the model uncertainty as well as the variability in the ground motion for a specified design response spectrum.

Table 6.1 Properties of cables used in numerical analyses

Property	Valerian	Syringa	Flag	Cowslip	Trillium
Young's modulus, N/m^2	70×10^9	70×10^9	70×10^9	70×10^9	70×10^9
number of layers except core	2	3	4	5	6
number of strands	19	37	61	91	127
strand diameter, mm	2.913	2.882	2.720	3.764	3.904
overall conductor diameter, mm	14.57	20.17	24.48	41.40	50.75
cross section area, mm^2	119	226	332	948	1,423
mass per unit length, kg/m	0.323	0.614	0.901	2.571	3.859
lay angle, degree	12	12	12	12	12
I_{min}, mm^4	66	123	160	878	1,417
I_{max}, mm^4	1,496	5,606	12,236	100,495	227,305

Table 6.2 Parameter values for numerical simulations.

Variable	Value 1	Value 2	Value 3	Value 4	Value 5
ω_1 / ω_2	0.2	0.4	0.6	0.8	1.0
m_1 / m_2	0.2	0.5	1	2	5
H / L	0	0.25	0.5	0.75	1.0
Angle at right end w.r.t. chord line	$-\pi/4$	$-\pi/6$	0	$\pi/6$	$\pi/4$
Angle at left end w.r.t. chord line	$-\pi/4$	$-\pi/6$	0	$\pi/6$	$\pi/4$
$(s_0 - c_0)/c_0$	0.02	0.03	0.04	0.05	0.06
Cable Type	Valerian 2 layers	Syringa 3 layers	Flag 4 layers	Cowslip 5 layers	Trillium 6 layers
$m_{\text{cable}} /(m_1 + m_2)$	0.01	0.05	0.1	0.15	0.2

Table 6.3 Posterior statistics of model parameters.

Parameters	Mean	c.o.v.	Correlation coefficient				
			θ_1	θ_2	θ_3	θ_4	σ
θ_1	0.209	0.214	1				
θ_2	0.109	0.204	–0.749	1			
θ_3	0.065	0.157	–0.646	0.208	1		
θ_4	0.459	0.084	–0.404	0.594	-0.198	1	
σ	0.351	0.025	0	0	0	0	1

Table 6.4 Predicted response ratios for example cable-connected equipment systems

$\omega_{other} / \omega_{self}$	m_{other} / m_{self}	H / L_0	β	$R \cdot \exp(-1.28\sigma)$	R	$R \cdot \exp(+1.28\sigma)$
0.2	0.5	0	0.5	1.045	1.637	2.565
0.2	0.5	0.5	1	1.474	2.310	3.620
0.2	0.5	0	2	2.079	3.259	5.107
0.2	5	0	0.5	1.399	2.193	3.437
0.2	5	0.5	1	1.974	3.094	4.849
0.2	5	0	2	2.786	4.366	6.842
0.5	0.5	0.5	0.5	1.143	1.791	2.807
0.5	0.5	0	1	1.358	2.128	3.334
0.5	0.5	0.5	2	2.703	4.236	6.638
0.5	5	0.5	0.5	1.531	2.400	3.761
0.5	5	0	1	1.819	2.851	4.467
0.5	5	0.5	2	3.621	5.675	8.893

Table 6.5 Required median cable slackness for several example cable-connected equipment systems using $R = 2$.

$\omega_{other} / \omega_{self}$	m_{other} / m_{self}	H / L_0	Required median slackness	
			Δ / L_0=0.05	Δ / L_0=0.1
0.2	0.5	0	0.053	0.107
0.5	0.5	0	0.058	0.116
0.2	1	0	0.058	0.116
0.5	1	0	0.063	0.126
0.2	5	0	0.167	0.334
0.5	5	0	0.219	0.439
0.2	0.5	0.8	0.046	0.091
0.5	0.5	0.8	0.049	0.099
0.2	1	0.8	0.049	0.099
0.5	1	0.8	0.054	0.108
0.2	5	0.8	0.143	0.285
0.5	5	0.8	0.219	0.439

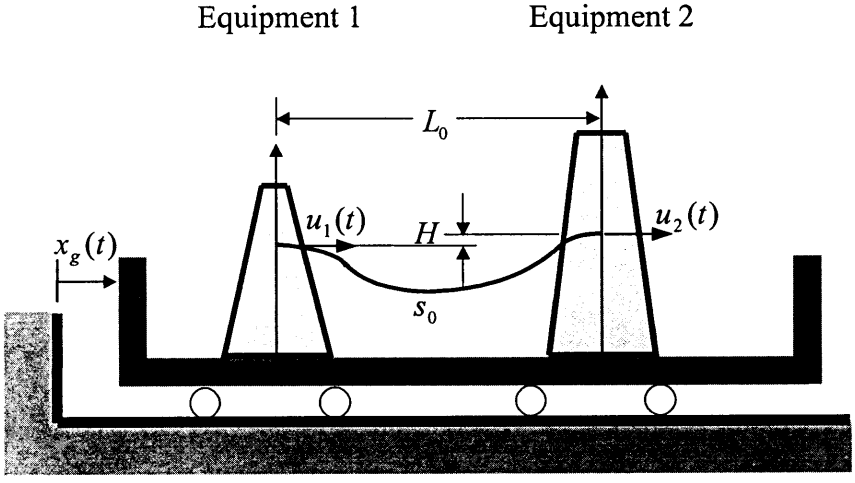

Figure 6.1 Cable-connected equipment items

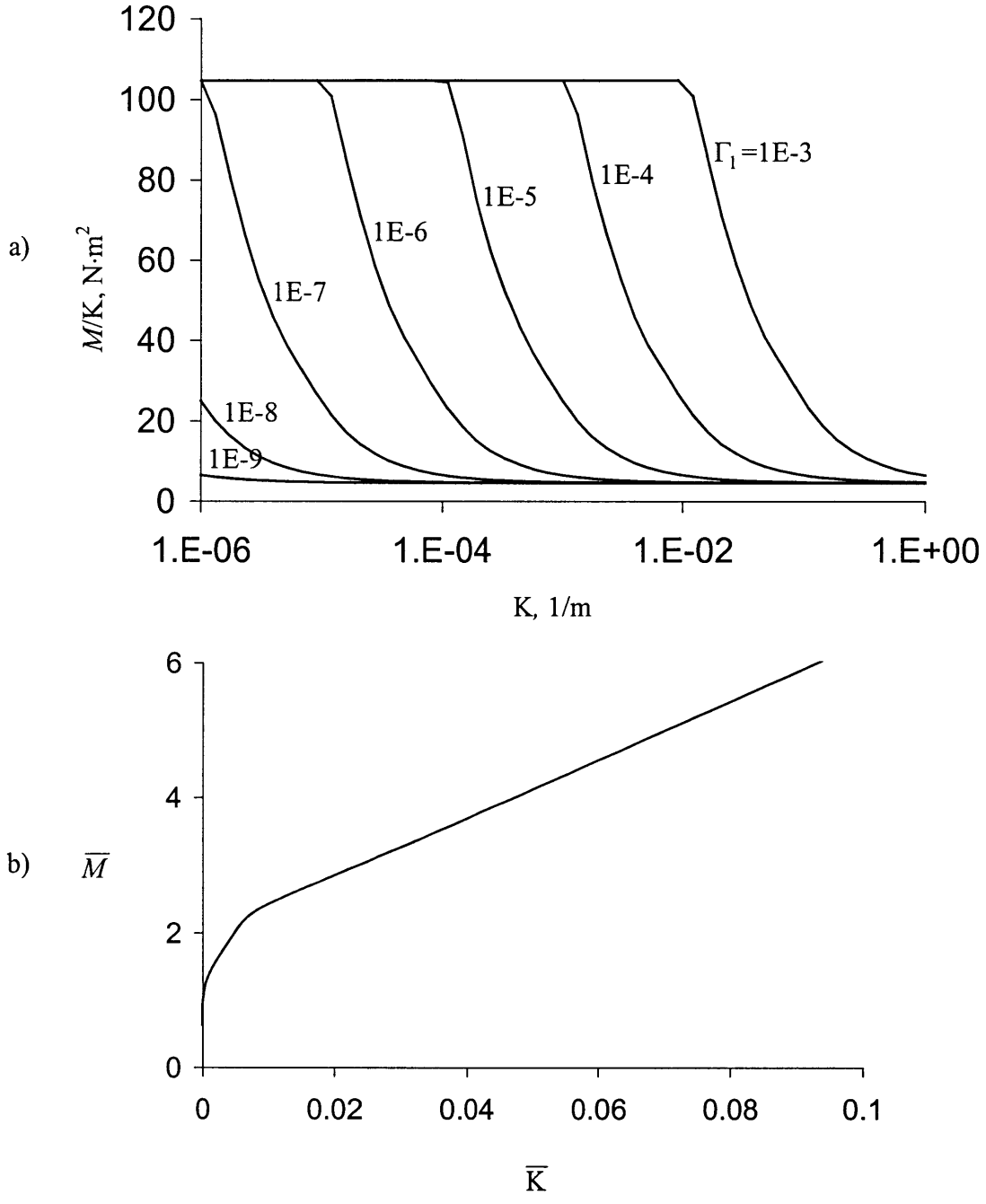

Figure 6.2 Nonlinear bending behavior of the Valerian cable:

a) secant flexural stiffness vs. curvature for different axial strain

b) normalized moment vs. normalized curvature relation

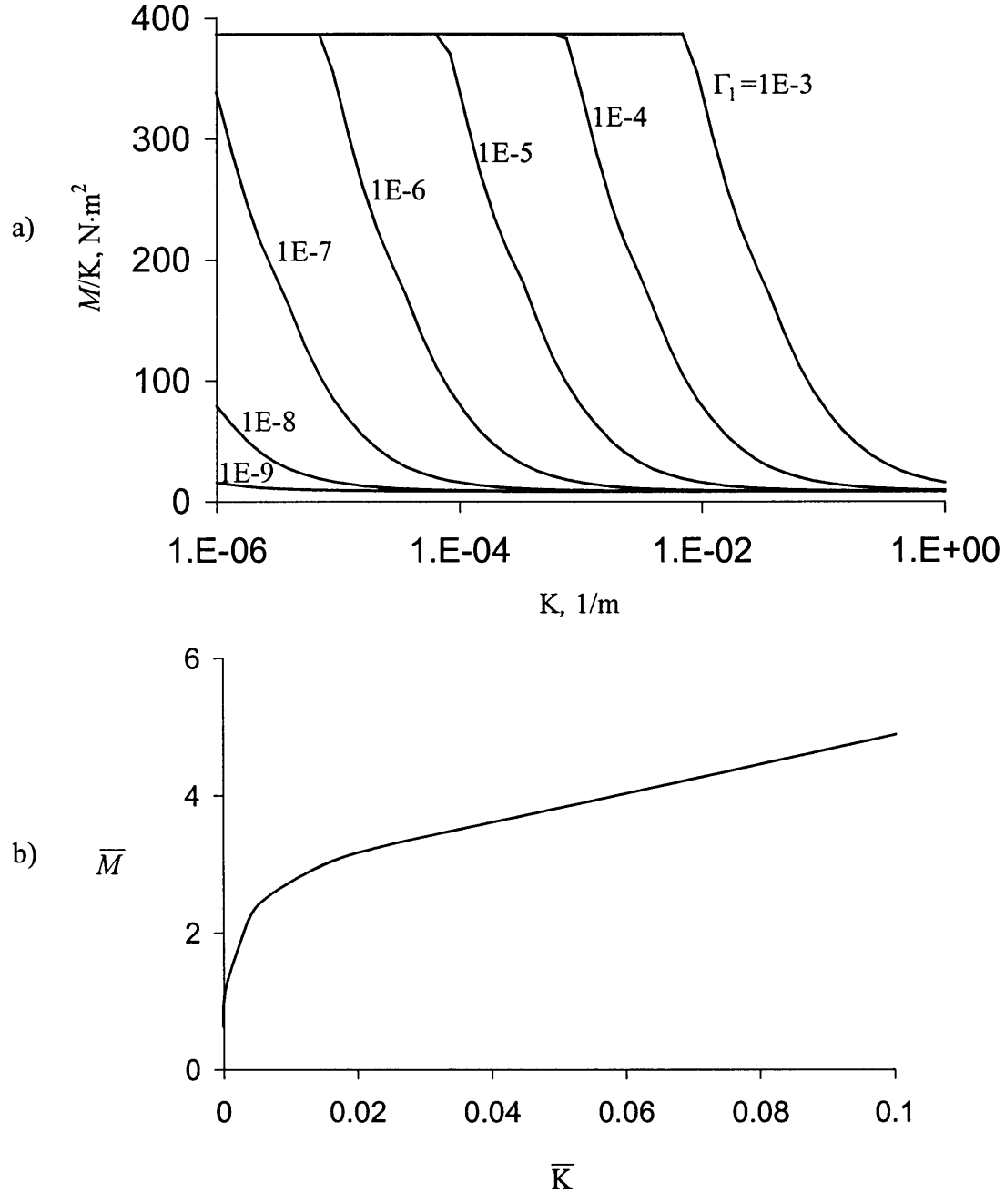

Figure 6.3 Nonlinear bending behavior of the Syringa cable:

a) secant flexural stiffness vs. curvature for different axial strain

b) normalized moment vs. normalized curvature relation

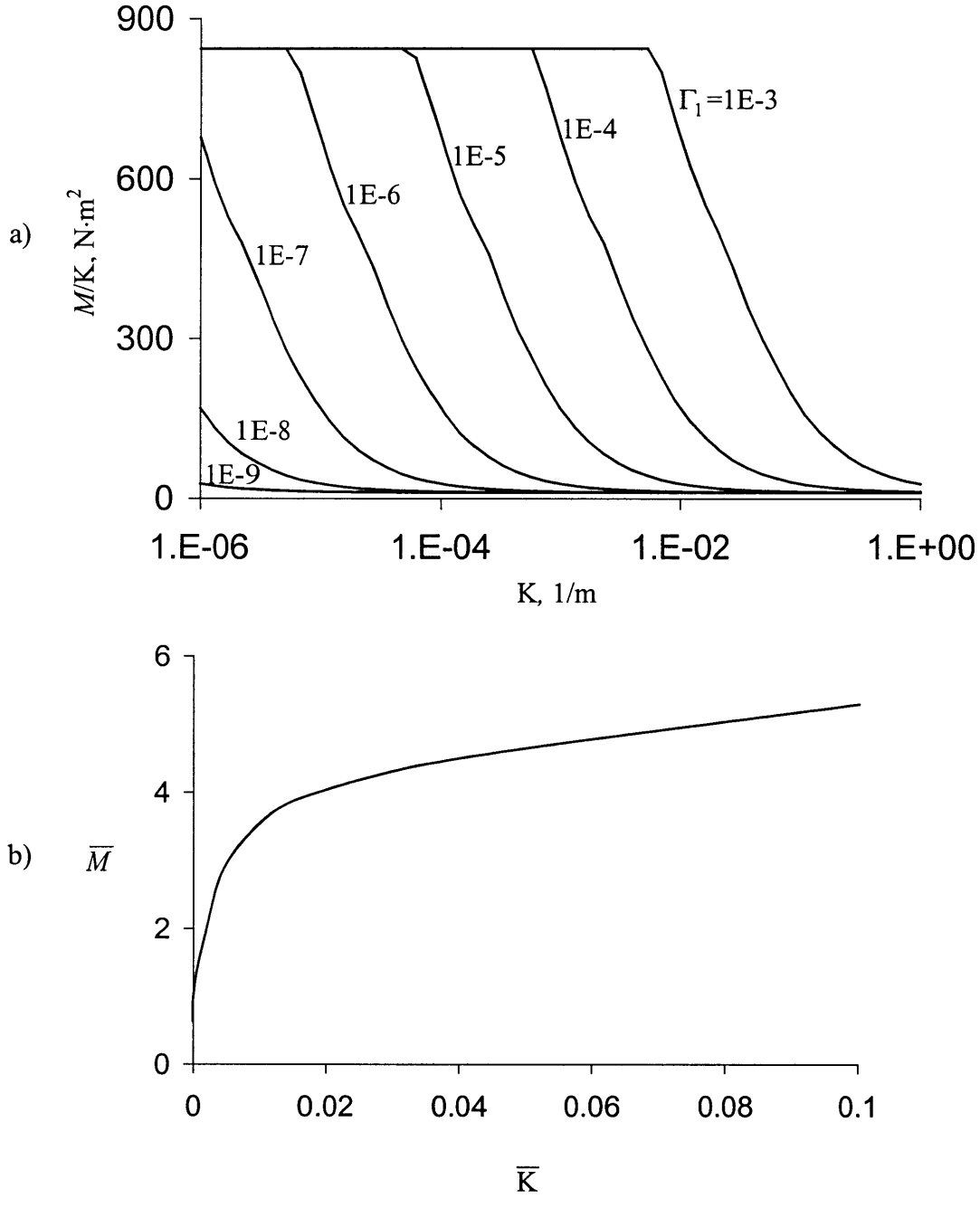

Figure 6.4 Nonlinear bending behavior of the Flag cable:

a) secant flexural stiffness vs. curvature for different axial strain

b) normalized moment vs. normalized curvature relation

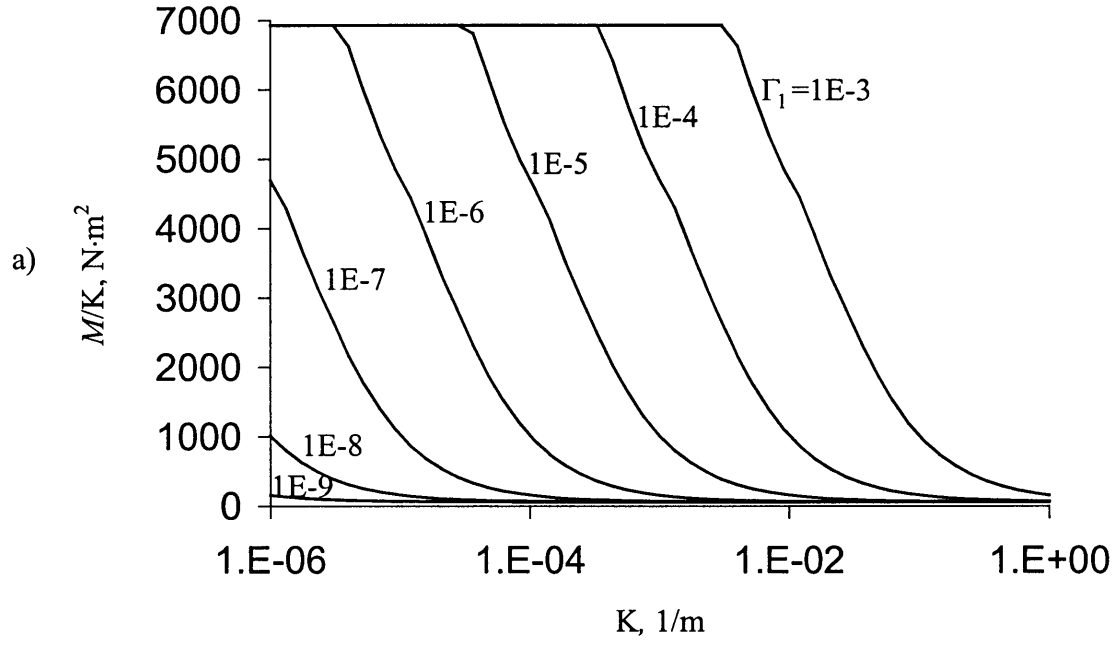

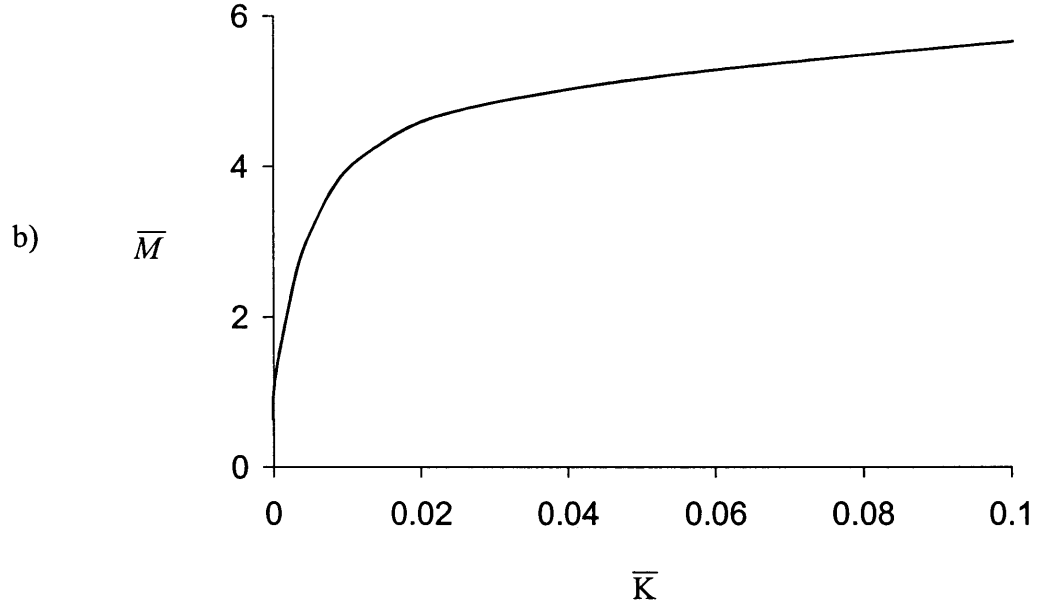

Figure 6.5 Nonlinear bending behavior of the Cowslip cable:

a) secant flexural stiffness vs. curvature for different axial strain

b) normalized moment vs. normalized curvature relation

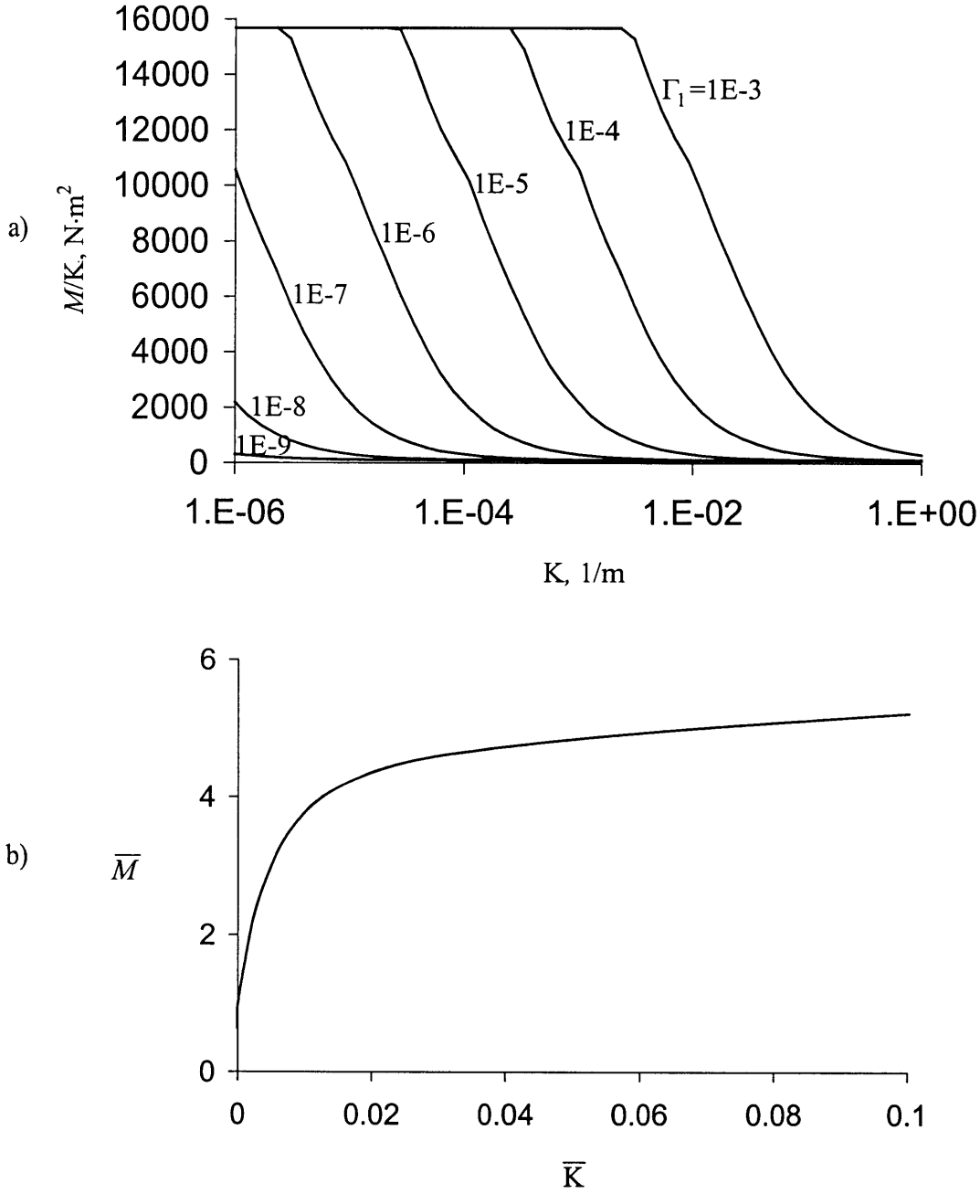

Figure 6.6 Nonlinear bending behavior of the Trillium cable:

a) secant flexural stiffness vs. curvature for different axial strain

b) normalized moment vs. normalized curvature relation

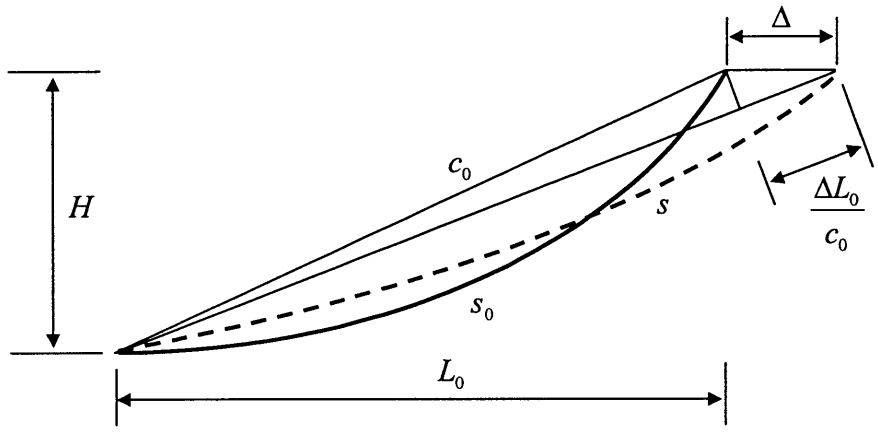

Figure 6.7 Change in slackness due to relative displacement Δ

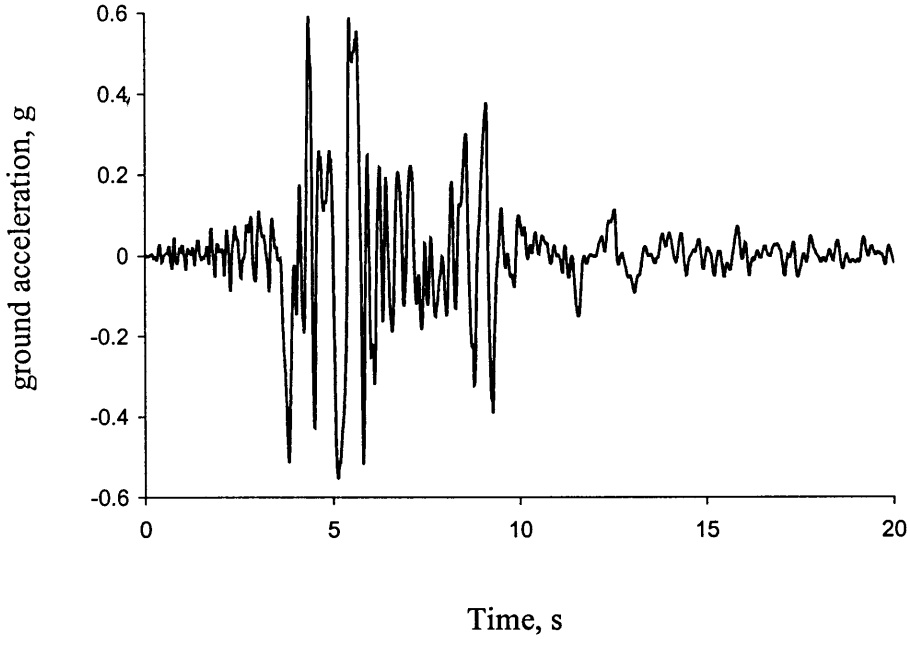

Figure 6.8 N-S component of Newhall record, 1994 Northridge Earthquake

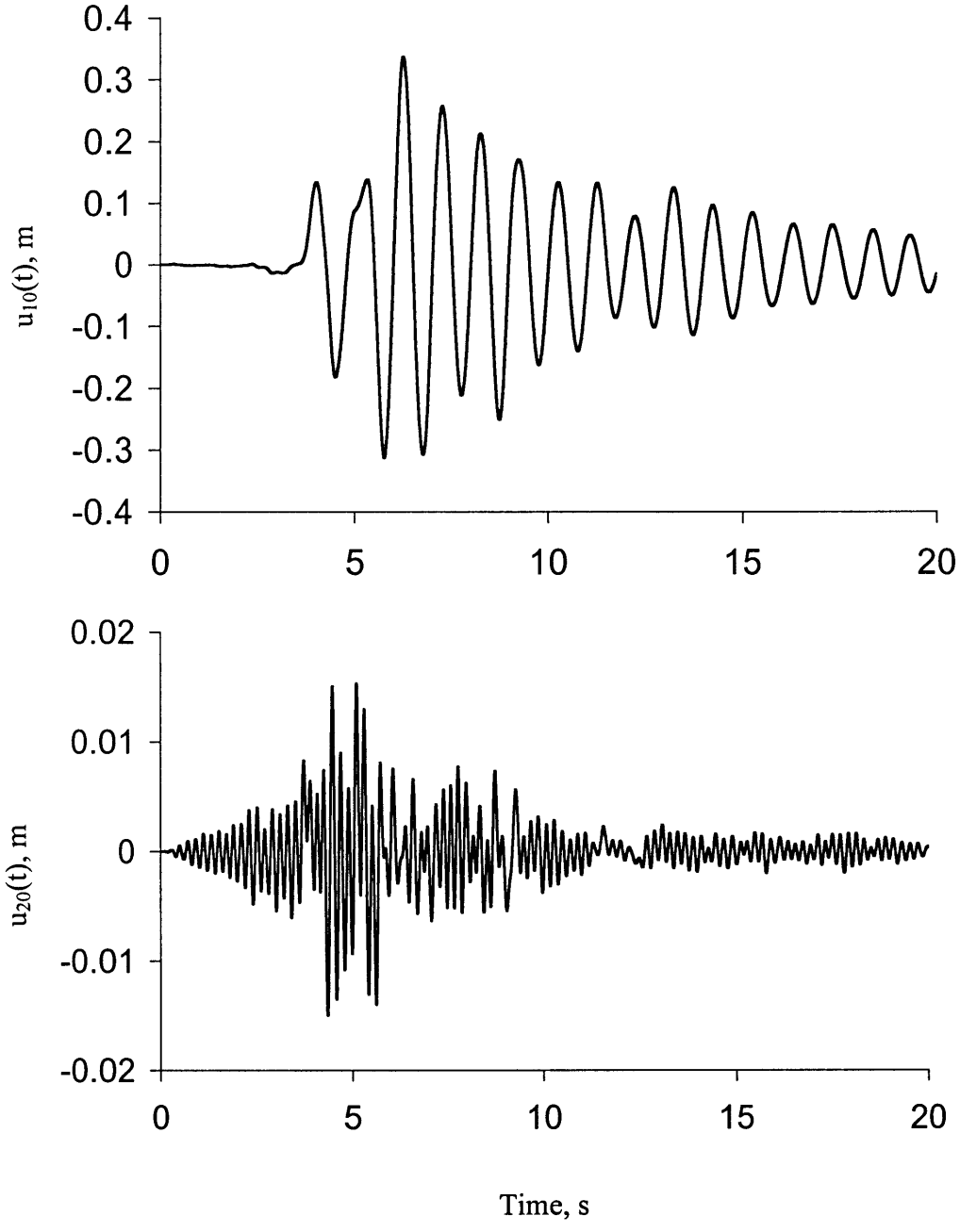

Figure 6.9 Displacement time histories of the stand-alone equipment items

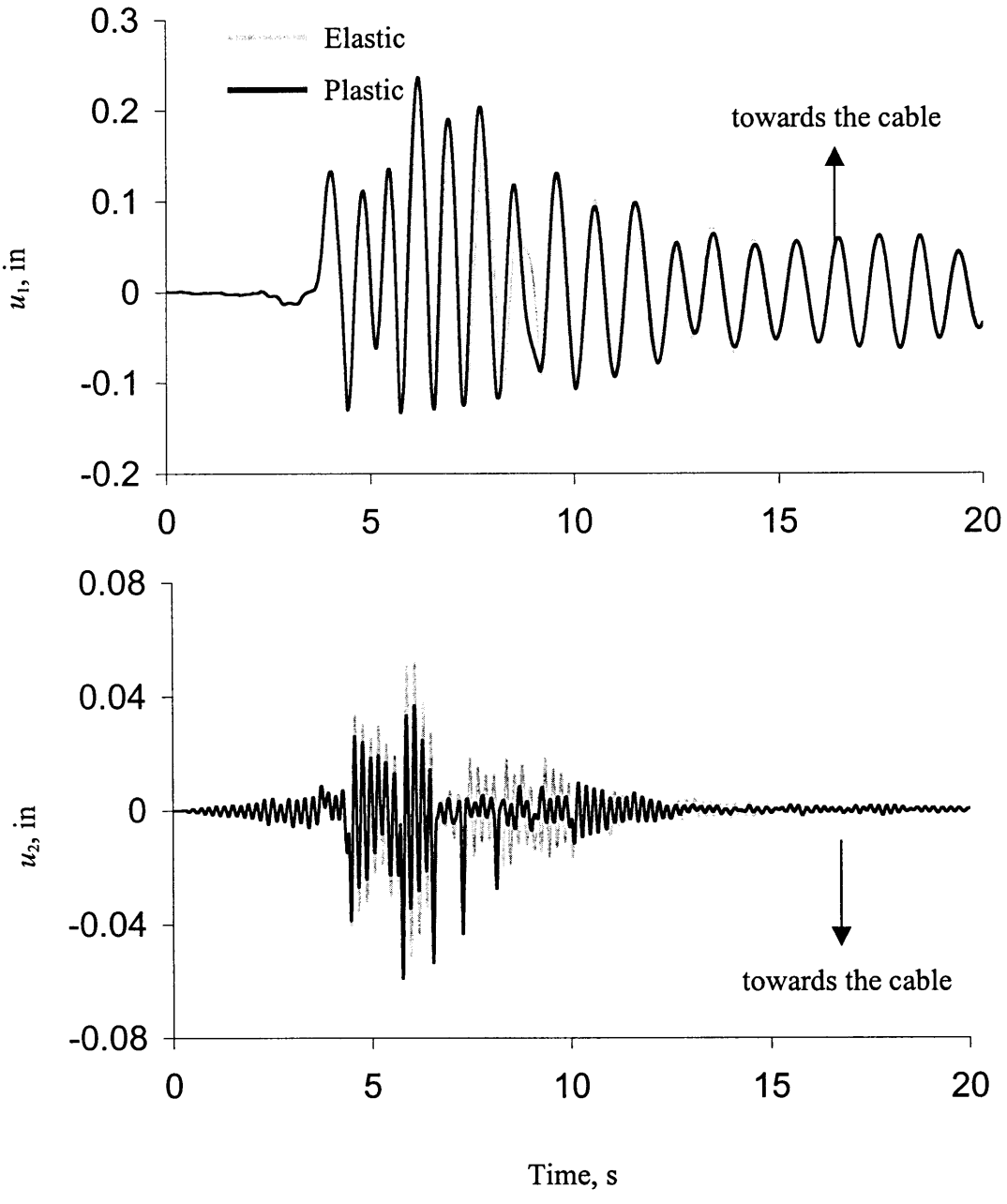

Figure 6.10 Displacement time histories of equipment items connected by the Valerian cable

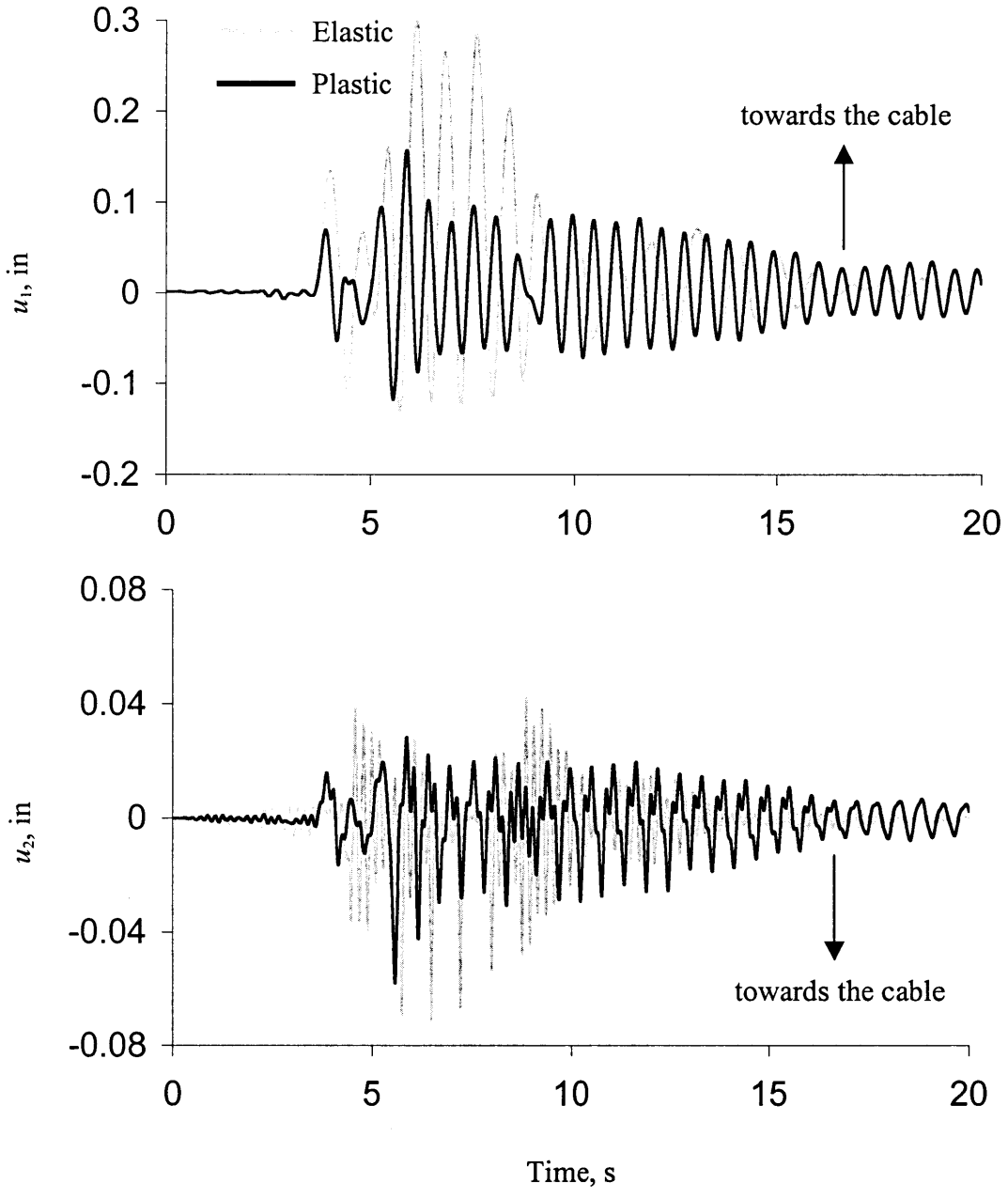

Figure 6.11 Displacement time histories of equipment items connected by the Trillium cable

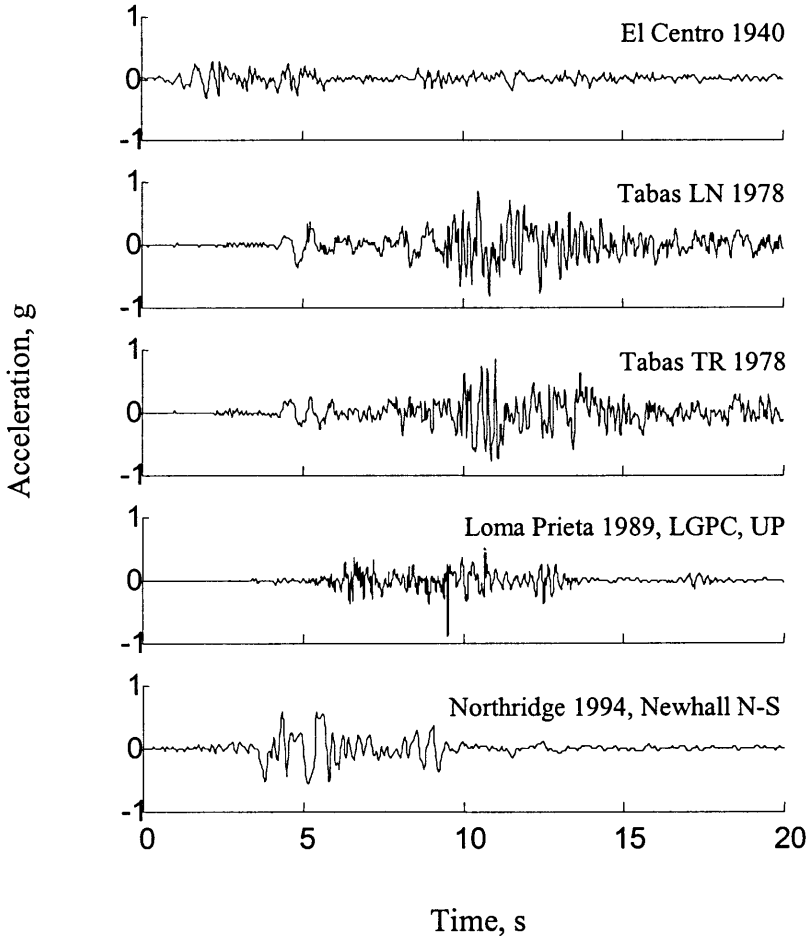

Figure 6.12 Selected accelerograms

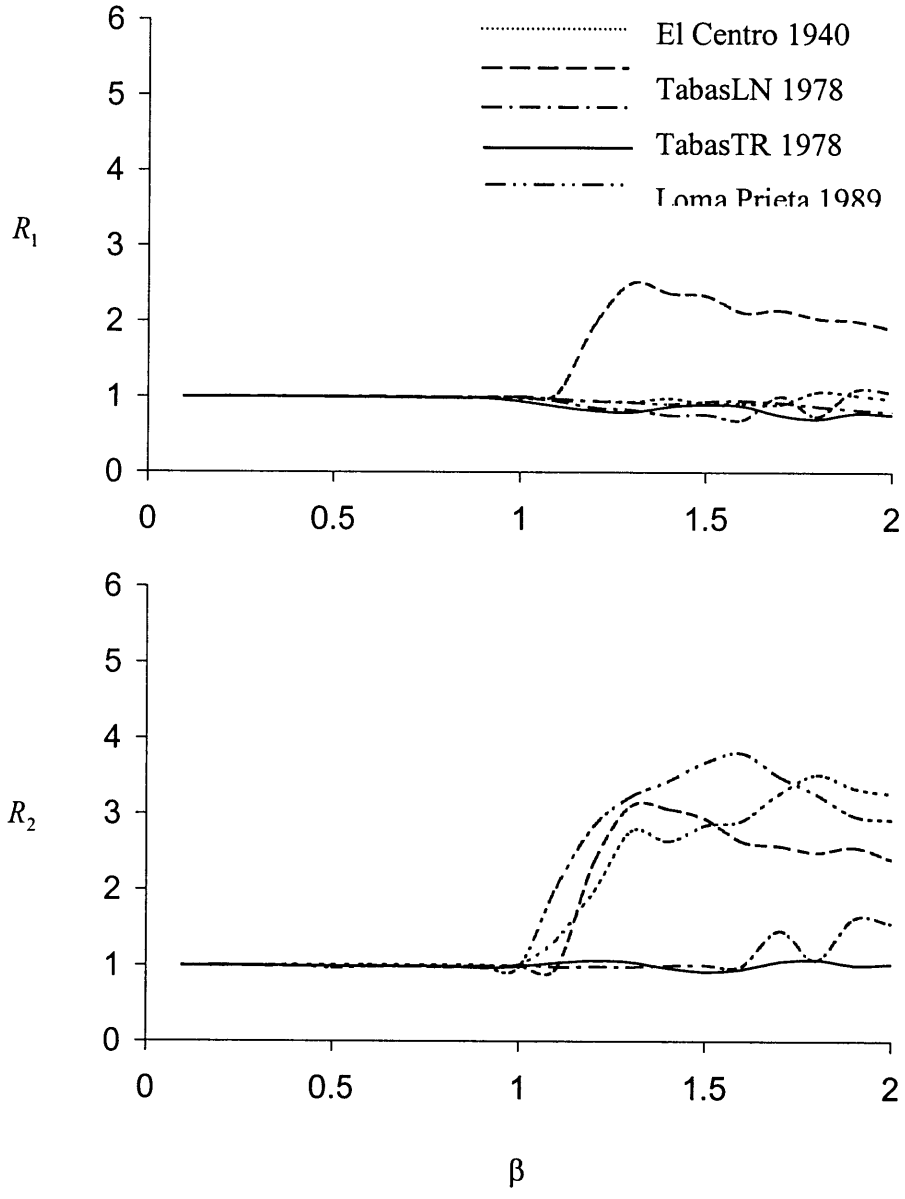

Figure 6.13 Response ratios for five earthquakes as functions of the interaction parameter calculated by the elastic finite element model for the systems connected by the Valerian cable

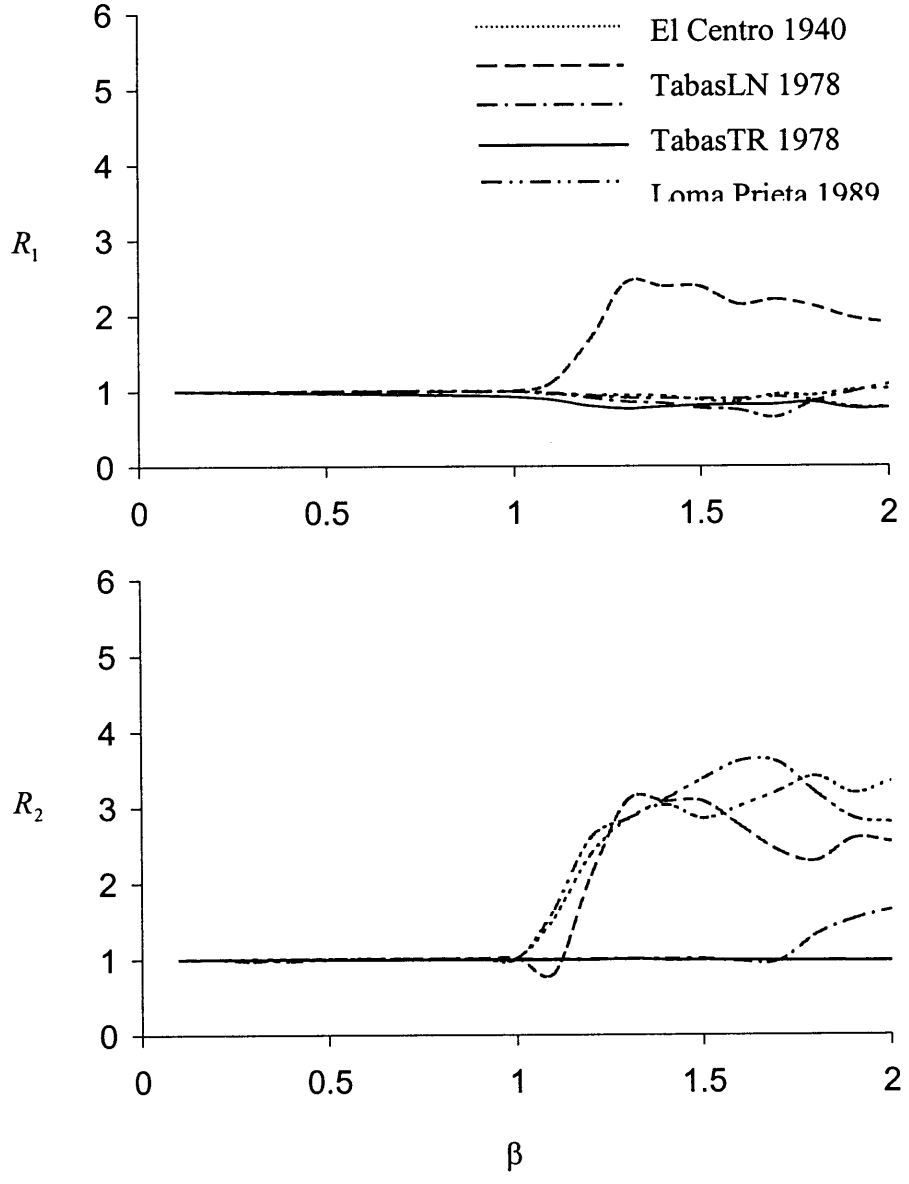

Figure 6.14 Response ratios for five earthquakes as functions of the interaction parameter calculated by the elasto-plastic finite element model for the systems connected by the Valerian cable

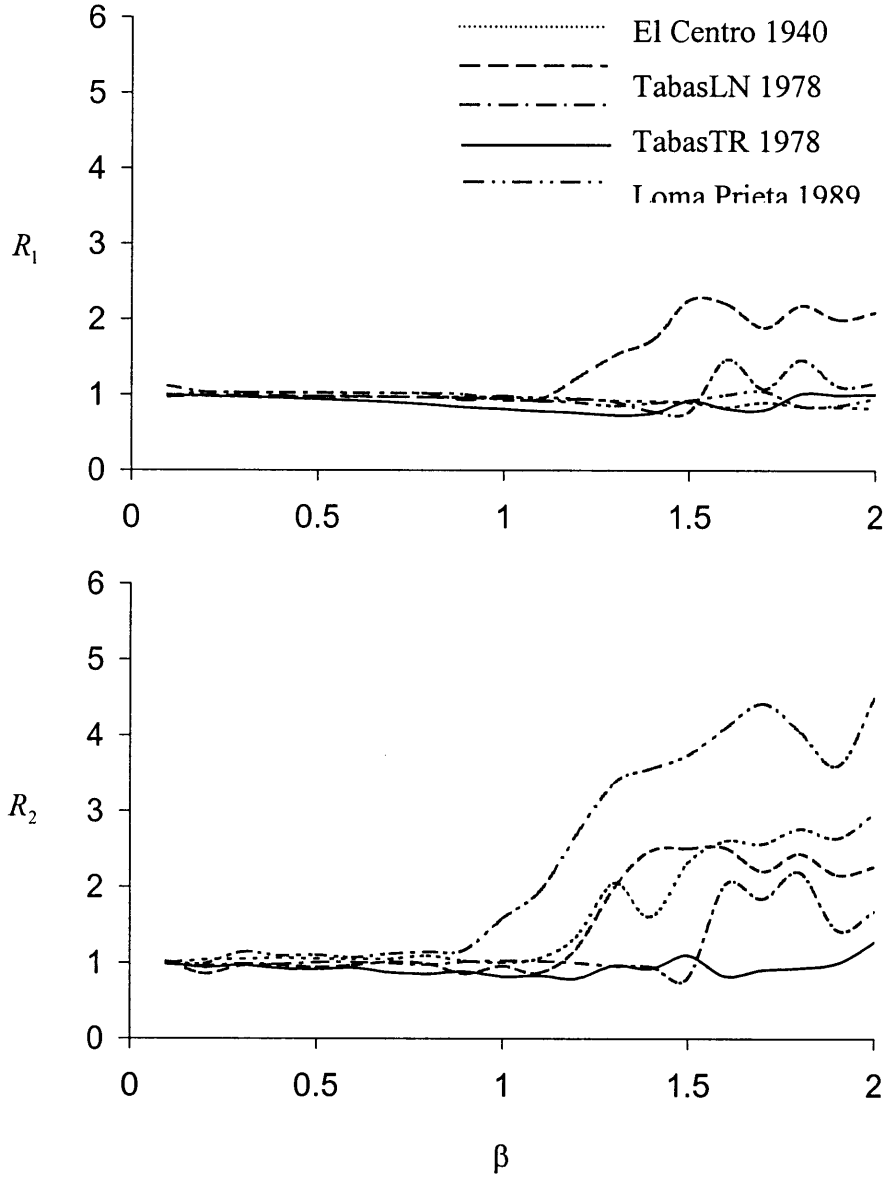

Figure 6.15 Response ratios for five earthquakes as functions of the interaction parameter calculated by the elastic finite element model for the systems connected by the Trillium cable

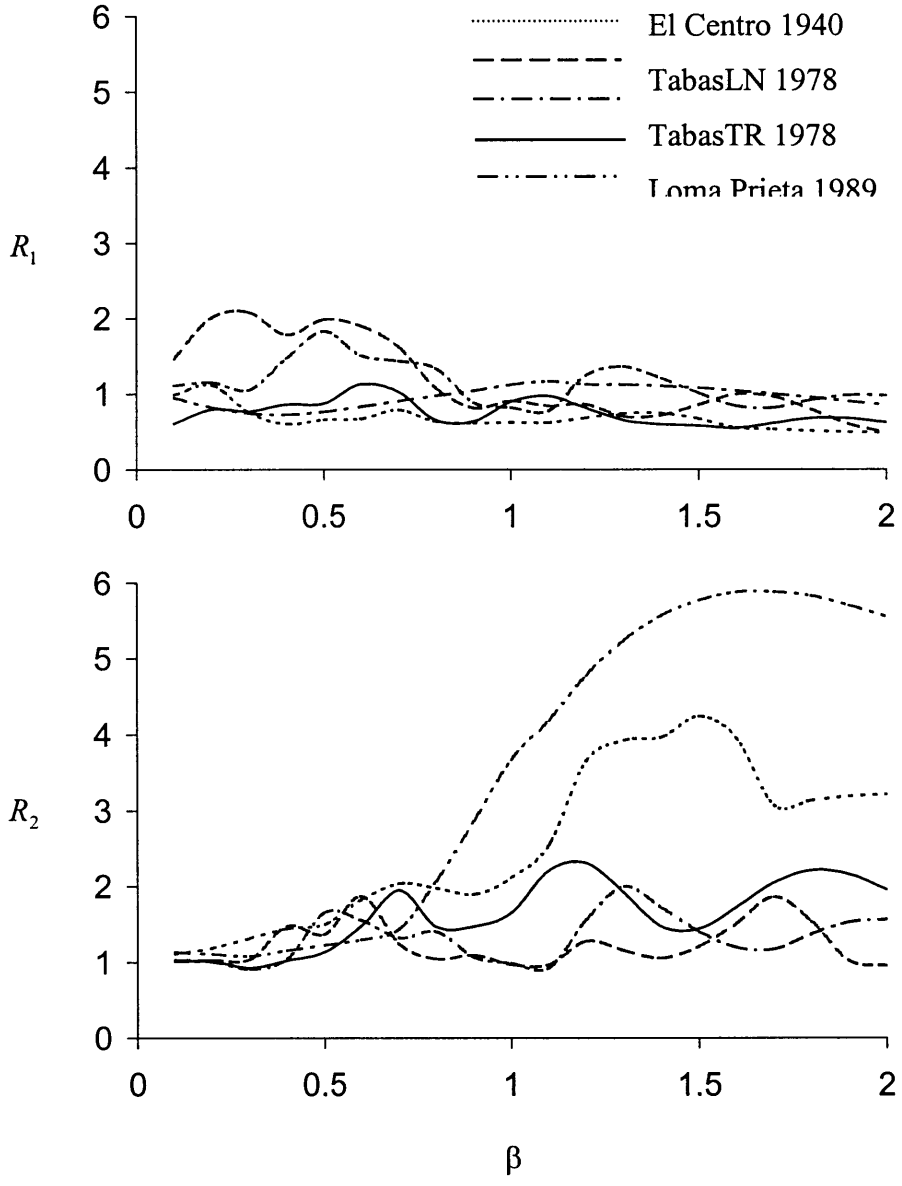

Figure 6.16 Response ratios for five earthquakes as functions of the interaction parameter calculated by the plastic finite element model for the systems connected by the Trillium cable

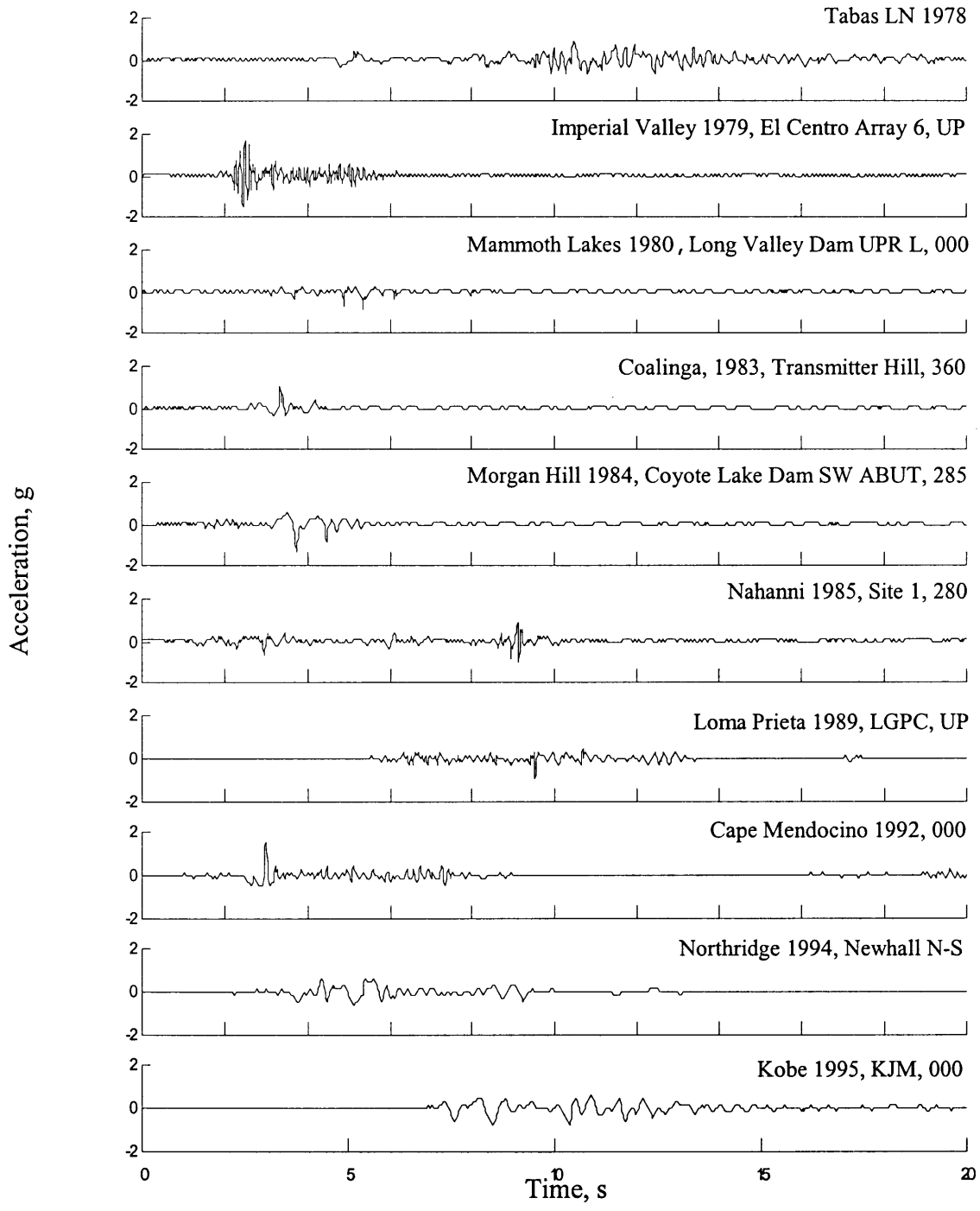

Figure 6.17 Selected accelerograms for numerical simulations

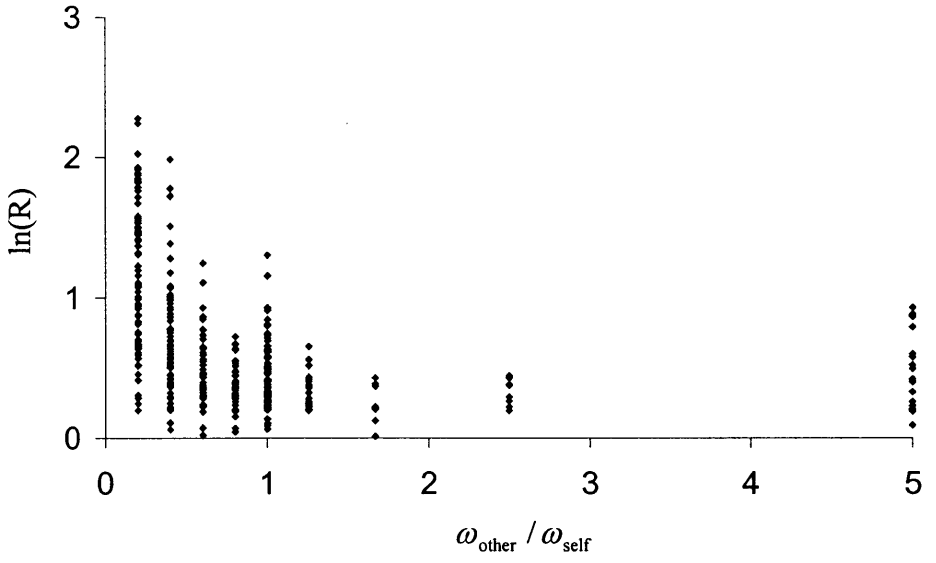

Figure 6.18 Scatter plot of the logarithm of the response ratio versus $\omega_{other} / \omega_{self}$

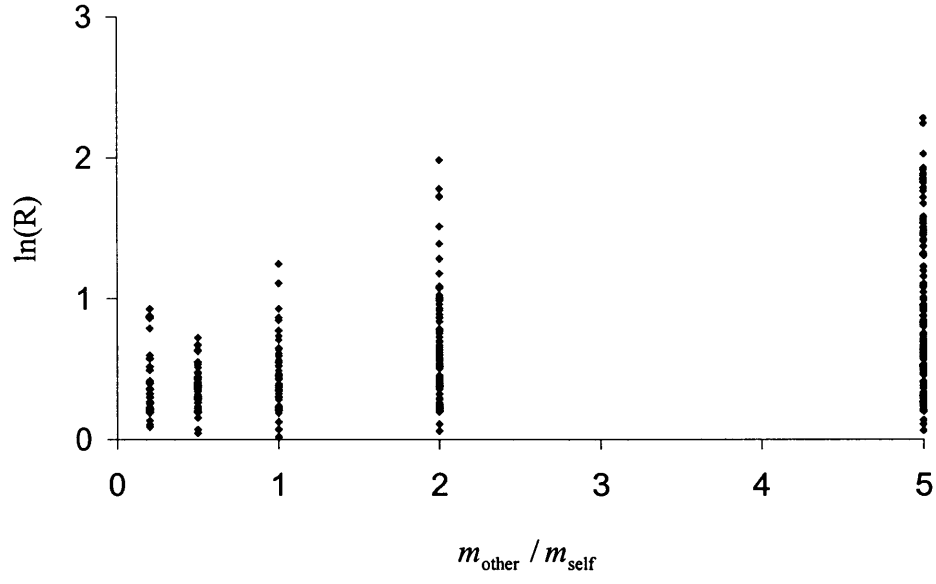

Figure 6.19 Scatter plot of the logarithm of the response ratio versus m_{other} / m_{self}

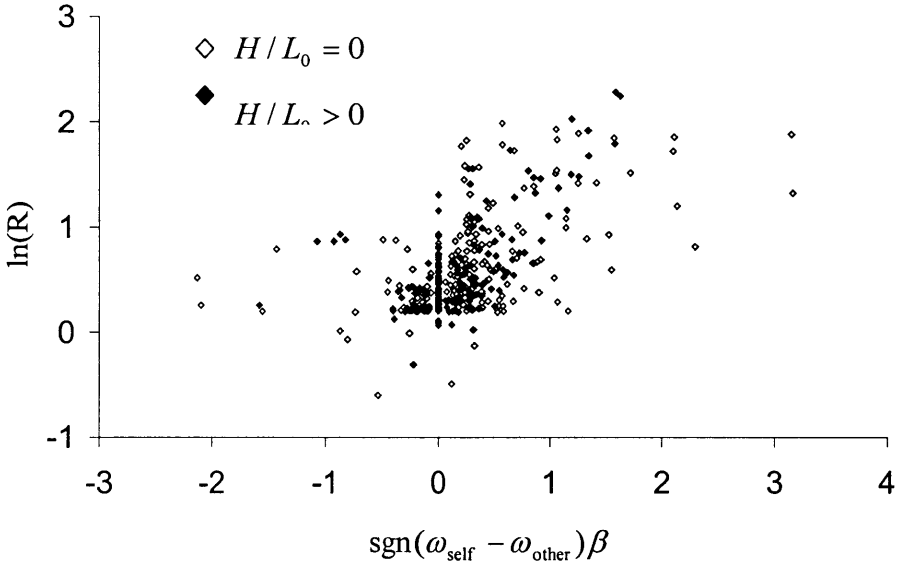

Figure 6.20 Scatter plot of the logarithm of the response ratio versus $\mathrm{sgn}(\omega_{\mathrm{self}} - \omega_{\mathrm{other}})\beta$

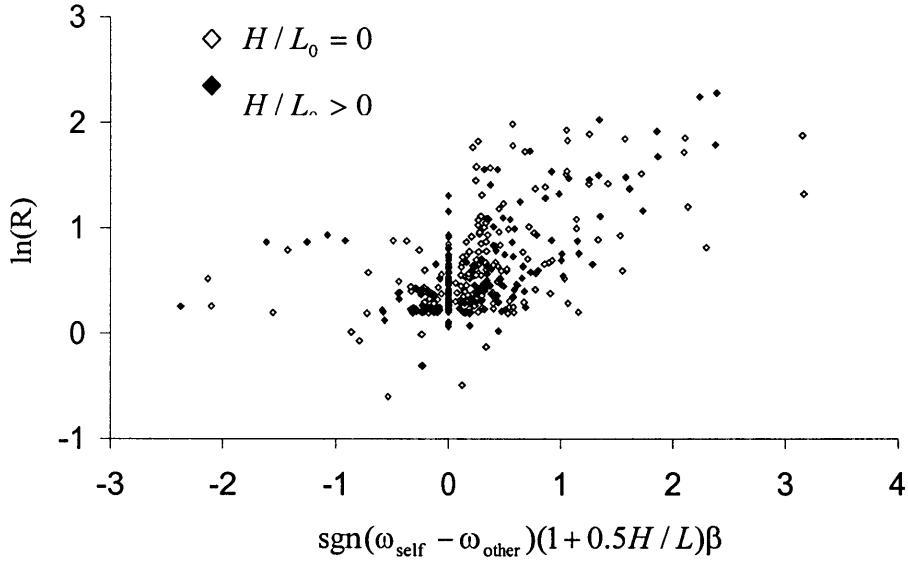

Figure 6.21 Scatter plot of the logarithm of the response ratio versus $\mathrm{sgn}(\omega_{\mathrm{self}} - \omega_{\mathrm{other}})(1 + 0.5H/L)\beta$

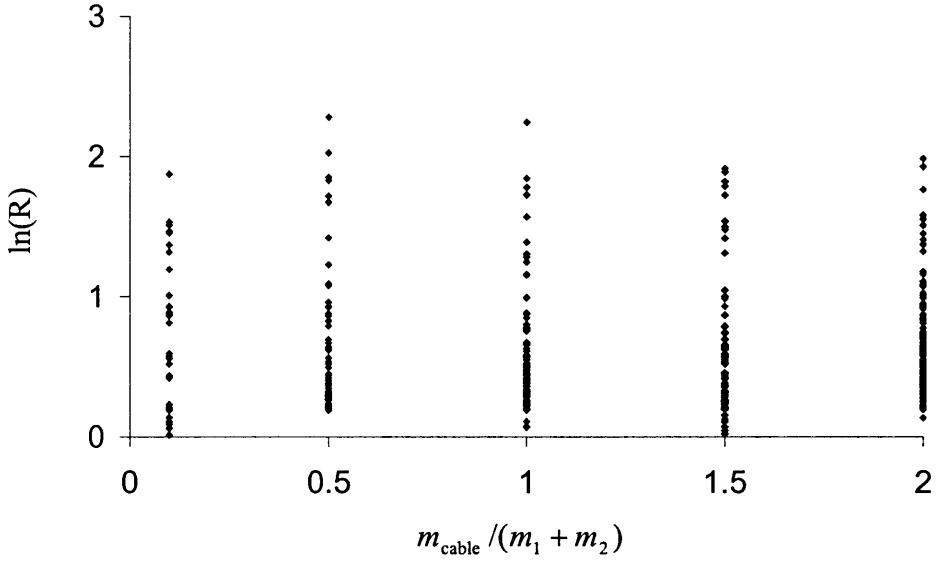

Figure 6.22 Scatter plot of the logarithm of the response ratio versus $m_{cable}/(m_1+m_2)$

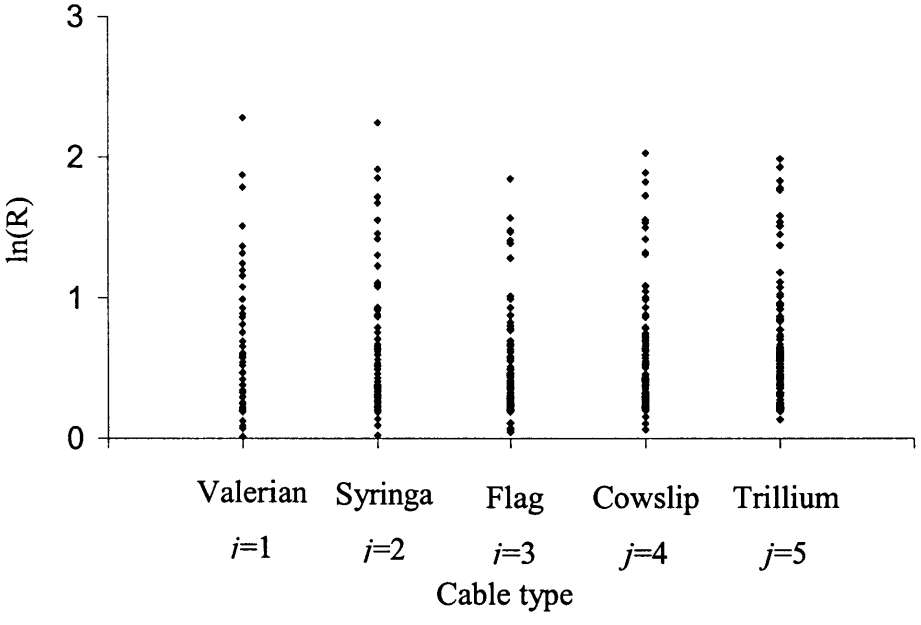

Figure 6.23 Scatter plot of the logarithm of the response ratio versus the cable type

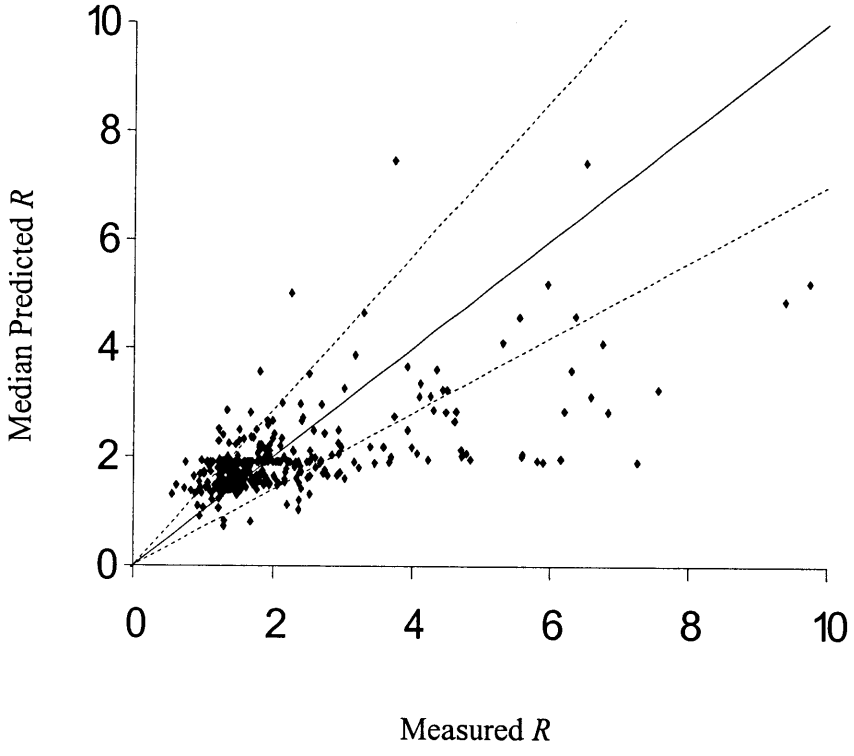

Figure 6.24 The median predicted values of the response ratios versus the measured response ratios

7 SUMMARY AND RECOMMENDATIONS FOR FURTHER STUDY

7.1 Summary

The main results of the present study can be summarized as follows:

a) An improved mechanical model for the bending behavior of conductor cables made of multiple layers of helically wrapped wires is developed. The model properly accounts for the slippage of wires under interlayer friction. The hysteretic moment-curvature relationship of the cable, resulting from the wire slippage, is derived and is shown to strongly depend on the axial force in the cable. The larger the axial tension, the larger the curvature at which wires start to slip. The model assumes the cable moves in a vertical plane, and it neglects the contribution of shear forces to the unbalanced wire tension causing the slippage.

b) A finite element formulation is developed to numerically solve for the dynamic response of the helically wrapped cable using the derived hysteretic bending moment-curvature-tension relationship. Use is made of the geometrically exact rod model developed by Simo and Vu-Quoc (1986a,b), which properly accounts for large displacements and rotations of the cable. The nonlinear hysteretic behavior of the cable is modeled by fitting a bi-linear elasto-plastic constitutive model to the nonlinear moment-curvature relationship, where the yield moment depends on the axial force in the cable. The formulation is successfully implemented in the finite element code FEAP (Taylor 1988) and is used to solve the cable plasto-dynamic problem.

c) The finite element model of the cable is used to numerically simulate static tests conducted by Filiatrault and Stearns (2002) and Dastous and Pierre (1996) on several conductor cables. The static test results by Filiatrault and Stearns (2002) for the bending moment-curvature-tension relationship are noisy and are strongly affected by conditions at support points. As a result, the comparisons with analytical predictions do not yield conclusive results. However, the comparison for global force-displacement relationship of the cable shows fairly close agreement between test results and analytical predictions. Somewhat larger energy dissipa-

tion is evident in test results compared to analytical predictions. This is partly attributed to friction in the elements of the experimental setup. Fairly good agreement is also obtained between the results of tests conducted by Dastous and Pierre (1996) and analytical predictions of the cable force versus displacement relationship. However, the tests results again show higher energy dissipation than predicted. The higher energy dissipation in the tests may also be due to yielding of wires at points of high curvature, an effect that is not included in the analytical model. Possible sources of discrepancy between test results and analytical predictions are discussed.

d) The finite element model of the cable is also used to numerically simulate dynamic tests conducted by Filiatrault and Stearns (2002) for cable-connected equipment systems and by Dastous and Pierre (1996) on horizontal conductor cables subjected to out-of-phase harmonic end displacements. Because of the complex nature of the nonlinear dynamic cable response and the sensitivity to initial conditions and model idealizations, agreement between tests results and analytical predictions on details of the response time histories is not achieved. However, several important common features between tests results and analytical predictions are observed. These include the observation of significant compression forces in the cable, which are attributed to the flexural stiffness and horizontal mass inertia of the cable; large amplification of the dynamic cable force relative to the cable force in the static equilibrium position, particularly for taut cables; and large amplification of connected equipment response relative to its stand-alone response due to the dynamic interaction and cable inertia, particularly for the higher frequency equipment item.

e) The finite element model is used to conduct parametric studies of the dynamic interaction effect between two idealized electrical substation equipment items connected by a conductor cable. Comparisons between analyses with elastic cable with minimum moment of inertia and elasto-plastic cable with full account of wire slippage demonstrate the effect of energy dissipation due to wire slippage, which is found to be significant in large-diameter cables with many layers of wires. Additional parametric studies explore the relation between the response ratio, which is a quantitative measure of the interaction effect, and the interaction parameter β. This parameter is found to be a simple and informative parameter for predicting the interaction effect, but it is found that our previous provisional recommendation to use

$\beta < 1$ to avoid the adverse interaction effect may not be sufficiently conservative in certain cases. To develop a simple predictive formula for the interaction effect, a large sample of cable-connected equipment systems are investigated to develop a large data set of response ratios. This data set is used in conjunction with well-established statistical techniques to develop a simple formula relating the response ratio to equipment, cable and ground motion characteristics. This formula is then recast to provide a rule for the required cable slackness in order to limit the response ratio to a specified value with a given exceedance probability. This formula can be used in practice as a guide to determine the needed length of the conductor cable for given equipment and ground motion characteristics.

The improved mechanical model and the finite element formulation for the helically wrapped conductor cable developed in this study can be used for many problems of practical interest beyond those reported herein. Dynamic analysis of power transmission lines subjected to earthquake, wind and ice loading, and of electrical substation equipment connected by vertical conductor cables to overhead transmission lines are two such examples. Other examples include cable-supported guyed towers, tension-leg platforms, and cable-stayed bridges.

7.2 Recommendation for Further Study

In light of the results obtained in the present study, consideration of the following topics for further study is recommended:

a) Further improve the mechanical model of the helically wrapped conductor cable by accounting for the influence of the shear force (varying bending moment) on the slippage of wires. It is also necessary to extend the model to 3-dimensional motions of the cable in order to more fully investigate the response to earthquake ground motions and wind effects.

b) Develop a more robust integration algorithm for solving the elasto-plastic dynamic cable problem with large displacements and rotations, which can handle the large mismatch between the flexural and axial stiffnesses of the cable and produce stable and accurate estimates of the cable force and other high-order responses.

c) There is need for further experiments under well controlled environment to better understand the hysteretic behavior of the helically wrapped conductor cable under bending and axial force, so as to provide a basis for the validation and calibration of analytical models,

including the one developed in this study. Experiments to determine the interlayer friction coefficient between the wires is also needed.

d) Despite its limitations, the finite element model for the helically wrapped cable developed in this study provides an unprecedented tool for dynamic analysis of conductor cables and cable-connected equipment systems. This tool can be used to study many systems of practical interest. Examples include power transmission lines subjected to earthquake, wind and ice loading; electrical substation equipment connected by vertical conductor cables to overhead transmission lines; cable-supported guyed towers; tension-leg platforms, and cable-stayed bridges.

REFERENCES

Applied Technology Council (1992). *Guidelines for Seismic Testing of Components of Steel Structures*. ATC-24, Applied Technology Council, Redwood City, CA.

Benuska, L. (Editor) (1990). Chapter 8 — Lifelines. *Earthquake Spectra* (Supplement) 6: 315-338.

Box, G. E. P. and G. C. Tiao (1992). *Bayesian Inference in Statistical Analysis.* Wiley classic library ed. Wiley, New York, NY.

Cardou, A. and C. Jolicoeur (1997). Mechanical models of helical strands. *Applied Mechanics Reviews*, 50(1): 1-14.

Cosserat, E., and F. Cosserat (1967). *Theory of Deformable Bodies*, National Aeronautics and Space Administration, Washington, D.C.

Costello, G. A. (1978). Analytical investigation of wire rope. *Applied Mechanics Reviews*, 31(7): 897-900.

Costello, G. A. (1997). *Theory of Wire Rope*, Springer, 2nd ed. New York, NY.

Costello, G. A. and G. J. Butson (1982). Simplified bending theory for wire rope. *ASCE Journal of the Engineering Mechanics Division*, 114(7): 1166-1182.

Dastous, J.-B., and J.-R. Pierre (1996). Experimental investigation on the dynamic behavior of flexible conductors between substation equipment during an earthquake. *IEEE Transaction on Power Delivery*, 11(2): 801-807.

Der Kiureghian, A., J. L. Sackman, and K.-J. Hong (1999). *Interaction in Interconnected Electrical Substation Equipment Subjected to Earthquake Ground Motions.* Report No. PEER 1999/01 University of California, Berkeley, CA.

Der Kiureghian, A., K.-J. Hong, and J. L. Sackman (2000). *Further Studies on Seismic Interaction in Interconnected Electrical Substation Equipment.* Report No. PEER 2000/01 University of California, Berkeley, CA.

Der Kiureghian, A., J. L. Sackman, and K.-J. Hong (2001). Seismic interaction in linearly connected electrical substation equipment. *Earthquake Engineering and Structural Dynamics*, 30: 327-347.

Division of Aluminum Company of America (1974). *Electrical Conductors*. Alcoa Products Company.

EPRI (1979). *Transmission Line Reference Book – Wind-Induced Conductor Motion*. Electrical Power Research Institute, Palo Alto, CA.

Filiatrault, A. and C. Stearns (2002). *Electrical Substation Equipment Interaction — Experimental Flexible Conductor Studies*. Report No. SSRP 2002/09 University of California, San Diego, CA.

Flouriot, S., S. Forest, and L. Remy (2003). Strain localization phenomena under cyclic loading: application to fatigue of single crystals. *Computational Materials Science*, 26: 61-70.

Gardoni, Paolo, A. Der Kiureghian, and K. M. Mosalam (2002). *Probablistic Models and Fragility Estimates for Bridge Components and Systems*. Report No. PEER 2002/13 University of California, Berkeley, CA.

Gere, J. M. and S. P. Timoshenko (1997). *Mechanics of Materials*, 4th ed. PWS Pub Co., Boston, MA.

Hall, J. (Editor) (1995). Chapter 4 — Lifelines. *Earthquake Spectra* (Supplement C) 11: 188-217.

Hilber, H. M., T. J. R. Hughes, and R. L. Taylor (1977). Improved numerical dissipation for time integration algorithms in structural dynamics. *Earthquake Engineering and Structural Dynamics*, 5: 283-292.

Hobbs, R. E. and M. Raoof (1982). Interwire slippage and fatigue prediction in stranded cables for TLP tethers. *Proceedings of 3rd International Conference on the Behavior of Offshore Structures*, C. Chryssostomidis and J. J. Connor, Eds. McGraw-Hill, New York, NY.

Hong, K.-J., A. Der Kiureghian, and J. L. Sackman (2001). Seismic interaction in cable-connected equipment items. *Journal of Engineering Mechanics*, 127(11): 1096-1105.

Huang, X. and O. Vinogradov (1993). Analysis of dry friction hysteresis in cables under uniform bending. *Proceedings of Damping 93*, San Francisco CA, FCA1-FCA20.

Hruska, F. H. (1951). Calculation of stresses in wire ropes. *Wire and Wire Products*, 26(9): 766-767, 799-801.

IEEE (1997). *IEEE 693 – Recommended Practices for Seismic Design of Substations.* IEEE Standard Draft No. 6. 1, IEEE Standards Department, Piscataway, NJ.

IEEE (1999). *Draft Recommended Practice for the Design of Flexible Buswork Located in Seismically Active Area.* IEEE P1527/D5, IEEE Standards Department, Piscataway, NJ.

Irvine, H. M. (1981). *Cable Structures*, MIT Press, Cambridge, MA.

Knapp, R. H. (1988). Helical wire stresses in bent cables. *Journal of Offshore Mechanics and Arctic Engineering*, 110: 55-61.

Lanteigne, J. (1985). Theoretical estimation of the response of helically armored cables to tension, torsion and bending. *Journal of Applied Mechanics*, 52: 423-432.

Love, A. E. H. (1944). *A Treatise on the Mathematical Theory of Elasticity*, Dover Publications, New York, NY.

Lutchansky, M. (1969). Axial stresses in armor wires of bent submarine cables. *Journal of Engineering for Industry, Transactions of ASME*, 91: 687-693.

McIver, D. B. (1995). A method of modeling the detailed component and overall structural behavior of flexible pipe sections. *Engineering Structures*, 17(4): 254-266.

Nutbourne, A. W. and R. R. Martin (1988). *Differential Geometry Applied to Curve and Surface Design.* Halsted Press, New York, NY.

Out, J. M. M. and B. J. von Morgen (1997). Slippage of helical reinforcing on a bent cable. *Engineering Structures*, 19(6): 507-515.

Papailiou, K. O. (1997). On the bending stiffness of transmission line conductors. *IEEE Transactions on Power Delivery*, 12(4): 1576-1588.

Phillips, J. W. and G. A. Costello (1973). Contact stresses in twisted wire cables. *ASCE Journal of the Engineering Mechanics Division*, 99(EM2): 331-341.

Raoof, M. (1989). Free bending tests on large spiral stands. *Proceedings of the Institution of Civil Engineers Part 2*, 87: 605-626.

Schiff, A. J. (Editor) (1995). *Northridge earthquake: lifeline performance and post-earthquake response*. ASCE, New York, NY.

Simo, J. C., and T. J. R. Hughes (1998). *Computational Inelasticity*. Springer, Verlag, Berlin.

Simo, J. C., N. Tarnow and M. Doblare (1995). Non-Linear Dynamics of Three-Dimensional Rods: Exact Energy and Momentum Conserving Algorithms. *International Journal for Numerical Methods in Engineering*, 38(9): 1431-1473.

Simo, J. C. and L. Vu-Quoc (1986a). On the dynamics of flexible beams under large overall motions — The plane case: Part I. *Journal of Applied Mechanics*, 53: 849-854.

Simo, J. C. and L. Vu-Quoc (1986b). On the dynamics of flexible beams under large overall motions — The plane case: Part II. *Journal of Applied Mechanics*, 53: 855-863.

Taylor, R. L. (1998). *FEAP Version 7.1 User Manual*. Department of Civil and Environmental Engineering, UC Berkeley, CA.

APPENDIX A

Derivation of (2.14)

The differential length ds can be written as

$$ds = ds_0\sqrt{\left(\frac{dX_1}{ds_0}\right)^2+\left(\frac{dX_2}{ds_0}\right)^2+\left(\frac{dX_3}{ds_0}\right)^2} \tag{A2.1}$$

Since s_0 and φ have a one-to-one relationship in the small segment of a wire, we can use the chain rule of differentiation to write

$$ds = ds_0\sqrt{\left[\left(\frac{dX_1}{d\varphi}\right)^2+\left(\frac{dX_2}{d\varphi}\right)^2+\left(\frac{dX_3}{d\varphi}\right)^2\right]\left(\frac{d\varphi}{ds_0}\right)^2} \tag{A2.2}$$

Using (2.5) and (2.11b), we have

$$\begin{aligned} ds &= ds_0\sqrt{\left(\left[\frac{d}{d\varphi}(r\cos(\varphi))\right]^2+\left\{\frac{d}{d\varphi}\left[(\rho_c+r\sin(\varphi))\cos(\theta_c)\right]\right\}^2+\left\{\frac{d}{d\varphi}\left[(\rho_c+r\sin(\varphi))\sin(\theta_c)\right]\right\}^2\right)\left(\frac{\sin(\alpha_0)}{r}\right)^2} \\ &= ds_0\sqrt{\left(r^2\sin^2(\varphi)+\left\{r\cos(\varphi)\cos(\theta_c)-\left[\rho_c+r\sin(\varphi)\right]\sin(\theta_c)\frac{d\theta_c}{d\varphi}\right\}^2+\left\{r\cos(\varphi)\sin(\theta_c)+\left[\rho_c+r\sin(\varphi)\right]\cos(\theta_c)\frac{d\theta_c}{d\varphi}\right\}^2\right)\left(\frac{\sin(\alpha_0)}{r}\right)^2} \\ &= ds_0\sqrt{\left\{r^2\sin^2(\varphi)+r^2\cos^2(\varphi)+\left[\rho_c+r\sin(\varphi)\right]^2\left(\frac{d\theta_c}{d\varphi}\right)^2\right\}\left(\frac{\sin(\alpha_0)}{r}\right)^2} \end{aligned} \tag{A2.3}$$

Accounting for (2.13), the expression becomes

$$\begin{aligned} ds &= ds_0\sqrt{\left\{r^2+\left[\rho_c+r\sin(\varphi)\right]^2\left[(1+\varepsilon_c)\frac{\kappa_c r}{\tan(\alpha_0)}\right]^2\right\}\left(\frac{\sin(\alpha_0)}{r}\right)^2} \\ &= ds_0\sqrt{\sin^2(\alpha_0)+\cos^2(\alpha_0)(1+\varepsilon_c)^2\left[1+\kappa_c r\sin(\varphi)\right]^2} \end{aligned} \tag{A2.4}$$

Derivation of (2.15)

The curvature vector $\boldsymbol{\kappa}_w$ is defined as

$$\boldsymbol{\kappa}_w = \frac{d}{ds}\left(\frac{d\mathbf{X}}{ds}\right) \tag{A2.5}$$

Since s and s_0 have a one-to-one relationship, we can use the chain rule of differentiation to write

$$\begin{aligned}\boldsymbol{\kappa}_w &= \frac{ds_0}{ds}\cdot\frac{d}{ds_0}\left(\frac{ds_0}{ds}\frac{d\mathbf{X}}{ds_0}\right)\\ &= \frac{ds_0}{ds}\cdot\left[\frac{d}{ds_0}\left(\frac{ds_0}{ds}\right)\cdot\frac{d\mathbf{X}}{ds_0}+\frac{ds_0}{ds}\cdot\frac{d}{ds_0}\left(\frac{d\mathbf{X}}{ds_0}\right)\right]\end{aligned} \tag{A2.6}$$

Using the chain rule between s_0 and φ, we can further write

$$\begin{aligned}\boldsymbol{\kappa}_w &= \frac{ds_0}{ds}\cdot\left[\frac{d\varphi}{ds_0}\cdot\frac{d}{d\varphi}\left(\frac{ds_0}{ds}\right)\cdot\frac{d\varphi}{ds_0}\cdot\frac{d\mathbf{X}}{d\varphi}+\frac{ds_0}{ds}\cdot\frac{d\varphi}{ds_0}\cdot\frac{d}{d\varphi}\left(\frac{d\varphi}{ds_0}\cdot\frac{d\mathbf{X}}{d\varphi}\right)\right]\\ &= \frac{ds_0}{ds}\cdot\left[\left(\frac{d\varphi}{ds_0}\right)^2\cdot\frac{d}{d\varphi}\left(\frac{ds_0}{ds}\right)\cdot\frac{d\mathbf{X}}{d\varphi}+\frac{ds_0}{ds}\cdot\left(\frac{d\varphi}{ds_0}\right)^2\cdot\frac{d}{d\varphi}\left(\frac{d\mathbf{X}}{d\varphi}\right)\right]\end{aligned} \tag{A2.7}$$

Using (2.14), we have

$$\begin{aligned}\boldsymbol{\kappa}_w &= \left(\frac{d\varphi}{ds_0}\right)^2\frac{ds_0}{ds}\cdot\left[\begin{array}{l}\dfrac{d}{d\varphi}\left(\dfrac{1}{\sqrt{\sin^2(\alpha_0)+\cos^2(\alpha_0)(1+\varepsilon_c)^2\{1+\kappa_c r\sin(\varphi)\}^2}}\right)\cdot\dfrac{d\mathbf{X}}{d\varphi}\\ +\dfrac{ds_0}{ds}\cdot\dfrac{d}{d\varphi}\left(\dfrac{d\mathbf{X}}{d\varphi}\right)\end{array}\right]\\ &= \left(\frac{\sin(\alpha_0)}{r}\right)^2\frac{ds_o}{ds}\cdot\left[\begin{array}{l}\left(\dfrac{-\kappa_c r\cos(\varphi)\cos^2(\alpha_0)(1+\varepsilon_c)^2\{1+\kappa_c r\sin(\varphi)\}}{\left[\sin^2(\alpha_0)+\cos^2(\alpha_0)(1+\varepsilon_c)^2\{1+\kappa_c r\sin(\varphi)\}^2\right]^{3/2}}\right)\cdot\dfrac{d\mathbf{X}}{d\varphi}\\ +\dfrac{ds_0}{ds}\cdot\dfrac{d}{d\varphi}\left(\dfrac{d\mathbf{X}}{d\varphi}\right)\end{array}\right]\end{aligned} \tag{A2.8}$$

By defining

$$B = \frac{r\cos(\varphi)\cos^2(\alpha_0)(1+\varepsilon_c)^2\{1+\kappa_c r\sin(\varphi)\}}{\left[\sin^2(\alpha_0)+\cos^2(\alpha_0)(1+\varepsilon_c)^2\{1+\kappa_c r\sin(\varphi)\}^2\right]^{3/2}} \tag{A2.9}$$

the curvature vector is written as

$$\kappa_w = \left(\frac{\sin(\alpha_0)}{r}\right)^2 \cdot \frac{ds_0}{ds} \cdot \left[-\kappa_c B \frac{d\mathbf{X}}{d\varphi} + \frac{ds_0}{ds} \cdot \frac{d}{d\varphi}\left(\frac{d\mathbf{X}}{d\varphi}\right)\right] \tag{A2.10}$$

which is identical to (2.15).

Linearization of (2.36)

From (2.36), the axial strain of a wire in the cable is

$$\varepsilon_w^{stick} = \sqrt{\sin^2(\alpha_0) + \cos^2(\alpha_0)(1+\varepsilon_c)^2\left[1+\kappa_c r \sin(\varphi)\right]^2} - 1 \tag{A2.11}$$

For small axial strain, ε_c, and curvature, κ_c, of the cable, the above expression can be approximated by a linearized expression as follows:

$$\begin{aligned}
\varepsilon_w^{stick} &= \varepsilon_w^{stick}\Big|_{\varepsilon_c=0,\,\kappa_c=0} + \left(\frac{d\varepsilon_w^{stick}}{d\varepsilon_c}\Big|_{\varepsilon_c=0,\,\kappa_c=0}\right)\varepsilon_c + \left(\frac{d\varepsilon_w^{stick}}{d\kappa_c}\Big|_{\varepsilon_c=0,\,\kappa_c=0}\right)\kappa_c \\
&= 0 + \left(\frac{\cos^2(\alpha_0)(1+\varepsilon_c)\left[1+\kappa_c r\sin(\varphi)\right]^2}{\sqrt{\sin^2(\alpha_0)+\cos^2(\alpha_0)(1+\varepsilon_c)^2\left[1+\kappa_c r\sin(\varphi)\right]^2}}\Big|_{\varepsilon_c=0,\,\kappa_c=0}\right)\varepsilon_c \\
&\quad + \left(\frac{\cos^2(\alpha_0)(1+\varepsilon_c)^2\left[1+\kappa_c r\sin(\varphi)\right] r\sin(\varphi)}{\sqrt{\sin^2(\alpha_0)+\cos^2(\alpha_0)(1+\varepsilon_c)^2\left[1+\kappa_c r\sin(\varphi)\right]^2}}\Big|_{\varepsilon_c=0,\,\kappa_c=0}\right)\kappa_c \\
&= \cos^2(\alpha_0)\left[\varepsilon_c + \kappa_c r\sin(\varphi)\right]
\end{aligned} \tag{A2.12}$$